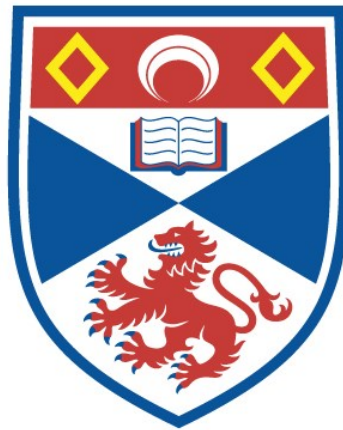# Electron microscopic studies of novel crystal morphologies and related growth mechanisms

Weihao Sun

A thesis submitted for the degree of PhD
at the
University of St Andrews

2022

Full metadata for this thesis is available in
St Andrews Research Repository
at:
https://research-repository.st-andrews.ac.uk/

Identifier to use to cite or link to this thesis:

DOI: https://doi.org/10.17630/sta/204

Declarations

Candidate's declaration

I, Weihao Sun, do hereby certify that this thesis, submitted for the degree of PhD, which is approximately 44,000 words in length, has been written by me, and that it is the record of work carried out by me, or principally by myself in collaboration with others as acknowledged, and that it has not been submitted in any previous application for any degree. I confirm that any appendices included in my thesis contain only material permitted by the 'Assessment of Postgraduate Research Students' policy.

I was admitted as a research student at the University of St Andrews in August 2018.

I received funding from an organisation or institution and have acknowledged the funder(s) in the full text of my thesis.

Date   07/Jul/2022   Signature of candidate

Supervisor's declaration

I hereby certify that the candidate has fulfilled the conditions of the Resolution and Regulations appropriate for the degree of PhD in the University of St Andrews and that the candidate is qualified to submit this thesis in application for that degree. I confirm that any appendices included in the thesis contain only material permitted by the 'Assessment of Postgraduate Research Students' policy.

Date   07/Jul/2022   Signature of supervisor

Permission for publication

In submitting this thesis to the University of St Andrews we understand that we are giving permission for it to be made available for use in accordance with the regulations of the University Library for the time being in force, subject to any copyright vested in the work not being affected thereby. We also understand, unless exempt by an award of an embargo as requested below, that the title and the abstract will be published, and that a copy of the work may be made and supplied to any bona fide library or research worker, that this thesis will be electronically accessible for personal or research use and that the library has the right to migrate this thesis into new electronic forms as required to ensure continued access to the thesis.

I, Weihao Sun, confirm that my thesis does not contain any third-party material that requires copyright clearance.

The following is an agreed request by candidate and supervisor regarding the publication of this thesis:

Printed copy

No embargo on print copy.

Electronic copy

Embargo on all of electronic copy for a period of 2 years on the following ground(s):

- Publication would preclude future publication

Supporting statement for electronic embargo request

There are two chapters unpublished.

Title and Abstract

- I agree to the title and abstract being published.

Date   07/Jul/2022   Signature of candidate

Date   07/Jul/2022   Signature of supervisor

Underpinning Research Data or Digital Outputs

Candidate's declaration

I, Weihao Sun, understand that by declaring that I have original research data or digital outputs, I should make every effort in meeting the University's and research funders' requirements on the deposit and sharing of research data or research digital outputs.

Date   07/Jul/2022   Signature of candidate

Permission for publication of underpinning research data or digital outputs

We understand that for any original research data or digital outputs which are deposited, we are giving permission for them to be made available for use in accordance with the requirements of the University and research funders, for the time being in force.

We also understand that the title and the description will be published, and that the underpinning research data or digital outputs will be electronically accessible for use in accordance with the license specified at the point of deposit, unless exempt by award of an embargo as requested below.

The following is an agreed request by candidate and supervisor regarding the publication of underpinning research data or digital outputs:

Embargo on all of electronic files for a period of 2 years on the following ground(s):

- Publication would preclude future publication

Supporting statement for embargo request

Thesis contains preliminary results that have not yet been published in the literature and so a 2-year embargo is requested.

Title and Description

- I require an embargo on the description only

Date   07/Jul/2022   Signature of candidate

Date   07/Jul/2022   Signature of supervisor

Acknowledgments

Foremost, I would like to express my gratitude to my supervisor, Professor Wuzong Zhou, for his valuable guidance and help throughout my doctorate study. I always admire his insightful ideas and suggestions during our discussions. He has not only been an excellent supervisor but also a friend-like mentor.

Thanks also goes to previous group members in Wuzong's group, Dr Jialu Chen and Dr Shitao Wu. As senior members, they assisted in many aspects during my PhD research. As friends, they brought joy and happiness to me during my time at St Andrews. The friendship will be treasured by me.

Then, I would like to thank Mr Ross Blackley, Dr Aaron Naden and Dr David Miller for their training and demonstration to get me familiar with electron microscopes. And Dr Yuri Andreev for his help in XRD operation. Furthermore, I sincerely thank Professor Manfred Buck and Dr Georg Haehner for their enlightening assessment and instructions as my annual assessors. My collaborators, Professor Rushi Liu and Dr Bao Zhen from National Taiwan University, Professor Wenbo Yue and Miss Jin Zhang from Beijing Normal University and many others are thanked for their cooperation and support in my experimental work. Members and staff in School of Chemistry and University of St Andrews are also thanked for their help in both my research and daily life.

I am also grateful for the company of my family and friends. Their encouragement and support are indispensable for my fulfilment of PhD study.

Finally, I appreciate the joint scholarship from Chinese Scholarship Council and University of St Andrews. It is really my honour to pursue a doctoral degree here at this wonderful university.

Publications

- R. G. E. Molloy, **W. H. Sun**, J. L. Chen and W. Z. Zhou, Structure and cleavage of monosodium urate monohydrate crystals, Chemical Communications. **2019**, 55, 2178-2181.

- Z. Bao, Y. J. Tseng, W. You, W. Zheng, X. Chen, S. Mahlik, A. Lazarowska, T. Lesniewski, M. Grinberg, C. Ma, **W.H. Sun**, W.Z. Zhou, R. S. Liu and J. P. Attfield, Efficient Luminescence from $CsPbBr_3$ Nanoparticles Embedded in Cs_4PbBr_6, Journal of Physical Chemistry Letters. **2020**, 11(18), 7637-7642.

- Z. Bao, C. Y. Hsiu, M. H. Fang, N. Majewska, **W.H. Sun**, S. J. Huang, E. C. Y. Yuan, Y. C. Chang, J. C. C. Chan, S. Mahlik, W.Z. Zhou, C. W. Yang, K. M. Lu and R. S. Liu, Formation and Near-Infrared Emission of $CsPbI_3$ Nanoparticles Embedded in Cs_4PbI_6 Crystals, ACS Applied Materials & Interfaces. **2021**,13(29),34742-34751 .

- **W.H. Sun** and W.Z. Zhou, Dual-step reduction of copper and formation mechanism of Cu pseudo-icosahedral microcrystals, Crystal Growth & Design. **2022**, 22, 2611–2619.

- **W.H. Sun** and W.Z. Zhou, Growth Mechanism and Microstructures of Cu_2O/PVP Spherulites, RSC Advances, **2022**, in press

- J. Zhang, **W.H. Sun**, W.Z. Zhou and W. Yue, Exfoliation of Ti_3C_2 MXene nanosheets to nanowires, **2022**, manuscript in preparation.

- **W.H. Sun** and W.Z. Zhou, Formation mechanism of embedding phenomenon of $CsPbBr_3$ Nanocrystallites in Cs_4PbBr_6 Crystals, **2022**, manuscript in preparation.

Abstracts

This project explores selected crystals with novel morphologies and corresponding growth mechanisms. Crystal samples from different growth stages are obtained by interrupting the reaction in order to study the growth mechanisms step by step. To achieve the characterisations of the crystals, electron microscopes and in-built electron spectroscopic techniques are the major implements. Together with electron microscopy, other techniques, such as X-ray diffraction and infrared spectroscopy, are also employed. Schematic visualisation is exploited to illustrate the formation mechanisms.

Copper pseudo-icosahedral crystals are prepared and studied. Polyvinylpyrrolidone - assisted growth route involving dual-step reduction and multiple intermediate phases is revealed. The attribute of pseudo-icosahedral is discussed morphologically. Using the same synthesis system but different reactant, Cu_2O spherulites are prepared. By examining the polarity of the spherulites and the feature of Cu_2O nanocrystallites in PVP matrix, the formation mechanism concerning intrinsic dipolar force is proposed.

Cs_4PbBr_6 rhombohedral crystals with embedded $CsPbBr_3$ nanocrystallites are produced via antisolvent preparation method. Despite the sensitivity to election beam exposure, we manage to visualise the material using electron microscopy. With observed evidence of amorphous precursor, a formation mechanism associated with the precursor amorphous phase is proposed. Different antisolvents are tested on their effects of the morphology. Water triggered transformation of Cs_4PbBr_6 to $CsPb_2Br_5$ and $CsPbBr_3$ is realised.

Electron microscopic and spectroscopic information of $Ti_3C_2T_x$ nanowire clusters synthesised at Beijing Normal University reveals the dimensional degradation mechanism. From the oxidation of layered $Ti_3C_2T_x$ structure, interconnected Ti_3C_2O and Ti_3C_2 nanowires are produced.

We anticipate that this doctorate project can provide new perspectives in understanding non-classical crystal growth, set an example for the study of beam sensitive materials and inspire the morphology engineering of crystalline materials.

Abbreviations

BF	Bright field
BFDH	Bravais–Friedel–Donnay–Harker
BSE	Backscattered electron
CCD	Charge-coupled device
CIF	Crystallographic information file
CTEM	Conventional transmission electron microscope
DF	Dark field
DMSO	Dimethyl sulfoxide
DMF	Dimethylformamide
ED	Electron diffraction
EELS	Electron energy loss spectroscopy / spectrometer
EDS, EDX	Energy dispersive X-ray spectroscopy / spectrometer
EM	Electron microscopy / microscope
FFT	Fast Fourier transform
FIB	Focused ion beam
FTIR	Fourier-transform infrared spectroscopy / spectrometer
HAADF	High-angle annular dark field
HRTEM	High resolution transmission electron microscopy
IR	Infrared spectroscopy / spectrometer
OA	Oleic acid
OLA, OAm	Oleyl amine
PVP	Polyvinylpyrrolidone
PXRD	Powder X-ray diffraction
SAED	Selected area electron diffraction
SE	Secondary electron
SEM	Scanning electron microscopy / microscope
STEM	Scanning transmission electron microscopy / microscope
SXES	Soft X-ray electron spectroscopy / spectrometer
TEM	Transmission electron microscopy / microscope
XRD	X-ray diffraction

Table of Contents

Chapter 1 Introduction

1.1 Basic Crystallography

A crystal is a solid material extending to 3 spatial dimensions consisting of atoms, molecules or ions packed regularly and periodically. Crystals play crucial roles in many aspects, including chemistry, physics, material sciences, geology, biology, etc.[1,2]

For any pattern composed of periodic fundamental parts, the fundamental part is defined as a motif. In crystallography, a lattice is a 3D pattern with periodic arrangement. A unit cell is the identical motif that stacks with each other to fill a lattice. The 3D unit cell has its three axes termed a, b and c, and three interaxial angles, α, β and γ.

When describing the lattice in its 3D space, as a basic motif, the unit cell can be provided certain repeating operations spatially to achieve the lattice arrangement. The operation is defined as symmetry. General symmetries are rotation, translation, reflection and inversion. Combining the symmetry operations in 2D and 3D, symmetry elements can be divided as mirror plane, rotation axis, screw axis, glide plane, inversion centre, roto-inversion and rotation-reflection.

Defined by the minimum symmetry elements, there are 7 crystal systems. Based on lattice centring types, primitive (P), body-centred (I), base-centred(B) and face-centred (F), 14 Bravais lattices are assigned. The 7 crystal systems can be split into 32 point groups based on point symmetry elements, such as rotation axis and roto-inversion. Furthermore, the 32 point groups can be expanded to 230 space groups with 2D and 3D symmetry elements (e.g. screw axis, glide planes).[1,3,4] **Figure 1.1** illustrates a 6-fold screw axis in a hexagonal structure. Towards the screw axis, every atom in the unit cell moves 1/6 unit-cell distance to form a 6-fold symmetry, which is expressed as 6_1.

Worth taking note of, in crystallography, the rotation axis and screw axis can only be 1, 2, 3, 4 and 6 fold as other options will not be able to fill the whole space, hence the crystallographic restriction theorem develops.[4] However, quasi-crystals with 5-fold symmetry and long-range ordered structures are discovered.[5,6]
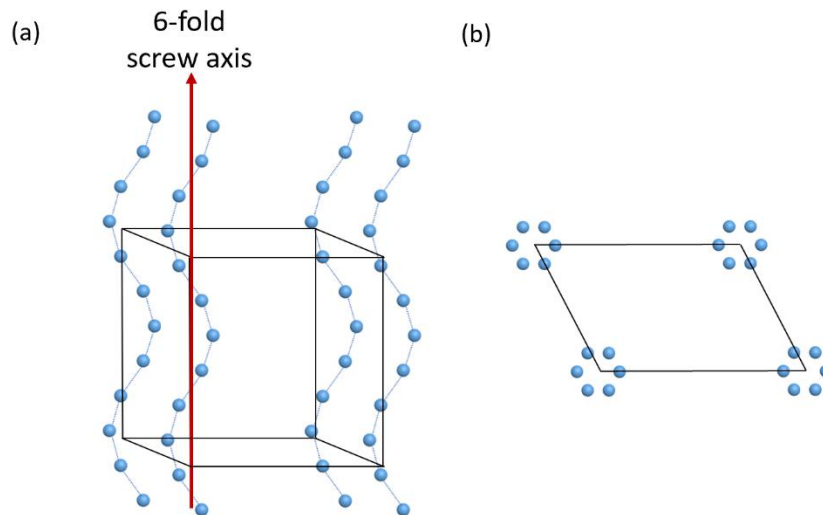
Figure 1.1 The 3-dimensional view (a) and the top view (b) of the schematic illustration of 6-fold screw axis symmetry in a hexagonal structure.

To describe the planes and directions of a Bravais lattice, Miller indices (hkl) are unveiled as the notation system[4] which is derived from the reciprocity of fractional axial intercepts.

The information of crystals is now included in respective crystallographic information files (CIF) promulgated by the International Union of Crystallography.[7] A CIF file contains at least the chemical information (name, elements, etc.), unit cell lengths in 3 directions (a, b, c), interaxial angles (α, β, γ), atomic coordinates and allocated space group with specified experimental conditions. By implementing a CIF file, one can visualise the crystal structure with specific software. In the present project, the visualisation of crystal structures and interpretation of XRD patterns, electron diffraction patterns and HRTEM images are based on the published CIF files from databases such as Inorganic Crystal Structure Database (ICSD).

Table 1.1 Types of defects in spatial classifications.

Classification	Types
Point defect	Atomic vacancy, interstitial, anti-site, impurity atom
Line defect	Dislocation, disclination, dispiration
Planar defect	Grain boundary, twinning, stacking fault
Bulk defect	Inclusion, Void

2

Theoretical crystals are always regarded to be idealised and perfect. In contrast, synthesised crystals can contain defects due to the existing impurities, unstable experimental conditions, etc. As shown in **Table 1.1**, based on the dimensions, defects can be classified as 0D defects (point defects), 1D defects (line defects), 2D defects (planar defects) and 3D defects (bulk defects).

Crystal defects impact the crystal quality which desire to be avoided when growing pure crystals. However, people's understanding of defects has changed as material science develops. Crystal defects change the crystal structure, hence altering the physical properties of a crystal.[2,8,9] The point defect atomic vacancy introduced into ionic Co_3O_4 crystal structure can change the charge distribution and electron density, thus enhancing the electrocatalysis performance.[10] Bulk inclusion defects which bring $CsPbBr_3$ nanoparticles into the original Cs_4PbBr_6 matrix can generate efficient and stable green luminescence.[11] Leveraging inevitable crystal defects for amplified physical properties has made crystal defect engineering a novel branch in material engineering field.[9,12,13]

1.2 Crystal Growth Theories

Crystals can be grown from liquid (solution), solid[14], melt[15] and vapour[16] techniques. Because the crystals involved in this project are prepared from solution techniques, crystal growth theories introduced in this section mostly concern solution crystal growth.

The traditional basic steps involved in the formation of a crystal from a liquid solution are[17]: achievement of supersaturation, nucleation and growth of the nuclei into crystals of distinct morphologies.

1.2.1 Nucleation Theories

Nucleation is the premier point of crystallisation where solid-phase nuclei firstly emerge. In a solution system, the driving force of nucleation is often supersaturation. If there are foreign particles which serve as nucleation sites, then the nucleation process is heterogeneous, otherwise the nucleation process is homogeneous. Both types are known as primary nucleation. Secondary nucleation occurs when nucleation is induced by the presence

of crystals of the same substance, which is the main source for the continuous creation of new particles in the crystallisation process. A nucleus is generally thought to have 10 to 1000 monomers (atoms, ions, molecules).[18]

Classical nucleation theory is widely used to describe the thermodynamics of nucleation with certain simplifications, which can be traced back to the free energy theory of Gibbs in 19th century, discussing the equilibrium of the isolated homogeneous system.[19] The theory supposes that the bulk energy of a nascent ideal nucleus drives nucleation. Assuming an ideal spherical nucleus of a radius r (typically formed during homogeneous nucleation), the total change of free energy of the system is

$$\Delta G_T = \Delta G_V + \Delta G_S = \frac{-4\pi r^3}{3v} \cdot kT\, lnS \,+\, 4\pi r^2 \sigma \qquad (1.1)$$

where ΔG_V represents the free energy change when forming a nucleus of a certain volume, ΔG_S represents the interfacial free energy change, v is the molecular volume, k is the Boltzmann constant (1.38 x 10^{-23} J·K^{-1}), T is the absolute temperature, r is the radius of the nucleus, S is the supersaturation ratio, and σ is the surface free energy per area. Atoms or ions need to overcome the nucleation energy barrier to aggregate together to form nuclei, of which the driving force is derived from supersaturation in the liquid situations.[20]
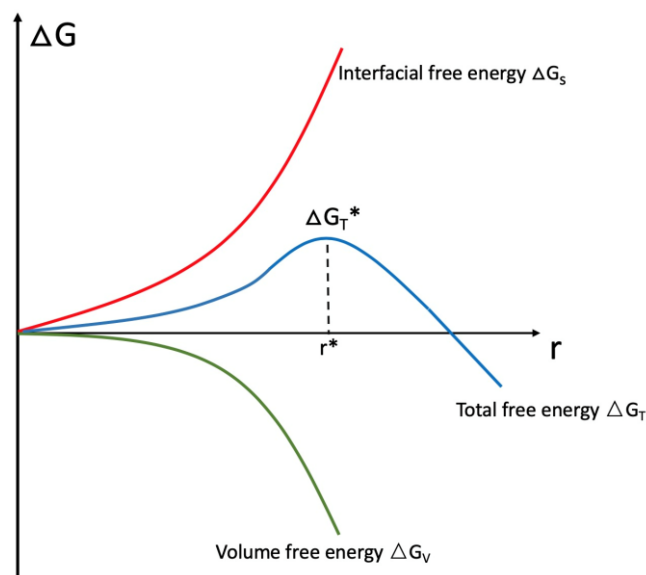
Figure 1.2 Schematic representation which shows the dependence of Gibbs free energy (nucleation barrier, ΔG_T) on nucleus size (r).

As shown in **Figure 1.2**, when r is relatively small, ΔG_S dominates the ΔG_T equation. As r increases, the effect of volume becomes more crucial. The value of r at the ΔG_T maximum is defined as the critical radius of the nucleus. The value of r* is derived as

$$r^* = \frac{2\sigma v}{kT \ln S}$$

(1.2)

J is defined as the nucleation rate (number of nuclei per unit volume per unit time), which can be expressed in the form of the Arrhenius reaction velocity equation,

$$J = A \exp\left(\frac{-\Delta G^*}{kT}\right)$$

(1.3)

where A is the pre-factor which is determined by supersaturation and T is the absolute temperature.[20]

Classical nucleation theory applies to the one-step nucleation systems with a low supersaturation and a slow nucleation process so that any microscopic disturbances can be discarded. It states that the structure of critical nuclei is identical to that of large crystals grown from the nuclei. However, many facts during nucleation, for instance, the existence of interfacial tension in a liquid crystal growth system and the dynamic equilibrium of slow-growing systems which leads to the dissolution of surface ions, impede the further development of classical nucleation theory. Furthermore, classical nucleation theory idealises that nucleation is a one-step process with mainly an energy barrier.[20,21]

As modern experimental and observation techniques develop, evidence of novel nucleation mechanisms is discovered, therefore the definition of non-classical nucleation is extended. Multi-step nucleation containing metastable phase or prenucleation cluster before distinct nuclei has been unearthed for miscellaneous cases including the crystallisation of biomaterials, organic and inorganic crystals.[20,22–24] Researches reveal that amorphous calcium carbonate is intimately involved in the nucleation of calcium carbonate as a pre-nucleation precursor.[23,25] Ruiz-Agudo *et al.* witnessed that before the crystallisation of calcium oxalate, Ca^{2+} and $C_2O_4^{2-}$ associate with each other to form polynuclear stable complexes prior to phase transformation and nucleation.[26] Liu *et al.* synthesised and investigated polymer-like $(CaCO_3)_n$ oligomer structure during the nucleation process by applying triethylamine as the stabiliser.[27]

Instead of focusing on the thermodynamics of nucleation and making assumptions, researches on non-classical pathways predominantly emphasise the direct observation of hidden procedures during crystal nucleation, proliferating novel nucleation pathways from practical experiments. Meanwhile, additives can be applied to preserve momentary nucleation precursors, alter the nucleation process and further control the nuclei size.[27,28]

1.2.2 Classical Theories of Crystal Growth

After the nuclei attain critical size, ions in the ambient phase transport to and attach to the surface of the nuclei to form crystals with distinct morphologies. Constant with nucleation, which is the first step of crystallisation, the driving force of further crystal growth is also supersaturation. As demonstrated in equation (1.1), supersaturation is crucial for nucleation. When the process comes to crystal growth by the attachment of the ambient phase, the free energy change per unit volume can be derived as

$$\Delta G_V = - kT \, lnS \tag{1.4}$$

Based on the free energy theory proposed by Gibbs, it is widely accepted that when a crystal reaches its dynamic equilibrium in the mother solution, the free energy is at a minimum value. Further theories of crystal growth are developed, discussing not only the thermodynamics but also the growth mechanism, equilibrium morphology, growth rate etc.

Surface energy theory emphasises the surface energy, thermodynamics and velocity of crystal growth. Gibbs firstly hypothesised that the surface energy of a grown shape was the lowest. Wulff proposed the famous Wulff theorem which was further applied to predict a crystal's equilibrium shape.[17,29] The value of surface energy of corresponding face σ_{hkl} determines the shape of a small crystal. If σ_{hkl} is isotropic for every face, the terminal shape would be spherical. Marc and Ritzel[30] further supplemented the theory with surface tension and solubility of surface components. When the solubility of ions back into the mother solution is almost the same, with isotropic σ_{hkl}, the morphology can still be spherical, otherwise the morphology would be determined by both surface energy and solubility.

Diffusion theory offers a new perspective toward crystallisation which assumes a concentration gradient in the vicinity of a growing surface and takes crystallisation as the reversed process of dissolution.[17]

For the study of crystal morphology, the adsorption layer theory proposed by Kossel, Stranski, Volmer and Weber[31–33] states that a new layer of crystal face starts from the centre. And the attachment energy (from either van der Waals forces or electrostatic forces) between building units and the growing sites increases from terrace to kink sites. Thus the crystal growth process and energy distribution are not continuous. Building units attach on the sites with discord attachment energies, causing inconsistent growth rates in corresponding directions, and eventually leads to different morphologies. This theory satisfies the situation of rapid growth caused by high supersaturation which emphasises the direction-dependent growth rate.

Screw dislocation theory (or BCF theory) developed by Burton, Cabrera and Frank is based on adsorption layer theory and was used to explain the high growth rate under low supersaturation.[34–36] Instead of discontinuous sites, the crystal surface has screw dislocations or spiral steps to serve as continuous anchors for growth steps. Growth takes place only by the rotation of steps around the dislocation point, as demonstrated in **Figure 1.3**. This theory was proved by the successful observation of hillocks and spirals on the crystal surface using the modern atomic force microscopy technique.[37]
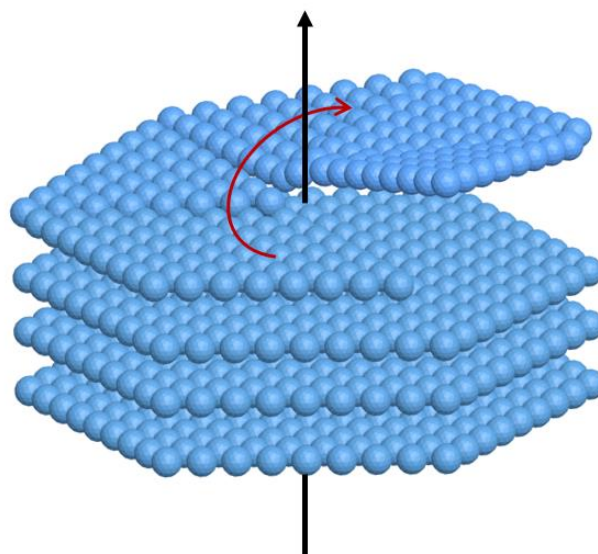

Figure 1.3 A model of a screw dislocation with the crystal growth direction marked.

To predict the theoretical morphology of a crystal, consolidating surface energy theory, the Bravais–Friedel–Donnay–Harker (BFDH) law was proposed.[38,39] Faces with large d-spacings d_{hkl} are expected to have low surface energy, displaying their importance in determining the final morphology. The BFDH law can also be stated as

$$R_{hkl} \propto \frac{1}{d_{hkl}} \tag{1.5}$$

where R_{hkl} is the growth rate along [hkl] direction and d_{hkl} is the interplanar spacing. The fast-growing faces of a crystal will always be covered by those slow-growing faces (as the fast ones may stop growing while the slow ones keep growing). Therefore, a crystal always has a finalised morphology with low-index faces. **Figure 1.4** demonstrates the growth rates of different faces and the 2D morphology evolution over time of a cubic crystal structure viewed from the c axis. As the d-spacing of (110) is smaller than those of (100) and (010) in a cubic crystal system, according to BFDH law, the growth rate of (110) is faster than those of (100) and (010). Initially, (110) plane will form first followed by (100) and (010) planes. When (110) plane finishes, the other two keep their growing, covering (110) plane, resulting in a cubic structure with (100) and (010) planes exposed.
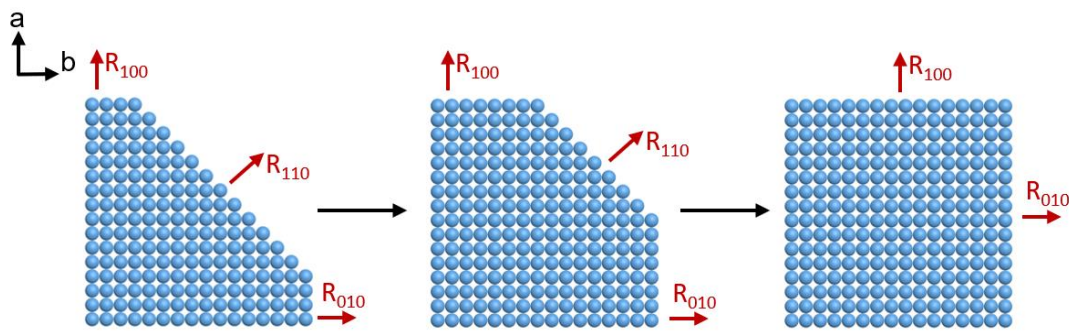
Figure 1.4 A 2D schematic demonstration of BFDH law.

Classical crystal growth theories based on the layer-by-layer growth on primary nuclei can explain the growth mechanism of simple crystal shapes and show the importance of crystallisation thermodynamics. However, applying modern electron microscopes, there are complicated crystal morphologies observed which may not obey the BFDH law and cannot be simply explained by the aforementioned theories. Therefore, many new mechanisms

regarding individual complicated crystal growth situations were proposed and assigned as non-classical crystal growth routes.

1.2.3 Non-classical Crystal Growth

Considering the sophisticated factors during crystal growth, such as synergy between crystallising phase and the mother solution, fluctuation of experimental conditions, various growth routes can happen, distinguishing themselves from classical layer-by-layer growth. Although non-classical crystal growth mechanisms are always identical to individual crystals, based on discovered cases, there are several sketchy subcategories. As the field of non-classical crystal growth develops, novel mechanisms in and out of those subcategories are still being investigated and published.

Ostwald ripening describes the phenomenon that small crystals or particles dissolve and deposit again onto the surface of larger ones, as demonstrated in **Figure 1.5(a)**. In thermodynamics, the driving force is that smaller particles possess higher interfacial energy. Based on the intention to minimise the surface free energy of the crystallisation system, large particles are favoured. Jia and Guo successfully synthesised α-Fe_2O_3 submicron cubes and discovered the hidden mechanism, Ostwald ripening of initial α-Fe_2O_3 nanorods derived from oriented aggregation.[40] Zhang *et al.* synthesised Pd nanocrystals with high uniformity by separating the nucleation and crystal growth steps, in which Ostwald ripening was emphasised.[41] Johnson *et al.* demonstrated an Ostwald ripening strategy of epitaxial growth and controllable layer creation by injecting small sacrificial nanocrystals as shell precursors onto large nanocrystals.[42]

Ostwald ripening can happen not only outside but also inside a grown structure. From reported works, Ostwald ripening can be the general template-free mechanism to fabricate certain hollow structures, either spherical or non-spherical.[43–46] When a loose structure forms, the interior is full of high-energy small particles formed in the early growth stage. As crystallisation executes, the small particles dissolve and contribute to building the shell, leaving an interior cavity. On the contrary, limiting Ostwald ripening process can produce and preserve quantum dots.[47]
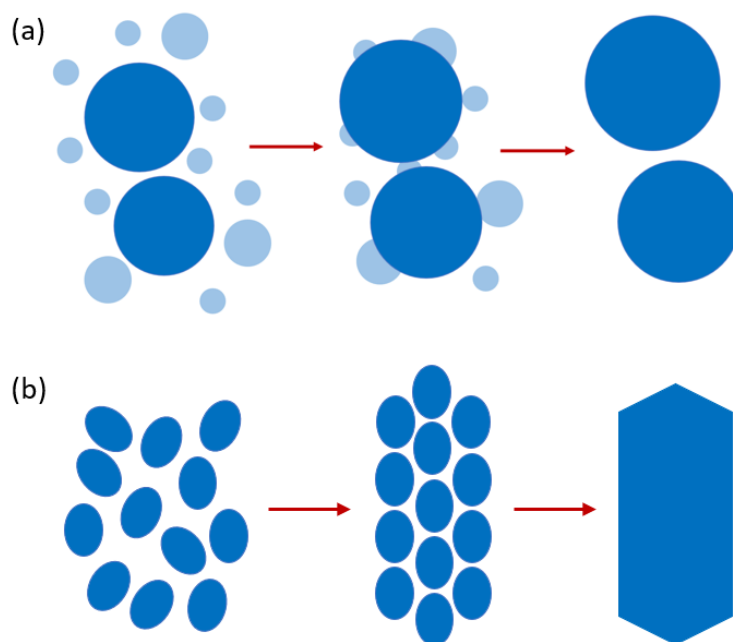
Figure 1.5 Simplified diagram illustration of (a) Ostwald ripening and (b) oriented attachment.

Based on the growth and coarsening of nanocrystalline TiO_2, Penn and Banfield proposed the oriented attachment mechanism in 1998, which is now a widespread non-classical growth mechanism.[48,49] Oriented attachment refers to the phenomenon when particles attach to a specific crystal surface to enable the crystal growth towards the corresponding crystallographic direction, as shown in **Figure 1.5 (b)**.

Oriented attachment plays a crucial role in bio-mineralisation.[50–52] Under the effect of oriented attachment, the final morphology will be anisotropic. In material science, the oriented attachment mechanism can be used to synthesise crystals with novel morphologies by the addition of organics or ligands.[53,54] To create anisotropic structures, such additives may attach to certain faces and deactivate the growth on those faces, therefore the growth in other directions is enhanced.

Reversed crystal growth route challenges the traditional view that a single crystal can only originate from the growth of a single nucleus. In 2007, Chen *et al.* studied zeolite analcime of confined hollow structure and discovered a growth route composed of inner nanocrystallite orientation and surface recrystallisation, which was believed to be the first case of reversed crystal growth mechanism.[55] The reversed crystal growth process involved an early-stage grown crystal structure and the Ostwald ripening inside the fixed structure.

Their work also indicates that superficial single crystals can be derived from the recrystallisation of polycrystalline.

Hollow $CaTiO_3$ perovskite crystals with different microstructures were obtained by the combination of oriented aggregation and interior Ostwald ripening, which was also an example of reversed crystal growth.[56] **Figure 1.6** illustrates a simplified Ostwald ripening of a cubic hollow structure during the late stage of reversed crystal growth, which provides the information of surface extension inwards. Reversed crystal growth mechanism was further developed for the cases of Zeolite A[57], ZnO microdisks[58] and metal-organic framework MIL-68 (In)[59]. Additionally, the reversed route was also witnessed in the naturally occurring growth of calcite.[60]
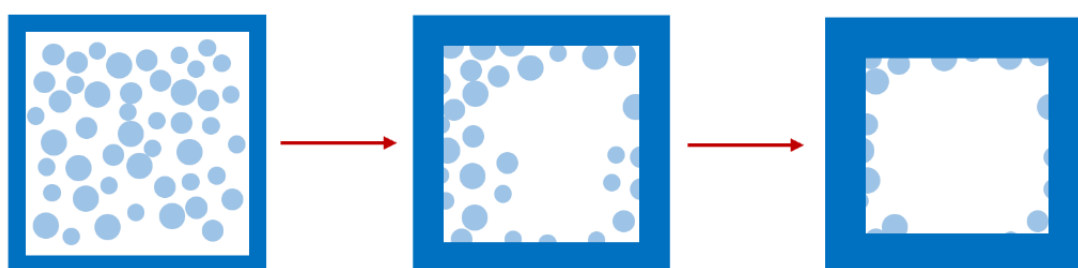
Figure 1.6 A schematic demonstration of interior Ostwald ripening to provide surface extension based on an early-formed cubic hollow structure.

The concept of reversed crystal growth offers a novel perspective on the unsolved growth mechanism of existing crystals. Crystals can form a mature architecture in an early stage but still have crystallisation behaviour inside which may be difficult to observe without modern electron microscopic techniques. The inside surface recrystallisation to form thick shells is actually the unusual interior Ostwald ripening process.

An electric dipole field represents the field between two equivalent but opposite charges. The dipole forces can exist in crystal structures. Although the charge of crystals is neutral, when the size is drilled down to nanocrystallites of several nanometres, the charge distribution of ions can generate a nanoscale dipole field. Those nanocrystallites then can orient themselves by applying dipole force and therefore grow into complicated morphology.

ZnO can form twinned crystals triggered by its intrinsic dipole field. For Wurtzite's hexagonal unit cell, in the c direction, the arrangement of Zn and O layers can create a dipole

field from the positively charged Zn to negatively charged O. With the present dipole field, individual nanocrystallites can then orient themselves to form large crystals. Morphologies of ZnO apple-like[61], twin-brush[62] and sea-urchin-like[63] mesocrystals based on dipole field were further reported. In those given cases of ZnO crystals, negatively charged organic agents were applied in order to stabilise the nanocrystallites during the growth using charge interaction. Dipole field also exists in nanoscale $CaCO_3$ crystals which results in the vaterite and calcite spherulites.[64,65] Dipole field driven crystal growth proves the existence of an electric field in the nanoscale crystal structure and extends the concept of non-classical crystal growth triggered by intrinsic forces.

Another non-classical route is the crystal defect driven growth. As claimed in **Section 1.1**, crystal defects can be significant for property optimisation. Moreover, crystal defects can be the driving force to trigger the formation of novel crystal morphologies. The most researched subclasses are dislocation driven crystal growth and twin defect driven crystal growth. Dislocation is generated by imperfect oriented attachment during crystal growth. While twin defect is the behaviour of two separate crystal planes contacting each other, creating a mirror symmetry.

Hierarchical crystal structure represents the type of structure with complicated sub-architectures or branches. Reported works show that by applying dislocation and twin defect, hierarchical structures can be obtained.

Gyro shape Ag_3PO_4 crystals were synthesised with the addition of the cooperation agent acrylamide by Wang *et al.*[66] They concluded that the helical growth towards the six <100> directions was triggered by the axial screw dislocation. Under visible-light irradiation, acrylamide executed polymerisation, simultaneously releasing energy. The energy satisfied the surface energy barrier to form dislocation and further led to the spinning growth towards three dimensions. PbTe hierarchical nanostructures on a large scale with various shapes, such as octapodal dendrites and hollow cubes, were synthesised by applying triethanolamine-assisted solvothermal method by Wang *et al.*[67] They stated that the screw dislocation prompted the formation of concave morphologies of those PbTe hierarchical structures. Another example is the screw dislocation driven formation of hierarchical superstructures of Ag-Ag_2O-AgO nanoparticles without the assistance of organic additives.[68]

Jun *et al.* synthesised TiO_2 hyper-branching nanocrystals via the solvothermal method and observed the twinning behaviour in those branch sites. One site can preserve multiple twinning to create hyper-branching hence producing star-like morphology based on the initial nanowire.[69] And based on their statement, the twinning occurred due to the instability during the 1D anisotropic nanowire growth. Ag and Cu nano dendrites containing twin defects and stacking faults were synthesised and studied by Chen *et al.* They claimed that the twin defects and stacking faults can be easily formed along a certain direction with a low stacking fault energy.[70] Furthermore, zigzag Zn_3P_2 and InP nanowires containing rigidly-ordered multiple twinning are synthesised through the vapour transport process.[71,72] **Figure 1.7** demonstrates a lattice scale twin defect.
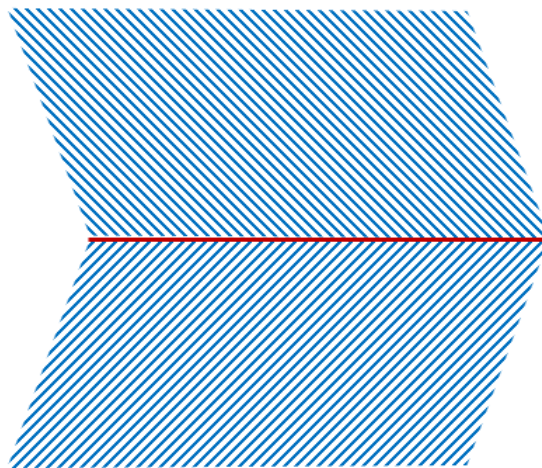
Figure 1.7 Schematic representation of a twin defect. The red line indicates the mirror symmetry of the two contacting crystal planes.

Even though classical crystal growth theories are not sufficient for the explanation of non-classical crystal growth routes, dividing non-classical routes into sub-steps, they still can be applied to explain some simplified steps. For example, the BFDH law and surface energy theory can be implemented to describe the initial growth stage when crystal faces of high surface energy exist.

Although those non-classical mechanisms have distinct features, they may not execute independently. As aforementioned, for reversed crystal growth, interior Ostwald ripening can be the intrinsic factor of the surface extension. Triggered by the dipole force, oriented attachment can indeed happen. Defects induced crystal growth is actually the oriented

growth triggered by defects, therefore the concept may have an intersection with oriented attachment. Overall, the definitions of those non-classical crystal growth routes may have overlapping parts. The definitions may evolve to be more precise as the non-classical crystal growth area develops.

Nevertheless, research on new growth routes and novel crystal morphologies are still undergoing, which will further expand the base of non-classical routes and offer references in designing crystalline materials with new shapes.

For instance, chiral and helical inorganic nanostructures have been intriguing to researchers nowadays as chirality may enable new applications. Chirality of crystalline structures may originate from screw dislocations and multiple twinning of both right-handed and left-handed styles.[73–76]

Another new mechanism was demonstrated by Turner *et al.* concerning octahedral zeolite X crystals. The final microscale zeolite X crystallised on the surface of prepared spherical zeolite P crystals, at the interface between the amorphous core and the shell of zeolite P. Their work elucidates that in a solvothermal condition, a new crystal phase can actually nucleate and crystallise on a large scale grown crystal, which differentiates itself from the process that the existing phase dissolves again to give rise to a new phase.[77] And during the whole crystal growth process, various phases of the same chemical formula can be produced and consumed in order to obtain the final phase. Xiao *et al.* elucidated in their work that $CaCO_3$ could undergo the preparation of amorphous calcium carbonate and vaterite to finally obtain calcite.[78]

1.2.4 Modern Electron Microscopic Investigation of Crystal Growth

Modern electron microscopes allow high-magnification and direct observation of crystal morphology and crystal structure which captures crystallographic information. Therefore, the detailed and unbiased crystal growth mechanism can be drawn relying on the direct observation of crystal growth.

Modern electron microscopic techniques include electron microscopy, electron diffractometry and electron spectroscopy. Principles of the techniques used in this project will be introduced in **Chapter 2**.

Typically to study the morphology evolution and growth process of a crystal, various specimens of different reaction times will be obtained to examine the characteristics of each growth stage. Scanning electron microscopy (SEM) and low magnification transmission electron microscopy (TEM) are leveraged to study the morphology which offers direct illustrations. Together with X-ray diffraction (XRD) and computational simulation of crystal structures, high resolution TEM (HRTEM) and electron spectroscopy are applied to check the crystallographic information, such as crystal phase, crystallinity, chemical composition, etc. Taking those into consideration, one may be capable of revealing the growth mechanism.

However, such analysis methods are actually ex-situ, which inevitably introduces interfering factors to some degree that one may not realise or observe. In ex-situ experiments, multiple syntheses with the same recipe can not guarantee the 100% repetition of the samples from different batches. Therefore, the in-situ electron microscopic technique is introduced into the crystal growth field. The in-situ method enables the real-time observation of reactions under TEM. Such a characterisation technique provides the direct observation of crystal growth without environmental disturbances, and can even generate a dynamic video of crystallisation motion which leaves many controversial crystallisation cases unambiguous.[79–81]

In-situ TEM has its advantages yet has its flaws. TEM uses an electron beam as the lighting source of which the accelerating voltage is high (typically over 200 kV). Such high-energy lighting source may offer substantial extra energy to the crystal growing system thus differing the crystallisation pathway from ex-situ preparation method. In-situ TEM specialises in fast crystal growth or the initial nucleation of slow crystal growth. It is unrealistic to grow crystals for days in a liquid cell sample holder of in-situ TEM. So crystallisation last for a longer time still requires ex-situ techniques to study the detailed growth stages. Additionally, samples can be manipulated (e.g. crushed or cut) to get more information (e.g. inner crystal structure) when applying ex-situ observation techniques. There are not many treatments that can be done towards the sample prepared inside in-situ TEM.

It is the single crystal XRD applied to reveal unknown crystal structures. Electron beam have smaller wavelength in comparison to X-ray, therefore, electron diffraction can do what XRD is capable of and perform beyond. Based on the related principle, rotary electron diffraction or 3D electron diffraction technique is developed. With rotary sample holder inside

a TEM, electron diffraction in 3 dimensions can be collected. Further using computational methods, a new real-space crystal structure with atomic coordinates can be drawn.[82–84]

Throughout this project, SEM and low-mag TEM are used to study the morphologies of crystalline materials. Together with X-ray diffraction and crystal structure modelling, HRTEM, selected area electron diffraction (SAED) and simulated electron diffraction (or fast Fourier transform) are used to examine the crystallinity, crystal size, crystal planar d-spacings, etc. infrared spectroscopy (IR) and electron spectroscopy are implemented to characteristic chemical bonding and elemental composition.

1.3 Aims and Objectives

The principal aims of this project are to reveal the unsolved non-classical crystal growth mechanisms of inorganic crystalline materials with novel morphologies and extend the case base of non-classical crystal growth by using electron microscopy, electron diffractometry, electron spectroscopy, X-ray diffractometry, infrared spectroscopy and crystallographic modelling. From the perspective of the application of electron microscopes, this project also aims to demonstrate the successful electron microscopic observation of electron beam sensitive crystalline materials and organic containing crystalline materials.

The detailed objectives of each project discussed in corresponding chapters are listed as follows:

1. To investigate the morphological and crystallographic characteristics of pseudo-icosahedral Cu microcrystals prepared via the solvothermal synthesis in the presence of polyvinylpyrrolidone (PVP). To demonstrate the multifunction of PVP during the crystal growth. To illustrate the dual step reduction, crystallisation and dissolution of intermediate phases as crystal growth processes. To challenge the current concept of icosahedral crystal based on the proposed theory and crystal growth mechanism.

2. To investigate the formation mechanism of Cu_2O/PVP spherulites. To provide a unique example of the existence of dipole force in cubic Cu_2O nanocrystallites, therefore expand the theme of dipole field driven crystal growth.

3. To synthesise Cs_4PbBr_6 rhombohedral microscale crystals with embedded $CsPbBr_3$ nanocrystallites by implementing antisolvent precipitation method and the low solubility of

the two phases in a mild condition. To demonstrate the embedding phenomenon (3D inclusion defect) of $CsPbBr_3$ nanoparticles in Cs_4PbBr_6 matrix. To reveal the incentive of the generation of embedded $CsPbBr_3$ containing Cs_4PbBr_6. To discuss the effects of solvent polarity on the morphology and crystallography of synthesised crystals. To demonstrate the water-triggered transformation of Cs_4PbBr_6 to $CsPb_2Br_5$, $CsPbBr_3$, $CsBr$ and $PbBr_2$.

4. To analyse the phase and morphological transformation from $Ti_3C_2T_x$ MXene layered structures to $Ti_3C_2T_x$ and Ti_3C_2 nanowire clusters. To examine the oxidation state change of Ti via electron spectroscopy and determine the phase evolution. To demonstrate the transformation mechanism based on the oxidation of layered MXene in the solution of KOH.

References

1   W. Borchardt-Ott, *Crystallography*, Springer, 3rd edn., 2011.

2   K.-W. Benz and W. Neumann, *Introduction to Crystal Growth and Characterization*, Wiley-VCH Verlag GmbH & Co., Weinheim, 2014.

3   C. Hammond, *The Basics of Crystallography and Diffraction*, Oxford University Press, Oxford, 3rd edn., 2009.

4   J. D. Patterson and B. C. Bailey, *Solid-State Physics*, Springer, 2018.

5   D. Shechtman, I. Blech, D. Gratias and J. W. Cahn, *Phys. Rev. Lett.*, 1984, **53**, 1951–1953.

6   D. L. D. Caspar and E. Fontano, *Proc. Natl. Acad. Sci.*, 1996, **93**, 14271–14278.

7   S. R. Hall, F. H. Allen and I. D. Brown, *Acta Crystallogr. Sect. A*, 1991, **47**, 655–685.

8   A. Kelly and K. M. Knowles, *Crystallography and Crystal Defects*, John Wiley & Sons, Ltd, 2nd edn., 2012.

9   J. Spitaler and S. K. Estreicher, *Front. Mater.*, 2018, **5**, 70.

10   Z. Cai, Y. Bi, E. Hu, W. Liu, N. Dwarica, Y. Tian, X. Li, Y. Kuang, Y. Li, X. Q. Yang, H. Wang and X. Sun, *Adv. Energy Mater.*, 2018, **8**, 1701694.

11   Z. Bao, Y. J. Tseng, W. You, W. Zheng, X. Chen, S. Mahlik, A. Lazarowska, T. Lesniewski, M. Grinberg, C. Ma, W. Sun, W. Zhou, R. S. Liu and J. P. Attfield, *J. Phys. Chem. Lett.*, 2020, **11**, 7637–7642.

12   Z. Dai, F. Qin, H. Zhao, J. Ding, Y. Liu and R. Chen, *ACS Catal.*, 2016, **6**, 3180–3192.

13   Z. Fang, B. Bueken, D. E. De Vos and R. A. Fischer, *Angew. Chemie. Int. Ed.*, 2015, **54**, 7234–7254.

14   A. McKinlay, P. Connor, J. T. S. Irvine and W. Zhou, *J. Phys. Chem. C*, 2007, **111**, 19120–19125.

15   E. V Zharikov, *J. Cryst. Growth*, 2012, **360**, 146–154.

16   R. Heinemann and P. Schmidt, *Cryst. Growth Des.*, 2020, **20**, 5986–6000.

17   K. B. Govindhan Dhanaraj and M. D. Vishwanath Prasad, *Springer Handbook of Crystal Growth*, Springer, Berlin Heidelberg, 2010.

18   S. Xu, Z. Hou, X. Chuai and Y. Wang, *Ind. Eng. Chem. Res.*, 2020, **59**, 18335–18356.

19   J. W. Gibbs, *Am. J. Sci.*, 1878, **s3**-**16**, 441–458.

20   S. Karthika, T. K. Radhakrishnan and P. Kalaichelvi, *Cryst. Growth Des.*, 2016, **16**, 6663–6681.

21   R. P. Sear, *Int. Mater. Rev.*, 2012, **57**, 328–356.

22   P. G. Vekilov, *Cryst. Growth Des.*, 2004, **4**, 671–685.

23   D. Gebauer and H. Cölfen, *Nano Today*, 2011, **6**, 564–584.

24   D. Zahn, *ChemPhysChem*, 2015, **16**, 2069–2075.

25   P. Raiteri and J. D. Gale, *J. Am. Chem. Soc.*, 2010, **132**, 17623–17634.

26 E. Ruiz-Agudo, A. Burgos-Cara, C. Ruiz-Agudo, A. Ibañez-Velasco, H. Cölfen and C. Rodriguez-Navarro, *Nat. Commun.*, 2017, **8**, 768.

27 Z. Liu, C. Shao, B. Jin, Z. Zhang, Y. Zhao, X. Xu and R. Tang, *Nature*, 2019, **574**, 394–398.

28 B. Jin, Z. Liu and R. Tang, *CrystEngComm*, 2020, **22**, 4057–4073.

29 G. Wulff, *Z. Krist.*, 1901, **34**, 449–530.

30 R. Marc and A. Ritzel, *Z. Phys. Chem*, 1911, **76**, 584.

31 W. Kossel, *Nachr. Ges. Wiss. Göttingen*, 1927, **135**, 135–143.

32 I. N. Stranski, *Z. Phys. Chem*, 1928, **136**, 259–278.

33 M. Volmer and A. Weber, *Z. Phys. Chem*, 1926, **119**, 277–301.

34 F. C. Frank, *Discuss. Faraday Soc.*, 1949, **5**, 48–54.

35 W. K. Burton, N. Cabrera and F. C. Frank, *Philos. Trans. R. Soc. London A*, 1951, **243**, 299–358.

36 M. Uwaha, *Prog. Cryst. Growth Charact. Mater.*, 2016, **62**, 58–68.

37 S. R. Qiu, A. Wierzbicki, C. A. Orme, A. M. Cody, J. R. Hoyer, G. H. Nancollas, S. Zepeda and J. J. De Yoreo, *Proc. Natl. Acad. Sci.*, 2004, **101**, 1811–1815.

38 J. D. H. Donnay and D. Harker, *Am. Mineral.*, 1937, **22**, 446–467.

39 J. Prywer, *J. Cryst. Growth*, 2004, **270**, 699–710.

40 B. Jia and L. Gao, *Cryst. Growth Des.*, 2008, **8**, 1372–1376.

41 Z. Zhang, Z. Wang, S. He, C. Wang, M. Jin and Y. Yin, *Chem. Sci.*, 2015, **6**, 5197–5203.

42 N. J. J. Johnson, A. Korinek, C. Dong and F. C. J. M. van Veggel, *J. Am. Chem. Soc.*, 2012, **134**, 11068–11071.

43 C. C. Yec and H. C. Zeng, *J. Mater. Chem. A*, 2014, **2**, 4843–4851.

44 J. Li and H. C. Zeng, *J. Am. Chem. Soc.*, 2007, **129**, 15839–15847.

45 T. P. Doan-Nguyen, S. Jiang, K. Koynov, K. Landfester and D. Crespy, *Angew. Chemie. Int. Ed.*, 2021, **60**, 18094–18102.

46 W. S. Wang, L. Zhen, C. Y. Xu, J. Z. Chen and W. Z. Shao, *ACS Appl. Mater. Interfaces*, 2009, **1**, 780–788.

47 R. D. Vengrenovich, Y. V Gudyma and S. V Yarema, *Semiconductors*, 2001, **35**, 1378–1382.

48 R. L. Penn, *Science.*, 1998, **281**, 969–971.

49 R. L. Penn and J. F. Banfield, *Am. Mineral.*, 1998, **83**, 1077–1082.

50 P. U. P. A. Gilbert, S. M. Porter, C.-Y. Sun, S. Xiao, B. M. Gibson, N. Shenkar and A. H. Knoll, *Proc. Natl. Acad. Sci.*, 2019, **116**, 17659–17665.

51 G. T. Zhou, Q. Z. Yao, J. Ni and G. Jin, *Am. Mineral.*, 2009, **94**, 293–302.

52 C. E. Killian, R. A. Metzler, Y. U. T. Gong, I. C. Olson, J. Aizenberg, Y. Politi, F. H. Wilt, A. Scholl, A. Young, A. Doran, M. Kunz, N. Tamura, S. N. Coppersmith and P. U. P. A. Gilbert, *J. Am. Chem. Soc.*, 2009, **131**, 18404–18409.

53   C. Zhu, S. Liang, E. Song, Y. Zhou, W. Wang, F. Shan, Y. Shi, C. Hao, K. Yin, T. Zhang, J. Liu, H. Zheng and L. Sun, *Nat. Commun.*, 2018, **9**, 421.

54   Y. Deng, C. W. Nan and L. Guo, *Chem. Phys. Lett.*, 2004, **383**, 572–576.

55   X. Y. Chen, M. Qiao, S. Xie, K. Fan, W. Zhou and H. He, *J. Am. Chem. Soc.*, 2007, **129**, 13305–13312.

56   X. Yang, J. Fu, C. Jin, J. Chen, C. Liang, M. Wu and W. Zhou, *J. Am. Chem. Soc.*, 2010, **132**, 14279–14287.

57   H. Greer, P. S. Wheatley, S. E. Ashbrook, R. E. Morris and W. Zhou, *J. Am. Chem. Soc.*, 2009, **131**, 17986–17992.

58   K. Self, H. Zhou, H. F. Greer, Z. R. Tian and W. Zhou, *Chem. Commun.*, 2013, **49**, 5411–5413.

59   K. McRoberts and W. Zhou, *CrystEngComm*, 2021, **23**, 7658–7662.

60   H. F. Greer, W. Zhou and L. Guo, *Cryst.*, 2017, **7**, 36.

61   Z. Liu, X. D. Wen, X. L. Wu, Y. J. Gao, H. T. Chen, J. Zhu and P. K. Chu, *J. Am. Chem. Soc.*, 2009, **131**, 9405–9412.

62   M. H. Liu, Y. H. Tseng, H. F. Greer, W. Zhou and C. Y. Mou, *Chem. Eur. J.*, 2012, **18**, 16104–16113.

63   B. M. Connolly, H. F. Greer and W. Zhou, *Cryst. Growth Des.*, 2019, **19**, 249–257.

64   H. F. Greer, M.-H. Liu, C.-Y. Mou and W. Zhou, *CrystEngComm*, 2016, **18**, 1585–1599.

65   S. Wu, J. I. Blake, L. Guo and W. Zhou, *Cryst. Growth Des.*, 2020, **20**, 3537–3545.

66   J.-D. Wang, J.-K. Liu, C.-X. Luo, Y. Lu and X.-H. Yang, *Cryst. Growth Des.*, 2013, **13**, 4837–4843.

67   Q. Wang, G. Chen and H. Yin, *J. Mater. Chem. A*, 2013, **1**, 15355–15369.

68   H. Yang, J. R. Zhang, W. Cao, J. Zhen and J. H. Wu, *Crystals*, 2020, **10**, 1084.

69   Y. Jun, H.-W. Chung, J. Jang and J. Cheon, *J. Mater. Chem.*, 2011, **21**, 10283–10286.

70   J. Chen, J. J. Davies, A. S. Goodfellow, S. M. D. Hall, H. G. Lancaster, X. Liu, C. J. Rhodes and W. Zhou, *Prog. Nat. Sci. Mater. Int.*, 2021, **31**, 141–151.

71   G. Shen, P.-C. Chen, Y. Bando, D. Golberg and C. Zhou, *J. Phys. Chem. C*, 2008, **112**, 16405–16410.

72   G. Shen, Y. Bando, B. Liu, C. Tang and D. Golberg, *J. Phys. Chem. B*, 2006, **110**, 20129–20132.

73   B. Sung, A. de la Cotte and E. Grelet, *Nat. Commun.*, 2018, **9**, 1405.

74   W. Ma, L. Xu, A. F. de Moura, X. Wu, H. Kuang, C. Xu and N. A. Kotov, *Chem. Rev.*, 2017, **117**, 8041–8093.

75   Y. Wang, J. Xu, Y. Wang and H. Chen, *Chem. Soc. Rev.*, 2013, **42**, 2930–2962.

76   S. W. Im, H. Y. Ahn, R. M. Kim, N. H. Cho, H. Kim, Y. C. Lim, H. E. Lee and K. T. Nam, *Adv. Mater.*, 2020, **32**, 1905758.

77 S. J. Turner, J. Chen, A. M. Z. Slawin and W. Zhou, *Chem. Commun.*, 2019, **55**, 862–865.

78 J. Xiao, Z. Wang, Y. Tang and S. Yang, *Langmuir*, 2010, **26**, 4977–4983.

79 C. M. Li, I. M. Robertson, M. L. Jenkins, J. L. Hutchison and R. C. Doole, *Micron*, 2005, **36**, 9–15.

80 M. H. Nielsen, S. Aloni and J. J. De Yoreo, *Science*, 2014, **345**, 1158–1162.

81 J. Wu, W. Gao, J. Wen, D. J. Miller, P. Lu, J. M. Zuo and H. Yang, *Nano Lett.*, 2015, **15**, 2711–2715.

82 X. Zou, S. Hovmöller and P. Oleynikov, *Electron Crystallography: Electron Microscopy and Electron Diffraction*, Oxford University Press, 2011.

83 D. Zhang, P. Oleynikov, S. Hovmöller and X. Zou, *Zeitschrift für Krist.*, 2010, **225**, 94–102.

84 Z. Huang, T. Willhammar and X. Zou, *Chem. Sci.*, 2021, **12**, 1206–1219.

Chapter 2 Experimental Methods and Characterisation

2.1 Crystal Growth Methods

Crystal growth techniques are classically divided into 3 ways, solid-to-solid growth, liquid-to-solid growth and gas-to-solid growth. In this project, the crystal growth of Cu icosahedra, Cu_2O spherulites, $CsPbBr_3$/Cs_4PbBr_6 cocrystals all happened in solution, involving liquid-to-solid transformation and supersaturation of the phase which crystallised. The solvothermal preparation method was applied when preparing Cu icosahedra and Cu_2O spherulites, which included the dissolution of reactants in organic solvent and the reduction reaction to create the crystalline phase in sealed Teflon autoclaves at a desired temperature. The growth of $CsPbBr_3$ and Cs_4PbBr_6 co-crystals was related to the low solubility and the supersaturation in the antisolvent toluene. The production of $Ti_3C_2T_x$ clusters involved solid-to-solid transformation which happened in KOH aqueous solution. Crystals at different growth stages might be collected to study the evolution by varying the reaction time.

Detailed synthesis methods and crystallisation techniques are discussed in each chapter.

2.2 Characterisation

To gain insights into the morphological and crystallographic information and further reveal the growth mechanisms, synthesised samples were characterised by diffraction techniques, electron microscopy and spectroscopy techniques. These techniques include powder X-ray diffraction (PXRD), selected area electron diffraction (SAED), scanning electron microscopy (SEM), transmission electron microscopy (TEM), high-resolution transmission electron microscopy (HRTEM), scanning transmission electron microscopy (STEM), soft X-ray electron spectroscopy (SXES) and energy dispersive X-ray spectroscopy (EDS). Additionally, infrared spectroscopy (IR) was applied to study the chemical bonding information. Based on the data obtained through those techniques, crystal modelling and visualisation were achieved via the following software, *Diamond, Auto CAD, 3Ds Max, Vesta* etc.

This chapter will briefly introduce the background theories and operation principles of the aforementioned techniques.

2.2.1 Powder X-ray Diffraction

XRD is a rapid and non-destructive technique to present the crystallographic information of given materials based on the diffraction behaviour of X-rays at specific angles.[1] X-ray is an electromagnetic wave which is produced by bombarding a metal target with high-energy electrons. Those high energy electrons knock orbital electrons out of the inner electron shell, creating shell vacancies. Then, electrons from the shells with higher energies fill up the vacancies, emitting characteristic X-rays corresponding to the energy difference between the two shells.

Diffraction is the slight bending of waves when passing around an obstacle. Worth taking note of, the size of the obstacle need to be comparable to the wavelength so that the wave can show its wave-like property and generate diffraction. X-rays can be harnessed to detect crystal structures because they have similar wavelengths (0.01 nm to 10 nm) to the spacing between crystal planes. Correspondingly, the wave nature of the X-rays gives rise to diffraction effects when passing through periodically-ordered crystal structures, producing diffraction patterns containing the information about the atomic arrangement in the crystal. This is the premise that X-ray diffraction can be a technique used for identifying phases and determining crystal structures.

XRD experiments are routinely carried out on either a single crystal or powder samples, therefore segmented into single crystal XRD and powder XRD (PXRD). PXRD was used in this project as the tool for characterising all the samples. A PXRD pattern is a 1D representation of 3D structural information, which is considered a unique feature of the provided crystalline material.[1]

The theory behind XRD is Bragg's law. Bragg's law was firstly proposed to demonstrate the X-ray diffraction behaviour of a crystal in 1913 by Lawrence Bragg and William Bragg.[2] And it is also applicable for electron diffraction.
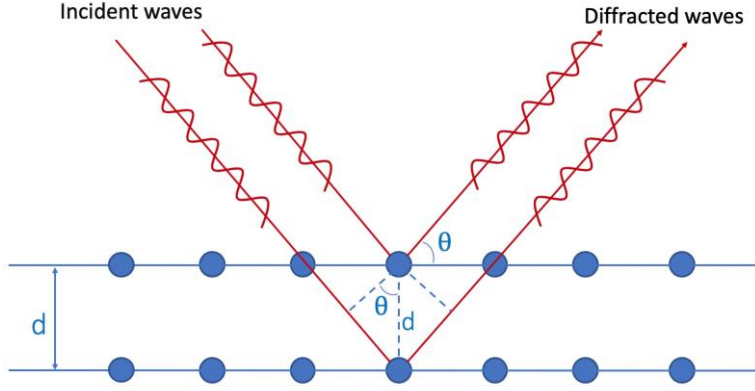
Figure 2.1 Schematic diagram illustrating the geometry of Bragg's law.

As demonstrated in **Figure 2.1**, two in-phase incident waves approach a crystal and are diffracted by two atoms from different layers. If the diffracted waves are still in phase, then the path difference (the extra distance that the lower one traverses) will be equal to an integer (here in **Figure 2.1**, the integer is 1) multiple of the wavelength. Thus, we have the Bragg's law as

$$2d\ sin\theta = n\ \lambda \tag{2.1}$$

where d is the spacing of two adjacent crystal planes, θ is the scattering angle, λ is the wavelength of X-ray and n is an integer which indicates the order of reflection. Strong diffraction patterns can be acquired when the scattering angles satisfy Bragg's condition.

The intensity of the diffraction peak I_{hkl} is determined by the periodic arrangement of the atoms in the crystal unit cell. For an individual diffraction peak of the related (hkl) crystal plane, the structural factor F_{hkl} implies the resultant of all the waves scattered by all the atoms on the (hkl) plane. The structure factor F_{hkl} depends on the position of each atom and the atomic scattering factor f_j. For n atoms in the unit cell located at (x_j, y_j, z_j),

$$F_{hkl} = \sum_{j=1}^{n} f_j\ e^{2\pi i(hx_j+ky_j+lz_j)} \tag{2.2}$$

where f_j is the scattering factor of the jth atom which quantifies the efficiency of the X-ray scattering at any angle by the atom, n is the total number of atoms in the unit cell, (x_j, y_j, z_j) is

the fractional coordinates of atom j, i is the imaginary number $\sqrt{-1}$. The intensity of the diffraction peak I_{hkl} is proportional to the square of F_{hkl},[3,4]

$$I_{hkl} \propto F_{hkl}{}^2 \tag{2.3}$$

From Euler's formula, the structure factor has another expression,

$$F_{hkl} = \sum_{j=1}^{n} f_j \left[cos2\pi(hx_j + ky_j + lz_j) + isin2\pi(hx_j + ky_j + lz_j) \right] \tag{2.4}$$

For a given crystal structure, the atomic coordinates (x_j, y_j, z_j) are fixed, the total structure factor and the diffraction intensity of a certain (hkl) plane depend on the plane indices, h, k and l. Thus, from (2.4), there is a possibility that scattering factors of atoms can cancel each other and result in a total F_{hkl} to 0. This is the systematic absence which leads to a peak extinction of some (hkl) planes in the XRD pattern (also a point extinction in the electron diffraction pattern). For instance, for a body-centred crystal structure, when h+k+l equals an odd number (2n+1), the systematic absence would occur.
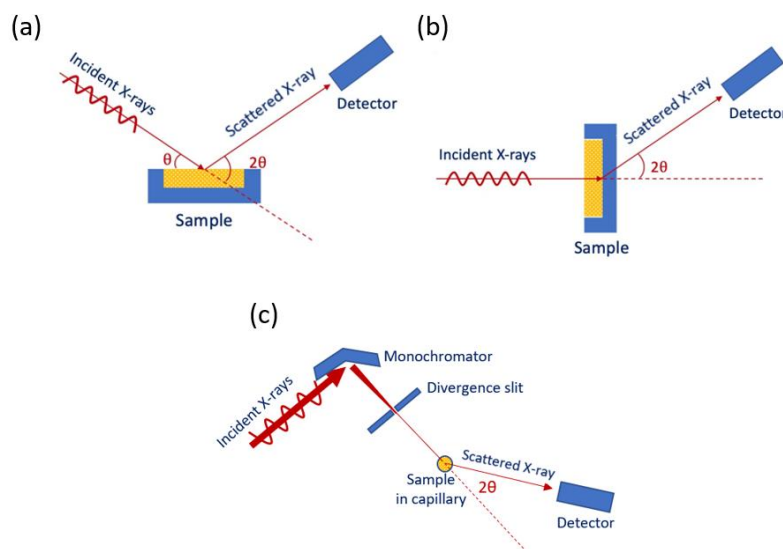
Figure 2.2 Geometries of different powder X-ray diffraction modes: (a) reflection mode (Bragg-Brentano geometry), (b) transmission mode, (c) capillary (Debye-Scherrer geometry).

Modern PXRD diffractometers have three modes, reflection (or Bragg-Brentano geometry), transmission and capillary (or Debye-Scherrer geometry), as shown in **Figure 2.2**. In reflection mode, X-rays are reflected by the sample towards the detector. Either the

detector or the X-ray source rotates within the desired angle range whilst collecting the intensity signals per angle (2θ). In transmission mode, the detector is set behind the sample to collect the X-ray that penetrates the thin sample and gets scattered. Either the sample or the detector rotates to collect the intensity signals plotted against the angle (2θ). In capillary mode, X-ray gets scattered by the spinning sample in the capillary and collected by the rotating detector to plot the PXRD pattern. Both reflection and transmission mode require dense samples to be placed in a sample holder, while capillary mode only demands a small amount of sample in a capillary.

For PXRD experiments, incident X-rays are required to be monochromatic, stable and intense enough to create patterns of good quality. Among all the candidate characterise X-rays, Cu Kα_1 and Mo Kα_1 radiations are intense enough to serve as X-ray sources for diffractometry and have respective wavelengths at 1.541 Å and 0.709 Å which approximate the values of crystal interplanar spacings so that the X-ray diffraction behaviour of crystals can distinctly occur.

By collecting the intensity signals over 2θ, the powder diffraction pattern with various peaks of the unique crystal structure can be produced. Implementing Bragg's law and the given wavelength of the X-ray, we can then get the crystal d-spacing values.

In the present project, PXRD patterns of all the crystals were obtained either in reflection mode (Cu Kα_1 as the X-ray source) or capillary mode (Cu Kα_1 or Mo Kα_1 as the X-ray source) at room temperature. The internal diameter of the capillaries used is 0.5 mm. PXRD experiments were run generally for 2 h for pattern collection. Analyses of XRD patterns were performed using *CrystalDiffact*, *Origin Pro* and *Panalytical X'pert*.

2.2.2 Electron Optics and Electron-matter Interaction

In 1924, Louis de Broglie formulated the de Broglie hypothesis, claiming that all matter has a wave-like property. For de Broglie waves, the wavelength can be calculated using the wavelength equation,

$$\lambda = \frac{h}{p} \tag{2.5}$$

where h is Planck's constant ($\sim 6.63 \times 10^{-34}$ kg·m^2/s) and p is the momentum.

Based on de Broglie's hypothesis, electrons could show wave motion phenomena such as interference and diffraction. For an electron of mass m_0, under a certain voltage (V_0) it travels at the velocity v, we have the momentum and kinetic energy as follows,

$$p = m_0 v \tag{2.6}$$

$$E_k = eV_0 = \frac{1}{2} m_0 v^2 \tag{2.7}$$

Combining the de Broglie equation (2.5) with the momentum equation (2.6) and the kinetic energy equation (2.7), the wavelength is deduced as

$$\lambda = \frac{h}{\sqrt{2m_0 eV_0}} \tag{2.8}$$

Under high voltage, the velocity of the electron might be comparable to light speed (c). Thus, the p in (2.5) and (2.6) needs relativistic correction to become p_r. In the situation of relativistic effect, the energy-momentum relation describes the relation of total energy (E), invariant mass (m_0) and momentum (p_r) as

$$E^2 = (p_r c)^2 + (m_0 c^2)^2 \tag{2.9}$$

And the total energy of an electron is

$$E = E_k + m_0 c^2 = eV_0 + m_0 c^2 \tag{2.10}$$

Then the relativistic wavelength can be derived[5,6],

$$\lambda = \frac{h}{p_r} = \frac{h}{\sqrt{2eV_0 m_0 (1 + \frac{eV_0}{2m_0 c^2})}} \tag{2.11}$$

As negatively-charged particles, electrons can be easily deflected when getting close to the electric fields of specimen atoms. Such Coulombic (electrostatic) interactions cause electron scattering, energy loss and electron knock-out which permeates electron microscopic theory and techniques.[6] **Figure 2.3** illustrates the signals created when an electron beam hits a specimen. Thanks to the wave-particle duality, those generated

electromagnetic signals can be used to generate electron microscopic images and electron spectroscopic spectra, and further be applied to characterise materials.
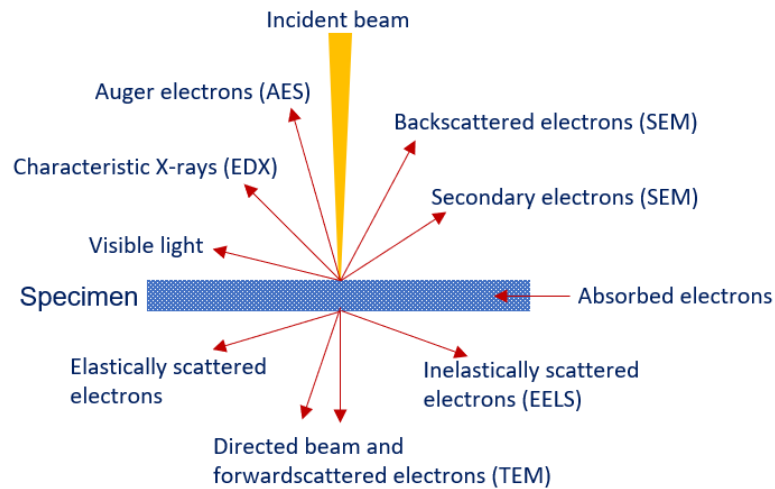
Figure 2.3 Different kinds of signals created from the interaction of an electron beam with matter and corresponding applications.

For the resolution of microscopes, in optics, Abbe firstly proposed an equation to discuss the resolution limit, which is written as

$$d \ = \ \frac{\lambda}{2NA} = \ \frac{\lambda}{2n\ sin\alpha} \tag{2.12}$$

where d is the smallest resolvable distance, NA is the numerical aperture, n is the time of refraction and α is the scattering semi-angle.[7] Rayleigh further refined the equation and proposed Rayleigh's criterion[8],

$$d = 1.22\ \frac{\lambda}{2NA} = \ \frac{0.61\lambda}{n\ sin\alpha} \tag{2.13}$$

From (2.11) and (2.13), it can be deduced that the higher the voltage V_0, the smaller the wavelength λ of the incident electron beam inside electron microscopes and the smaller the resolvable distance d, thus the higher resolution. Below (**Table 2.1**) is the table of theoretical wavelengths λ and resolution d under some given accelerating voltage V without considering lens aberrations, which are commonly applied in the electron microscopes (EMs) used in this project.

Table 2.1 Wavelengths and resolutions at given accelerating voltages in the used EMs.

Accelerating Voltage V, kV	Wavelength λ, nm	Theoretical resolution d, nm	EM
5	1.73×10^{-2}	1.06	SEM
10	1.22×10^{-2}	0.75	SEM
15	9.95×10^{-3}	0.61	SEM
20	8.59×10^{-3}	0.53	SEM
30	6.98×10^{-3}	0.43	SEM
200	2.51×10^{-3}	0.15	TEM

2.2.3 Scanning Electron Microscopy

A scanning electron microscope (SEM) is one type of electron microscope which produces images of a specimen by using a focused electron beam to scan its surface. Electron beam bombards and interacts with the sample, creating miscellaneous signals that contain information of the morphology, topography and composition. When interacting with the specimen, the incident electron beam can knock out electrons from atoms on the surface of the specimen to create secondary electrons (SEs) and be reflected by the specimen to generate backscattered electrons (BSEs), which are the two main signals used to produce SEM images. Modern SEMs may not only have the basic image forming component, but may be equipped with EDX (energy dispersive X-ray spectroscopy) detector, SXES (soft X-ray electron spectroscopy) detector and FIB (focused ion beam) setup to obtain spectroscopic data and allow treatments towards the specimen.

Basic SEM consists of an electron gun (thermionic or field emission), electromagnetic lenses and apertures to focus and manipulate the electron beam, a whole vacuum chamber, detectors, and a display system to collect electron signals and form SEM images. **Figure 2.4** demonstrates the basic construction of an SEM.
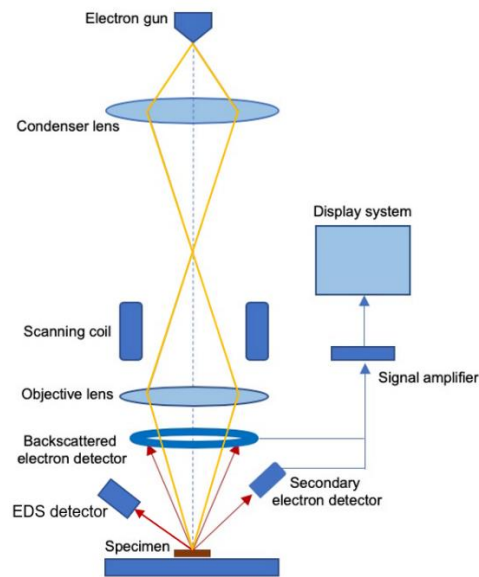
Figure 2.4 Schematic diagram of the basic construction of an SEM.

To avoid electrons accumulating on the samples and causing charging effect (especially for non-conductive samples), gold or carbon coating layers with proper thickness will be applied to enhance the conductivity.

When discussing the theoretical aspects of electron microscopy (EM), the physical flaws and defects of components are always neglected. However, practical mirror lenses and electromagnetic lenses can not be perfect. Accordingly, one should take into consideration the lens aberration when operating electron microscopes. There are many possible aberrations in modern EMs, such as spherical aberration, astigmatism, coma, chromatic aberration, field curvature, distortion etc. Among them, the most crucial ones are spherical aberration, chromatic aberration, coma and astigmatism.[5,9] For SEM, resolution may not be comparable to TEM and STEM, thus the aberration should be emphasised is astigmatism. Astigmatism occurs when a lens is not cylindrically symmetric which can be compensated by placing a stigmator inside the objective lens. A stigmator introduces a balancing cylindrical lens field perpendicular to the astigmatic effect of the lens. Operators can then adjust the stigmator to cancel the astigmatism in x and y directions, respectively.

Contrast is the difference in brightness and colour that make an object distinguishable in an image. Topographic contrast and Z-contrast are the two types of contrast for SEM images.[5,10,11] The local inclination of the specimen and the location of detectors make the trajectories of SEs and BSEs from different areas localised, contributing to the topographic

contrast. Elements with different atomic numbers have different abilities to reflect electrons, so regions of high atomic numbers appear to refract more electrons and are brighter. For BSE images, Z-contrast is the major contrast and the images can be applied to study the elemental composition of the specimen.

SEM is the technique commonly used in this project to study the morphological information of solid materials. During this project, four SEM models, JEOL JSM-5600, JEOL JSM-6700F, JEOL JSM-IT200 and JEOL JSM-IT800, were utilised for sample observation. JSM-5600 is fitted with a tungsten filament with accelerating voltage ranging from 0.5 kV to 30 kV. The theoretical resolution can reach 3.5 nm. JSM-6700F has the same voltage range but is equipped with a field emission gun (FEG) which can generate electrons with monodispersed wavelength and high stability. The resolution can reach 1.0 nm. JSM-IT200 has its voltage range between 0.5 kV to 30 kV and is equipped with a tungsten filament gun. The gun alignment of JSM-IT200 can be automatically achieved. The theoretical resolution can reach 1 nm. JSM-IT800 is equipped with an in-lens FEG and low aberration condenser lens to achieve high beam brightness. The accelerating voltage is from 0.01 kV to 30 kV. The theoretical resolution can reach 0.5 nm and below. Both EDX detector and SXES detector are installed inside JSM-IT800 to provide electron spectroscopic data with high sensitivity.

Samples were either coated with gold or non-coated before SEM observation. Quorum Q150R ES Sputter was used for gold coating. Samples were coated for 60-90 seconds using the current at 10 mA to make sure good conductivity under electron beam and thus high image quality. Coated samples were then adhered to carbon films before putting into SEMs. Uncoated samples were either directly deposed onto the carbon films or dispersed onto silica substrate for SEM observations.

2.2.4 Transmission Electron Microscopy

In comparison to an SEM, a transmission electron microscope (TEM) uses higher-voltage electrons to penetrate thin specimens and collect projected images containing profile (low-magnification) or crystallographic information (high-magnification). TEM mainly utilises transmitted electrons and forward scattered electrons (**Figure 2.4**) to create images.

Functionally, a TEM is composed of four systems, electron illumination system containing electron source and condenser lens to originate focused electron beam, specimen stage allowing the insertion, taking-out and tilting of the sample holder, image forming system including objective lens, intermediate lens and projector lens to magnify and project images or diffraction patterns, and vacuum system holding all above components and allowing the traveling of electron beam with no contamination. Modern commercial TEMs have not only imaging mode, but diffraction mode to acquire electron patterns and spectroscopy detectors to capture electron spectroscopic data.[6,9] **Figure 2.5** demonstrates the geometric optics of a basic TEM in imaging and diffraction mode, respectively.

To ensure remarkable transmitted electron density, high magnification and decent resolution, commercial TEMs are always operated at a high voltage between 100 kV to 300 kV, which gives ultra-small wavelength and fine resolution. The TEM machines used in this project operate at 200 kV, of which the wavelength is 0.0251 Å, as shown in **Table 2.1**.
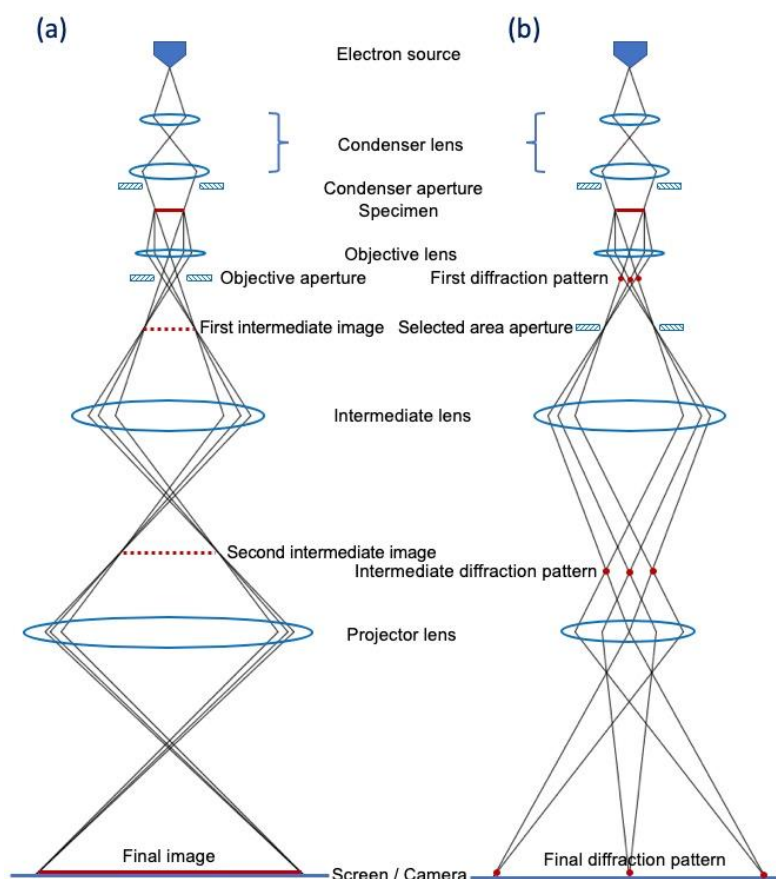
Figure 2.5 The geometric optics and related components of a TEM. (a) Imaging mode with objective aperture inserted. (b) Selected area diffraction mode with selected area aperture inserted and objective aperture taken-out.

At low magnification, for instance, when operating SEMs or low-magnification TEMs, aberrations may be ignored. However, when it comes to HRTEM, aberrations, defects of the lenses and the proper alignment of the observation conditions become crucial for the quality of images.

Prior to any other, astigmatism is the foremost aberration that needs to be solved. As for SEM, there will be stigmators installed in TEMs for compensation. Furthermore, both condenser and objective lenses in TEMs require routine astigmatism corrections. Condenser astigmatism will be compensated to produce a circular incident beam while objective astigmatism will be compensated for better resolution.[6]

Spherical aberration exists in optical microscopes because the centre and the edge of the mirror lens have different abilities to refract light, reducing the quality of an image. The situation is also applicable to the electromagnetic lens in TEMs and STEMs. During image formation, a point will become a blurred disc in the image plane due to spherical aberration. Considering spherical aberration, the practical resolution of TEM would be[6]

$$d_{min} \approx 0.91(C_s\lambda^3)^{0.25} \tag{2.14}$$

where d_{min} is the smallest resolvable distance, C_s is the spherical aberration coefficient (a length constant for the lens) and λ is the wavelength of the electron beam.

Even though the electron gun in a modern TEM is stable enough to generate an electron beam with almost monodispersed wavelength, factors such as fluctuation of the accelerating voltage, current fluctuation of electromagnetic lenses and the absorption of the electron energy by the specimen, will produce error in the electron beam wavelength, which further leads to the failure of focusing the electrons perfectly in one focal plane. This is chromatic aberration.[12] Chromatic aberration will also make a point become a disc in the image plane and reduce the focus quality. In consideration of chromatic aberration, the radius of the disc, r_{chr} will be written as

$$r_{chr} = C_c \frac{\Delta E}{E}\beta \tag{2.15}$$

where C_c is the chromatic coefficient of the lens, ΔE is the energy difference between the initial electron energy and the energy of the refracted electrons, β is the collection angle of

the lens. **Figure 2.6** schematically illustrates the spherical aberration and chromatic aberration. Both demonstrate the elongation of a point object in the image plane.
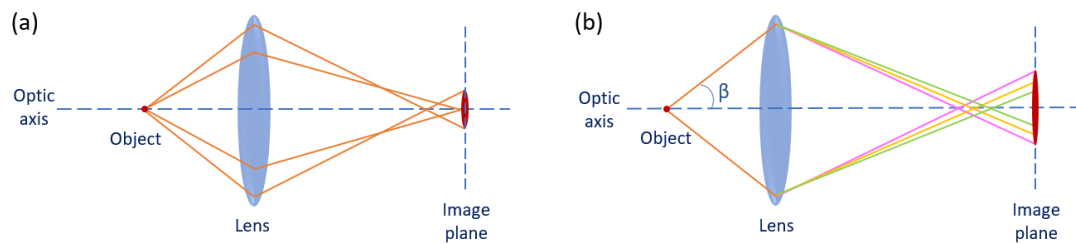
Figure 2.6 Schematic illustration of (a) spherical aberration and (b) chromatic aberration. With the inevitable aberrations, a point object will be blurred in the image plane.

Aberration correctors have now been added to commercial TEMs and STEMs so even at the subatomic scale, unblurred images with good quality can be obtained with proper alignment.

To generate a TEM image, mass-thickness contrast, diffraction contrast and phase contrast are the major three contrast mechanisms. Mass-thickness contrast and diffraction contrast are amplitude contrasts which are the mechanisms of low-magnification TEM images. Thicker areas and domains with greater mass scatter electrons at bigger angles, which means the electron portions penetrating the sample become less, leading to the darkness. Different orientations and the crystal plane distortions of a given crystal affect the diffraction behaviour of electrons, which produce identical diffraction contrast. Apart from the transmitted direct beam to form bright-field (BF) images, the forward-diffracted beam can also be selected to form images, which are defined as dark-field (DF) images. When a TEM reaches high resolution, the interaction between the electron beam and crystal structure brings the crucial difference in the phases of electron waves. Such difference results in interference patterns, which can be recorded to form HRTEM images based on the phase contrast so that we can observe columns of atoms in a crystalline material.[6,13]

In this project, JEOL JSM-2011 and Titan Themis STEM (in TEM mode) were applied to study the materials. JSM-2011 is equipped with a LaB_6 thermionic filament, and the working voltage is 200 kV. Images are recorded on a Gatan 794 CCD (charge-coupled device) camera. Titan Themis also functions at 200 kV and the recording camera is a 16 mega-pixel CMOS

camera. Titan Themis is equipped with correctors to cancel spherical aberration (in STEM mode only).

For TEM sample preparation, the powder samples were firstly grounded and dispersed either in acetone or ethanol. Then the acetone/ethanol suspension containing samples was dripped onto TEM copper grids and left still for the full solvent evaporation before putting into the TEM specimen chamber. TEM images were analysed using *Fiji (ImageJ)* and *Gatan Microscopy Suite (Digital Micrograph)*.

2.2.5 Scanning Transmission Electron Microscopy

A scanning transmission electron microscope (STEM) is a type of TEM while its working principle varies from that of a conventional TEM (CTEM). In STEM, the electron beam is focused on an ultra-fine spot which is used for a raster scan over the sample. Signals are then collected to form STEM images.
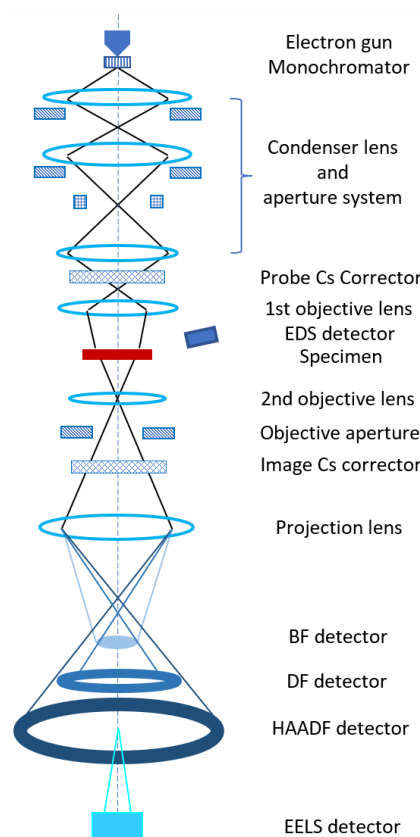
Figure 2.7 Schematic illustration of the main components of an aberration-corrected STEM, adapted from the construction of the model FEI Titan Themis (in STEM mode).

Typical STEMs have both CTEM and STEM modes, although dedicated STEMs are also manufactured. Modern STEMs may be equipped with aberration correctors to provide images with less disturbance from hardware defects. **Figure 2.7** shows the main components of an aberration-corrected STEM. In the illustrated STEM, chromatic aberration can be cancelled by the monochromator while spherical aberration can be cancelled by the two Cs correctors.

In a modern STEM, multiple electron signals collected using different detectors can be harnessed to form EM images and energy spectra.

BF and DF detectors, respectively, capture transmitted electron beam and diffracted electron beam to form BF and DF images. High-angle annular dark field (HAADF) detector collects high-angle scattered incoherent electrons to generate HAADF images. HAADF technique is highly sensitive to the atomic numbers of the elements in the sample because elements with higher Z can scatter electrons at higher angles. Thus, Z contrast is the major contrast mechanism for high-resolution atomic scale HAADF images. Electron energy loss spectroscopy (EELS) detector filters and collects electrons with energy loss to get characteristic EELS spectra. The electron signal detectors are retractable, which ensures different signals will not interfere with each other.

STEM operation was carried out using Titan Themis at 200 kV. In this project, STEM mode was used to obtain low-magnification HAADF images as well as collect spectroscopic data. The sample preparation for STEM is similar to that for TEM.

2.2.6 Electron Diffraction and Fourier Transform

Selected area electron diffraction (SAED) is an electron diffraction (ED) technique which is performed inside the TEM by simply inserting a selected area aperture into the image plane of the objective lens to select electron waves to contribute to the SAED pattern, as shown in **Figure 2.5(b)**. SAED can be used to identify the crystallinity, phase and crystal planes of a material. Researchers are now capable to reveal unknown crystal structures by applying 3-dimensional rotary electron diffraction techniques.[14,15]

To extend the explanation of diffraction geometry and mathematical relationships, shortly after Bragg's law, Paul Peter Ewald established the concept of the Ewald sphere, which was later commonly used to elucidate electron diffraction.[16]
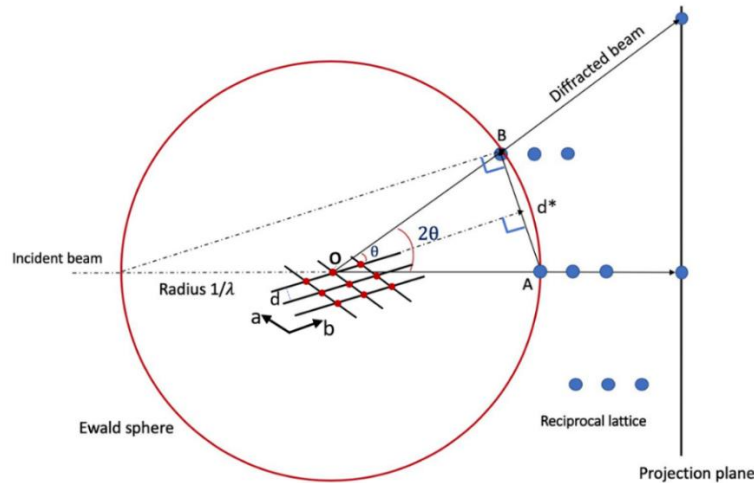
Figure 2.8 Ewald sphere revealing the behaviour of electron diffraction, viewed from the c axis.

From **Figure 2.8**, the geometry of reciprocal lattice and Ewald sphere is shown, and Bragg's law can be derived,

$$OA = OB = \frac{1}{\lambda} \tag{2.16}$$

$$d^* = 2 \times OA \sin \theta = 2 \times \frac{1}{\lambda} \sin \theta \tag{2.17}$$

Any characteristics and properties which repeat at regular intervals can be expressed by wavefunctions of certain shapes and complexity. And wavefunctions can be written as a series of sine and cosine waves containing their frequencies and amplitudes. Such expansion of periodic wavefunctions into a series of simple fixed components is called Fourier transform. The electron density of a crystal is exactly periodic, which can be expressed as a wavefunction. And electron diffraction with bright spots of a crystal expresses the crystal's periodicity, which relates to the amplitude of the electron density wave.[16]

Thus a diffraction pattern in reciprocal space is actually a Fourier transform of a crystal interacting with an electron beam in real space. When dealing with HRTEM images containing crystal d-spacing information, image processing software can now offer fast Fourier transform (FFT) of HRTEM images. So that we can quickly get the periodicity and d-spacing information of the given crystal by analysing the FFT pattern. In SAED patterns and FFT patterns, the spots imply the periodicities of corresponding planes, and their brightness indicates the electron

diffracting level of each plane which can also be calculated using the structure factor equation (2.2).

From the Bragg's law (2.1) and the geometrical relation (2.17), we deduce the mathematic relation between crystal d-spacing d in a crystal direction in real space and the crystal d-spacing d^* in reciprocal space as,

$$d = \frac{1}{d^*} \tag{2.18}$$

Besides, from the geometry in **Figure 2.8**, the direction of d^* is perpendicular to the crystal direction b. And considering the Ewald sphere is a 3D construction, d^* thus is perpendicular to the viewing direction c. A 2D diagram of the relation is shown in **Figure 2.9**. Therefore, we have the direction relation of reciprocal space parameters and real space parameters as,

$$a^* \perp b \text{ and } a^* \perp c \tag{2.19}$$
$$a^* \cdot b = 0 \text{ and } a^* \cdot c = 0 \tag{2.20}$$
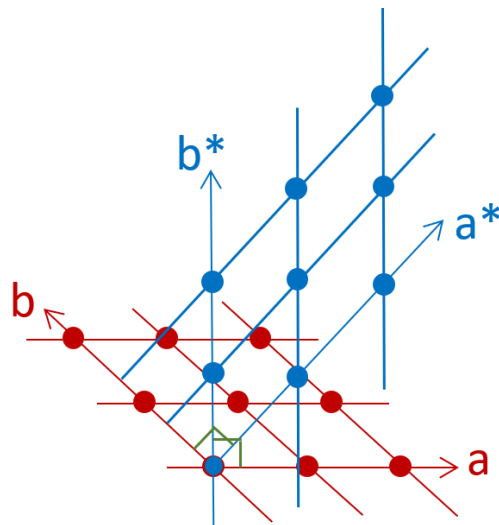
Figure 2.9 A 2D representation of the relationship between real-space crystal parameters and the reciprocal crystal parameters, viewed from the c axis.

Equations (2.18), (2.19) and (2.20) are applied for the interpretation of crystal d-spacings in HRTEM images and diffraction spots in SAED and FFT patterns. There are three types of SAED and FFT patterns derived from the crystal orientations in the HRTEM images, as

demonstrated in **Figure 2.10**. Pattern composed of individual spots indicating the sample is monocrystalline. While discrete ring pattern indicates the sample is polycrystalline. And diffused ring pattern indicates the sample is amorphous.
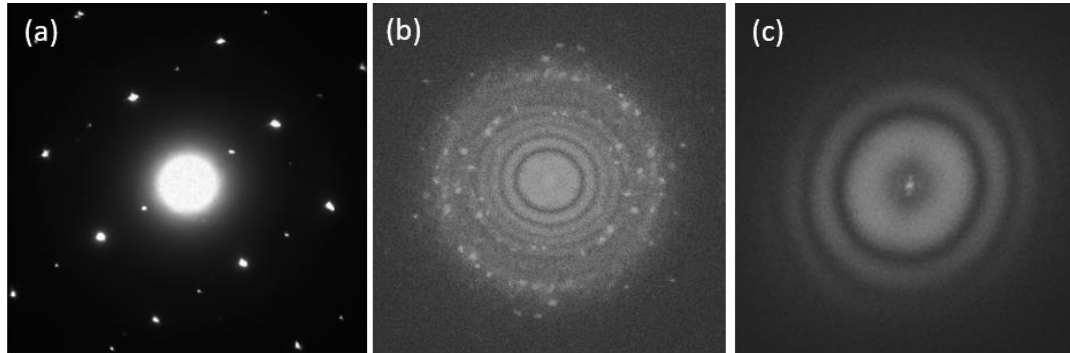
Figure 2.10 (a) SAED pattern indicating the domain is monocrystalline. (b) FFT pattern indicating that the domain is polycrystalline and composed of crystals with various orientations. (c) FFT pattern with diffused rings indicating the domain is amorphous.

To examine the crystallinity and crystal orientations of the materials, SAED experiments were run in the TEMs, Jeol JSM-2011F and FEI Titan Themis (TEM mode) by just inserting proper selected area apertures. To analyse the crystal structure information from HRTEM images, the FFT patterns were implemented as the media. The analyses of SAED and FFT patterns were achieved using the software, *SingleCrystal, CrystalDiffract, Fiji (ImageJ)* and *Gitan Microscopy Suite (Digital Micrograph)*.

2.2.7 Energy Dispersive X-ray Spectroscopy

As elucidated when introducing XRD and demonstrated in **Figure 2.11**, characteristic X-rays can be generated when an incident electron beam stimulates a material and knocks out inner shell electrons, leaving vacancies which will be later occupied by higher-energy outer shell electrons. Energy dispersive X-ray spectroscopy (EDX or EDS) detectors collect such characteristic X-rays which derive from the interaction between matter and electron beam in the EMs to form unique spectra of corresponding elements and corresponding electron shells.[13] Thus, EDX is commonly used to identify the elemental information of materials.
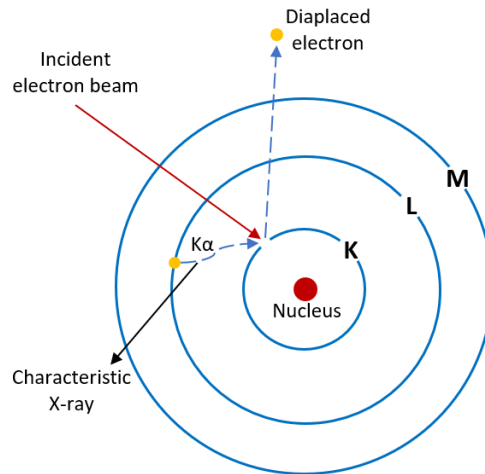
Figure 2.11 Schematic demonstration of the production of the characteristic X-ray from a single atom stimulated by the incident electron beam.

SEM, TEM and STEM can all be used for recording EDX spectra as long as the EDX detector is equipped. Although EDX is now a widespread technique, there are still distinct flaws. Light elements have weak X-ray signals, which can be absorbed again by the specimen or by the detector, thus EDX shows its inability when dealing with organic materials and materials with light elements. Nevertheless, strong EDX signals can be used for mapping the elemental distribution in the specimen and even used for quantitative analysis of the atomic ratio. But accurate mapping and quantitative analysis are applicable only when a long collection time and high elemental intensity are provided. Normally, the resolution of EDX is about 0.1 KeV.

EDX acquisitions, including spectra collection and elemental mapping, were achieved using the SEM Jeol JSM-IT800, and Titan Themis in both TEM and STEM modes. When collecting EDX spectra using JSM-IT800, a high working distance (over 15 mm) and a high voltage (over 20 kV) are applied to guarantee enough characteristic X-ray intensity. The inbuilt EDX detector can be used to analyse the elements from B to U. The collection was set for 2 min. While for Titan Themis EDX acquisitions, the working voltage at 200 kV is already adequate. The collection of EDX spectra used the 4 symmetrically arranged silicon detectors with high sensitivity.

Samples for SEM-EDX were uncoated and either deposited on carbon film when focusing on metal elements or deposited on silica substrates when light elements, such as carbon and oxygen, were required to be analysed in the samples. Samples for TEM-EDX were prepared exactly the same way for TEM imaging.

2.2.8 Soft X-ray Electron Spectroscopy

Soft X-Ray Emission Spectroscopy (SXES) is an ultra-high resolution electron spectroscopy to detect X-rays emitted from light elements using a newly-developed diffraction grating and a high-sensitivity X-ray CCD camera.

Figure 2.12 illustrates the detection of soft X-rays. The principle of soft X-rays is exactly the same as characteristic X-rays for EDX since soft X-rays are characteristic X-rays from light elements which have lower energies. Emitted soft X-rays will be graded using the diffraction grating, thus characteristic X-rays from different elements and different atomic structures will be collected without disturbing each other. Due to the high-sensitivity diffraction grating and CCD camera, the resolution of SXES in JSM-IT800 can be drilled down to 0.3 eV, therefore elemental and chemical bonding information with high energy resolution can also be obtained.[17,18]
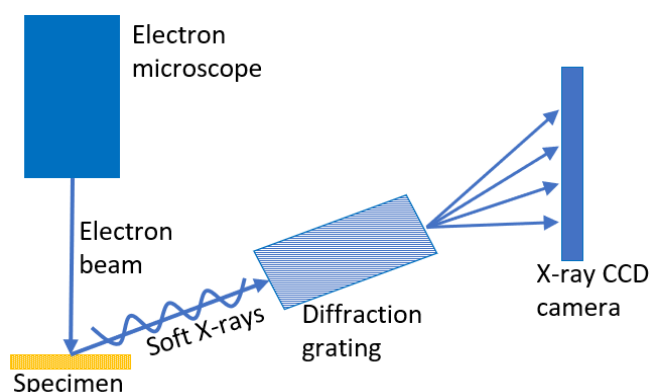
Figure 2.12 Schematic drawing of the SXES detector inside an SEM.

In this project, SXES spectra were acquired using JSM-IT800 for examining the existence of light elements, such as C, N and O in the materials. SXES detector was cooled to -70 °C before operation. The accumulation time of SXES spectra was set at 1.5 h to guarantee distinct signals. Samples used for SXES were uncoated and deposited on silica substrates to avoid impurity signals from carbon films. Plasma treatments were also applied to remove any possible organic solvents and greases on the substrates. Analyses of SXES spectra were achieved by using the authorised SXES software from JOEL.

2.2.9 Electron Energy Loss Spectroscopy

As demonstrated in **Figure 2.3**, when interacting, the incident beam can give a part of its energy to the electrons in the matter. Such scattering with the change of kinetic energy is defined as inelastic scattering, in contrast to the elastic scattering with kinetic energy conserved but trajectory changed.[19,20] The energy loss of those electrons can be measured and recorded by an energy filter at the end of the path of the electron beam. The EELS detector set-up in the STEM is already illustrated in **Figure 2.7**. **Figure 2.13** demonstrates the inner construction of an EELS spectrometer and the trajectory of the inelastically scattered electron beam inside the EELS spectrometer.[6]
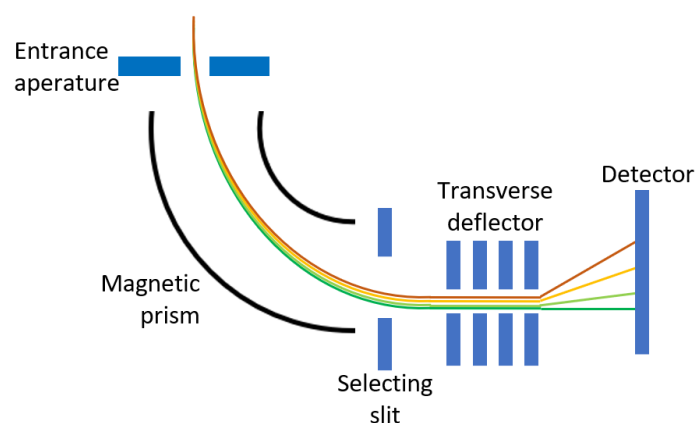
Figure 2.13 Adapted demonstration of the construction of an EELS spectrometer.

When an electron beam penetrates atoms of different elements, the energy loss of inelastic electrons becomes element-dependent. Additionally, when hitting atoms with different bonding information, the energy loss of incident electrons can also be distinctive. Such unique features make peaks in the EELS spectrum identical to elements as well as to atomic structures. EELS detectors can provide an energy resolution down to 0.1 eV, making the detection of atoms with various bonding structures utterly accurate. EELS requires the samples to be ultra-thin to avoid plural scattering.

In this project, EELS was applied to investigate the oxidation states of Ti. EELS experiments were run using the STEM FEI Titan Themis, thus the preparation of EELS samples was exactly the same as TEM samples. EELS results was analysed using *Gatan Microscopy Suite (Digital Micrograph)*.

2.2.10 Infrared Spectroscopy

Infrared spectroscopy (IR) is a non-destructive spectroscopic technique based on the vibrations of the atoms of molecules. Infrared spectroscopy exploits the fact that molecules absorb frequencies that are characteristic of their structure. By penetrating infrared radiation through a sample, a certain fraction of the radiation will be absorbed. Each peak in an IR spectrum corresponds to a frequency of vibration of any part of the molecule. Thus, IR can be employed to perform molecular structure and chemical bonding identification[21].
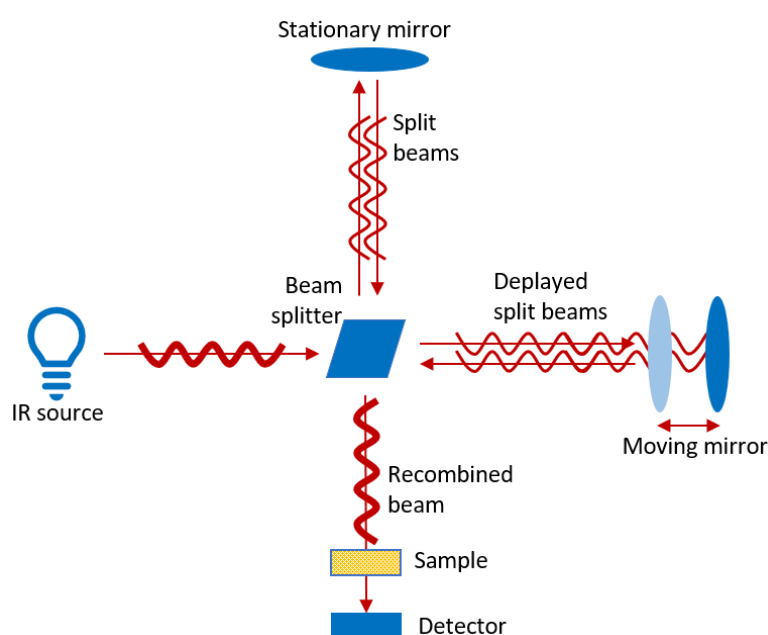
Figure 2.14 Schematic of the inner Michelson interferometer in an IR spectrometer and the pathways of the IR beams inside.

Figure 2.14 demonstrates a typical Michelson interferometer in an IR spectrometer. After its generation from IR light source, the IR beam is split equally by the beam splitter. The two individual beams are then reflected from the moving and stationary mirror and finally recombined together. With the moving mirror, the path difference of the recombined lights can change over time, creating an interferogram against time.

Fourier transform infrared (FTIR) spectrometer is the most common type of infrared spectrometer nowadays, which records the interferogram data against time and further uses software to run Fourier transform to switch the data to readable spectrum against wavelength.[22]

In this project, solid-phase and liquid-phase FTIR was applied to examine the existence of organic component of materials as well as to prove the bonding of organic compounds with cations. The FTIR spectrometer implemented was Shimadzu IRAffinity-1s, of which the mode was transmission. The spectrum wavelength range was typically set between 4000 cm^{-1} to 400 cm^{-1}. Background scan was performed to remove any potential signals from the spectrometer. The IR spectra were analysed using the software *Origin*.

2.2.11 Crystal Modelling and Visualisation

The crystal modelling and visualisation were applied to demonstrate the structures and unit cells of the researched crystals in this project, in order to associate the crystal growth processes with crystal structures.

Modelling of crystal structures, schematic drawing of morphologies and visualisation of crystal formation mechanisms were achieved by utilising the following software, *Crystal Diffract, Single Crystal, Diamond, Vesta, Chemdraw, Auto CAD, 3Ds Max,* etc.

References

1　R. Sharma, D. P. Bisen, U. Shukla and B. G. Sharma, *Recent Res. Sci. Technol.*, 2012, **4**, 77–79.

2　W. H. Bragg and W. L. Bragg, *Proc. R. Soc. London. Ser. A, Contain. Pap. a Math. Phys. Character*, 1913, **88**, 428–438.

3　C. Hammond, *The Basics of Crystallography and Diffraction*, Oxford University Press, Oxford, 3rd edn., 2009.

4　Y. Waseda, E. Matsubara and K. Shinoda, *X-Ray Diffraction Crystallography*, Springer, Heidelberg, 2011.

5　L. Reimer and H. Kohl, *Transmission Electron Microscopy Physics of Image Formation*, Springer, 5th edn., 2008.

6　D. B. Williams and C. B. Carter, *Transmission Electron Microscopy A Textbook for Materials Science*, Springer, 2009.

7　P. W. Hawkes and J. C. H. Spence, *Science of Microscopy*, Springer, 2007.

8　R. F. Egerton, *Physical Principles of Electron Microscopy*, Springer, 2005.

9　B. Fultz and J. Howe, *Transmission Electron Microscopy and Diffractometry of Materials*, Springer, 4th edn., 2013.

10　M. Kotera, T. Fujiwara, N. Kanai and H. Suga, *Jpn. J. Appl. Phys.*, 1991, 30, 3287–3293.

11　G. E. Lloyd, *Mineral. Mag.*, 1987, **51**, 3–19.

12　N. Tanaka, *Electron Nano-imaging Basics of Imaging and Diffraction for TEM and STEM*, Springer, 2017.

13　C. B. Carter and D. B. Williams, *Transmission Electron Microscopy Diffraction, Imaging, and Spectrometry*, Springer, 2016.

14　X. D. Zou, Z. M. Mo, S. Hovmöller, X. Z. Li and K. H. Kuo, *Acta Crystallogr. Sect. A*, 2003, **59**, 526–539.

15　T. Sun, L. Wei, Y. Chen, Y. Ma and Y. B. Zhang, *J. Am. Chem. Soc.*, 2019, **141**, 10962–10966.

16　C. Hammond, *The Basics of Crystallography and Diffraction*, Oxford University Press, 3rd edn., 2009.

17　M. Terauchi, H. Takahashi, M. Takakura, T. Murano and S. Koshiya, *Handbook of Soft X-ray Emission Spectra*, JOEL, 5th edn., 2009.

18　H. Watabe, M. Iwami, M. Hirai, M. Kusaka and H. Nakamura, *Jpn. J. Appl. Phys.*, 1991, **30**, 1928–1930.

19　V. J. Keast, *Mater. Charact.*, 2012, **73**, 1–7.

20　R. F. Egerton, *Reports Prog. Phys.*, 2008, **72**, 16502.

21　B. H. Stuart, *Infrared Spectroscopy: Fundamentals and Applications*, Wiley, 2004.

22　R. Valand, S. Tanna, G. Lawson and L. Bengtström, *Food Addit. Contam. Part A*, 2020, **37**, 19–38.

Chapter 3 Crystal Growth of Cu Pseudo-icosahedral Microcrystals

3.1 Introduction

The formation and controlled synthesis of metal crystals with polyhedral morphologies has been investigated for over one century. Although polyhedral crystals seem to be morphologically simple, they may not actually form via simple classical crystal growth starting from simple nuclei.[1–6]

Multi-twinned particles (MTPs) with multiple twinning planes which appear to be polyhedral have received substantial attention because of their formation mechanism and their catalytic properties. Among MTPs, the most studied and applied materials are Cu, Ag, Au and Pd nanocrystals crystallised in the morphologies of the five-fold twinned nanowire, decahedron and icosahedron.[7–13] A Platonic icosahedron preserves 20 triangular facets, with 5 of them meeting at each of the 12 vertices. Viewed from each vertex, the triangular facets are 5-fold twinned. A synthesised icosahedron of fcc metal crystals contains 20 {111} facets, of which the interplanar angle is 70.53 °. The so-called 5-fold twinning of the {111} facets leads to only 352.65 °, leaving the total angular mismatch at 7.35 ° and an evenly-distributed angular mismatch at 1.47 °.

To cancel the angular mismatch, when an icosahedron is of small size (e.g. several nm), the internal strain caused by the angular misfit can easily be released by elastic lattice expansion. Thus, such an approximately spherical shape with low surface energy is favoured in small size. However, it is always a synergy between total surface energy and intrinsic strain energy in growing multi-twinned crystals. When crystals grow to a critical size, the intrinsic strain energy becomes crucial and unrealistic to be released by slight elastic lattice expansion, causing icosahedral morphology unfavoured, leading to decahedron, nanowire with five-fold twinned heads, tetrahedron and cubes, making the icosahedral morphology difficult to be preserved at microscale.[10,14–17]

Tsuji *et al.* proposed a stepwise growth of silver tetrahedral units to demonstrate the growth of Ag icosahedra, forming multiple twin planes on the {111} faces. In their statement, a tetrahedron forms first. The second tetrahedron grows on the first tetrahedron by sharing a (111) plane to form a twin defect.[18] In addition to silver crystals, the icosahedral nanoparticles of gold[10,11] and copper[8] were also synthesised. Using in-situ TEM, Ma *et al.*

observed not only the successive stepwise growth process of Au icosahedral nanoparticles but also classical crystal growth from early-stage twinned nuclei within several minutes. They claimed that in a weak reducing condition, stepwise growth might be preferred, while in a strong reducing condition, twined nuclei might form followed by classical growth, leading to big icosahedrons.[10]

However, such metallic icosahedra obtained from solvothermal methods all stay at nanoscale. Annealing process and chemical vapour deposition were applied to produce microscale icosahedral crystals[19–21], while the angular mismatch always exists, which may be overcome by filling extra atoms in the gaps between adjacent tetrahedra. Consequently, due to the inevitable angular mismatch, all these traditionally called icosahedral crystals formed by 20 {111} facets are not Platonic icosahedral solids. Therefore, the morphology should be actually named pseudo-icosahedra.

Cu is one of the most applied and attractive industrial metals in modern life because of its natural abundance, low cost in obtaining and straightforward methods of preparation. Its crystals with certain morphologies have been widely applied in industry fields, such as catalysis, conductivity and antibacterial activity.[22–25]

Herein, we report the synthesis of pseudo-icosahedral Cu microcrystals via a solvothermal method using $CuSO_4 \cdot 5H_2O$ as the starting material, DMF as the solvent and PVP as the agglomerating surfactant and mild reductant. Based on the microstructural investigations of the specimens obtained from different crystal growth stages, a new formation mechanism involving multiple intermediate phases is revealed. The term pseudo-icosahedral is proposed to describe the morphology with 20 {111} facets instead of icosahedral because the gaps between {111} facets due to that angular misfits can not be avoided, and the {111} facets are not from direct twinning at atomic scale but grow themselves independently. The pseudo-icosahedral Cu microcrystals do not form from the assembly of tetrahedra or classical growth from multi-twinned nuclei, but are constructed by 20 {111} plates due to surface recrystallisation of polycrystalline spherical particles, followed by a process of reversed crystal growth. The thermodynamics of the crystal growth and equilibrium morphology are discussed. This work may provide new insights into polymer-assisted crystal growth, polymer's multifunction in altering crystal habit and crystal morphology prediction.

3.2 Experimental Methods

Chemicals:

CuSO$_4$·5H$_2$O (Sigma-Aldrich), polyvinylpyrrolidone (PVP, Sigma, molecular weight about 360000), dimethylformamide (DMF, Acros Organics, 99+%), deionised water (DI water) with a resistivity of 18.3 M Ω·cm. All chemicals were used without further purification.

Preparation of Pseudo-icosahedral Cu crystals:

In a typical synthesis, 0.5 g PVP was fully dissolved in 25 ml DMF and pre-heated to 150 °C before adding 1.25 mmol (0.313 g) CuSO$_4$·5H$_2$O. The solution was stirred continuously until it became a green suspension. The suspension was then transferred into an autoclave vessel and left heated in the oven at 150 °C for 12 h. Samples from earlier growth stages were obtained by keeping the same experimental conditions while applying different reaction times, such as 1.5, 2, 3, 6 and 9 h.

When the reaction finished, the autoclave vessels were immediately cooled down under flowing water. The solid precipitates were filtered and washed three times with DI water to remove excess SO$_4^{2-}$, DMF and PVP. Finally, the obtained powder was dried at 50 °C before putting into sample vials for further characterisations. All experiments were performed three times to make sure they were repeatable.

3.3 Results and Discussion

3.3.1 Prepared Icosahedral Morphology

In the synthetic solution containing CuSO$_4$·5H$_2$O, PVP and DMF, Cu^{2+} cations were reduced step by step to Cu crystals. After a reaction for 12 h, a large amount of Cu pseudo-icosahedral microparticles (1-5 μm in diameter) were obtained, as shown in **Figure 3.1**. The morphology of those microparticles is similar to an ideal Platonic icosahedron, as displayed in the inset of **Figure 3.1(b),** which has 30 edges and 20 equilateral triangular faces with 5 of them meeting at each of the 12 vertices.
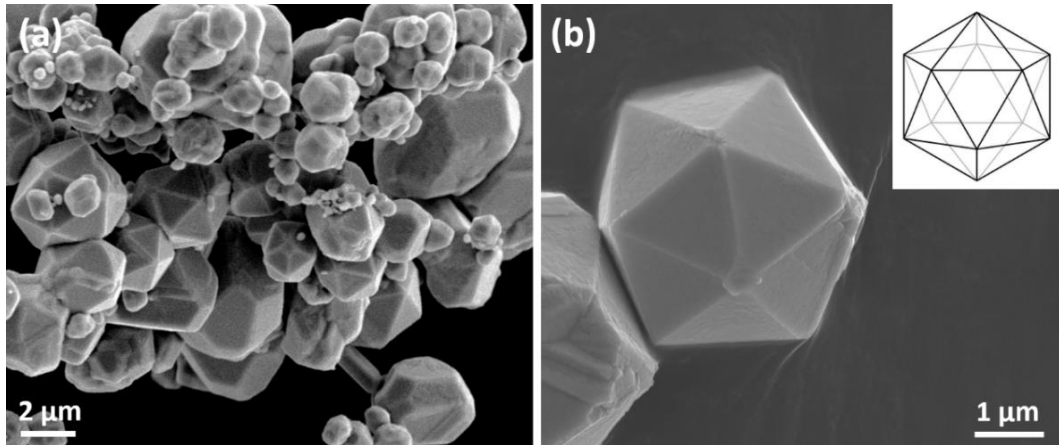
Figure 3.1 (a) SEM image of the Cu pseudo-icosahedral crystals after a reaction for 12 h. (b) SEM image of a single pseudo-icosahedron. The inset shows the geometry of an ideal Platonic icosahedron.

In most current studies, such morphology is simply defined as icosahedral. However, the so-called icosahedron of cubic metal phases formed by 20 tetrahedra, which is constructed by congruent, regular, polygonal faces with the same number of faces meeting at each vertex, will not be a perfect Platonic solid.
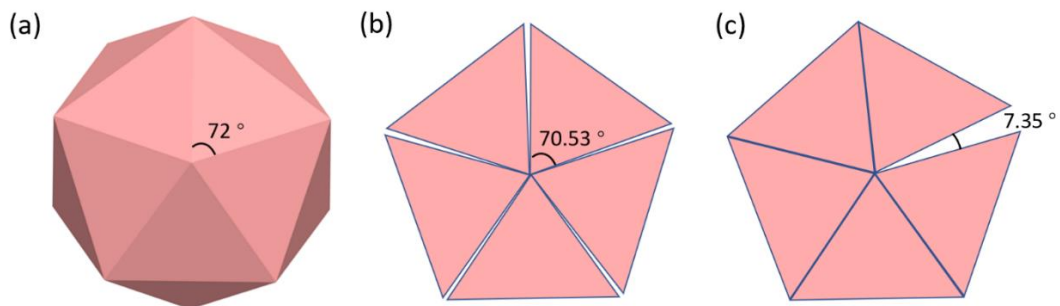
Figure 3.2 (a) An ideal icosahedron (Platonic solid) viewed along one vertex with the projected angle of 72 ° between the adjacent ridges. (b) Projection of a pseudo-icosahedron formed by five tetrahedra with the interplanar angle of adjacent {111} facets parallel to the view direction, 70.53 °. (c) Projection of a stepwise growth of tetrahedra via twinning, resulting in a 7.35 ° total angular mismatch at the final step.

As shown in **Figure 3.2**, the projected angle between two adjacent ridges of an ideal icosahedron is 72 °, while for the particle formed by 20 tetrahedra, the angle between two adjacent {111} planes is 70.53 °. An average mismatch between the tetrahedra is 1.47 °. And as demonstrated in **Figure 3.2(c)**, a stepwise growth of tetrahedra brings a total angular

mismatch of 7.35 ° at the final step. Therefore, the stepwise intergrowth of tetrahedra via twin defects would not lead to an ideal decahedral morphology with 5 tetrahedra and icosahedral morphology with 20 tetrahedra. It was realised that icosahedra of silver could only exist when the particle size was small[9], in which the lattice tension at the boundaries could be released by surface relaxation.

3.3.2 Crystallographic Evolution Over Time

To reveal the microstructural change and morphology evolution over time, the reaction was stopped at 1.5, 2, 3, 6, 9 and 12 h to collect specimens at different growth stages. Meanwhile, 1.5 h is the earliest time to obtain distinct solid precipitates. Characterisations were performed on each specimen for comparison. Powder XRD patterns of the specimens at different reaction times were obtained and interpreted (**Figure 3.3**).
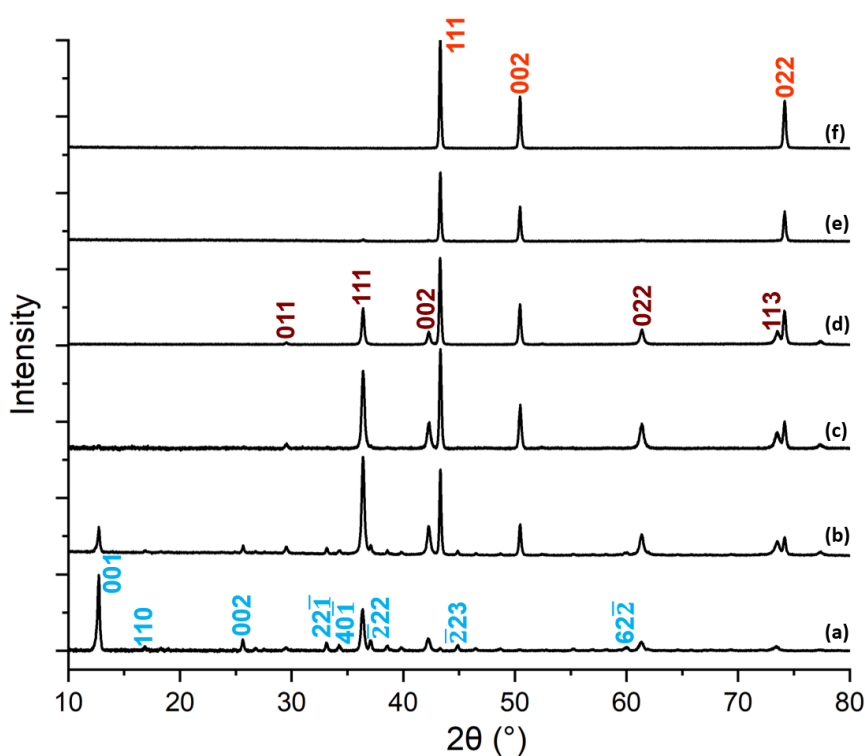
Figure 3.3 Powder XRD patterns of specimens prepared from different reaction times (a) 1.5, (b) 2, (c) 3, (d) 6, (e) 9 and (f) 12 h. The X-ray radiation source is Cu Kα1. Indices marked blue, brown and red corresponding to their optical colours represent the phases of $Cu_4SO_4(OH)_6 \cdot H_2O$, Cu_2O and Cu, respectively.

There are 3 crystalline phases chronologically, monoclinic $Cu_4SO_4(OH)_6 \cdot H_2O$, cubic Cu_2O and cubic Cu. Monoclinic $Cu_4SO_4(OH)_6 \cdot H_2O$ belongs to space group Pa, with unit cell parameters a = 10.578 Å, b = 6.345 Å, c = 7.863 Å, β = 117.98 ° (ICSD Code-100276). Its corresponding mineral name is posnjakite, which optically shows a greenish blue colour and demonstrates rhombus habit. $Cu_4SO_4(OH)_6 \cdot H_2O$ exists in 1.5 h and 2 h. The second phase is cubic Cu_2O with unit cell parameter a = 4.268 Å (ICSD Code-67850) which presents in the samples from 1.5 h to 9 h. The final phase is cubic Cu with unit cell parameter a = 3.615 Å which emerges from 2 h and stays. Based on the phase evolution, the reaction can be divided into 3 stages, the early stage is the formation of $Cu_4SO_4(OH)_6 \cdot H_2O$, the middle stage is the formation of Cu_2O, and the final stage is the production of Cu.

The powder XRD results indicate that Cu^{2+} formed $Cu_4SO_4(OH)_6 \cdot H_2O$ crystals initially with the oxidation state of Cu unchanged and was reduced by PVP to form Cu_2O. Cu_2O was further reduced by PVP to produce Cu crystals. Commercially available PVP normally contains hydroxyl groups due to the existence of H_2O and H_2O_2 in its industrial production process of polymerisation. **Figure 3.4** displays the monomer of PVP, the structures of hydrogen-terminated and hydroxyl-terminated PVP. PVP can also serve as a dispersant to prevent inorganic nanoparticles from aggregation.[26,27] On the other hand, nanoparticles capped by PVP can agglomerate into large composite particles due to the strong intermolecular interaction of PVP. Hydroxyl-terminated PVP preserves a mild reducing ability to reduce metal cations.[28–30]
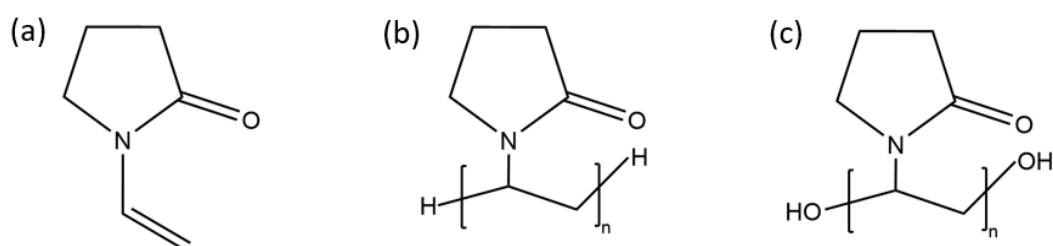
Figure 3.4 (a) Molecular structure of the monomer N-vinylpyrrolidone. (b) The formula of PVP terminated in H atom. (c) The formula of PVP terminated in hydroxyl group.

The colour appearance of the samples underpins the XRD results, as demonstrated in **Figure 3.5**. In 10 min, the solution turned into a green suspension. 1.5 h sample displayed grey

blue colour, which is attributed to the mixture of $Cu_4SO_4(OH)_6 \cdot H_2O$ (greenish blue) and Cu_2O (brown red).

When the reaction time extends to 2 h, the XRD peak intensities of $Cu_4SO_4(OH)_6 \cdot H_2O$ decrease while those of Cu_2O increase (**Figure 3.3b**). The colour of the specimen became darker and browner (**Figure 3.5c**), indicating a significant decrease in the ratio of $Cu_4SO_4(OH)_6 \cdot H_2O$ to Cu_2O. Cu phase also emerges at this stage. No peaks of $Cu_4SO_4(OH)_6 \cdot H_2O$ are shown in the XRD pattern of 3 h or any later samples.
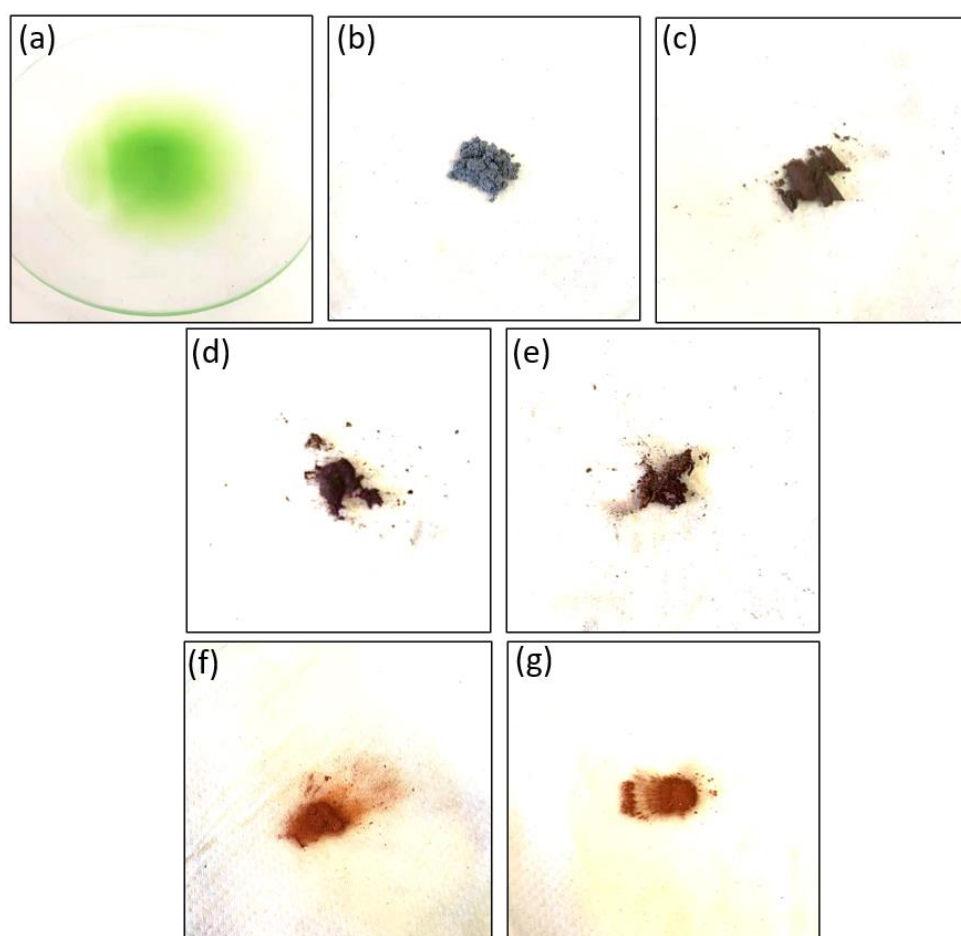
Figure 3.5 Optical images of samples prepared at different reaction times, showing colour of samples from the time (a) 10 min (suspension), (b) 1.5, (c) 2, (d) 3, (e) 6, (f) 9, and (g) 12 h.

The middle stage of the reaction is the time when Cu_2O dominates in the samples. As the reaction time lengthens, the peaks of Cu_2O become weaker and those of Cu grow stronger. The colour gradually changes from deep brown to red, implying the transformation from Cu_2O to Cu (**Figure 3.5 c** to **f**). In the XRD pattern of 9 h sample, only a small bump of Cu_2O (111)

peak is seen. In 12 h sample, Cu_2O completely disappears, leaving a pure Cu phase in the reaction system. The bright red colour of 9 h and 12 h samples (**Figure 3.5 f** and **g**) is typical for Cu metal.

3.3.3 Precursor Posnjakite Before Reduction

Transformed from $CuSO_4 \cdot 5H_2O$, $Cu_4SO_4(OH)_6 \cdot H_2O$ was the first solid phase precipitated. SEM images of 1.5 h specimen show that the phase exhibits thin microflake morphology, as shown in **Figure 3.6**. As aforementioned, XRD pattern of 1.5 h sample indicates that there are $Cu_4SO_4(OH)_6 \cdot H_2O$ and Cu_2O. From **Figure 3.6(a)**, there are also spherulites along with the clumping $Cu_4SO_4(OH)_6 \cdot H_2O$ microflakes, which are later proven to be Cu_2O.
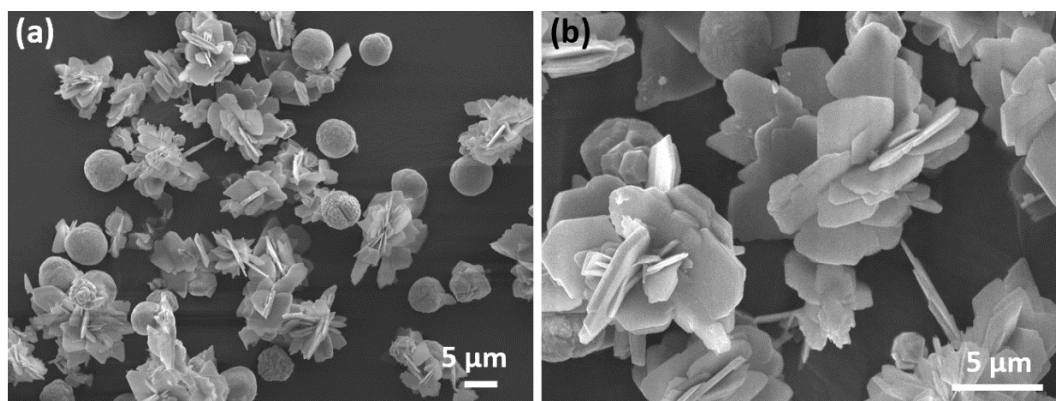
Figure 3.6 (a). Low magnification SEM image of a general view towards crystals in 1.5 h sample. (b) A close-up SEM image of the clumping $Cu_4SO_4(OH)_6 \cdot H_2O$ microflakes.

EDX spectrum in **Figure 3.7** illustrates that microflakes contain Cu, S and O, and therefore confirms the phase from the elemental aspect. PVP is proven to significantly interact with the crystalline phases during crystal growth, hence carbon signal is strong for later samples. While at this precursor stage, carbon signals from microflakes are weak, indicating that PVP might have not yet reacted with Cu. Si signal is attributed to the silica substrate which the powder sample is deposited on for SEM and EDX experiments.
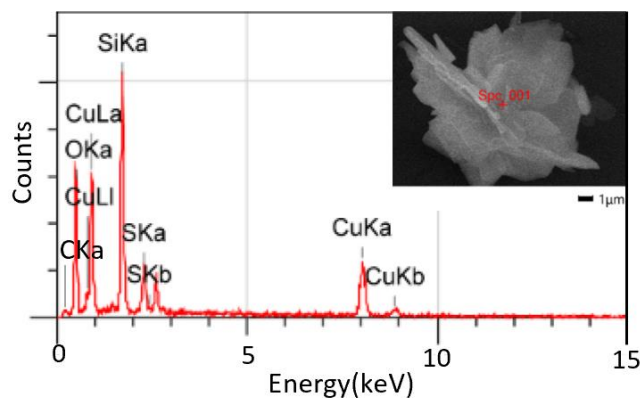
Figure 3.7. EDX spectrum of $Cu_4SO_4(OH)_6 \cdot H_2O$ microflakes from 1.5 h sample. Inset is the corresponding flakes where the spectrum was collected. Si signal is attributed to the silica substrate to support samples.
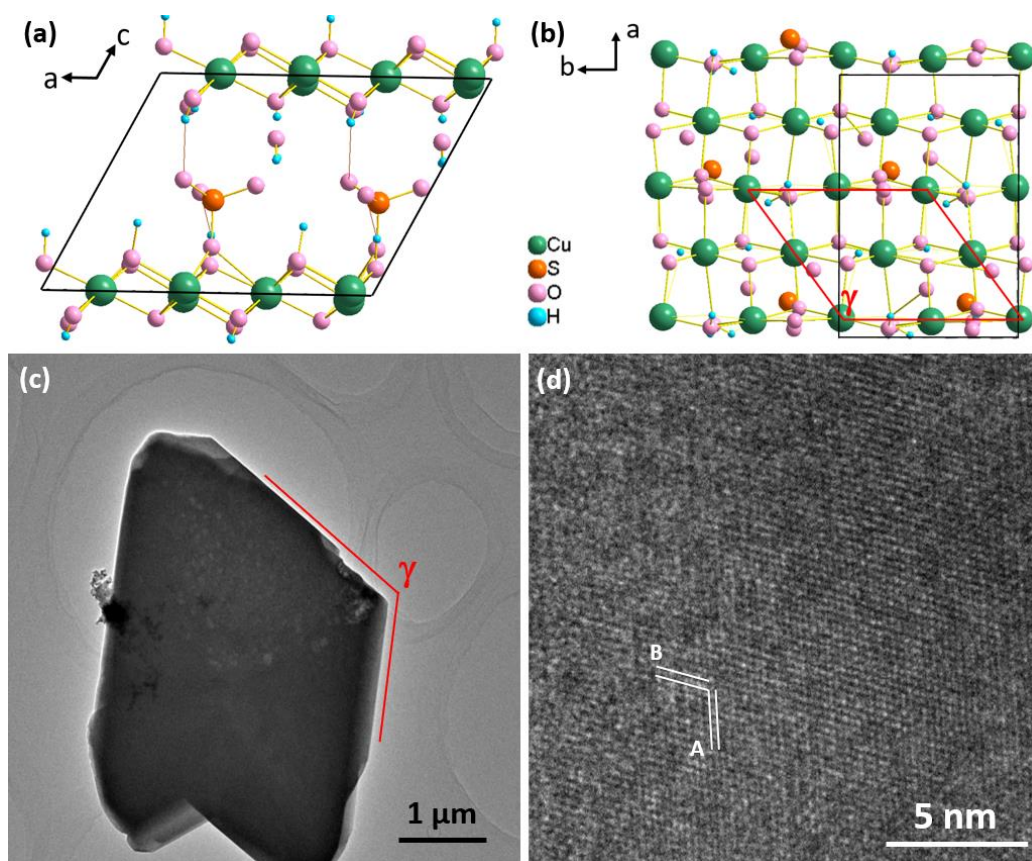
Figure 3.8 (a) Structural model of $Cu_4SO_4(OH)_6 \cdot H_2O$, viewing from the [010] axis. (b) Structural model of $Cu_4SO_4(OH)_6 \cdot H_2O$, viewing down the [001] axis. The monoclinic unit cell is shown by solid black lines. The solid red lines in (b) show a rhombus unit cell composed of (200) and (220) planes with the interplanar angle γ = 124.19 °. (c) Low-magnification TEM image of a $Cu_4SO_4(OH)_6 \cdot H_2O$ microflake from 1.5 h sample. The inter-edge angle γ is measured at 123.91 °. (d) HRTEM image of a $Cu_4SO_4(OH)_6 \cdot H_2O$ microflake from 1.5 h sample. The d-spacings marked A and B are measured at 2.33 Å and 2.68 Å, which are assigned to ($\bar{4}$00) and (220) planes of monoclinic $Cu_4SO_4(OH)_6 \cdot H_2O$.

54

Low magnification TEM and HRTEM images of $Cu_4SO_4(OH)_6 \cdot H_2O$ microflakes were captured. Crystallographic analyses were performed together with HRTEM interpretation. **Figure 3.8(a)** and (**b**) reflect that the crystal structure consists of relatively stable $Cu_4(OH)_6^{2+}$ layers parallel to the (ab) plane. The layers are connected by SO_4^{2-} anions via hydrogen bonds along the c axis. The typical shape of the microflakes is rhombus plate, as demonstrated in **Figure 3.8(c)**. The obtuse angle of this rhombus plate is measured at 123.91 ° which matches the obtuse angle γ between {200} and {220} planes (**Figure 3.8 b**). The d-spacings from the HRTEM image (**Figure 3.8 d**) are measured at 2.33 Å and 2.68 Å, which correspond to $(\bar{4}00)$ and (220) planes.

For the precursor $Cu_4SO_4(OH)_6 \cdot H_2O$, the valence of Cu stayed at 2+. The reduction behaviour of Cu by PVP has not yet happened. However, the $Cu_4SO_4(OH)_6 \cdot H_2O$ phase was soon reduced by PVP to form Cu_2O and disappeared.

3.3.4 Intermediate Cu_2O Spherulite

As implied in the XRD pattern (**Figure 3.3a**), Cu_2O co-existed with $Cu_4SO_4(OH)_6 \cdot H_2O$ in 1.5 h sample. Meanwhile, from the SEM image (**Figure 3.6a**), spherical particles co-exist with $Cu_4SO_4(OH)_6 \cdot H_2O$ microflakes. The spherical particles are about 5 to 10 μm in diameter and preserve grainy surface, as shown in **Figure 3.9(a)**. Cross-section image shows a spherulite construction (**Figure 3.9b**) with needle-like bundles lying along the radial directions. **Figure 3.9(c)** shows a fragment of spherulite from sample grinding which also shows needle-like bundle construction.
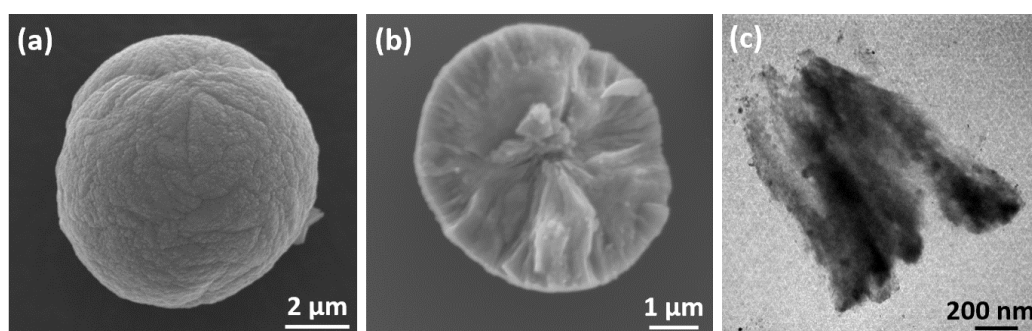
Figure 3.9 (a) SEM image of a spherical particle in 1.5 h specimen. (b) SEM image of a cross-section of a sphere, revealing the spherulite structure consisting of needle-like bundles lying down along the radial directions. (c) Low magnification TEM image of a piece of spherulite fragment which shows bundle components.

Spherulites refer to the aggregates which comprise radially arranged acicular crystals.[31] A similar structure was found in naturally occurring and biomimetic synthesised calcite spherulites, in which the needle-like particles contained oriented calcite nanocrystallites embedded in alginate polymer matrix.[32] The self-oriented assembly of calcite nanocrystallites was due to their dipolar property. In the present work, HRTEM images also witnessed nanocrystallites embedded in a polymer matrix, as shown in **Figure 3.10(a)**, implying that the nanocrystallites of Cu_2O may generate a dipolar field to form spherulites. The corresponding fast Fourier transform (FFT) pattern of the multi-orientated nanocrystallites is shown in **Figure 10(b)**. The d-spacings marked A to F are measured at 3.02 Å, 2.47 Å, 2.15 Å, 1.71 Å, 1.52 Å, 1.24 Å, and are assigned to (110), (111), (200), (211), (220), (222) planes of cubic Cu_2O phase.
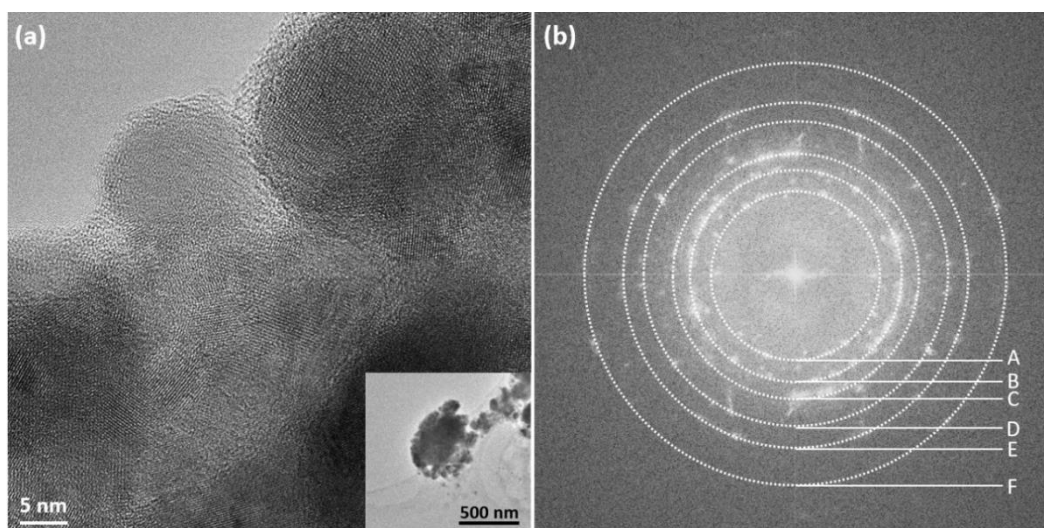
Figure 3.10 (a) HRTEM of a spherulite fragment from 1.5 h specimen. Crystal fringes present themselves in nanocrystallite form. The inset is where the HRTEM image was captured. (b) Corresponding FFT pattern which indicates the multiple orientations of crystal fringes. The d-spacings of the polycrystalline rings marked A, B, C, D, E and F are measured respectively at 3.02, 2.47, 2.15, 1.71, 1.52 and 1.24 Å.

Elemental analyses of the Cu_2O spherulite were performed to check the existence of PVP and prove its function as an aggregating surfactant. EDX spectrum, as displayed in **Figure 3.11(a)**, witnesses the existence of C, O and Cu elements in the spherulite. While SXES technique which is sensitive to light elements, detects C, N and O elements in the spherulite (**Figure 3.11b**). Both indicate that the spherulites contain PVP.
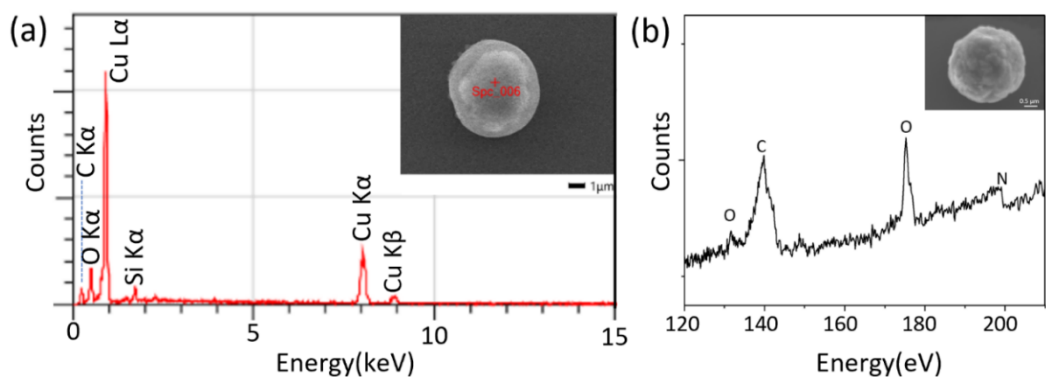
Figure 3.11 EDX spectrum of a Cu_2O spherulite from 1.5 h sample. Inset is the corresponding crystal where the spectrum was collected. (b) SXES spectrum of a Cu_2O spherulite from 1.5 h sample. Inset is the corresponding crystal where the spectrum was collected. Both spectra were collected on silica substrates to avoid any unexpected carbon element signal from SEM carbon tape.
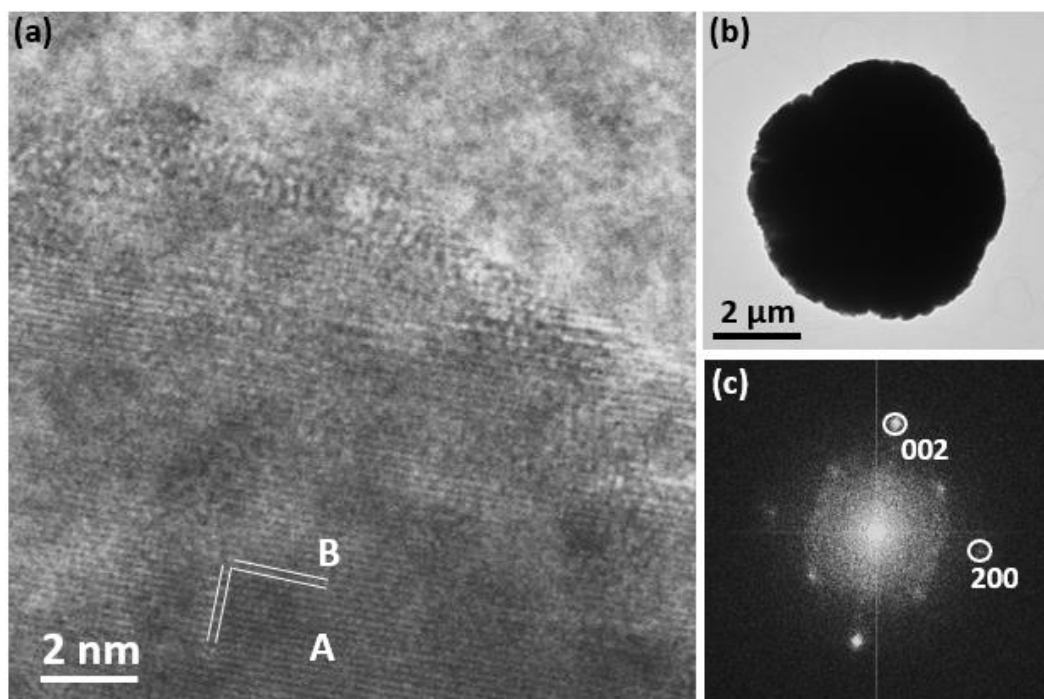
Figure 3.12 (a) HRTEM image from a spherulite in 1.5 h specimen. The d-spacings of A and B are both measured at 2.14 Å, which are indexed to the (200) and (002) planes of cubic Cu_2O. (b) Low magnification TEM image of the spherulite where the HRTEM image was captured which displays a spherical profile. (c) Corresponding FFT pattern with the crystal planes marked as (200) and (002).

Similar to the system of calcite spherulite, Cu_2O might also undergo self-orientation in PVP to form well-aligned crystalline domains. Well-aligned Cu_2O crystalline domains and

corresponding low magnification TEM images are demonstrated in **Figure 3.12**. Such spherulites only exist for a short time in the system and transform into later crystals momentarily. Applying $Cu(NO_3)_2 \cdot H_2O$ as the starting material, the spherulite morphology of Cu_2O can be preserved. The dipole field driven growth of Cu_2O/PVP spherulites will be analysed in **Chapter 4**.

To further confirm the existence of PVP in the spherulites, FTIR was applied to characterize the chemical bonds in the sample. The FTIR spectrum of 2 h sample shows many bands from PVP (**Figure 3.13a**). The relatively sharp absorption band at 3668 cm^{-1} is assigned to OH stretching from the hydroxyl terminations of PVP. The bands of CH_2 and CH stretching (2970 cm^{-1}, 2900 cm^{-1}, 1394 cm^{-1}, 893 cm^{-1}) are assigned to the CH_2 groups in the PVP chain. The band at 1250 cm^{-1} is related to the C-N bending vibration from the pyrrolidone structure in PVP. In addition, an absorption band is observed at 600 cm^{-1} which derives from the vibrational mode of Cu_2O nanostructure.[33,34] In comparison to the PVP signal from 2 h specimen, the FTIR spectrum of pure PVP was collected, as shown in **Figure 3.13(b)**. The intensity of the band of C-O stretching (1066 cm^{-1}) significantly increases, but the intensity of the C=O stretching (1647 cm^{-1}) almost disappears. These dissimilarities may be attributed to the oxidation of PVP and the molecular scale change when reducing Cu cations, similar to the FTIR results of Ag/PVP.[35]
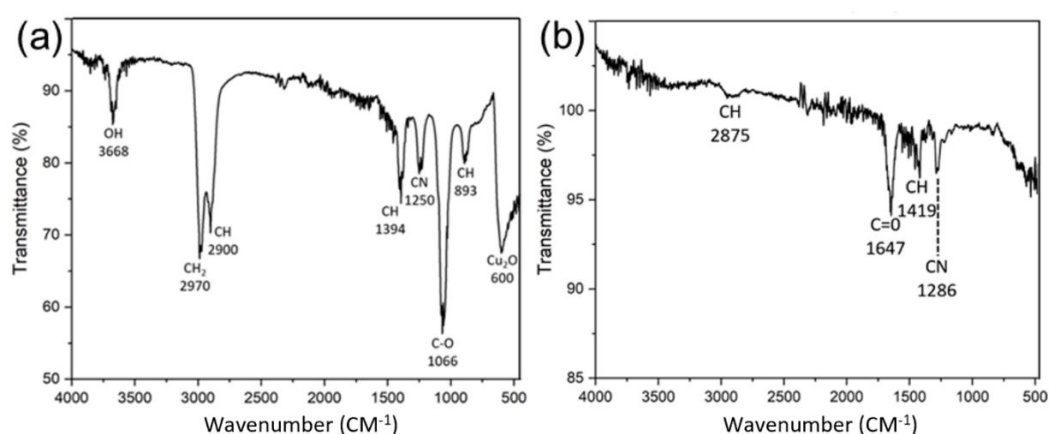
Figure 3.13 FTIR spectra of (a) 2 h sample and (b) pure PVP with peaks interpreted.

Notably, in the middle stage of the reaction time from 2 h to 6 h, dispersed nanoparticles were observed on the carbon film of the TEM specimen grids, as displayed in **Figure 3.14(a)**. HRTEM image and corresponding FFT pattern (**Figure 3.14 b** and **c**) indicate that these

nanoparticles are not monophasic. In **Figure 3.14(c)**, the d-spacings marked A, B and G are indexed to the ($\bar{1}$12), (211) and (014) planes of $Cu_4SO_4(OH)_6 \cdot H_2O$. The d-spacings marked C, D and H are assigned to the (111), (200), and (221) planes of Cu_2O. The d-spacings marked E and F are interpreted to the (111) and (200) planes of Cu. The results imply that the nanocrystallites are from the decomposition of the $Cu_4SO_4(OH)_6 \cdot H_2O$ microflakes and step-by-step reduction of Cu^{2+} to Cu^+ and Cu. In other words, the microflakes are gradually reduced to Cu_2O nanocrystals, some of which are further reduced to Cu nanocrystals. $Cu_4SO_4(OH)_6 \cdot H_2O$ nanocrystallites are derived from the breakage of the microflakes when being reduced by PVP. Chronologically, these nanocrystallites of $Cu_4SO_4(OH)_6 \cdot H_2O$ transform to Cu_2O nanocrystallites which act as the building units of spherulites. Subsequently, Cu_2O would be further reduced to Cu, producing final morphology.
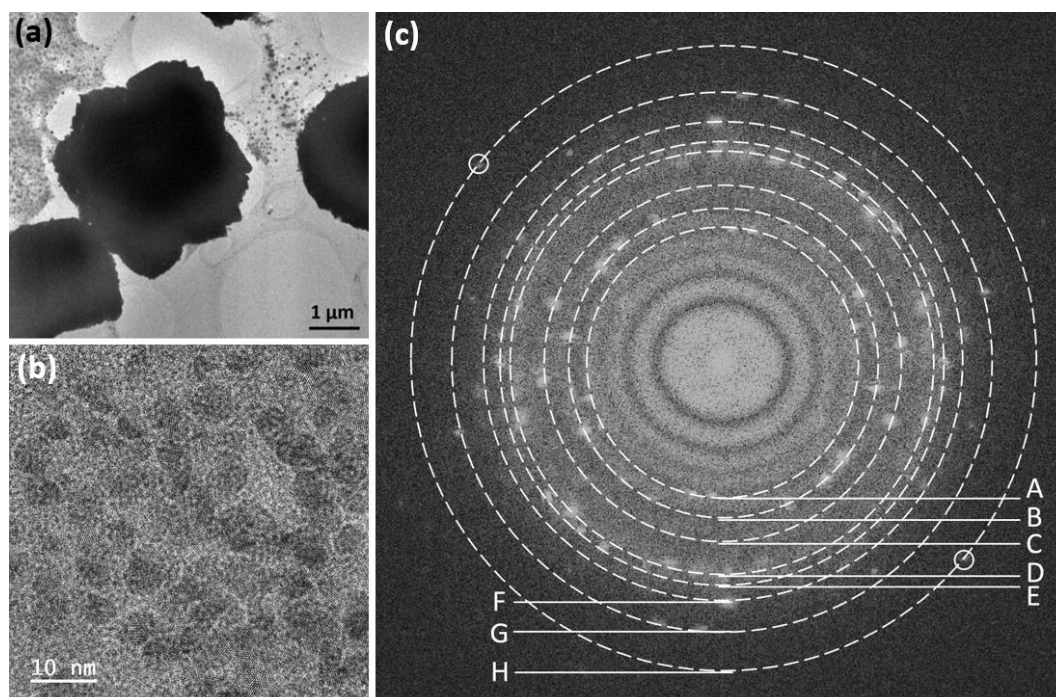
Figure 3.14 (a) TEM image of 2 h sample showing many nanoparticles along with bulk spherulites. (b) HRTEM image of 6 h sample showing nanocrystallites. (c) Corresponding FFT pattern of the HRTEM image of nanocrystallites in (b). The d-spacings of the polycrystalline rings marked A, B, C, D, E, F, G and H are measured at 3.31, 2.87, 2.49, 2.13, 2.03, 1.85, 1.66 and 1.42 Å.

During the middle stage, the Cu_2O/PVP spherulites did not exist for a long time either. The surface of Cu_2O/PVP spherulites quickly became rough with irregular polyhedral crystals,

as shown by typical SEM images in **Figure 3.15**. As displayed in **Figure 3.15(c)**, the needle-like component in the inner structure of these rough surface particles confirms that these rough-surface particles are developed from Cu_2O/PVP spherulites via a further crystal growth of Cu_2O.
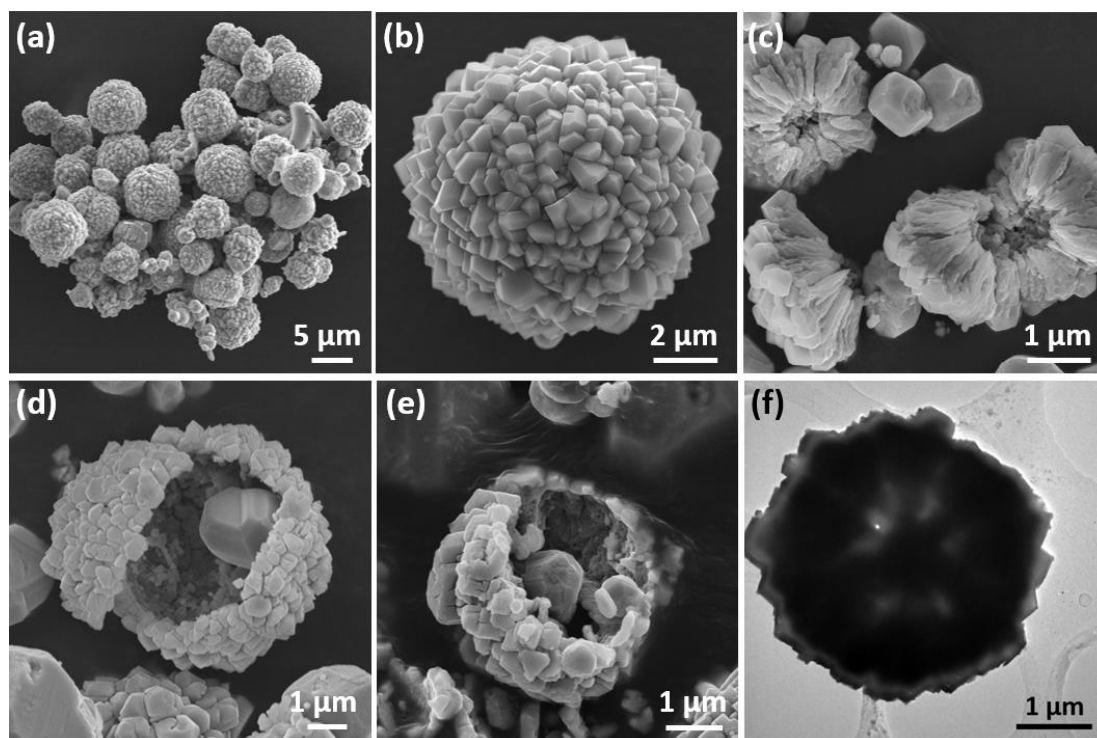
Figure 3.15 (a) Low magnification image of spherulites with rough surface in 2 h sample. (b) SEM image of a rough-surface spherulite with irregular polyhedral crystals from 4 h sample. (c) SEM image of broken rough surface spherulites in 4 h sample, which demonstrates that the inner structure is still radially oriented. (d, e) Broken spherulites from 6 h sample with their cores turned into small polyhedra, forming yolk-shell structures. (f) Low magnification TEM image of a rough-surface spherulite from 6 h sample. The dark contrast indicates the spherulite preserves a yolk-shell structure.

The inner structure of spherulite was isolated from the solvothermal environment, therefore mass transportation was limited. PVP inside the spherulite could further reduce Cu_2O nanocrystallites, producing a single Cu polyhedron for every spherulite, leading to rough-surface spherulites with a yolk-shell structure (**Figure 3.15 d, e and f**). EDX spectrum from the rough-surface (**Figure 3.16**) shows peaks of Cu and O, implying that the major phase of surface crystals is still Cu_2O.
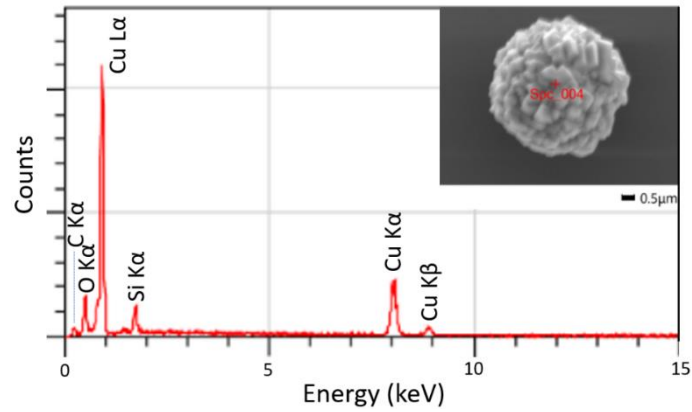
Figure 3.16 EDX spectrum of a rough-surface spherulite from 6 h sample. Inset is the SEM image of the corresponding spherulite where the spectrum was recorded.
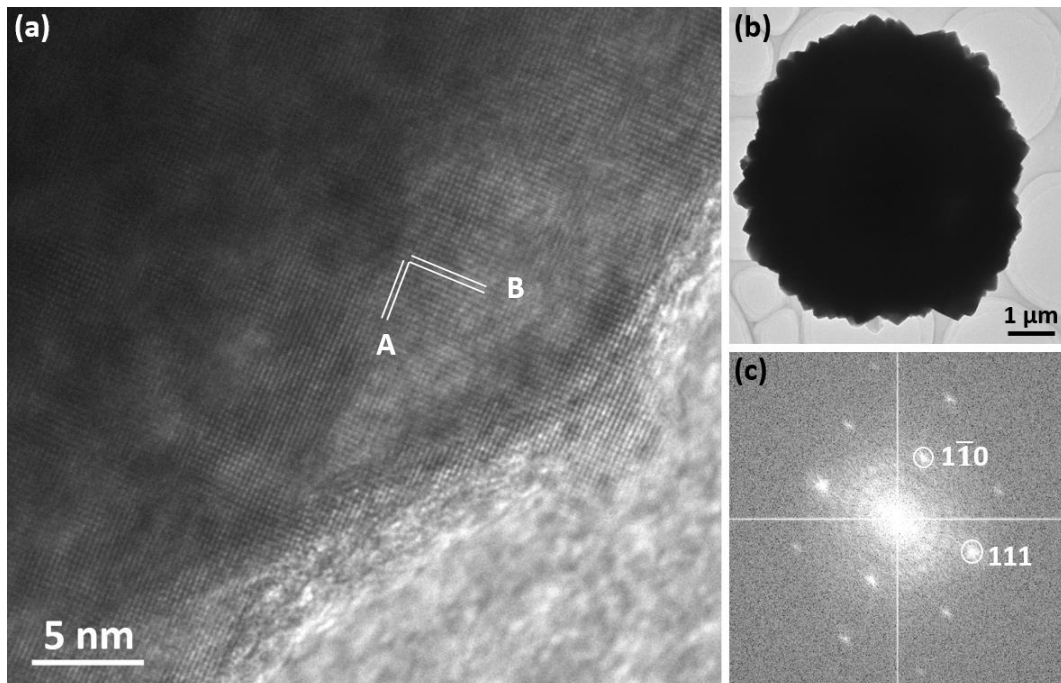
Figure 3.17 (a) HRTEM image of a polyhedron from a rough-surface spherulite. The d-spacings marked A and B are respectively measured at 2.41 Å and 2.99 Å. (b) Low magnification TEM of the spherulite from which the HRTEM image was collected. (c) Corresponding FFT pattern of the crystal fringes indexed to the Cu_2O crystal structure.

HRTEM was also performed on the rough-surface spherulites to examine the crystalline phase of those polyhedra, as displayed in **Figure 3.17**. The two perpendicular d-spacings in **Figure 3.17(a)** are measured at 2.41 Å and 2.99 Å which are assigned to (111) and ($1\bar{1}0$) planes of Cu_2O correspondingly. HRTEM interpretation indicates that the phase is still Cu_2O.

61

The premise of Cu$_2$O spherulite undergoing further crystal growth to form big polyhedra is that PVP's reducing ability is weak, therefore the reduction process is slow, leaving enough time for Cu$_2$O to proceed with self-orientation and crystallisation. In the growing solution, the Cu$_2$O polyhedra did not stay long but were reduced by PVP and decomposed subsequently.

3.3.5 Morphological Evolution of Cu Pseudo-icosahedra

After the transformation of Cu$_2$O/PVP spherulites to Cu$_2$O yolk-shell microspheres, the weak reducing agent PVP further reduces Cu$_2$O to Cu which eventually leads to the late stage of the crystal growth process. For the reduction reaction alone, Cu is the final product which can not be further reduced by PVP. Cu is also proven to be the final phase by the XRD pattern of 9 and 12 h samples (**Figure 3.3 e and f**).
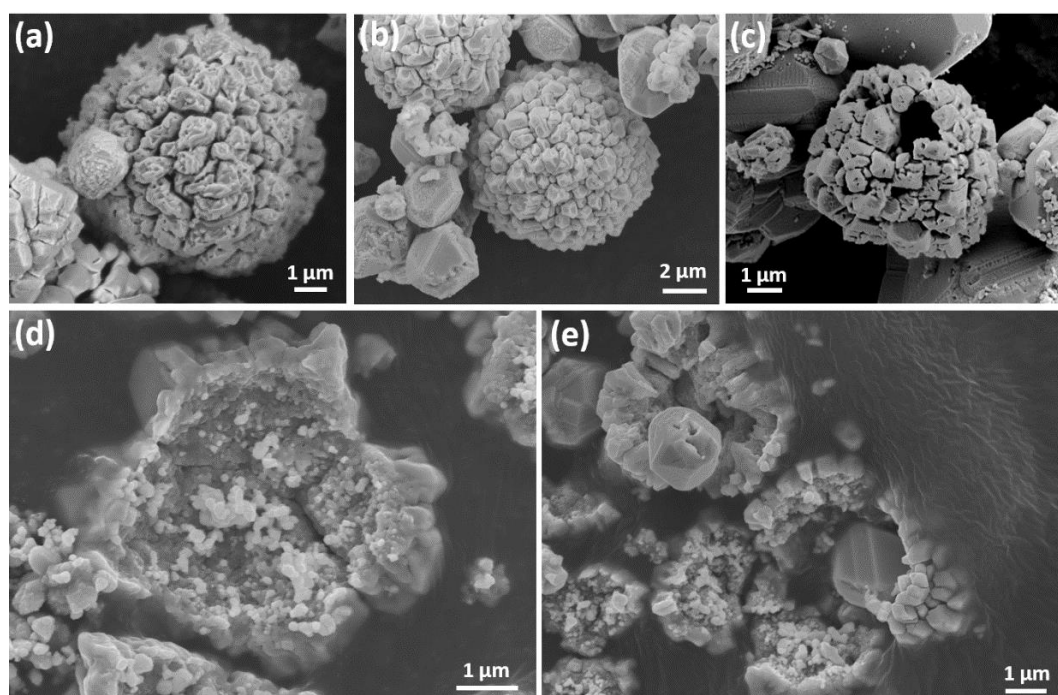
Figure 3.18 SEM images of rough surface spherulites showing corrosion and decomposition of the surface irregular polyhedral Cu$_2$O crystals from (a) 5 h, (b) 7 h and (c) 9 h samples. (d, e) SEM images of 9 h samples. The nanocrystallites deposited on fragments of Cu$_2$O/PVP spherical particles resulted from the reduction and decomposition.

From the XRD pattern of 9 h sample, there are only small bumps of Cu$_2$O peaks, indicating Cu$_2$O is mostly reduced, leaving Cu alone to proceed with crystallisation and morphology

evolution. The XRD result of 9 h sample is also consistent with the SEM images. There are still a few rough-surface spherulites and related fragments observed, but the majority are nanoparticles and polyhedra, as demonstrated in **Figure 3.18** and **Figure 3.19**.

Figure 3.18(a), (b) and **(c)** show corroded Cu_2O/PVP spherulites which are being reduced, while **Figure 3.18(d)** and **(e)** display the nanoparticles along with fragments of previous spherulites. The distinct surface of these crystals becomes blurry. Reduction of Cu_2O by PVP leads to the morphology corrosion of spherulites and triggers the production of Cu nanocrystallites and further Cu pseudo-icosahedral crystals.
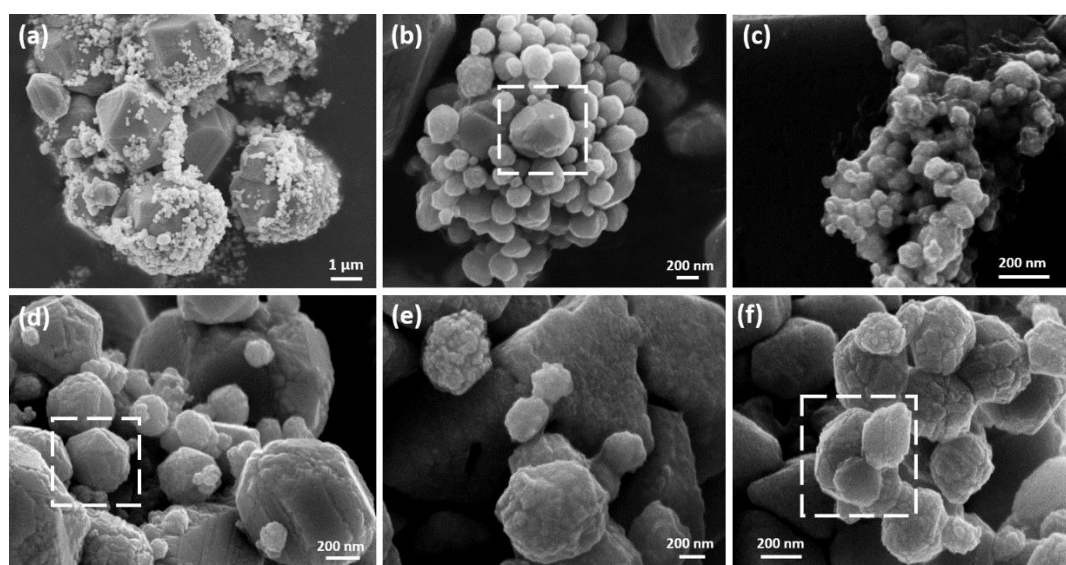
Figure 3.19 SEM images of 9 h samples which display the feature of nanoparticles and aggregates of nanoparticles. (a) Co-existence of nanoparticles and microscale polyhedra. (b) Close-up of nanoparticles over 200 nm in diameter. (c) Clumped and sticky nanoparticles below 100 nm. (d, e, f) Aggregates over 200 nm. Some particles already have polyhedral shape, even icosahedral features, as selected by dashed squares.

With the consumption of Cu_2O crystals, nanocrystallites and Cu polyhedra become the major two morphologies in 9 h sample, as demonstrated in **Figure 3.19(a)**. **Figure 3.19(b)** to **(f)** exhibit the features of nanoparticles and aggregates of nanoparticles. Apart from the reducing ability, PVP shows its aggregating capability again. **Figure 3.19(c)** displays that the smallest nanoparticles are in tens of nanometres. Moreover, these nanoparticles stick together, indicating the aggregating ability of PVP in the growing system. For some big spherical aggregates over 200 nm in diameter, planes are grown on their surfaces, indicating

their path of evolution to Cu polyhedral and even icosahedral morphology. Notably, these spherical aggregates are different from the Cu_2O spherulites, and Cu nanocrystallites randomly locate in the particles along with PVP without forming needle-like nanorods. From the perspective of the driving force, because electrons can freely travel between metal bonds in a metal crystal and metal bonds are non-polar bonds, Cu crystal structure will have no possibility to generate a dipole field and show polarity in its structural scale. Structures of cubic Cu_2O and face-centred cubic Cu crystals are schematically illustrated in **Figure 3.20**.
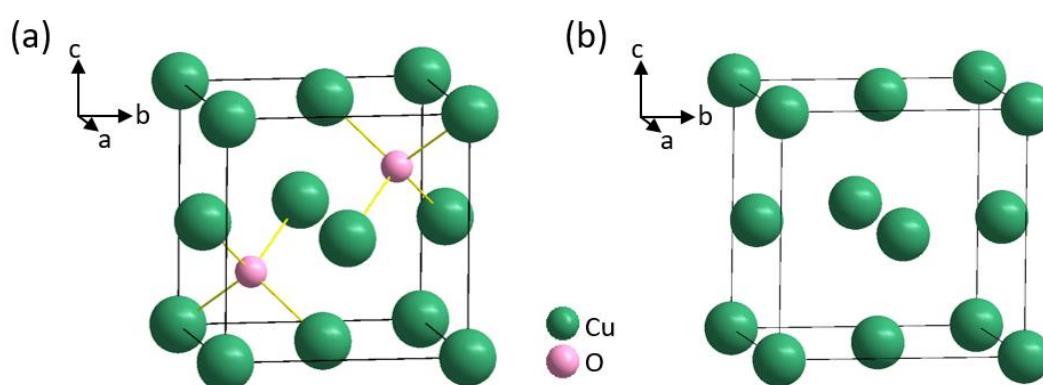
Figure 3.20 Schematic illustration of cubic Cu_2O (a) and face-centred cubic Cu (b) crystals.

Cu/PVP spherical particles do not stay long in the system and their surface soon undergoes recrystallisation to crystal planes. This process produces Cu icosahedral crystals. **Figure 3.21** shows representative aggregates with plane growing and early-stage icosahedral Cu crystals with uneven surface. For one single Cu nanoparticle aggregated by PVP, on its surface, Cu nanocrystallites keep being adsorbed onto and recrystallise into triangular crystal planes. A morphologic evolution from aggregation to nanoparticle adsorption and to plane growth can be perceived by comparing **Figure 3.19(c)**, **(e)**, **(f)** and **Figure 3.21**. Although those triangular planes grow on the surface almost simultaneously, they develop themselves independently on the particle surface and never actually contact with each other. The non-contacting feature of the adjacent planes in **Figure 3.21(e)** indicates that the growth of those planes is totally independent.
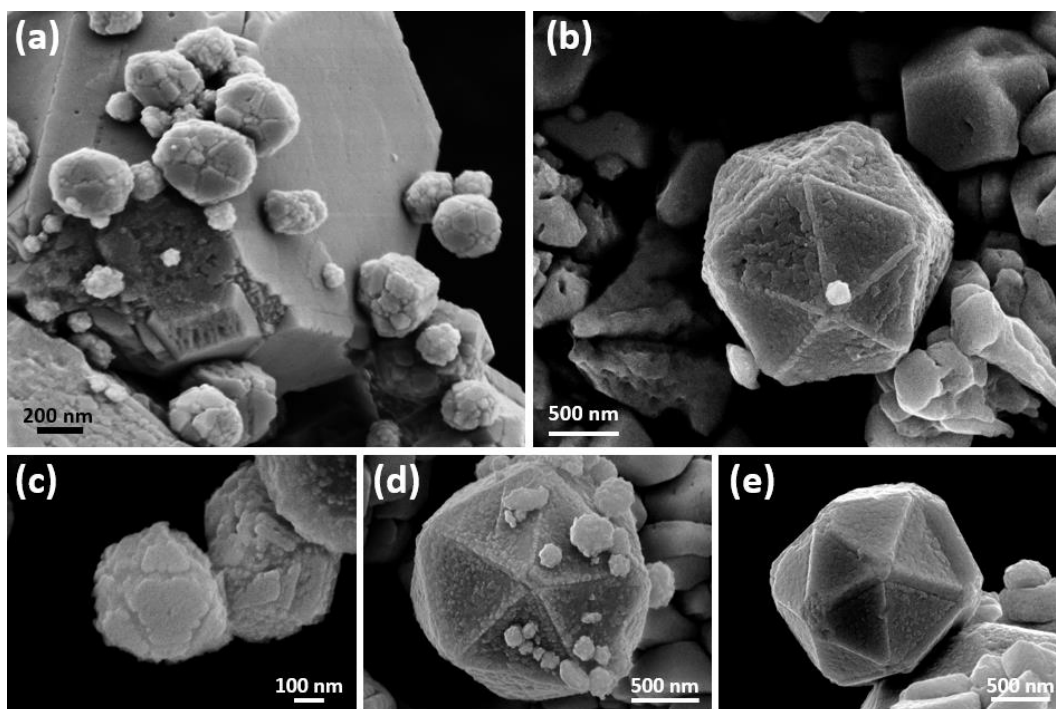
Figure 3.21 SEM images of Cu/PVP aggregates with surface recrystallisation and early-stage Cu icosahedral crystals from 6 and 9 h samples. (a) Several Cu/PVP aggregates over 200 nm in diameter which have clearly crystal planes on the surface. (b) An icosahedral Cu crystal with uneven triangular planes and distinct boundaries between the planes. (c) A small early-stage icosahedral Cu crystal with growing surface planes. (d) An icosahedral Cu crystal with uneven triangular planes and nanoparticles attached on, indicating the process of nanoparticle adsorption and surface recrystallisation. (e) An icosahedral Cu crystal with almost flat surface planes but those planes can be clearly seen not contacting each other closely, leaving rugged boundaries.

HRTEM image of an icosahedral crystal and a SAED pattern of a single triangular plate were recorded to examine the crystal plane assignment, as illustrated in **Figure 3.22**. The d-spacing marked in the HRTEM image (**Figure 3.22a**) is measured at 2.56 Å which is interpreted to (110) of cubic Cu. The two typical spots in the SAED pattern (inset of **Figure 3.22b**) of the triangular plate are indexed to the ($\bar{2}$02) and (0$\bar{2}$2) planes of cubic Cu. The zone axis which allows the two planes visible is then calculated as [111], which means that the triangular planes are all on [111] axes and are from the {111} plane family. Additionally, from [111] axis, {110} plane interpreted from the HRTEM image can be seen which also proves that they are {111} triangular family. The HRTEM and SAED interpretations elucidate that the aggregates with surface planes grown are the Cu phase, and the triangular grown facets on the surface belong to the {111} plane family.
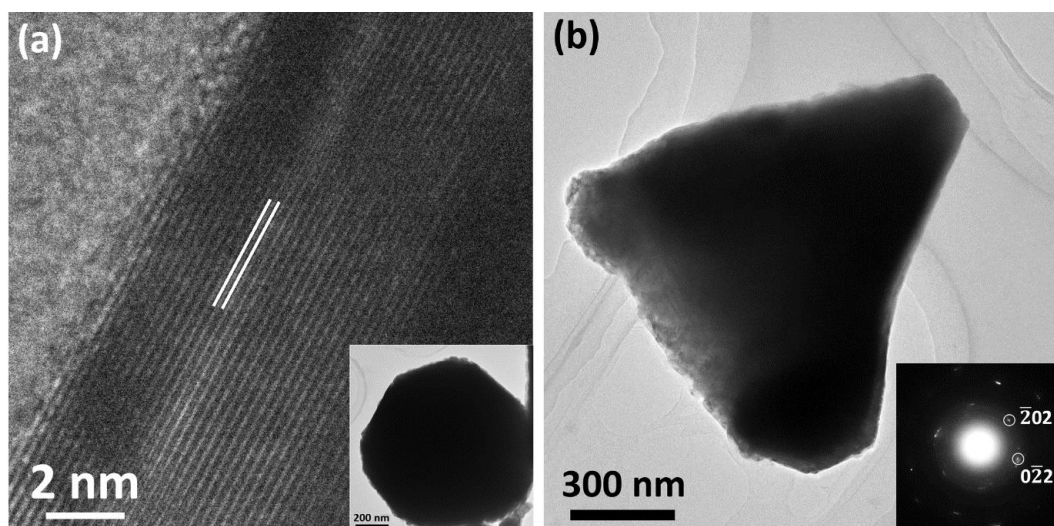
Figure 3.22 (a) HRTEM image of an icosahedral Cu crystal with d-spacing marked. The inset is the corresponding low magnification TEM image of the icosahedral crystal. (b) A low magnification TEM image of a single triangular plate. The inset is the corresponding SAED pattern with a camera length of 320 mm. The representative spots are assigned to related plane indices.

The growth of {111} planes can be explained by thermodynamics, surface free energy and BFDH law. In the stable experimental condition (150 °C to offer thermal energy for the reaction, PVP as agglomerating surfactant and reducing agent), Cu nanoparticles keep being produced from the reduction of Cu_2O by PVP. Cu nanoparticles then are agglomerated by PVP to form almost spherical aggregates and keep adsorbing Cu nanocrystallites, undergoing Ostwald ripening. For face-centred cubic crystals, the surface free energy γ is in the order of γ(111) < γ(200) < γ(220). In one specific system, crystals tend to grow into a stable morphology as a consequence of minimising the surface free energy. From the perspective of thermodynamics of crystal growth, for the early stage of Cu crystals in this system, the Cu phase would initially grow in all directions and into all facets, leading to polycrystalline domains on the surface, and the polycrystalline is indeed Cu monocrystalline with multiple orientations. As illustrated in **Figure 3.19(e), (f)** and **Figure 3.21(a)**, for some spherical Cu/PVP aggregates, there are obviously many small crystalline domains on their surface. When the aggregates grow bigger, {111} planes will cover other planes, e.g., {200} and {220}, and be the major facets to grow in order to obtain a low total surface free energy.

In this PVP-assisted high temperature system, ideally for one single icosahedral Cu, PVP adsorbs Cu nanoparticles from all directions to form an early-stage perfectly spherical Cu/PVP aggregates. On the surface of the perfectly spherical aggregate, Ostwald ripening and recrystallisation occur, allowing Cu crystal planes to grow on the spherical aggregate dimensionally in all directions. As the crystal growth goes, low energy {111} planes also grow in all directions (independently but almost simultaneously) to cover other planes with higher energy and stay to the end. The simultaneous and almost same-speed growth of {111} planes in all directions spherically leaves the icosahedral morphology with 20 {111} facets evenly distributed on the surface. Noteworthy, it is the aggregate's perfectly spherical shape and the simultaneous growth of {111} which help produce icosahedral morphology. **Figure 3.21(c)** demonstrates an aggregate with its {111} behaviour ongoing.
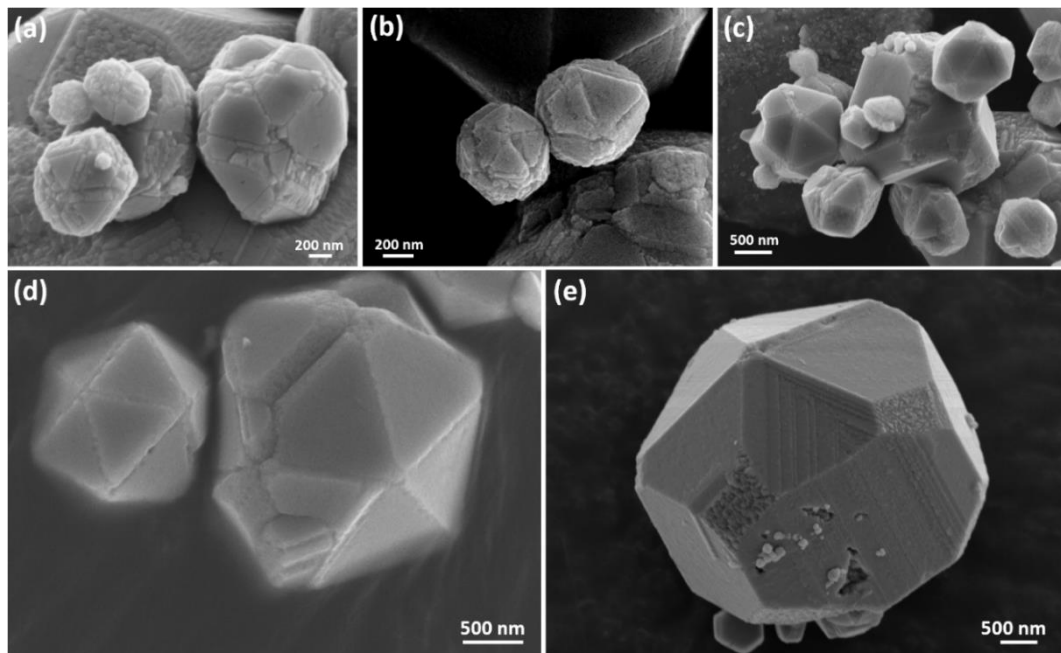
Figure 3.23 SEM images from 6 h and 9 h samples showing irregular aggregates and fault polyhedral crystals on their way to the lowest surface free energy and icosahedral morphology. (a) Non-spherical aggregates fail to build 20-fold arranged {111} facets on their surfaces. (b) A comparison of a spherical aggregate with a 5-fold grown {111} facet from the viewing direction and a non-spherical aggregate without icosahedral feature. (c) A comparison of an icosahedral crystal and a polyhedron which preserve partial icosahedral features in one vertex. (d) A comparison of icosahedral and polyhedral crystals. (e) A grown Cu polyhedral crystal with partial icosahedral features.

However, errors can happen during the ideally simultaneous growth of {111} facets and the Cu/PVP aggregates are not necessarily spherical, which lead to a yield decrease of icosahedral morphology. **Figure 3.23** illustrates several aggregates which fail to grow {111} simultaneously and evenly on their surface, and polyhedra that are not icosahedra but have partial icosahedral features.

Therefore, icosahedral crystals with 20 {111} facets can only be achieved from spherical aggregates. Ideally, on those spherical aggregates, Ostwald ripening occurs at the same speed on the surface in 3 dimensions, therefore {111} facets grow and cover the surface independently and simultaneously in 3 dimensions.

Additionally, it is at this stage when we realise that the icosahedral crystals are actually pseudo-icosahedral. As discussed in **Section 3.3.1**, the interplanar angle between {111} facets is 70.53 °. Viewed from one vertex, the angle between adjacent edges of Platonic icosahedron is 72 °. There are 5 edges from one vertex, making the sum of 5 inter-edge angles to be circularly 360 °. However, a combination of 5 {111} interplanar angles only reaches a total value of 352.65 °, leaving a total misfit of 7.35 °. Therefore, no matter how {111} facets are arranged, adjacent facets will never intercept each other in one line. As aforementioned, icosahedral crystals are in small nanoscale below 10 nm, and lattice expansion can occur to cancel the angular misfits.[10,16] When it comes to microscale which crystal d-spacing is not comparable to, distinct gaps or overgrowth of high-indices planes between {111} facets will be presented, representing the angular misfits.

For the factor of angular misfit and the difference between synthesised Cu icosahedral crystals and Platonic icosahedron, we hereby propose that these crystals with 20 {111} facets should be named pseudo-icosahedral crystals. The term pseudo- is used in order to distinguish the synthesised 20-facet crystal from Platonic icosahedron and emphasise the inevitable angular misfit when forming 20-facet crystals. Hereafter, we refer to such morphology as pseudo-icosahedral. Besides, a commonly-called 5-fold twinning of {111} facets viewed from any vertex is actually not a twinning defect. Because due to the angular misfit, the twinning of 5-fold can not be achieved and these {111} facets are grown independently, not from direct twinning in a nucleation stage.

Grown pseudo-icosahedral particles in 9 h and 12 h samples are observed, as demonstrated in **Figure 3.1** and **Figure 3.24**. As illustrated in **Figure 3.24**, there can be either

gaps or overgrowth of high-indice facets between {111} facets which represents the angular misfit and the actual non-contacting feature of adjacent {111} facets.
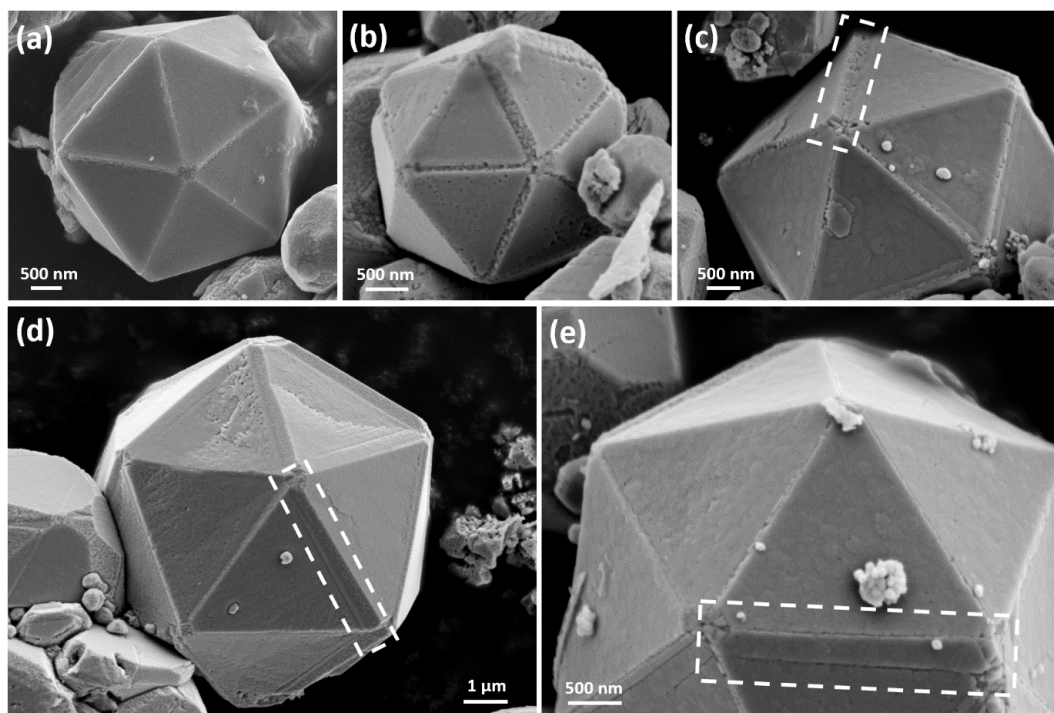

Figure 3.24 Grown pseudo-icosahedra with distinct misfit features from 9 h and 12 h samples. (a) A grown pseudo-icosahedral crystal with minor and non-obvious gaps between adjacent {111} planes. (b) A grown pseudo-icosahedral crystal with clear gaps between adjacent {111} facets. (c, d, e) Grown pseudo-icosahedral crystal with clear overgrowth of high-indice facets between adjacent {111} facets. The overgrowths of facets are marked with dashed rectangles.

FTIR and EDX have been used to examine the existence of PVP and the elemental composition. Same as the FTIR spectrum of 2 h sample (**Figure 3.13a**), CH_2, CH, CN and C-O bands are observed and assigned to PVP for the spectrum of 12 h sample (**Figure 3.25a**). The result elucidates the existence of PVP inside the particles, which further implies that the icosahedral crystals are grown from the aggregation of Cu by PVP. Additionally, the Cu-O band at 600 cm^{-1} in the spectrum no longer exists, compared to that from **Figure 13(a)**, indicating that all Cu_2O crystallites have been reduced to Cu. EDX spectrum (**Figure 3.25b**) of a pseudo-icosahedron shows the major element is Cu, accompanied by weak peaks of C and O. The reason for low C and O intensities is that these elements from PVP molecules are inside the Cu pseudo-icosahedral crystal, which may be hard to capture due to the weak penetration of EDX radiation. The emitted characteristic X-rays of the light elements further suffer from a

large absorption by the sample again and the EDX detector, generating decreases of peak intensity of C and O.
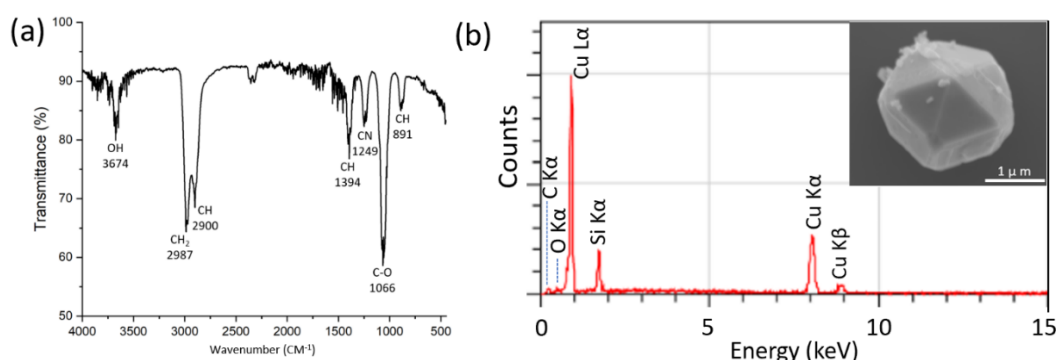
Figure 3.25 (a) FTIR spectrum of 12 h sample with some peaks interpreted and marked. (b) EDX spectrum collected from a Cu pseudo-icosahedral crystal. Inset is the corresponding Cu pseudo-icosahedral crystal where the EDX spectrum was collected.

Noteworthy, for a cubic structure, there are 8 {111} equivalent planes. A 20-facet pseudo-icosahedral crystal can not be generated by applying single crystal growth which only grows 8 {111} facets at maximum. 20-facet pseudo-icosahedral crystals grow from polycrystalline Cu/PVP aggregates which contains Cu nanocrystallites with random orientations.

In the synthesis of zeolite analcime, nanocrystallites aggregated into large spheres. Surfaces of these spheres then recrystallised into a thin icositetrahedral single-crystalline shell consisting of 24 identical {211} facets, followed by the extension of recrystallisation from the surface to the core[36], which was an example of reversed crystal growth. A similar process in zeolite A led to a cubic single-crystalline shell with an amorphous core.[37] When the precursor materials inside were completely consumed by inner Ostwald ripening, the particles became hollow crystals. The reversed crystal growth has also been found in metal oxides, carbonates, metallic organic frameworks, organic crystals, etc.[38] In fact, the formation of polycrystalline or non-crystalline aggregates is the first and crucial step of the reversed crystal growth mechanism. A similar phenomenon was observed in the present work.[36,37]

The formation of pseudo-icosahedral Cu crystals is not the end of the crystal growth. Triangular plates joint together, covering the surface of the particles, although the (111) twin planes would never achieve due to the mismatch of 1.47 ° per gap between adjacent {111} facets. PVP and Cu nanocrystallites exist in the pseudo-icosahedral particles as the particles

grow themselves on the surface of initial Cu/PVP aggregates. Then the inner surface recrystallisation and interior Ostwald ripening help to extend the thin planes to thick plates from the surface to the core. Consequently, we witness the thickness of surface {111} plates increases until all the Cu nanocrystallites in the core are consumed via inner Ostwald ripening and recrystallisation. Eventually, hollow pseudo-icosahedral particles with thick triangular {111} plates are produced, as demonstrated in **Figure 3.26**.
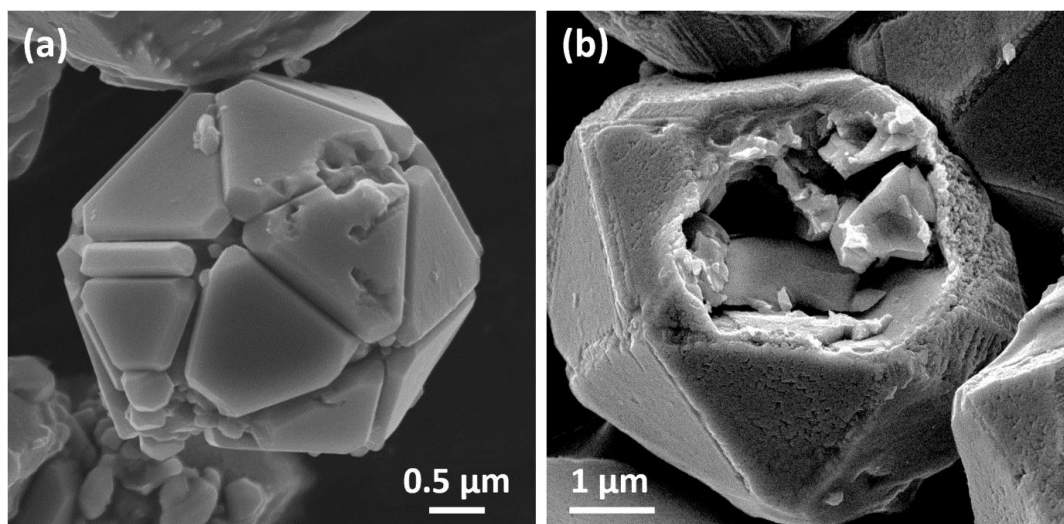
Figure 3.26 (a) SEM image of a pseudo-icosahedral particle of Cu from 12 h sample with thick triangular plates. (b) SEM image of a pseudo-icosahedral particle of Cu from 9 h sample, showing a hollow feature.

3.3.6 Proposed Formation Mechanism

Based on the experimental results and related analyses presented above, we are now able to elucidate the phase transformations and propose a formation mechanism of Cu pseudo-icosahedral microparticles step-by-step, as demonstrated in **Figure 3.27**. The multifunction of PVP and a thermodynamic control during the crystal growth are also discussed.
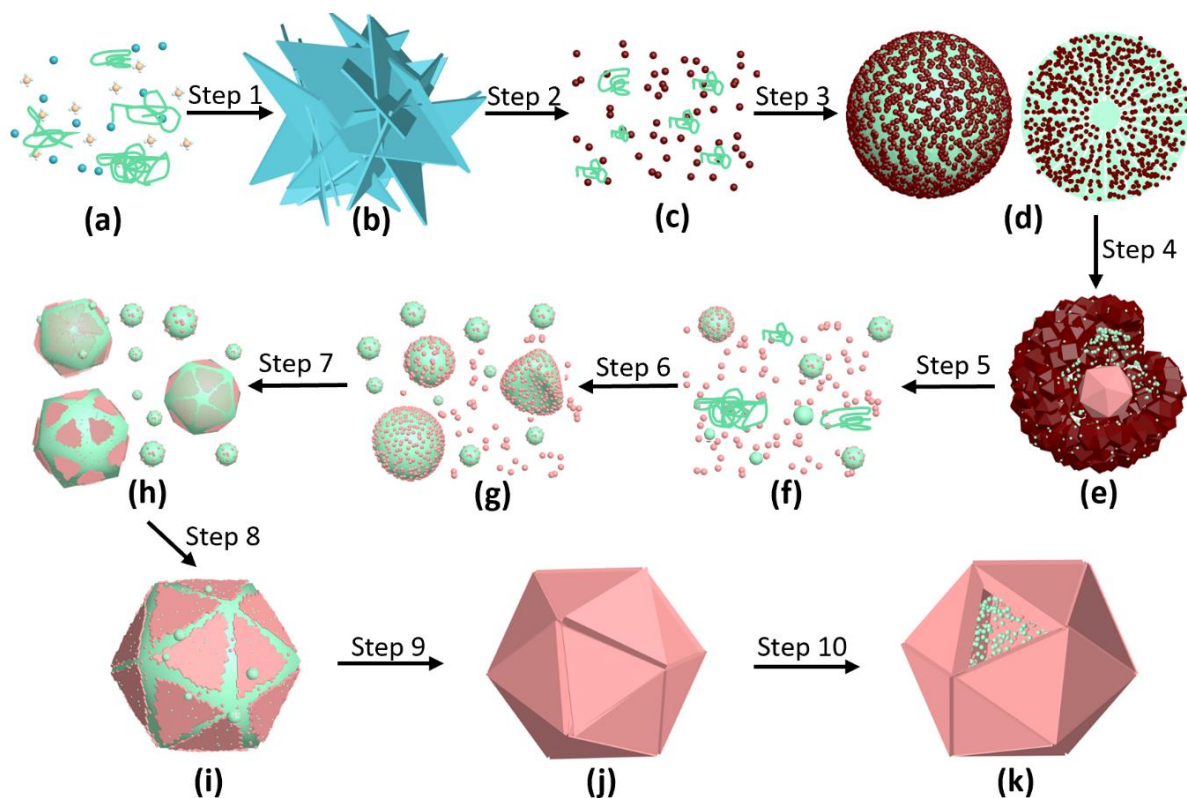
Figure 3.27 Schematic diagram of the proposed reduction process and formation mechanism of Cu pseudo-icosahedra. (a) Cu^{2+} (blue), SO_4^{2-}(light brown), PVP molecules (light green) in a DMF solution. (b) $Cu_4SO_4(OH)_6 \cdot H_2O$ microflakes which appeared to be optically light blue. (c) Cu_2O nanocrystallites (dark brown) were derived from the reduction and decomposition of $Cu_4SO_4(OH)_6 \cdot H_2O$ microflakes. (d) Cu_2O/PVP spherulites from PVP-led oriented attachment. (e) Cu_2O/PVP spherulite with irregular Cu_2O crystals on the surface from recrystallisation. A Cu pseudo-icosahedron inside was developed by the reduction behaviour of interior Cu and PVP, forming a yolk-shell structure. (f) Cu nanocrystallites from second reduction and decomposition of Cu_2O crystals. (g) Spherical Cu/PVP aggregates. (h) Ostwald ripening and Surface recrystallisation to form triangular {111} plates on the surfaces of those spherical aggregates. (i) Recrystallisation on the surface to form 20 triangular {111} plates. (j) Cu pseudo-icosahedron with gaps between adjacent {111} plates. (k) Extension of {111} plates due to interior oriented attachment of Cu.

Initially, $CuSO_4 \cdot 5H_2O$ and PVP are dissolved in a DMF solution at 150 °C. Rhombus-shaped microflakes of $Cu_4SO_4(OH)_6 \cdot H_2O$ appear, which is the first solid precipitate in the system (**Step 1**).

As the reaction continues, $Cu_4SO_4(OH)_6 \cdot H_2O$ microflakes decompose to nanoscale fragments and nanocrystallites when Cu^{2+} cations in the microflakes are gradually reduced by the mild reducing agent PVP to form Cu_2O nanocrystallites (**Step 2**).

In **Step 3**, the Cu_2O nanocrystallites capped with PVP aggregate into spherulites. The cross section of the spherulites demonstrates radially oriented nanorods. Based on the possibility of generating dipolar force and the agglomerating effect of PVP, we deduce the possible driving force of self-orientation of Cu_2O nanocrystallites along the radial direction in the spherulites would be a dipolar field generated by the nanocrystallites themselves.

Considering the weak reducing ability of PVP, there is enough time for Cu_2O to proceed with self-orientation to large crystalline domains. Cu_2O nanocrystallites near the surface of the spherulites undergo further growth to form larger irregular polyhedral Cu_2O crystals, deriving rough surfaces of the spherulites (**Step 4**). Spherulites with smooth surfaces are no longer observed. A similar morphology of rough surface Cu_2O hollow particles was recently reported.[39] For those spherulites, the mass transportation between the outside and interior of the spherulites is restricted.

However, PVP exists in the spherulites, capable of showing its reducing ability and agglomerating function, reduces the Cu_2O nanocrystallites inside the spherulites and produces individual Cu polyhedral crystal for every spherulite. Among such polyhedral Cu crystals, a pseudo-icosahedral morphology may appear. A similar process reappears in the morphology evolution of the Cu/PVP spheres in the solution, as demonstrated in subsequent steps. Therefore, the space inside every Cu_2O spherulite can be regarded as a smaller growth system to grow Cu polyhedra in comparison to the DMF solution growth system, as the components, Cu_2O and PVP, are all presented in the sealed spherulite interior space.

Furthermore, the Cu_2O irregular crystals are then slowly reduced by the mild reducing agent PVP in the solution and decompose into Cu nanocrystallites (**Step 5**). PVP then only functions as the agglomerating surfactant. Cu nanocrystallites capped with PVP subsequently assemble to form spherical Cu/PVP particles (**Step 6**).

Like the typical reversed crystal growth routes[40], recrystallisation of the Cu nanocrystallites inside Cu/PVP aggregates is suppressed due to the limited PVP amount inside and blocked mass transportation. The initial active sites for crystal growth are on the surface of the particles. In fact, 20 triangular {111} plates of the fcc Cu structure are developed on the particle surface and their locations match the final facets of an icosahedron (**Step 7 and Step 8**). The selection of the {111} planes as the exposed faces can be explained thermodynamically, firstly according to Curie and Wulff's theorem.[41,42] Because the {111} facet family have the

largest d-spacing therefore the minimum binding energy in the Cu crystals, ensuring that the particles can achieve a minimum local surface free energy by keeping {111} exposed.

These thin plates grow themselves by absorbing Cu phase from the growing system (Ostwald ripening). The growths of individual {111} facets are totally separate and independent to each other. Such morphology appears to be multi-fold twinning is not derived from the contact twinning of {111} facets. Additionally, the angular misfit determines that the contacting of those facets is never multi-fold twinning. So the term pseudo-icosahedral is proposed. Pseudo-icosahedral morphology forms via the adsorption of Cu phase from the solution and corresponding Ostwald ripening on the surface of initial spherical Cu/PVP aggregates.

By absorbing Cu nanocrystallites from the solution and executing recrystallisation, Cu pseudo-icosahedral morphology forms (**Step 9**). Notably, Cu phase and the surfactant PVP also exist in the initial spherical aggregates. Therefore, the interior oriented attachment and recrystallisation further extend the {111} facets to thick plates inwards. The thickness of {111} plates increases till all Cu nanocrystallites inside are consumed in the process of interior recrystallisation, generating a hole at the centre (**Step 10**).

3.3.7 Discussion of Thermodynamics

If a Cu crystal grows via a classical growth route, starting from a single nucleus, followed by layer-by-layer deposition of Cu atoms without twin defects, an octahedral morphology may be achieved with 8 {111} facets.[43] This process will not lead to an icosahedron because the total number of the {111} faces in a single crystal is 8. If the crystal growth starts from a nucleus containing several twin defects, a pseudo-icosahedral particle consisting of 20 tetrahedra may form only when the particle size is at nanoscale. In this case, the lattice tension at the boundaries between adjacent tetrahedra may be eased by d-spacing expansion and surface relaxation. While the d-spacing is not comparable to micrometre, making it unrealistic to form icosahedral morphology at microscale[14,44]. However, by applying the polymer assisted crystal growth method, microscale Cu icosahedra are successfully synthesised. And only when the size reaches microscale, the angular mismatch becomes

obvious and unneglectable, therefore the term pseudo-icosahedral becomes a proper adjective to describe the morphology.

The formation of pseudo-icosahedral morphology with 20 {111} facets exposed can be explained thermodynamically. First, the particles would eventually preserve the {111} facets, because the {111} planes have the largest d-spacing and the lowest surface binding energy (E_b) or minimum surface free energy per unit of area, σ. Second, the overall morphology tends to possess a minimum specific surface area, therefore the smallest total surface energy. The total surface free energy would be

$$E_{tot} = \sigma \times A_s \tag{3.1}$$

There are three possible polyhedra formed only by the {111} facets, tetrahedron, octahedron and icosahedron. All of them have the same E_b, but different specific surface areas, A_s. When given morphology is in the same volume, the specific surface area will vary, leading to different minimum total surface energy. We assume for given typical shapes, sphere, cube, tetrahedron, octahedron, icosahedron, the volumes are the same at 100. Then, we calculate the surface area and corresponding specific surface area as the ratio of surface area to total volume. The results are shown in **Table 3.1**.

Table 3.1 Summary of morphological surface to volume ratio with the same volume at 100.

Morphology	Volume	Surface area	Surface to volume ratio
Sphere	100	104.19	1.042
Cube	100	129.27	1.293
Tetrahedron	100	155.24	1.552
Octahedron	100	123	1.230
Icosahedron	100	110.91	1.109

From **Table 3.1**, sphere preserves the smallest specific surface area and icosahedron, which is close to sphere morphologically, has the second smallest specific surface area when having the same volume. The specific surface area of an icosahedron is about 90% (1.109/1.230) of that of an octahedron and about 71% (1.109/1.552) of that of a tetrahedron. Therefore, the total specific surface free energy of an icosahedron is much lower. Although a

real synthesised icosahedron is actually a pseudo-icosahedron with boundaries between the facets, the small rebound of surface free energy due to the mismatch of edges of pseudo-icosahedron may not lead to a drastic increase to reach the total surface free energy of octahedron or tetrahedron.

Comparing an icosahedron with a sphere, the decrease of total surface free energy by growing {111} plates on a spherical particle associates with the cost of a small increase of the specific surface area as spherical morphology preserves the smallest specific surface area when having the same volume. So the synthetic pseudo-icosahedral morphology derives from the game theory that a minimum surface free energy of total planes grown would be required and a relatively small specific surface area would be achieved so the total energy can be preserved to have a stable morphology.

To conclude, it is demonstrated that in a thermodynamically controlled growth process of surface crystallisation, crystalline shells would naturally choose a morphology as close as possible to the morphology with minimum total surface free energy, E_{tot}, by two fundamental approaches, preferentially forming those plates with the minimum surface binding energy, E_b, and achieving a minimum specific surface area, A_s, by forming an almost spherical morphology. When there is only one type of facet to stably grow, in the cases of Cu octahedron with 8 {111} facets and icosahedron with 20 {111} as we discussed in this work, the particles grow into icosahedron in order to reduce A_s and therefore reduce E_{tot} by about 10% (1.109/1.230 in **Table 3.1**).

When plates with the lowest E_b form, the A_s value may increase, as shown in **Table 3.1** for a sphere and icosahedron. Therefore, a balance of the two factors would be preferably chosen to stabilise the final morphology. Many polyhedral may consist of more than one group of facets to reduce the total specific surface area, A_s, with a cost of increasing E_b. Then the total surface free energy would be

$$E_{tot} = \sum_1^i (E_{bi} \times A_{si})$$ (3.2)

where i represents different type of facets, e.g. {111}, {110} and {100} of fcc Cu. Consequently, in a thermodynamically controlled crystal growth system, the final polyhedral morphology at an equilibrium state can be predicted, although in practice, the morphology may be disturbed by external conditions and fail to achieve this. A truncated icosahedron which is even close to

spherical shape can have a slightly lower surface free energy than icosahedron, therefore closer to the equilibrium state because facets are grown at the vertex sites to cover high-energy acute vertices. **Figure 3.28** illustrates an SEM-observed truncated icosahedron and the visualised theoretical morphology.
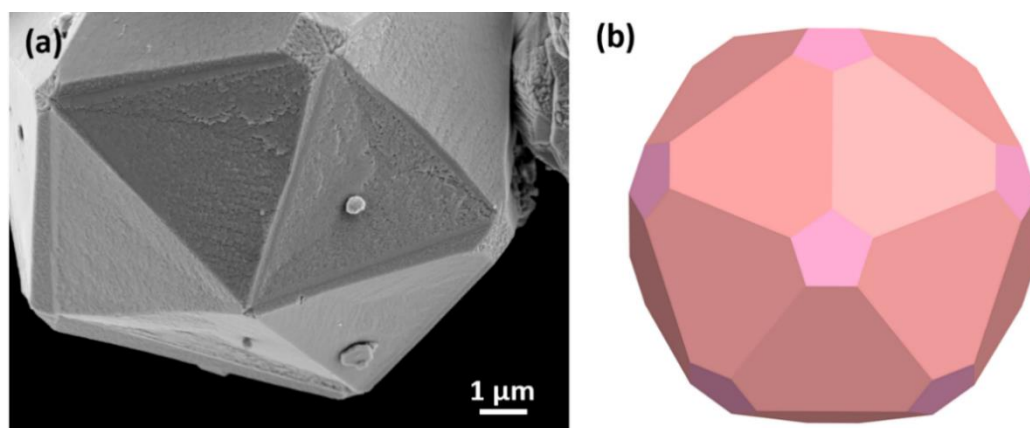
Figure 3.28 (a) SEM image of pseudo-icosahedral Cu crystal with truncated features. The vertex site appears to be flat, not acute. (b) A model of a truncated icosahedron, more approaching to spherical morphology as the equilibrium state with the smallest total surface energy.

To summarise, the formation of the morphology of pseudo-icosahedron Cu is resulted from a balance between the formation of the {111} facets with the lowest surface binding energy and the intention of approaching to the minimum specific surface area.

3.4 Conclusion

Pseudo-icosahedral Cu microcrystals have been synthesised in a solvothermal process containing $CuSO_4 \cdot 5H_2O$ as the starting material, polymer polyvinylpyrrolidone (PVP, MW~360000) as the reductant/agglomerating agent and dimethylformamide (DMF) as the solvent. The structural and morphological evolution over reaction time is investigated by electron microscopic, diffraction and spectroscopic techniques, which enables us to establish a novel formation mechanism of pseudo-icosahedral Cu crystals. Based on the BFDH law, during the surface recrystallisation of polycrystalline spheres, the most stable {111} planes of the face-centred cubic structure of Cu last till the end as the exposed faces because they have the minimum surface binding energy. Additionally, pseudo-icosahedra which generate from

spherical Cu/PVP particles has a relatively small specific surface area and a relatively small total surface free energy.

Overall, although it is challenging to obtain microscale icosahedral Cu crystals via the classical crystal growth route, Cu pseudo-icosahedra of a few micrometres in diameter, have been successfully synthesised in a solvothermal system by a non-classical crystal growth route. The pseudo-icosahedral morphology is construction of 20 {111} thin plates on the particle surface. The formation mechanism of the pseudo-icosahedral morphology is proposed based on the experimental observation and characterisation of the morphologic and structural evolution. The most crucial step is the formation of spherical particles containing Cu nanocrystallites capped by PVP polymer. The polycrystalline particles proceed with surface recrystallisation to form 20 separated {111} planes of Cu and gradually formed a pseudo-icosahedral shell, followed by interior recrystallisation which leads to the extension of {111} plates. Throughout the whole process, PVP not only serves as a mild reducing agent which reduced Cu^{2+} to Cu^+ and to Cu in a multistep process, but also functions as agglomerating surfactant participating in the crystal growth.

This project is one of the pioneering works in the microscale synthesis of icosahedral metal crystals. A thermodynamic discussion provides a new perspective on such morphology. A proposal of using the term pseudo-icosahedron instead of icosahedron to describe such morphology tells the truth that the morphology is not derived from direct {111} twinning and is never multi-twinned. Besides, such a formation mechanism involving multiple intermediate morphologies extends the pool of non-classical crystal growth routes. We also demonstrate that even if a crystal seems to be monocrystalline and originates itself from the growth of a single nucleus, it may actually come from polycrystalline growth and further recrystallisation. The newly proposed formation mechanism of pseudo-icosahedra Cu sheds light on the understanding of the formation of polyhedral crystals.

References

1   M. Görke and G. Garnweitner, *CrystEngComm*, 2021, **23**, 7916–7927.

2   Y. Xia, Y. Xiong, B. Lim and S. E. Skrabalak, *Angew. Chemie. Int. Ed.*, 2009, **48**, 60–103.

3   J. Yin, F. Gao, C. Wei and Q. Lu, *Inorg. Chem.*, 2012, **51**, 10990–10995.

4   K. Self, H. Zhou, H. F. Greer, Z. R. Tian and W. Zhou, *Chem. Commun.*, 2013, **49**, 5411–5413.

5   H. F. Greer, M. H. Liu, C. Y. Mou and W. Zhou, *CrystEngComm*, 2014, **18**, 1585.

6   A. W. Ritchie, M. I. T. Watson, R. Turnbull, Z. Z. Lu, M. Telfer, J. E. Gano, K. Self, H. F. Greer and W. Zhou, *CrystEngComm*, 2013, **15**, 10266–10271.

7   H. J. Yang, S. Y. He and H. Y. Tuan, *Langmuir*, 2014, **30**, 602–610.

8   F. Silly and M. R. Castell, *ACS Nano*, 2009, **3**, 901–906.

9   M. Tsuji, M. Ogino, R. Matsuo, H. Kumagae, S. Hikino, T. Kim and S. H. Yoon, *Cryst. Growth Des.*, 2010, **10**, 296–301.

10   X. Ma, F. Lin, X. Chen and C. Jin, *ACS Nano*, 2020, **14**, 9594–9604.

11   D. Seo, C. Il Yoo, I. S. Chung, S. M. Park, S. Ryu and H. Song, *J. Phys. Chem. C*, 2008, **112**, 2469–2475.

12   N. Goubet, Y. Ding, M. Brust, Z. L. Wang and M. P. Pileni, *ACS Nano*, 2009, **3**, 3622–3628.

13   B. Lim, Y. Xiong and Y. Xia, *Angew. Chemie. Int. Ed.*, 2007, **46**, 9279–9282.

14   W. Zhang, Y. Liu, R. Cao, Z. Li, Y. Zhang, Y. Tang and K. Fan, *J. Am. Chem. Soc.*, 2008, **130**, 15581–15588.

15   T. Ling, J. Zhu, H. Yu and L. Xie, *J. Phys. Chem. C*, 2009, **113**, 9450–9453.

16   F. Baletto, C. Mottet and R. Ferrando, *Phys. Rev. B - Condens. Matter Mater. Phys.*, 2001, **63**, 155420.

17   S. M. Rupich, E. V. Shevchenko, M. I. Bodnarchuk, B. Lee and D. V. Talapin, *J. Am. Chem. Soc.*, 2010, **132**, 289–296.

18   M. Tsuji, M. Ogino, M. Matsunaga, N. Miyamae, R. Matsuo, M. Nishio and M. J. Alam, *Cryst. Growth Des.*, 2010, **10**, 4085–4090.

19   A. A. Vikarchuk and M. V. Dorogov, *JETP Lett.*, 2013, **97**, 594–598.

20   M. Xu, L. Zhang and F. Zhao, *ACS Appl. Mater. Interfaces*, 2020, **12**, 12186–12194.

21   G. Ji, A. Ji, N. Lu and Z. Cao, *J. Cryst. Growth*, 2019, **518**, 89–94.

22   S. Wu, *Mater. Lett.*, 2007, **61**, 1125–1129.

23   A. R. Rathmell, S. M. Bergin, Y. L. Hua, Z. Y. Li and B. J. Wiley, *Adv. Mater.*, 2010, **22**, 3558–3563.

24   C. Wang, C. Wang, L. Xu, H. Cheng, Q. Lin and C. Zhang, *Nanoscale*, 2014, **6**, 1775–1781.

25   S. Venkatakrishnan, G. Veerappan, E. Elamparuthi and A. Veerappan, *RSC Adv.*, 2014,

4, 15003–15006.

26   R. Si, Y. W. Zhang, L. P. You and C. H. Yan, *J. Phys. Chem. B*, 2006, **110**, 5994–6000.

27   K. M. Koczkur, S. Mourdikoudis, L. Polavarapu and S. E. Skrabalak, *Dalt. Trans.*, 2015, **44**, 17883.

28   Y. Xiong, I. Washio, J. Chen, H. Cai, Z.-Y. Li and Y. Xia, *Langmuir*, 2006, **22**, 8563–8570.

29   I. Washio, Y. Xiong, Y. Yin and Y. Xia, *Adv. Mater.*, 2006, **18**, 1745–1749.

30   B. Lim, M. Jiang, J. Tao, P. H. C. Camargo, Y. Zhu and Y. Xia, *Adv. Funct. Mater.*, 2009, **19**, 189–200.

31   A. G. Shtukenberg, Y. O. Punin, E. Gunn and B. Kahr, *Chem. Rev.*, 2012, **112**, 1805–1838.

32   S. Wu, J. I. Blake, L. Guo and W. Zhou, *Cryst. Growth Des.*, 2020, **20**, 3537–3545.

33   I. A. Safo, M. Werheid, C. Dosche and M. Oezaslan, *Nanoscale Adv.*, 2019, **1**, 3095.

34   V. Sudha, G. Murugadoss and R. Thangamuthu, *Sci. Rep.*, 2021, **11**, 3413.

35   Y.-J. Song, M. Wang, X.-Y. Zhang, J.-Y. Wu and T. Zhang, *Nanoscale Res. Lett.*, 2014, **9**, 17.

36   X. Chen, M. Qiao, S. Xie, K. Fan, W. Zhou and H. He, *J. Am. Chem. Soc.*, 2007, **129**, 13305–13312.

37   H. Greer, P. S. Wheatley, S. E. Ashbrook, R. E. Morris and W. Zhou, *J. Am. Chem. Soc.*, 2009, **131**, 17986–17992.

38   W. Zhou, *Cryst.*, 2019, **9**, 7.

39   T. T. Lv, H. Z. Xing, H. M. Yang, H. X. Wang, J. Shi, J. P. Cao and B. L. Lv, *CrystEngComm*, 2021, **23**, 7985–7993.

40   B. Lim, M. Jiang, J. Tao, P. H. C. Camargo, Y. Zhu and Y. Xia, *Adv. Funct. Mater.*, 2009, **19**, 189–200.

41   P. Curie, *Bull. Minéralogie*, 1885, 145–150.

42   R. Docherty, G. Clydesdale, K. J. Roberts and P. Bennema, *J. Phys. D. Appl. Phys.*, 1991, **24**, 89–99.

43   S. C. Lu, M. C. Hsiao, M. Yorulmaz, L. Y. Wang, P. Y. Yang, S. Link, W. S. Chang and H.-Y. Tuan, *Chem. Mater.*, 2015, **27**, 8185–8188.

44   S. Bao, J. Zhang, Z. Jiang, X. Zhou and Z. Xie, *J. Phys. Chem. Lett.*, 2013, **4**, 3440–3444.

Chapter 4 Dipole Field Driven Growth of Cu_2O/PVP Spherulites

4.1 Introduction

Firstly discovered in the early 19 century, spherulite refers to the spherical aggregate comprised of radially arranged acicular components.[1,2] Spherulites not only have been found in the case of natural mineralisation,[3,4] but also are prepared experimentally using biomimetic conditions with the addition of polymers.[5–7] From the perspective of energy, although spherulites seem to be spherically isotropic and homogeneous, the acicular crystalline building units are indeed morphologically anisotropic and preserve high surface energy. Such hierarchical structure makes the formation of spherulites difficult to be explained thermodynamically.

The formation of acicular subcomponents inside the spherulites are always related to the orientation behaviour of nanocrystallites in polymer matrix. One principal argument for the driving force of self-orientation of nanocrystallites in spherulites is the dipolar field generated in those nanocrystallites.[8–10] Polarity is a distinct separation of electric charge which leads to an electric dipole moment in a molecule or a chemical group. A bulk crystal may not generate a dipolar field even if it is constructed alternately by negatively and positively charged atomic layers. The surface roughness from the horizontal zig-zag arrangement of atoms can readily make the surface atomic layers neutral. Nevertheless, when it comes to nanocrystallites with only several unit cells in each dimension, every charge from atoms is significant, therefore terminal atomic layers on the surface with either positive or negative charge can form readily, leading to a dipolar field. Greer *et al.* reported the dipolar field originated from the vaterite crystal structure.[7] Inside the vaterite spherulites, nanocrystallites self-oriented into a parallel manner when there was not a strong electric field in the core while turned to radial orientation when a strong dipolar field from a double layered core was present.[7]

Spherulites have been discovered for various crystals, inclusive of naturally occurring rhyolite,[11] corallites,[12] and synthetic $CaCO_3$,[3,5] ZnO,[6,13] Ni_3Ge,[14] polymer,[15] MOF,[16] *etc*. However, their microstructures and formation mechanisms are not fully understood. Spherulites typically possess complicated microstructures with nanocrystallites embedded in polymer substrates. Knowing the growth mechanism of spherulites may provide an understanding of natural mineralisation and bio-mineralisation.

In **Chapter 3**, we introduce the formation of Cu pseudo-icosahedral microcrystals using $CuSO_4·5H_2O$ as the starting reactant, polyvinylpyrrolidone (PVP) as the reductant/capping agent and dimethylformamide (DMF) as the solvent. Cu_2O/PVP spherulites are observed as an intermediate phase.[17] The Cu_2O nanocrystallites in these spherulites are further reduced to Cu nanocrystallites, therefore are not preserved. While using $Cu(NO_3)_2·2H_2O$ as the starting material, the Cu_2O spherulites are preserved. The characterisations of the Cu_2O spherulites can then be executed to reveal the formation mechanism of Cu_2O/PVP spherulites.

Cu_2O is a common material can be applied as a promising semiconductor and photocatalyst in CO_2 reduction[18], dye degradation[19], H_2 production[20], *etc*. The polymorphs of Cu_2O are studied on their morphologies, for instance, cube[21], dendrite[22], hollow structure[23] and 26-facet polyhedron.[24] However, the morphology of spherulitic Cu_2O and related growth mechanism have not been investigated in details.

As a pioneer work, we report the growth and characterisation of Cu_2O/PVP spherulites and propose the formation mechanism. The multifunction of polyvinylpyrrolidone (PVP) as an agglomerating surfactant as well as a weak reducing agent is discussed. The radial alignment of nanocrystallites guided by the negatively charged PVP cores results in the whole surface of the spherulites being negatively charged. We anticipate this work can be a representative work of dipole field driven crystal growth and shed light on the future studies and control of spherulitic morphologies.

4.2 Experimental Methods

Chemicals:

$Cu(NO_3)_2·2H_2O$ (Sigma-Aldrich), polyvinylpyrrolidone (PVP, Sigma, mol wt. 360000), dimethylformamide (DMF, Acros Organics, 99+%), deionised water (DI water) with a resistivity of 18.3 M Ω·cm. All chemicals were used without further purification.

Preparation of Cu_2O Spherulites:

0.5 g PVP was fully dissolved in 25 ml DMF and pre-heated to 150 °C before the addition of 1.25 mmol (0.302 g) $Cu(NO_3)_2·H_2O$. The solution was stirred continuously for about 15 min before it became a green suspension. The suspension was then transferred into a Teflon

autoclave vessel and put into the oven at 150 °C. The suspension was kept at the temperature for the crystal growth. Varied reaction times (1.5, 2, 6, 12, 24 and 96 h) were applied to obtain specimens from different growth stages for the study of morphology evolution and microstructural changes. When the reaction was terminated, samples were filtered and washed three times using DI water to remove excess DMF and PVP. Finally, the obtained solids were dried at 50 °C before collection and further characterisations. All experiments were performed three times to make sure they were repeatable.

Test of Surface Charge:

To examine whether the synthesised Cu_2O/PVP spherulites preserve a negatively or positively charged surface, surface stain experiments using dyes with positive and negative charges were conducted. Solutions of the two dyes, Safranin T and Congo Red, with the concentration of 0.4 g/L were firstly prepared using DI water. 0.5 g 3 h Cu_2O spherulite sample was dispersed in 10 ml DI water to form a suspension. 10 mL suspension and 10 mL respective dye solution were mixed and sonicated for 5 min before leaving still overnight. After 24 h, the suspension was then sonicated again for 5 min, followed by dripping 0.5 mL onto a glass slide and drying at 50°C for optical microscopy observation. Parallel experiments of pure PVP with dye solutions were performed to exclude the effect of PVP's polarity on surface stain, and furthermore prove the dipole force of Cu_2O.

Agglomeration experiments were applied to confirm the surface charge of the spherulites. 0.05 g alginate sodium salt was dissolved in 10 mL DI water. The solution was kept stirring when 10 mL Cu_2O (3 h sample) suspension was added into. The mixture was then stirred for another 30 min before taking 10 mL to be dried at 50 °C. In a parallel experiment, chitosan was used to replace alginate sodium salt with all other conditions unchanged.

4.3 Results and Discussion

4.3.1 Morphology, Crystallography and Composition

All the samples with different reaction times from 1.5 to 96 h optically appeared to be dark brown, a typical colour for Cu_2O. The synthesised samples were examined on their morphologies using SEM. SEM images reveal that the morphologies of all obtained samples

are spherical with smooth surfaces, as shown in **Figure 4.1** and **Figure 4.2**. Broken particles marked in dashed squares **in Figure 4.1(a)** display linear components lying along with the radial directions, implying that these particles are spherulites formed by radially oriented acicular subcomponents.

During the process of solvothermal preparation, 1.5 h was the earliest reaction time when visible spherical solid precipitates could be collected. And the majority of these spherical particles from 1.5 h sample already appear to be at microscale, indicating a relatively rapid formation of the spherulites.
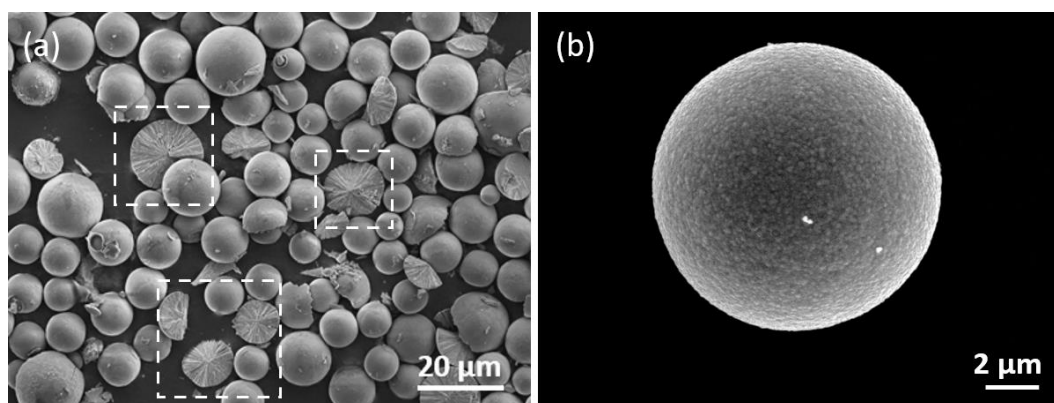
Figure 4.1 SEM images of spherulites from the samples of reaction time at (a) 1.5 h and (b) 24 h. The white dash squared areas indicate the typical cross section of the spherulites.

Figure 4.2 shows the series of SEM images of the specimens obtained from different reaction times and the corresponding size distribution diagrams based on the diameter measurement of 200 particles for each sample.

The average size of the spherulites in 1.5 h sample is 9.46 µm in diameter. The average size is 10.11 µm for 3 h sample, 10.27 µm for 6 h sample, 10.33 µm for 12 h sample and 10.46 µm for 96 h (4-day) sample. As the reaction time lengthens, the particle size increases gradually with an obvious decline in size growth rate.
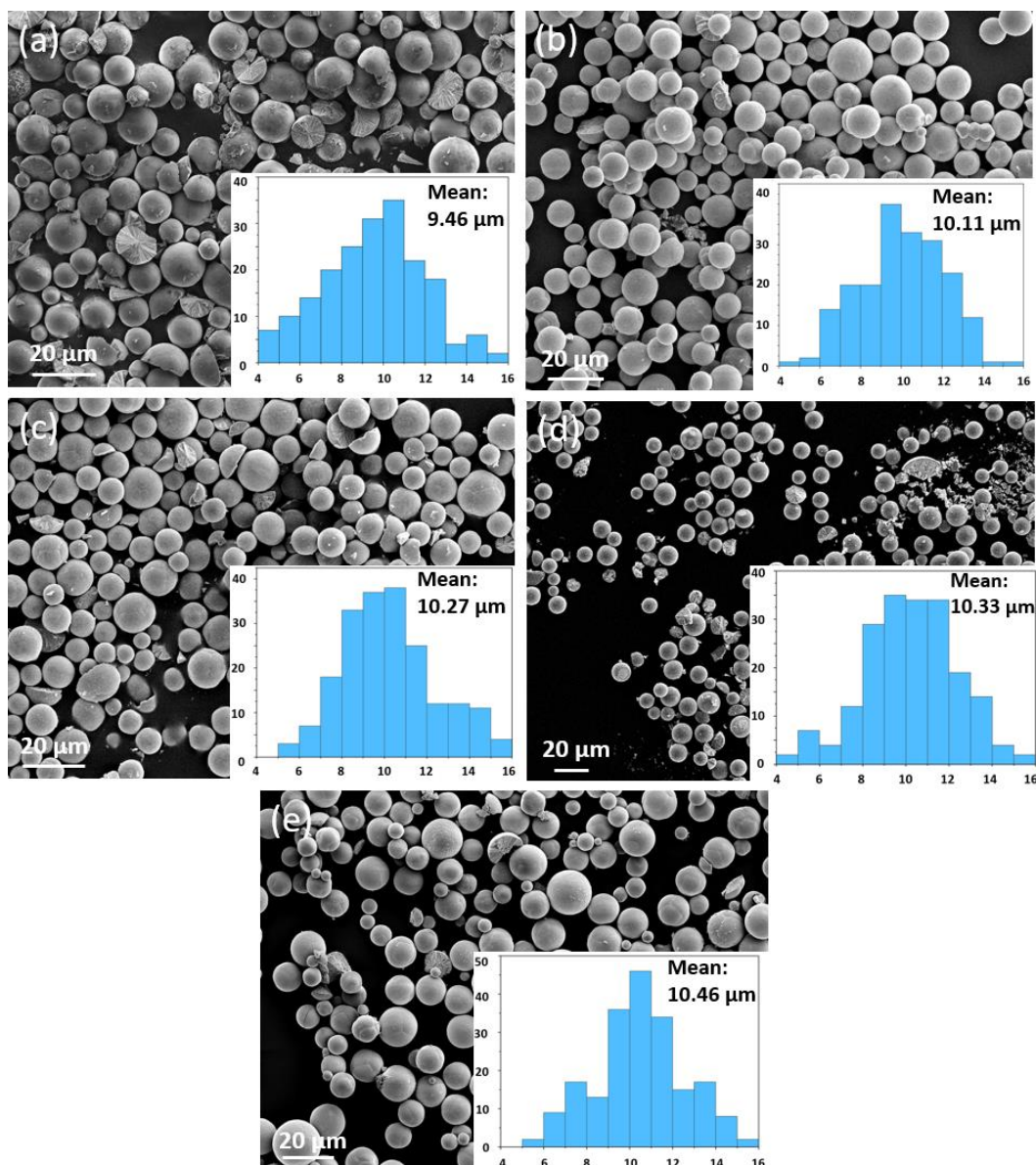
Figure 4.2 SEM images of spherulites from the samples of the reaction time at (a) 1.5 h, (b) 3 h, (c) 6 h, (d) 12 h and (e) 96 h. The insets are the corresponding size distribution histograms.

XRD was initially applied to examine the crystalline phases of the samples and the corresponding crystallinities. As displayed in **Figure 4.3**, as the reaction time extends, the intensity and sharpness of XRD peaks increase, indicating a remarkable improvement in crystallinity. There are two phases indicated by the series of XRD patterns chronologically. 2 h and 6 h samples appear to be pure Cu_2O which has a cubic structure with the unit cell parameter a = 4.268 Å (ICSD Code-172174). In 12 h sample, two extra weak peaks appear and are assigned to the face-centred cubic structure of Cu with a = 3.615 Å (ICSD Code-16010). Cu

85

as a minor phase is believed to originate from the further slow reduction of Cu_2O by the weak reducing agent PVP.
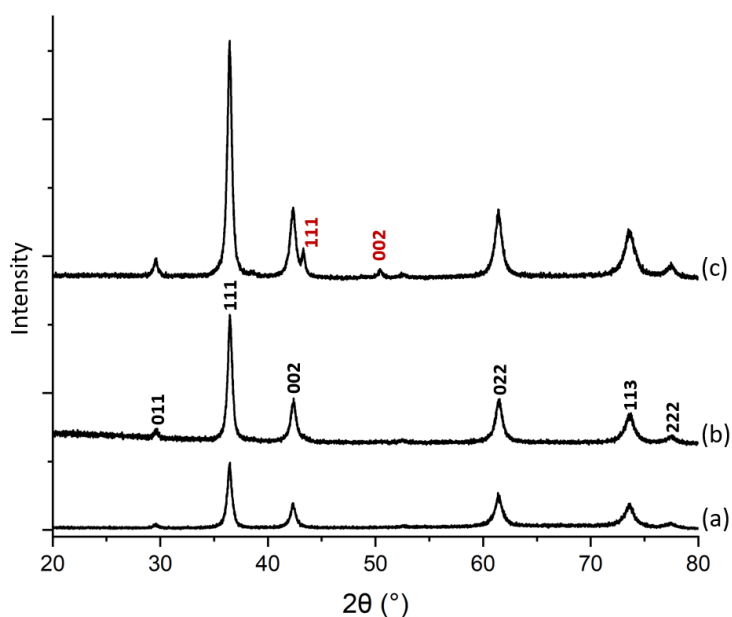
Figure 4.3 XRD patterns of the samples from the reaction time of (a) 2 h, (b) 6 h and (c) 12 h. Indices marked in black represent the planes from Cu_2O while indices marked in red represent the planes from Cu. The XRD patterns are collected using Cu Kα1 X-ray source.

The synthesis conditions of this work were almost identical to the conditions used for the growth of Cu pseudo-icosahedra[17], which has been introduced in **Chapter 3**, except that the primary reactant $CuSO_4 \cdot 5H_2O$ was replaced by $Cu(NO_3)_2 \cdot 2H_2O$. In the system containing copper sulphate, the first crystalline phase was monoclinic $Cu_4SO_4(OH)_6 \cdot H_2O$, as observed in 1.5 h sample. These crystals were gradually reduced to form Cu_2O nanocrystallites, which underwent aggregation to form spherulites. However, the Cu_2O crystals were further reduced immediately to Cu and finally resulted in Cu pseudo-icosahedra in 12 h. In the present work, using copper nitrate as the reactant, on the other hand, Cu_2O/PVP spherulites is the only product in 1.5 h to 6 h samples. The 12 h sample contains a small proportion of Cu derived from over reduction, indicating that Cu_2O/PVP spherulites form quickly with no previous precursor phase and are much more stable in the nitrate system.

Spherulites are usually not monophasic but composed of inorganic crystals and organic substrate which permits the crystals to orient. Spectroscopic techniques were applied to study the composition and chemical bonding information in the spherulites.

Figure 4.4 shows the FTIR spectra of the samples. The FTIR spectrum (**Figure 4.4a**) of the mother solution containing DMF, PVP and $Cu(NO_3)_2 \cdot H_2O$ is very similar to the spectrum of pure DMF,[25] with additional contribution from PVP. The latter increases the peak intensities of CH_2 (2987 cm^{-1}), CH (2900, 1384 and 870 cm^{-1}), and CN (1255 cm^{-1}). In the FTIR spectra of 2 h and 6 h solid samples (**Figure 4.4b** and **c**), the C=O peak (1658 cm^{-1}) from both DMF and PVP almost disappears, while all CH bonds and C–O bond (1087 cm^{-1}) still exist. This result indicates the successful removal of solvent DMF during the extraction of the precipitates. While the solid spherulites still contain PVP. The fact that C=O peak disappears and C-O peak remains can be attributed to the formula change of PVP after reducing Cu^{2+} and the coordination of PVP with Cu cations. A similar situation was observed previously in an Ag/PVP system.[26] Worth taking note of, a new peak in these FTIR spectra at 600 cm^{-1} emerges and is attributed to crystalline Cu_2O.[27] FTIR spectra prove that the particles are Cu_2O/PVP composite microscale spherulites.
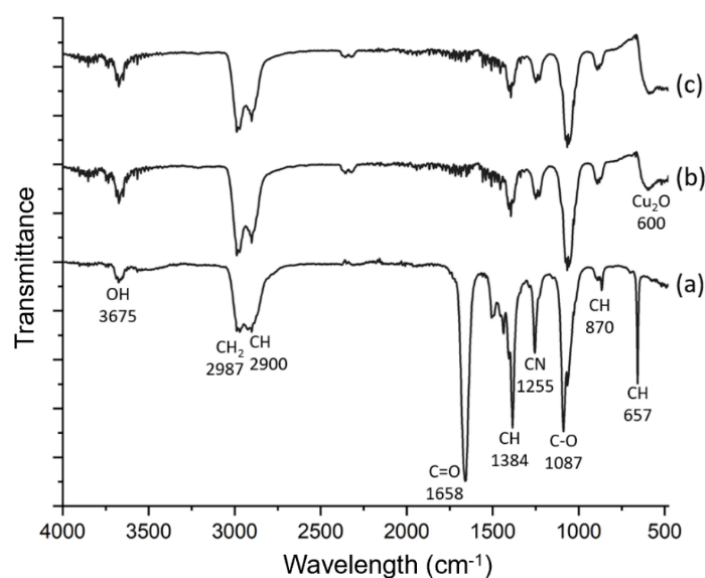
Figure 4.4. FTIR spectra of (a) DMF solution of $Cu(NO_3)2 \cdot H_2O$ and PVP, (b) 2 h sample and (c) 6 h sample.

To examine the light elements in the spherulites and further confirm the involvement of PVP, SXES was performed. The sample was deposited on a silica substrate instead of a carbon tape to avoid carbon signals from the background. The spectrum is displayed in **Figure 4.5**. Si peak is derived from silica substrate. SXES spectrum shows the existence of C, O, N in a spherulite, implying the co-existence of PVP with Cu_2O.
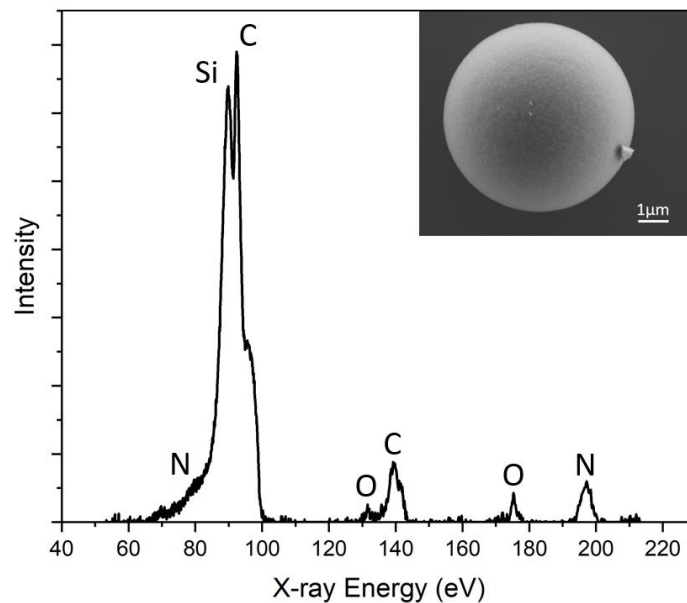
Figure 4.5. SXES spectrum of a Cu$_2$O spherulite. The Si peak is from Si substrate. Inset is the corresponding SEM image of the spherulite.

4.3.2 Observation of Hierarchical Components

To reveal the inner structure of the spherulites, SEM images of the cross sections of the particles were recorded, as shown in **Figure 4.6**. At low magnification, it shows that the whole particle consists of radially directed needle-like components with a spherical core of a diameter at about 1 μm. The solid core is missing probably during sample treatment before putting into the SEM chamber for observation, and a cavity is present (**Figure 4.6a**). **Figure 4.6(b)** shows a spherulite with a solid core from 12 h sample, also at about 1 μm in diameter. At a relatively high magnification, it is revealed that, hierarchically, the needle-like components are composed of many smaller submicron particles below 200 nm in diameter, as shown in the SEM image of 1.5 h sample (**Figure 4.6c**). These small particles line up along the radial directions and finally align together to form dense needle-like components.
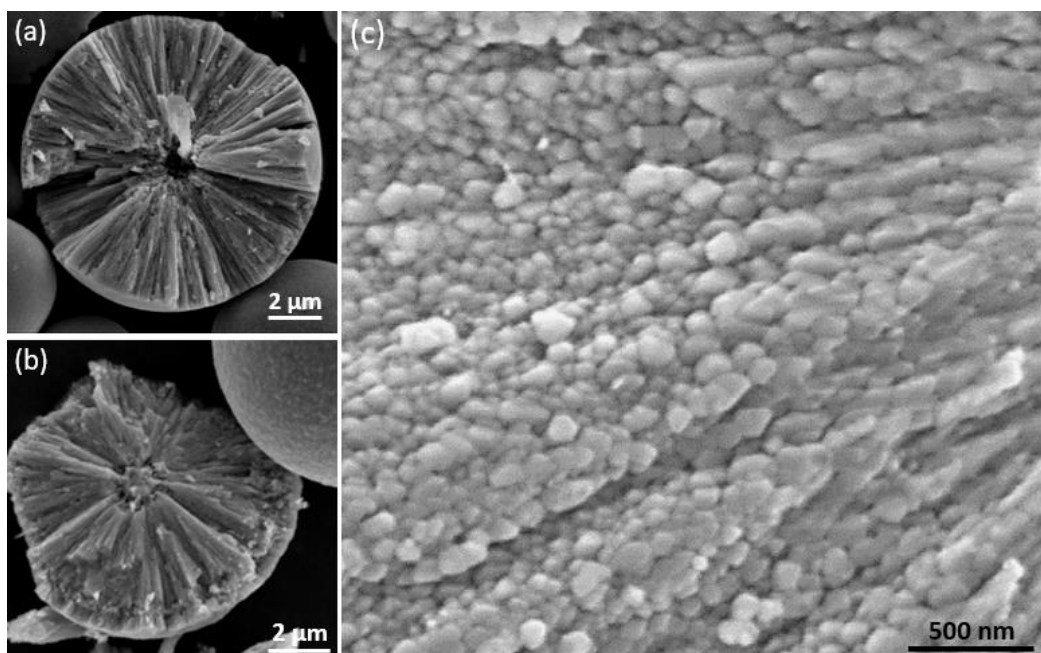
Figure 4.6. SEM images of the cross sections of the Cu₂O/PVP spherulites from broken particles. (a) Low magnification SEM image from 12 h sample, showing that the particle is constructed by needle-like components. A cavity at the centre is visible. (b) SEM image from 12 h sample, showing a core at the centre of the spherulite. (c) Magnified SEM image from 1.5 h sample showing small spherical particles below 200 nm, which acts as the building units of the needle-like components.
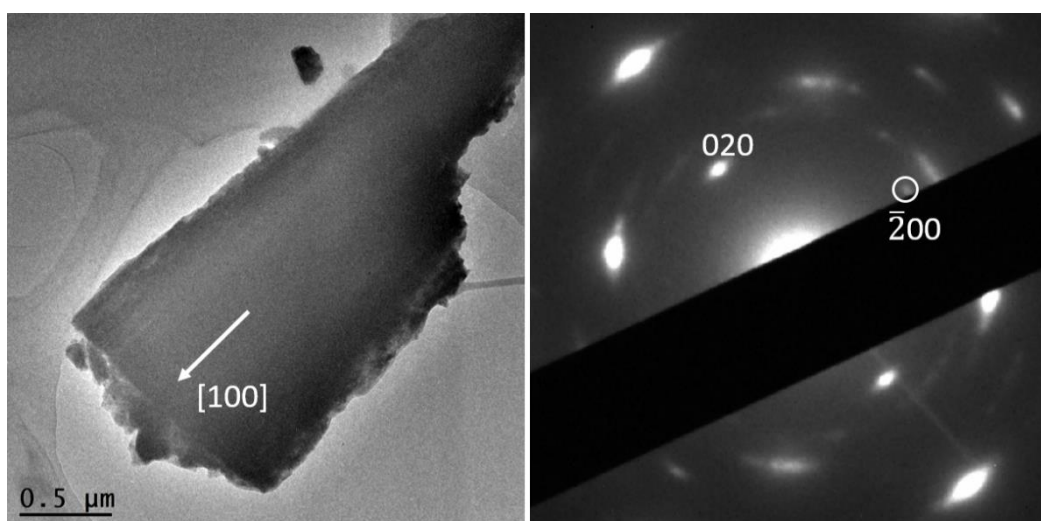
Figure 4.7 (a) TEM image of a fragment of a Cu₂O spherulite from 1.5 h sample. The arrow indicates the radial direction in the spherulite. (b) The corresponding SAED pattern indexed to the cubic structure of Cu₂O.

TEM observation was carried out to characterise the structure of spherulites. **Figure 4.7(a)** shows a TEM image of a fragment of a needle-like particle. The arrow shows the radial

89

direction. **Figure 4.7(b)** is the corresponding SAED pattern of the fragment. The principal spots can be indexed to cubic Cu_2O structure when viewing down the [001] direction. The [100] zone axis of Cu_2O is parallel to the radial direction in the spherulite.
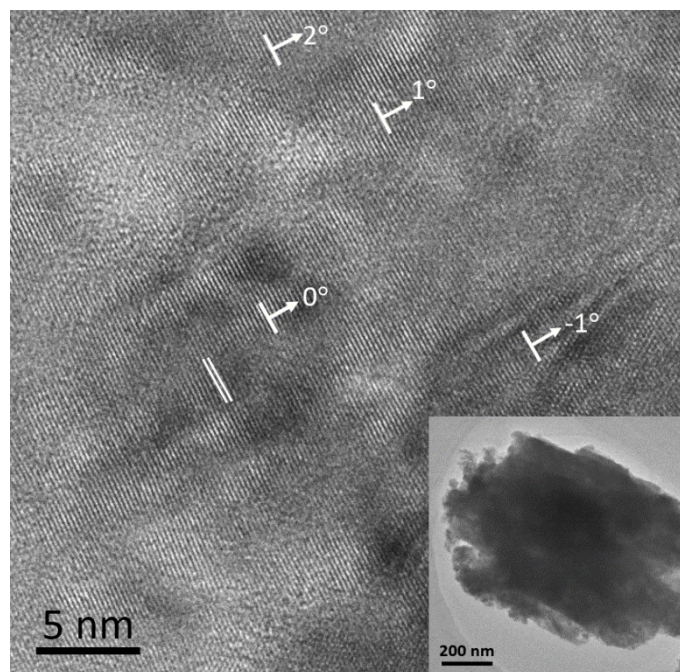
Figure 4.8 HRTEM image of a fragment of a spherulite from 12 h sample. The double lines measure a d-spacing at 2.15 Å, which can be indexed to the (200) planes of Cu_2O. The [200] orientations of some nanocrystallites are indicated by the arrows and their angular off-alignment is marked. Inset is the low magnification TEM image of the spherulite fragment where the HRTEM is collected.

The detailed crystal fringes of the spherulites were revealed by HRTEM. As shown in the HRTEM image (**Figure 4.8**), from a spherulite fragment in 12 h sample, nanocrystallites with monodispersed fringes are visible in a disordered substrate. Their orientations are almost consistent with small angular offsets. The monodispersed d-spacing corresponding to the fringes is about 2.15 Å, which can be indexed to the (200) plane of cubic Cu_2O. The bright and dark contrast in **Figure 4.8** indicates the heterogeneous thickness and further implies that the crystalline domain is not derived from monocrystalline classical growth. Consequently, the produced spherulites contain self-oriented Cu_2O nanocrystallites embedded in a PVP substrate. And PVP, as a surfactant, participates in the self-orientation process of Cu_2O nanocrystallites.

Figure 4.9 demonstrates an HRTEM image with fringes. The fringes are discontinuous, and the angular offset can be clearly seen, indicating the fringes are not from direct monocrystalline classical growth, but the orientation of nanocrystallites under the function of the PVP substrate. The marked d-spacing measured at 2.50 Å is assigned to the (111) plane of cubic Cu_2O.
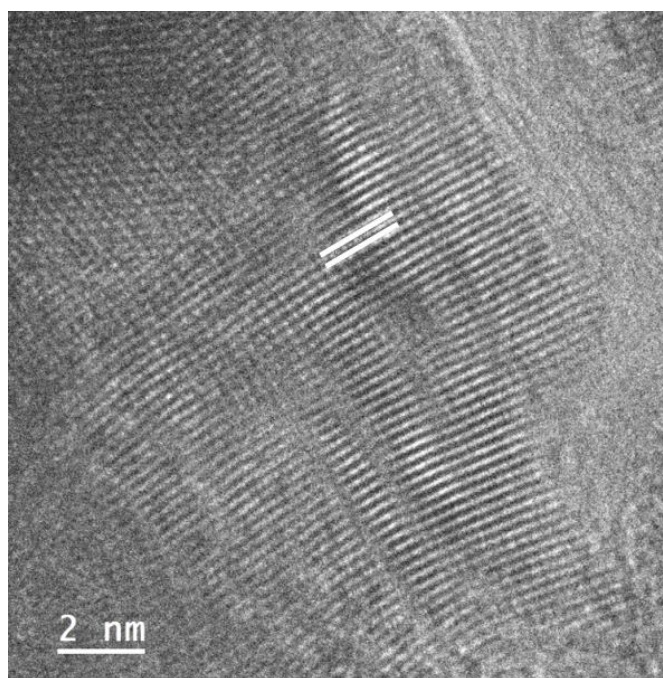
Figure 4.9 HRTEM image of fringes with discontinuity and angular offset. The marked d-spacing is measured at 2.50 Å.

To reveal the formation mechanism of the spherulites, it is vital to obtain structural information at earlier growth stages. Although 1.5 h is the earliest time to collect spherulites of large quantity, the formation of the submicron spherical particles which comprise the needle-like bundles, as demonstrated in **Figure 4.6(c)**, must occur at an earlier time.

A DMF solution containing $Cu(NO_3)_2 \cdot H_2O$ and PVP was stirred and left evaporating for 15, 30 and 45 min in an oil bath at 150°C. Subtle greenish brown residues at these reaction times were scratched off the beaker wall and characterised using SEM and TEM. **Figure 4.10** displays that the residues contain bulk particles as well as submicron spherical particles in two particle sizes, about 300 nm and 60 nm in diameter. The large spherical particles with smooth surfaces are already larger than the building units of the needle-like components, as shown in **Figure 4.6(c)**. While the core to form spherulite is at about 1 μm, as shown in **Figure 4.6(b)**.

Considering the growth of crystals over time, we conclude that the spherical particles at about 300 nm may be the primitive forms of the cores of the spherulites, while the particles at about 60 nm are the building units. **Figure 4.10(b)** illustrates the particles in 45 min sample. The surface is rough, which indicates the behaviour of absorbing Cu_2O nanocrystallites and PVP polymer to grow into bigger size. HRTEM image of 15 min sample reveals the existence of nanocrystallites with low crystallinity embedded in the amorphous PVP substrate (**Figure 4.10c**). The measured d-spacings from these nanocrystallites are at about 2.14 Å, which can be indexed to the (200) planes of the Cu_2O structure. Significantly, compare **Figure 4.10(c)** to **Figure 4.8(c)**, these nanocrystallites are randomly oriented, indicating that the interaction between the nanocrystallites is not strong enough to induce self-orientation as observed in spherulites at this stage.
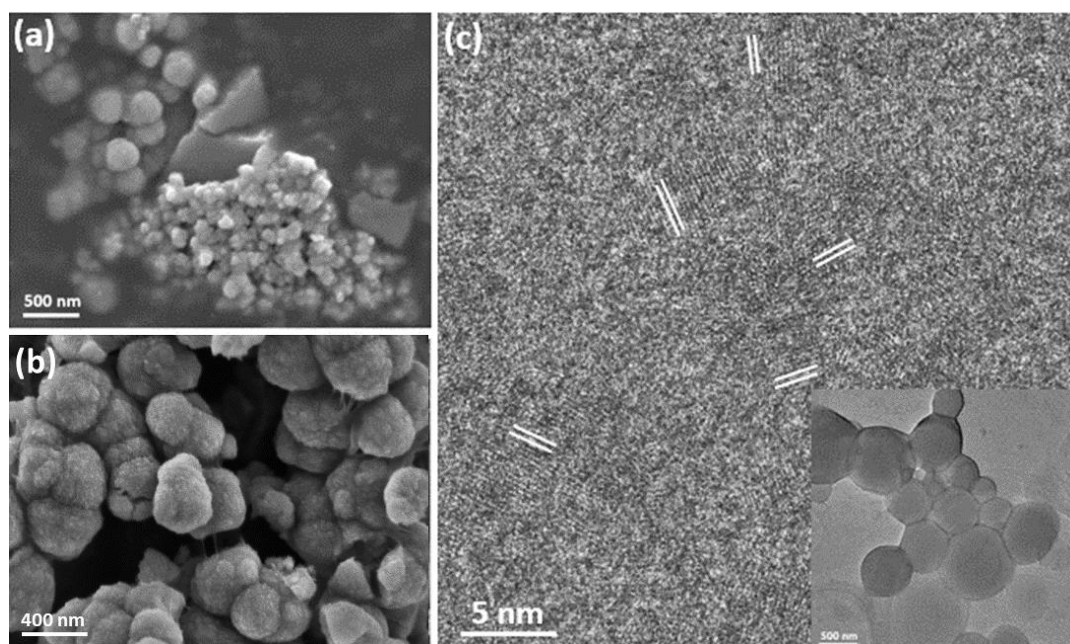
Figure 4.10 SEM images of submicron sized spheres from (a) 15 min sample and (b) 45 min sample. (c) HRTEM of a submicron sized sphere from 15 min sample displaying embedded nanocrystallites in amorphous matrix with d-spacings marked. The orientations of these d-spacings are random. Inset is the low magnification TEM image of the sphere where the HRTEM image was captured.

The elemental compositions of the spherulites and spherical particles were analysed using the EDX technique in both TEM and SEM. **Figure 4.11** displays a TEM image of a submicron sphere and the corresponding EDX elemental mapping of Cu element. The

distribution of Cu is uniform which fits the profile of the spherical particle. TEM-EDX mapping of C element is not achieved because the carbon film on the TEM specimen grid can also generate C signal, interfering with the mapping result. Additionally, EDX spectra of particles from 15 min sample and a spherulite from 1.5 h sample on silica substrates are presented in **Figure 4.12**. The EDX spectra consistently show the signals from Cu, C and O, indicating the participation of these elements and the polymer PVP throughout the whole growth process.
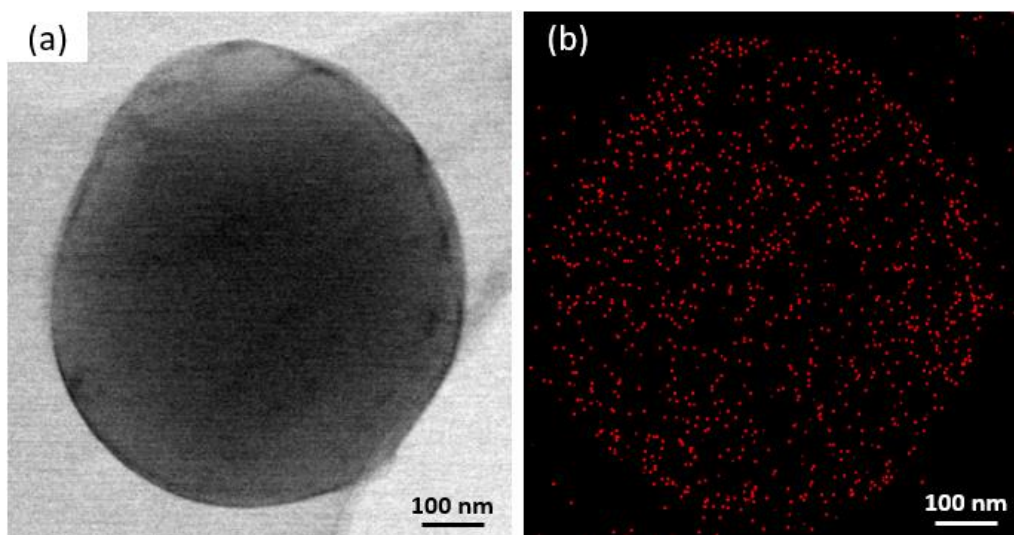
Figure 4.11 (a) Bright field HAADF image of a submicron sphere from 15 min sample. (b) The corresponding EDX elemental mapping of Cu.
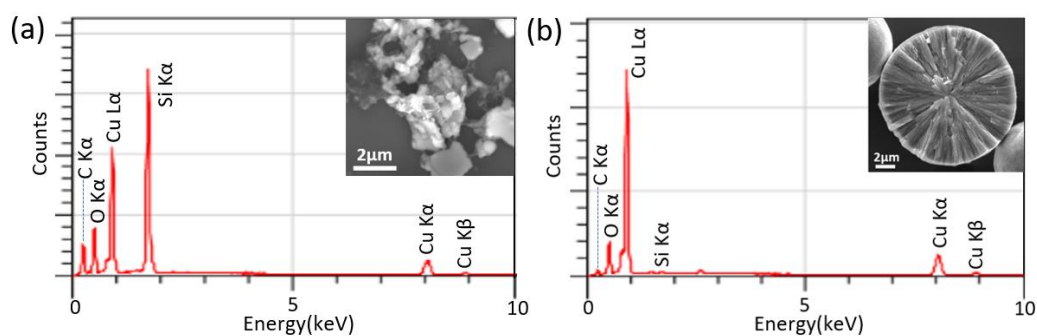
Figure 4.12 EDX spectra of (a) 15 min residue and (b) 1.5 h spherulite. Insets are the corresponding SEM images of the areas where the spectra were collected.

4.3.3 Evidence and Simulation of Polarity

To examine the polarity of spherulites and further examine whether the driving force of Cu$_2$O spherulite growth is dipole force, dye staining experiments and surfactant

agglomeration experiments were performed. The dye candidates were Safranin T (positively charged due to the amine groups) and Congo Red (negatively charged due to the $-SO_3^-$ groups).

Presumably, the whole particles of spherulites are neutral. If all the nanocrystallites as dipoles orient themselves along the radial directions induced by an electric field from the negatively charged core,[28] all the Cu_2O dipoles would turn their positive ends towards the core and their negative ends to the surface. The whole surface of the spherulites would be therefore negatively charged and absorb the positively charged dye molecules. **Figure 4.13** illustrates the possible Cu_2O nanocrystallite dipole and the alignment of the nanocrystallites with negatively charged ends to the surface.
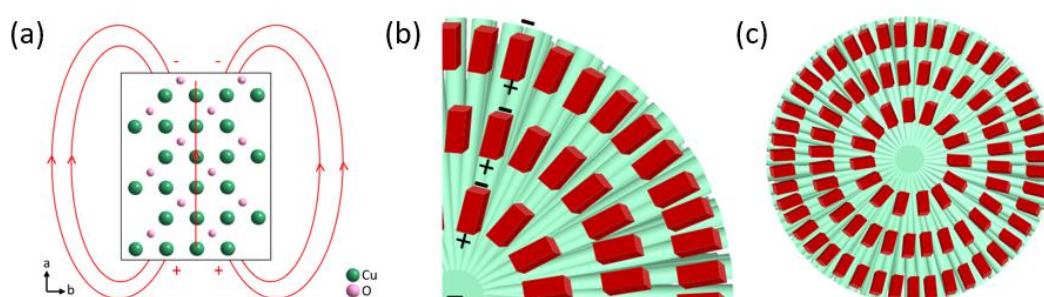
Figure 4.13 (a) Structural model of a Cu_2O nanocrystal, generating a dipolar field along the [100] axis. (b) Schematic drawing showing the oriented Cu_2O nanocrystallites and corresponding dipole force towards the core. (c) Schematic drawing showing the radical feature of cross section. Red bricks represent Cu_2O nanocrystallites and green substrate represents PVP.

As demonstrated in **Figure 4.14(a),** there are clear adsorption layers of positively charged Safranin T on the surface of the spherulites at about 20 μm in thickness. While on the contrary, the negatively charged dye Congo Red shows no association with the spherulites (**Figure 4.14b**). For the time being, we conclude that the surface of the spherulites is negatively charged.

Nevertheless, the origin of the negative charge could be either from the polar PVP or the negatively charged ends of the Cu_2O nanocrystallites. To exclude the effect of PVP on attracting positively charged Safranin T, parallel experiments using pure PVP for dye stain were conducted. **Figure 4.14(c)** and (**d**) demonstrate that there is no strong interaction of pure PVP with both Congo Red and Safranin T. Therefore, we conclude that PVP shows no

strong affinity with either negatively charged dye or positively charged dye and has no distinct contribution to the polarity of the spherulites.

We may now deduce that the deposition of Safranin T dye on the surface of Cu_2O/PVP spherulites is mainly attributed to the negatively charged surface due to the radially oriented dipoles of Cu_2O nanocrystallites with negatively charged ends pointing outwards. It is also confirmed that the driving force behind the self-orientation of the Cu_2O nanocrystallites in the spherulites is the Coulombic force interaction between the PVP-dominant core and Cu_2O dipoles.
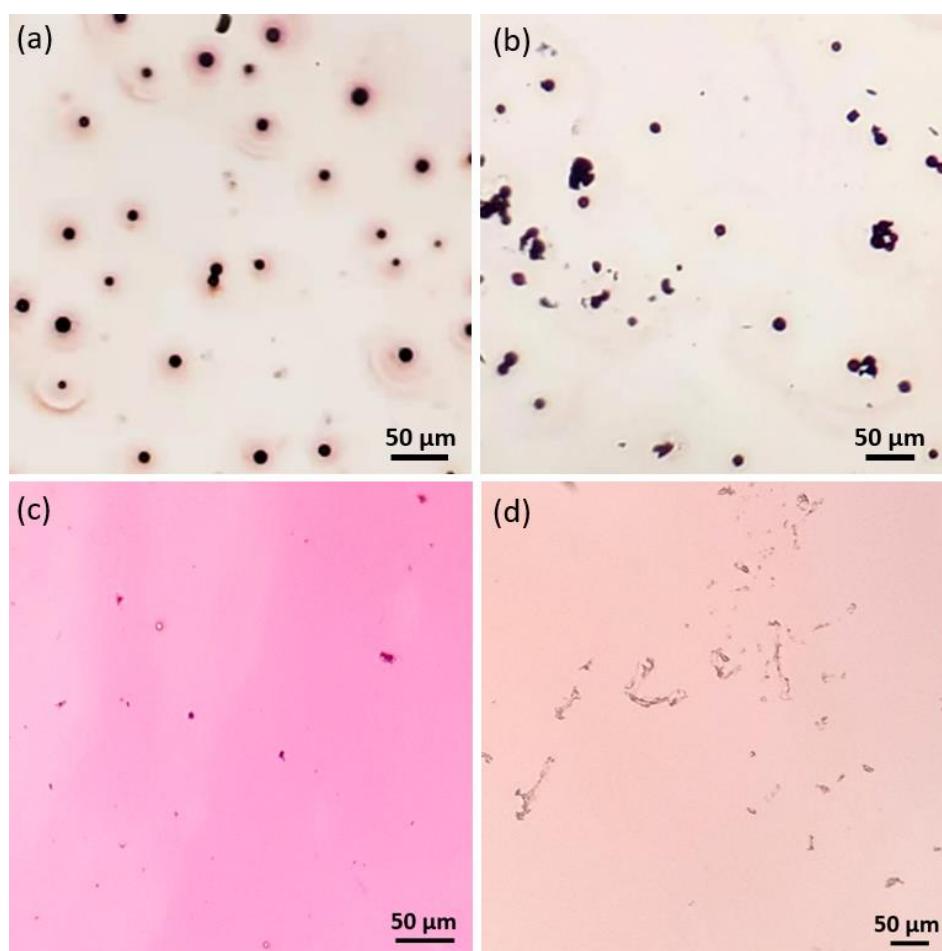
Figure 4.14 (a) Optical microscopic image of Cu_2O spherulites with Safranin T. The surrounding of the spherulites shows blurring red, indicating the successful stain by Safranin T. (b) Optical microscopic image of Cu_2O spherulites with Congo Red. The spherulites appear to be undyed, indicating the unsuccessful interaction with Congo Red. Optical microscopic images of pure PVP with (c) Safranin T and (d) Congo Red. PVP shows no strong interaction with both dyes, indicating its weak polarity.
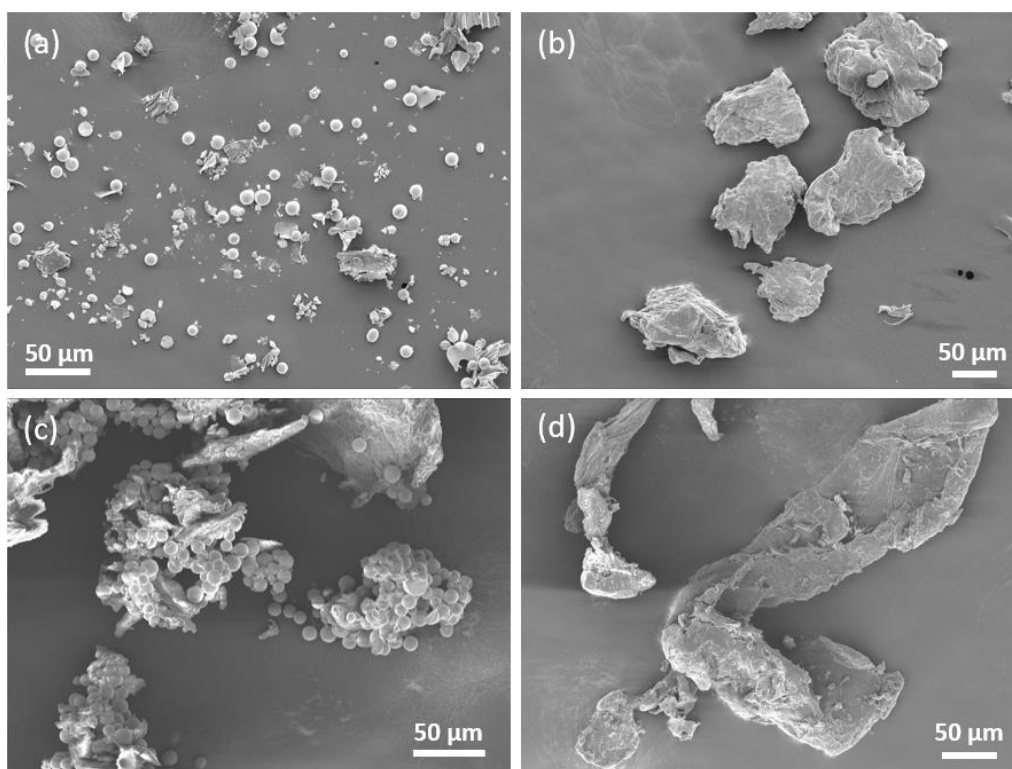
Figure 4.15 SEM images of (a) separate Cu_2O spherulites from 3 h sample and the negatively charged surfactant, alginate sodium salt, (b) pure alginate sodium salt, (c) agglomerated Cu_2O spherulites on the surface of positively charged surfactant chitosan, (d) pure chitosan.

The polarity of the Cu_2O/PVP spherulites was also examined by surfactant agglomeration experiments. **Figure 4.15** shows the corresponding SEM images. Cu_2O/PVP spherulites agglomerate on the surface of chitosan (positively charged due to the amine groups) in aqueous environment, while exhibit no interaction with alginate (negatively charged due to the acidic groups). The results are consistent with those from the surface stain experiments and underpin the proposed polar model of spherulites.

To summarise, PVP plays multiple roles during the growth of Cu_2O/PVP spherulites. After reducing Cu^{2+} to Cu_2O as a reducing agent, PVP also serves as the nucleation site and agglomeration agent to accommodate Cu_2O nanocrystallites. PVP-dominant spheres offers initial negatively charged core for the growth of the spherulites triggered by dipolar force. Furthermore, its soft matter property allows nanocrystallites to shift and rotate locally, allowing the self-orientation of the nanocrystallites driven by dipolar field to form large crystalline domains in PVP matrix.

4.3.4 Formation Mechanism of Dipole Driven Growth

On the grounds of the analyses of Cu_2O spherulites from different growth times and the evidence of polarity, we may now propose the overall growth mechanism, as demonstrated in **Figure 4.16**.

To begin with, Cu^{2+} cations, NO_3^- ions and PVP co-exist in the DMF solution at 150°C (**Figure 4.16a**). In the mean time, commercial PVP preserves weak reducing capability due to the hydroxyl terminations.

Soon after, Cu^{2+} cations are reduced by PVP to form Cu_2O nanocrystallites. PVP polymer serves as nanoparticle dispersant, wrapping the nanocrystallites, producing PVP/Cu_2O microscale spheres, as shown in **Figure 4.10**. The Cu_2O nanocrystallites in these spheres are small with a low crystallinity and have random orientations (**Figure 4.10c**). At this stage, dipolar field is not generated in the nanocrystallites (**Figure 4.16b**).

Some submicron spheres with high percentage of PVP further attach PVP to grow up to a large size so that they act as cores which attract small Cu_2O containing spheres as building units to their surface to grow spherulites (**Figure 4.16c**). For an individual spherulite, the dense core with polar PVP polymer generates a negatively charged centre, while Cu_2O nanocrystallites embedded in the small spheres increase their crystallinity and develop intrinsic dipolar fields. The interaction between the negative cores and surrounding Cu_2O nanocrystallites leads to self-orientation (**Figure 4.16d**). The Cu_2O nanocrystallites in the small spheres orient themselves along the radial directions with their positive ends facing the core and their negative ends pointing to the surface of the spherical particles under the function of dipolar force.

Simultaneously, the Coulombic electric field generated in the cores enhances the continuous piling-up of the building nanosphere units to form the needle-like bundles (**Figure 4.16e**). Locally, those nanocrystallites orient themselves to large crystalline domains in PVP substrates with <100> directions radially pointing towards the surface (**Figure 4.8** and **Figure 4.9**).

Eventually, polar Cu_2O/PVP spherulites form rapidly with the whole surface being negatively charged (**Figure 4.16f**).
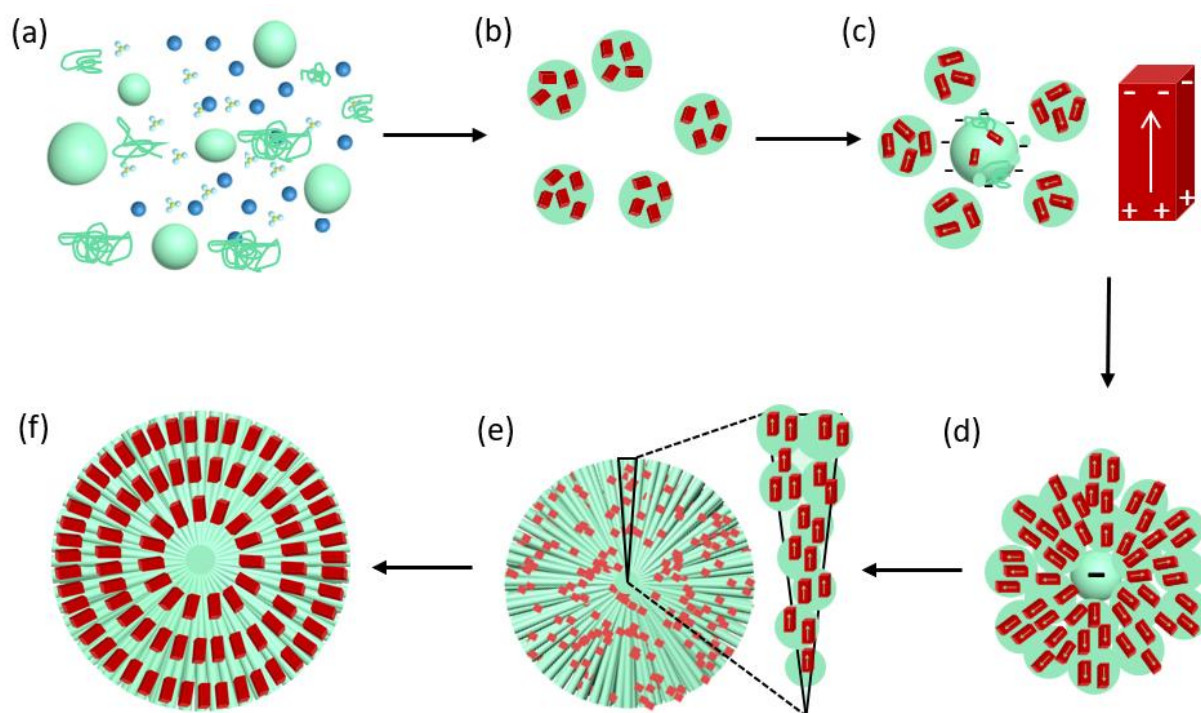
Figure 4.16 Schematic drawing illustrating the formation mechanism and morphological evolution of Cu_2O/PVP spherulites. (a) Co-existence of PVP polymer, Cu^{2+} and NO_3^- in the DMF solution. (b) PVP/Cu_2O submicron spheres. At this stage, the embedding Cu_2O nanocrystallites in PVP have a low crystallinity. (c) A core with the deposition of small spheres. In the core, polar PVP dominates the composition, resulting in the core being negatively charged. In the submicron spheres, the Cu_2O nanocrystallites have high crystallinity and are able to generate dipolar fields. (d) Ongoing simultaneous piling-up of PVP/Cu_2O submicron spheres and oriental alignment of nanocrystallites radially. (e) Growing Cu_2O/PVP spherulite and the zoomed-in representation of the needle-like bundle. (f) A cross section structure of the grown Cu_2O/PVP spherulites.

A pivotal feature of the spherulites is that the Cu_2O nanocrystallites inside are manacled by the electric field generated in the core. A direct effect of this property is that surface recrystallisation into monocrystalline polyhedral shell would not take place in the spherulites, no matter whether they are naturally occurring spherulites,[3,5] or synthetic spherulites.[5,6] Sulphate synthesis process (**Chapter 3**) leads to the precursor $Cu_4SO_4(OH)_6 \cdot H_2O$ before reducing Cu^{2+} while the nitrate synthesis system involves only the reduction. And intermediate Cu_2O/PVP spherulites quickly transform to polyhedral Cu_2O and are further reduced to Cu in the sulphate system. While the Cu_2O/PVP spherulites prepared using $Cu(NO_3)_2 \cdot 2H_2O$ manage to preserve the morphology in the growing system for a relatively long time. Crystallographically, the Cu_2O phase dominates in the spherulites. We suspect

Cu$_2$O/PVP spherulites form quickly without a formation of precursor and are more stable in the nitrate system.
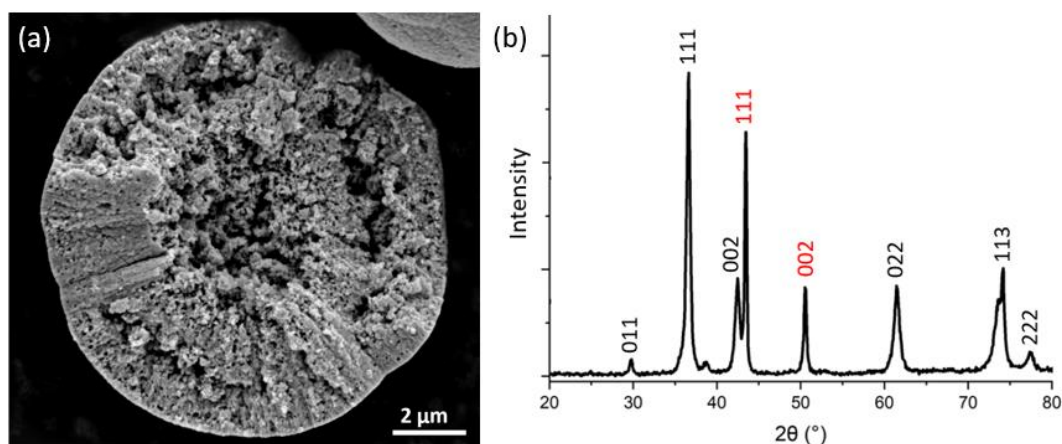
Figure 4.17 (a) SEM image of a spherical particle from 96 h sample. The structure is still spherical while the Cu$_2$O nanocrystallites are reduced to Cu and the radial interior comprised of needle-like bundles no longer exists. (b) XRD pattern of 96 h sample. Indices marked in black are from cubic Cu$_2$O while indices marked in bright red are from cubic Cu. The XRD pattern is collected using Cu Kα1 X-ray source.

Moreover, PVP as a polymerised surfactant helps to hold and stabilise the Cu$_2$O/PVP spherulite structure while itself as a weak reducing agent can further reduce Cu$^+$ to Cu, as indicated in the XRD pattern of 12 h sample (**Figure 4.3c**). 12 h sample contains a small proportion of Cu which derives from the over reduction of Cu$_2$O by PVP. **Figure 4.17(a)** shows the SEM image of a spherulite from 96 h sample. The needle-like morphology of the inner structure is no longer preserved. **Figure 4.17(b)** shows the corresponding XRD pattern of 96 h sample which indicates that the cubic Cu phase is produced. We assume only under the circumstance of over reduction of Cu$_2$O by PVP can the balance of the dipolar field be ruined. And therefore, the spherulite morphology with radially arranged Cu$_2$O/PVP bundles is destroyed, as shown in **Figure 4.17(a)**.

4.4 Conclusion

With the proven polarity of the spherulites and the observed subcomponents and building units, the formation mechanism of Cu$_2$O/PVP spherulites in the solvothermal process has been discussed. PVP, as a multifunctional surfactant, reduces Cu^{2+} to Cu$^+$ as a reducing

99

agent and offers a confining substrate for the growth of Cu_2O nanocrystallites. As a dispersant, PVP also restricts the further growth of the nanocrystallites. The soft substrate property of PVP allows the local embedded nanocrystallites to orient themselves which makes it possible for the dipolar force to trigger the radial alignment of the nanocrystallites. PVP is the main component in the core, generating a negative charge centre, absorbing Cu_2O containing spheres for crystal growth, and inducing the alignment of Cu_2O nanocrystallites to produce polar spherulites with the negatively charged ends of Cu_2O nanocrystallites pointing to the surface radially.

The interaction of this central electric field and the Cu_2O nanocrystallite dipoles is the driving force for the radially directed self-orientation of the nanocrystallites. Such microstructure preserves a negatively charged surface and relatively high stability of embedded nanocrystallites without further surface recrystallisation into large crystals. The present work sheds light on the investigations of spherulites, polymer assisted crystal growth and the impact of the dipolar force in crystal growth aspect.

References

1   A. G. Shtukenberg, Y. O. Punin, E. Gunn and B. Kahr, *Chem. Rev.*, 2012, **112**, 1805–1838.

2   W. H. F. Talbot, *Phil. Trans. R. Soc. London*, 1837, **127**, 25–35.

3   S. Wu, C.Y. Chiang and W. Zhou, *Cryst.*, 2017, 319.

4   C.-Y. Sun, L. Gránásy, C. A. Stifler, T. Zaquin, R. V Chopdekar, N. Tamura, J. C. Weaver, J. A. Y. Zhang, S. Goffredo, G. Falini, M. A. Marcus, T. Pusztai, V. Schoeppler, T. Mass and P. U. P. A. Gilbert, *Acta Biomater.*, 2021, **120**, 277–292.

5   S. Wu, J. I. Blake, L. Guo and W. Zhou, *Cryst. Growth Des.*, 2020, **20**, 3537–3545.

6   B. M. Connolly, H. F. Greer and W. Zhou, *Cryst. Growth Des.*, 2018, **19**, 249–257.

7   H. F. Greer, M. H. Liu, C. Y. Mou and W. Zhou, *CrystEngComm*, 2016, **18**, 1585–1599.

8   K.-S. Cho, D. V Talapin, W. Gaschler and C. B. Murray, *J. Am. Chem. Soc.*, 2005, **127**, 7140–7147.

9   Z. . Tang, N. A. Kotov and M. Giersig, *Science*, 2002, **297**, 237–240.

10   X. Zhang, Z. Zhang and S. C. Glotzer, *J. Phys. Chem. C*, 2007, **111**, 4132–4137.

11   W. R. Vennum and G. D. Eberlein, *J. Res. U. S. Geol. Surv.*, 1977, 445–451.

12   M. S. Studivan, G. Milstein and J. D. Voss, *PLoS One*, 2019, **14**, e0203732.

13   M. H. Liu, Y. H. Tseng, H. F. Greer, W. Zhou and C. Y. Mou, *Chem. Eur. J.*, 2012, **18**, 16104–16113.

14   N. Haque, R. F. Cochrane and A. M. Mullis, *Cryst.* , 2017, **7**, 100.

15   E. M. Woo, G. Lugito, C. E. Yang and S. M. Chang, *Cryst.* , 2017, **7**, 274.

16   L. Feng, K. Y. Wang, T. H. Yan and H. C. Zhou, *Chem*, 2020, **6**, 460–471.

17   W. Sun and W. Zhou, *Cryst. Growth Des.*, 2022, **22**, 2611–2619.

18   H. Jung, S. Y. Lee, C. W. Lee, M. K. Cho, D. H. Won, C. Kim, H. S. Oh, B. K. Min and Y. J. Hwang, *J. Am. Chem. Soc.*, 2019, **141**, 4624–4633.

19   M. R. Abhilash, G. Akshatha and S. Srikantaswamy, *RSC Adv.*, 2019, **9**, 8557–8568.

20   C. Y. Toe, Z. Zheng, H. Wu, J. Scott, R. Amal and Y. H. Ng, *Angew. Chemie. Int. Ed.*, 2018, **57**, 13613–13617.

21   L. Gou and C. J. Murphy, *Nano Lett.*, 2003, **3**, 231–234.

22   J. Xue, W. Liang, X. Liu, Q. Shen and B. Xu, *CrystEngComm*, 2012, **14**, 8017–8022.

23   S. Sun, *Nanoscale*, 2015, **7**, 10850–10882.

24   R. Guo, J. Chang, H. Li, J. He, P. Pan, Z. Yang and J. Wei, *J. Alloys Compd.*, 2022, **895**, 162630.

25   P. Zhu, Y. Ma, Y. Wang, Y. Yang and G. Qian, *J. Mater. Cycles Waste Manag.*, 2020, **22**, 1184–1195.

26   Y. J. Song, M. Wang, X. Y. Zhang, J. Y. Wu and T. Zhang, *Nanoscale Res. Lett.*, 2014, **9**,

17.

27   V. Sudha, G. Murugadoss and R. Thangamuthu, *Sci. Rep.*, 2021, **11**, 3413.

28   C. Hao, Y. Zhao, D. Wang and G. Lai, *J. Appl. Polym. Sci.*, 2012, **123**, 375–381.

29   X. Y. Chen, M. Qiao, S. Xie, K. Fan, W. Zhou and H. Y. He, *J. Am. Chem. Soc.*, 2007, **129**, 13305–13312.

30   H. Greer, P. S. Wheatley, S. E. Ashbrook, R. E. Morris and W. Zhou, *J. Am. Chem. Soc.*, 2009, **131**, 17986–17992.

31   H. Zhan, X. Yang, C. Wang, J. Chen, Y. Wen, C. Liang, H. F. Greer, M. Wu and W. Zhou, *Cryst. Growth Des.*, 2012, **12**, 1247–1253.

32   W. Zhou, *Cryst.*, 2019, **9**, 7.

Chapter 5 Embedding Phenomenon of CsPbBr$_3$ Nanocrystallites in Cs$_4$PbBr$_6$ Matrix

5.1 Introduction

Over the past several years, inorganic halide perovskite crystals with a composition of Cs, Pb and X (X = Cl, Br, I) have been developed and drawn much attention because of their excellent photoluminescence property and high stability in ambient environment.[1–3]

Cs$_4$PbBr$_6$ has also been found to have distinct green photoluminescence. However, debates existed concerning the origin of the photoluminescence emission. Some researches attributed the photoluminescence property to the intrinsic crystal structure of Cs$_4$PbBr$_6$.[4,5] Seth and Samanta concluded that the photoluminescence of Cs$_4$PbBr$_6$ was due to the crystal defects of Cs$_4$PbBr$_6$, not from the CsPbBr$_3$ phase as characterisation results excluded the existence of CsPbBr$_3$.[4]

While there were still scientists insisting that the photoluminescence was from CsPbBr$_3$ although it was not observed. Akkerman *et al.* compared the green-emitting properties of non-luminescent pure Cs$_4$PbBr$_6$, Cs$_4$PbBr$_6$ doped with 2% CsPbBr$_3$ and pure CsPbBr$_3$, and concluded that photoluminescent CsPbBr$_3$ was the reason for synthesised Cs$_4$PbBr$_6$ to emit green colour although it was not traced to exist.[6]

It was until the direct observation of embedded CsPbBr$_3$ in Cs$_4$PbBr$_6$ crystals when the origin of light emission was determined.[7–9] Xu *et al.* successfully captured the diffraction spots of CsPbBr$_3$ using SAED and therefore proved the existence of CsPbBr$_3$ in the Cs$_4$PbBr$_6$ matrix.[7]

CsPbBr$_3$ quantum dots and nanocrystals crystallise in cubic system on their own have been widely studied on their excellent photoluminescence property yet are thermally unstable and preserve a decay in luminescence as time lengthens.[10,11] Artificial encapsulation using SiO$_2$ and atomic layer deposition using silica have been reported to passivate the CsPbBr$_3$ quantum dots and increase their stability.[10,12]

The antisolvent precipitation method has been applied widely to synthesis Cs$_4$PbBr$_6$ crystals with embedded CsPbBr$_3$ nanoparticles.[13–15] For a typical synthesis, Cs$^+$, Pb^{2+} and Br$^-$ are dissolved in a polar solvent to form a stable mother solution. A portion of the solution is then transferred into an antisolvent (organic solvents in which Cs$^+$ and Pb^{2+} cations are

insoluble, toluene, acetone etc.). Due to the insolubility and ultimate supersaturation in the antisolvent, crystallisation then occurs to precipitate the $CsPbBr_3$ containing Cs_4PbBr_6 crystals. Despite that the novel material has been synthesised and discussed regarding its green photoluminescence, the mechanism behind its formation remains ambiguous.

The structures of $CsPbBr_3$ and Cs_4PbBr_6 are versatile. Through the addition and extraction of CsBr and $PbBr_2$, reversible transformation between $CsPbBr_3$ and Cs_4PbBr_6 can be achieved.[3,13,16] Wu *et al.* reported the transformation of Cs_4PbBr_6 to $CsPbBr_3$ at the interface of water and hexane. A CsBr-stripping mechanism triggered by water was revealed.[16]

In this chapter, we discuss the synthesis of Cs_4PbBr_6 rhombohedral microcrystals with embedded $CsPbBr_3$ nanoparticles. Factors affecting the morphology and composition of $CsPbBr_3$ containing Cs_4PbBr_6 are analysed, including the ratio of starting materials CsBr and $PbBr_2$, the choice of initial solvent and antisolvent, the ratio of oleic acid and oleyl amine, etc. A mechanism involving the formation of amorphous precursor and localised crystallisation is proposed concerning the formation of the embedding phenomenon. The water induced transformation from Cs_4PbBr_6 to $CsPb_2Br_5$, $CsPbBr_3$ and CsBr, $PbBr_2$ is discussed.

5.2 Experimental Methods

Chemicals:

CsBr (Alfa Aesar, 99 %), $PbBr_2$ (Alfa Aesar, 98 %), 2-methylimidazole (MeIm, Aldrich, 99 %), oleic acid (OA, Aldrich, 90 %), oleyl amine (OLA or OAm, Sigma-Aldrich), dimethylformamide (DMF, Acros Organics, 99+ %), dimethyl sulfoxide (DMSO, Alfa Aesar, 99+ %), toluene (Fluorochem, $\geqslant$ 99%), hexane (Fisher Scientific, laboratory reagent grade), isopropanol (Fisher Scientific, laboratory reagent grade), methanol (Fisher Scientific, $\geqslant$ 99.9 %), acetone (Fisher Scientific, $\geqslant$ 99 %), ethanol (VWR Chemicals), deionised water (DI water) with a resistivity of 18.3 M Ω·cm.

All chemicals were used without further purification.

Preparation:

$CsPbBr_3$ embedded Cs_4PbBr_6 was synthesised via the antisolvent precipitation method. A solvent combination of 10 mL DMF and 10 mL DMSO was preheated to 50 °C and kept stirring

in an oil bath. 0.5 mmol (0.041 g) MeIm was added into the solvent, as well as 0.1 mL OA and 0.5 mL OLA.

0.4 mmol (0.1468 g) PbBr$_2$ was added to the stirring solution, followed by 1.6 mmol (0.3405 g) CsBr in order to keep the molar ratio of CsBr and PbBr$_2$ at 4 : 1. Different molar ratios (4.5 : 1, 3.5 : 1, 3 : 1, 2 : 1 and 1 : 1) of CsBr and PbBr$_2$ were practised based on the fixed molarity of PbBr$_2$ at 0.4 mmol. The solution was kept stirring for 1 h to guarantee the total dissolution of the reactants.

When the stirring was accomplished, half of the solution was transferred into 10 mL stirring toluene. The mixture quickly turned white opaque suspension, soon the suspension changed its colour to light green. After stirring for 5 min, the up layer of solution was removed and another 10 ml toluene was added into the beaker containing solid precipitates. A second addition into toluene was not only for further crystal growth but also for the removal OA, OLA, MeIm because the organic additives were soluble in toluene. Then the solid precipitate was isolated from toluene and put into the oven at 50 °C for drying. Finally, the dried sample was transferred to sealed vials for further characterisations.

Preparation with different antisolvents:

A solvent combination of 10 mL DMF and 10 mL DMSO was preheated to 50 °C and kept stirring in an oil bath. 0.5 mmol (0.041 g) MeIm was added into the solvent, as well as 0.1 mL OA and 0.5 mL OLA.

The ratio of CsBr and PbBr$_2$ was kept at 2 : 1 with fixed PbBr$_2$ molarity at 0.4 mmol because 2 : 1 ratio with toluene treatment produced the most decent rhombohedral crystals. The same method of antisolvent precipitation using hexane, isopropanol, methanol, acetone and ethanol was attempted.

Transformation of Cs$_4$PbBr$_6$ to Cs$_2$PbBr$_5$ and CsPbBr$_3$:

0.25 g Cs$_4$PbBr$_6$ sample synthesised from the precursor with a Cs$^+$ to Pb^{2+} ratio at 4.5 : 1 was dispersed in 20 ml stirring DI water at 50 °C. The solution was stirred for 1 h before being transferred to a watch glass for drying at 50 °C. Solid precipitates were then transferred to sealed vials for further characterisations.

Transformation of Cs$_4$PbBr$_6$ and CsPbBr$_3$ to CsBr and PbBr$_2$:

0.25 g Cs_4PbBr_6/$CsPbBr_3$ sample synthesised from the precursor with a Cs^+ to Pb^{2+} ratio at 2:1, without the addition of OA and OLA in DMF/DMSO solution, was dispersed in 20 ml stirring DI water at 50 °C. After the addition of the solids into stirring DI water, the yellow solids quickly dissolved to form a colourless transparent solution. The solution was stirred 1 h before being transferred to a watch glass for drying at 50 °C. Solid precipitates containing both yellow and white crystals were then transferred to sealed vials for further characterisations.

5.3 Results and Discussion

5.3.1 Crystallography and Morphology of Synthesised Samples

To synthesis either Cs_4PbBr_6 or $CsPbBr_3$, the reactions would be,

$$4\ CsBr + PbBr_2 \rightarrow Cs_4PbBr_6 \qquad\qquad (5.1)$$

$$CsBr + PbBr_2 \rightarrow CsPbBr_3 \qquad\qquad (5.2)$$

From the reaction formulae, a higher ratio of CsBr to $PbBr_2$ favours the formation of Cs_4PbBr_6 while a lower ratio results in the production of $CsPbBr_3$. Theoretically, producing the combination of Cs_4PbBr_6 and $CsPbBr_3$ would require the ratio of CsBr to $PbBr_2$ to be between 4 : 1 to 1 : 1.

However experimentally, a starting molar ratio of CsBr to $PbBr_2$ at 4.5 : 1, 4 : 1, 3.5 : 1, 3 : 1, 2 : 1 and 1 : 1 all lead to a major phase of Cs_4PbBr_6. Cs_4PbBr_6 crystallises in the hexagonal system with a = 13.73 Å and c = 17.32 Å (ICSD Code: 1538416) and appears to be optically white.[17] The XRD pattern series of these ratios are displayed in **Figure 5.1**. For the ratios at 4.5 : 1, 4 : 1 and 3.5 : 1, CsBr co-existed with Cs_4PbBr_6 in the samples. CsBr crystallises in the cubic system with its unit cell parameter a = 4.30 Å (ICSD Code: 236387) and also appears to be optically white. From the corresponding patterns, for the ratios at 3 : 1 and 2 : 1, Cs_4PbBr_6 is the only phase. The phase $CsPbBr_3$ uniquely emerges in the sample of 1 : 1 ratio with small bumps shown in the XRD pattern. The $CsPbBr_3$ phase detected is cubic-$CsPbBr_3$ with the unit cell parameter a = 5.87 Å (ICSD Code: 1533063) which shows an orange colour optically.[17] For molar ratios at 4.5 : 1, 4 : 1 and 3.5 : 1, CsBr exists in the samples, which indicates that CsBr is

not totally consumed. There are no peaks of $PbBr_2$ for all the ratios. From the reaction to synthesis Cs_4PbBr_6, for the starting ratio at 4.5 : 1, when $PbBr_2$ is totally consumed, a portion of CsBr naturally remains. For the ratios at 4 : 1 and 3.5 : 1, no $PbBr_2$ peaks are shown in the XRD patterns, which indicates its total consumption, then there should also be no extra CsBr in the synthesis systems as the ratio is set at the exact stoichiometry or slightly under.
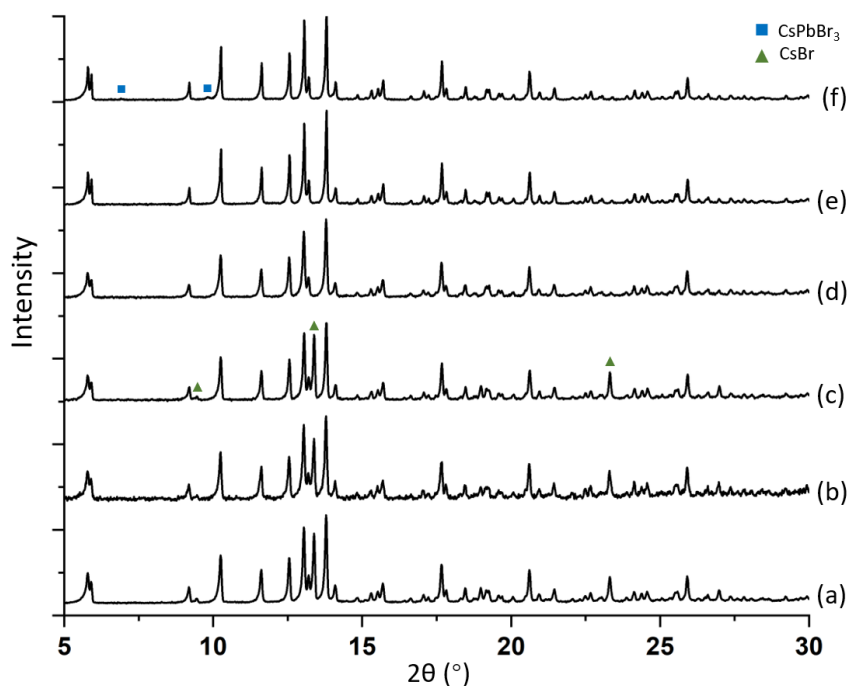
Figure 5.1 XRD patterns of the samples from the synthesis of the ratio of CsBr to $PbBr_2$ at (a) 4.5 : 1, (b) 4 : 1, (c) 3.5 : 1, (d) 3 : 1, (e) 2 : 1 and (f) 1 : 1. The green triangles represent the diffraction peaks of CsBr emerged in (a), (b) and (c). While the blue cubes indicate the peaks of cubic $CsPbBr_3$ emerged in (f). Unmarked distinct peaks can be assigned to the planes of Cs_4PbBr_6. The XRD patterns are based on the Mo Kα1 X-ray source.

Figure 5.2 illustrates the crystal structures of hexagonal-Cs_4PbBr_6 and cubic-$CsPbBr_3$ from different viewing directions correspondingly. Importantly, from [111] direction the {110} plane families of cubic-$CsPbBr_3$ can be seen while from [1$\bar{2}$1], perpendicular {111} and {$\bar{1}$01} are visible. Both crystals are composed of Cs^+ cations and $[PbBr_6]^{4-}$ polyhedra. The simulation of the embedding phenomenon will be demonstrated based on their crystal structures.

Apart from the cubic phase (ICSD Code: 1533063), $CsPbBr_3$ can also crystallise in other polymorphs. With a slight tilt, a quasi-cubic monoclinic phase (ICOD Code: 00-018-0364) with the parameter a = b = 5.83 Å, c = 5.89 Å and γ = 89.65 °, can be derived. These two phases possess similar lattice arrangements and exhibit similar photoluminescence.[18,19] This

monoclinic phase can be regarded as a derivative of the cubic phase. Meanwhile, orthorhombic (ICOD Code: 01-074-2251) and monoclinic (ICOD Code: 00-054-0751) CsPbBr$_3$ with distinct differences have been reported. Orthorhombic CsPbBr$_3$ appears to be white.[20]
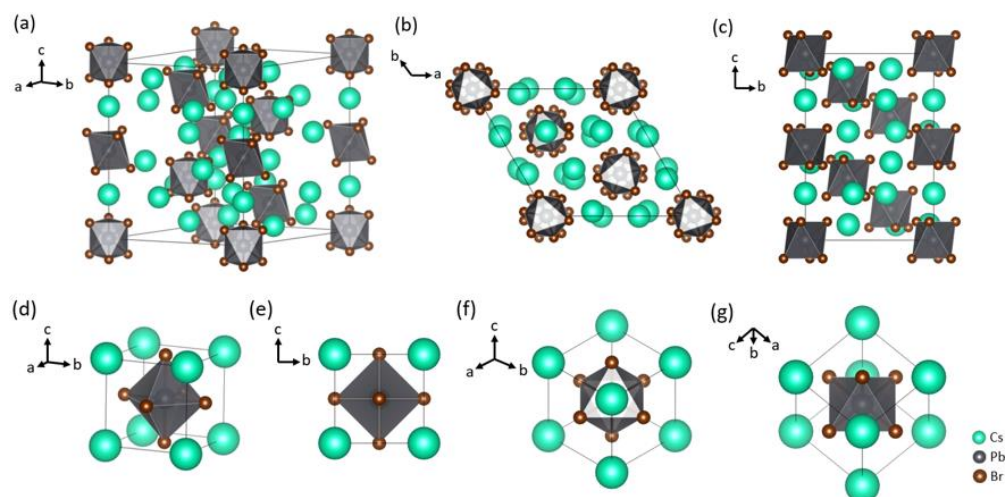
Figure 5.2 Schematic representations of Cs$_4$PbBr$_6$ crystal structure (a) in a 3-dimensional view, (b) viewed from the **c** axis, (c) viewed from the a axis. Schematic representations of CsPbBr$_3$ crystal structure (d) in the 3-dimensional view, (e) viewed from the a axis, (f) viewed from the [111] direction, (g) viewed from the [1$\bar{2}$1] axis.

Considering the optical colours of all phases (white Cs$_4$PbBr$_6$, white CsBr and yellow cubic-phase CsPbBr$_3$) and that pure Cs$_4$PbBr$_6$ shows no photoluminescence under UV light while CsPbBr$_3$ emits luminescent green, the comparison of the optical colours and green-emitting properties under UV light of all the samples can be a superficial way to distinguish the phases macroscopically.

Figure 5.3 demonstrates the colours of the samples from all the ratio series both under optical light and UV light (wavelength 365 nm). The sample from the ratio of 4.5 : 1, as a combination of Cs$_4$PbBr$_6$ and CsBr, exhibits the white colour of Cs$_4$PbBr$_6$ and CsBr optically. Under UV light, the sample from 4.5 : 1 ratio shows slight photoluminescence which indicates a minor existence of CsPbBr$_3$. As the ratio decreases from 4.5 : 1 to 1 : 1, the colours of the samples gradually change from white to light green and to yellow, which indicates the rise of the quantity of orange CsPbBr$_3$ phase. The photoluminescence properties are also enhanced as the ratio decreases to 1 : 1, which indicates the increase of the CsPbBr$_3$ portion in the bulk samples.
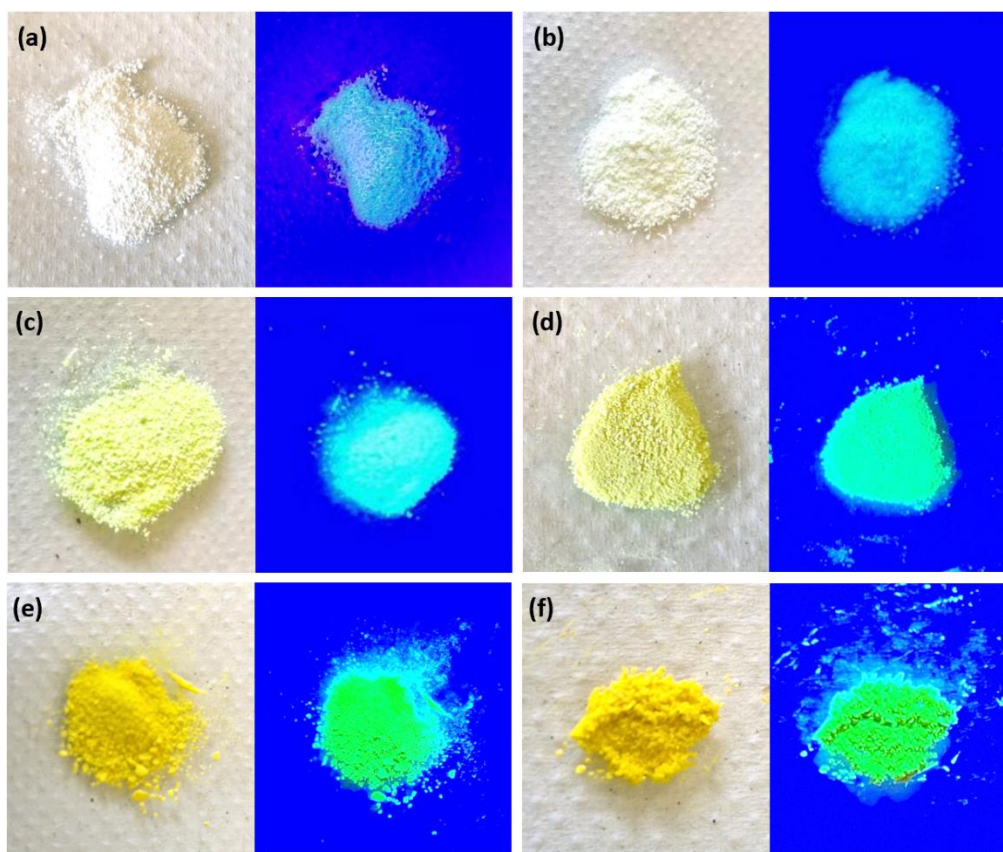
Figure 5.3 Images of the samples from the starting ratio of CsBr to PbBr$_2$ at (a) 4.5 : 1, (b) 4 : 1, (c) 3.5 : 1, (d) 3 : 1, (e) 2 : 1 and (f) 1 : 1 under (left) visible light and (right) UV light (365 nm).

Although most XRD patterns in **Figure 5.1** exhibit no signals of CsPbBr$_3$ except for the pattern of the ratio at 1 : 1, the optical colours and photoluminescence properties of the samples indicate that there is X-ray undetected CsPbBr$_3$ phase in all the samples. The absence of CsPbBr$_3$ in the XRD patterns but the presence of CsPbBr$_3$ captured by optical colour and UV-light photoluminescence are consistent with published works.[9,21,22]

We reckon the vanishing of CsPbBr$_3$ peaks in the XRD patterns (**Figure 5.1b** to **e**) can be attributed to the overlap of the intense peaks from the main phase Cs$_4$PbBr$_6$ and the unperceivable feature of ultra-small CsPbBr$_3$ nanocrystallites buried in the bulk Cs$_4$PbBr$_6$.

SEM was applied to investigate the morphologies of all the sample series, as displayed in **Figure 5.4**. For the cation ratio at 4.5 : 1 and 4 : 1, the size of the crystals is diverse from hundreds of nanometres to about 1 μm. And the morphology of individual crystals is not rhombohedral. For the ratios at 3.5 : 1 and 3 : 1, the size of the crystals appears to be almost

uniform at the 0.5 μm scale yet the rhombohedral morphology is not distinct. Crystals from

2 : 1 ratio have the monodispersed rhombohedral morphology and the size is mostly over 0.5

μm. The crystals from 1 : 1 ratio are also all rhombohedral with the size all over 1 μm. The

size of rhombohedral Cs_4PbBr_6 crystals increases and becomes monodispersed as the ratio of

Cs^+ to Pb^{2+} drops from 4.5 : 1 to 1 : 1.
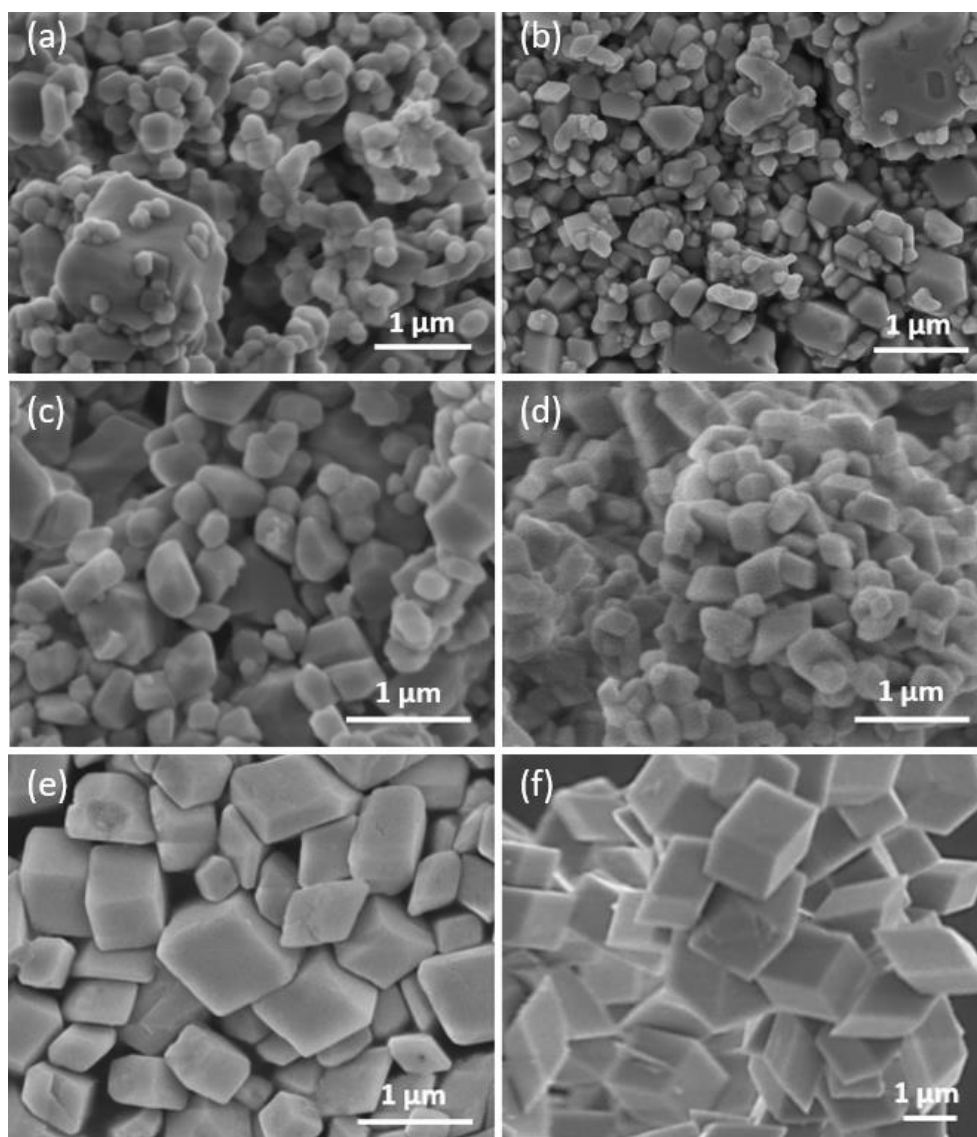
Figure 5.4 SEM images of the samples from the CsBr to $PbBr_2$ ratio at (a) 4.5 : 1, (b) 4 : 1, (c) 3.5 : 1, (d) 3 : 1, (e) 2 : 1 and (f) 1 : 1.

In the DMF/DMSO solution, the binding of Pb^{2+} to the ligands OA and OLA confines the

concentration of free Pb^{2+}, therefore the actual ratio of the cations would be lower . While

MeIm helps to control the size and composition.[17,23] **Figure 5.5** demonstrates the binding

effect of OA and OLA on Cs^+ and Pb^{2+}. The coupling effect of OA derives from its dissociated -OH group and the lone pair of electrons from O. While that of OLA derives from the lone pairs of electrons from N. Additionally, the oxidation state of Pb is higher, resulting in stronger confinement of Pb^{2+} by the bindings. Therefore, even partial Cs^+ ions are restricted as well, the free Pb^{2+} ions are far less. With more severe confinement of Pb^{2+} cations, the crystal growth system of all ratio series tends to form Cs-rich Cs_4PbBr_6 with rhombohedral morphology. Such limitation in cations releasing explains that even if the starting ratio is below 4 : 1, Cs_4PbBr_6 is the main phase.
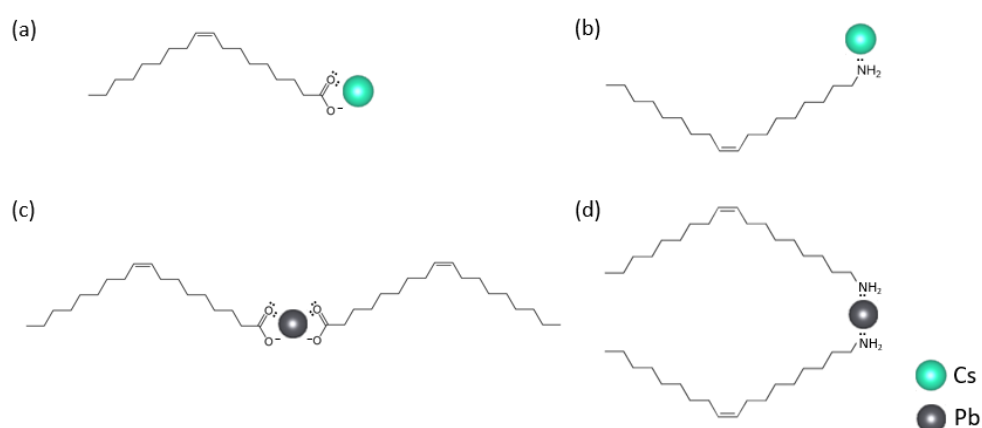
Figure 5.5 (a) Binding of OA to Cs^+. (b) Binding of OLA to Cs^+. (c) Binding of OA to Pb^{2+}. (d) Binding of OLA to Pb^{2+}.

From the perspective of crystal growth, high supersaturation or fast crystal growth tends to create more nuclei during the nucleation process of crystal growth, and fast but random adsorption of ions onto those nuclei. Then with fixed cations and ions for growth, the crystal growth on more nuclei generates a small crystal size. In contrast, slow crystal growth or low supersaturation implies fewer nuclei are formed. And there is enough time for slow realising of ions to allow precise adsorption onto the nuclei and eventually monodisperse morphology with large size. A decrease in Cs^+ concentration leads to the tendency to produce large rhombohedral Cs_4PbBr_6 crystals with monodispersed size which is illustrated from **Figure 5.4**.

Considering the absence of CsBr in the specimens of low ratios, the good photoluminescence derived from $CsPbBr_3$, the monodispersed morphology and size, for further characterisations, samples from the ratios at 2 : 1 and 1 : 1 are the main targets to be investigated.

TEM and HRTEM were applied to study the morphology and embedding feature of CsPbBr$_3$-containing Cs$_4$PbBr$_6$. **Figure 5.6a** demonstrates the rhombohedral morphology of the synthesised Cs$_4$PbBr$_6$ from 2 : 1 ratio.
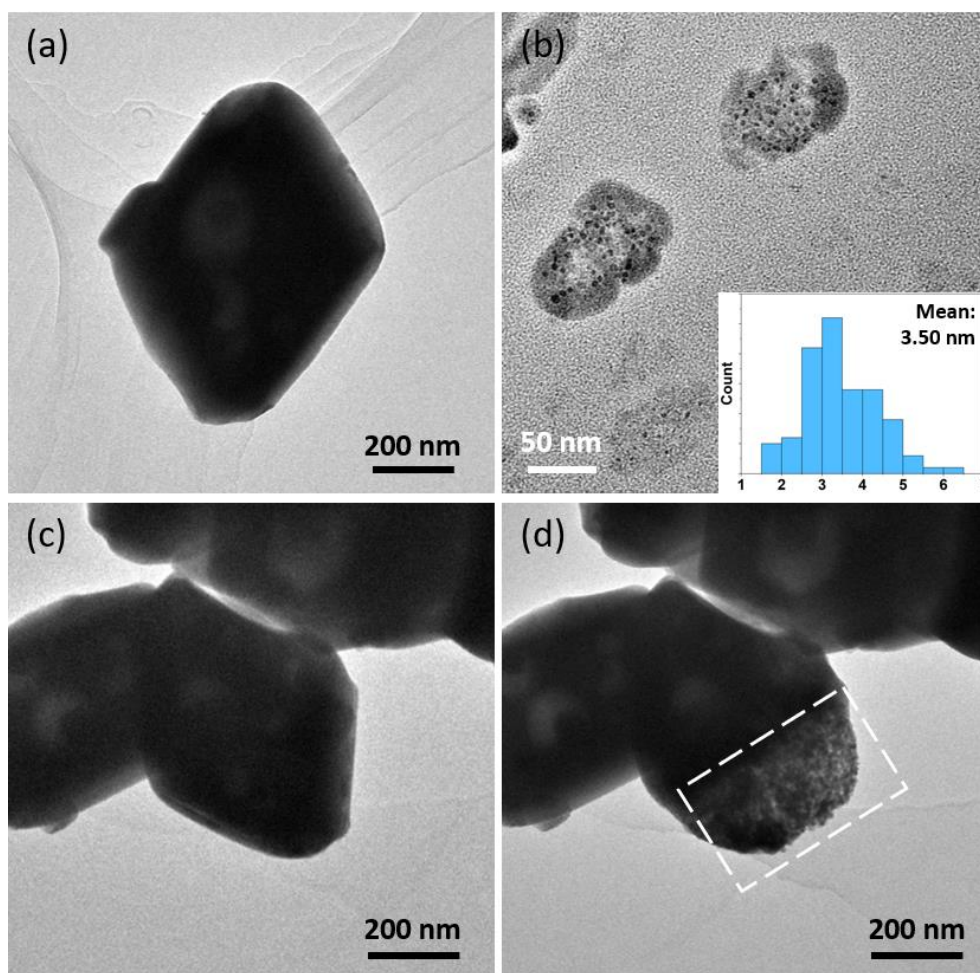
Figure 5.6 Low magnification TEM images from the sample of 2:1 ratio. (a) A Cs$_4$PbBr$_6$ crystal of hexagonal morphology. (b) Fragments of Cs$_4$PbBr$_6$ which contains nanocrystallites as dark spots. Inset is the size distribution of nanocrystallites. (c, d) A hexagonal Cs$_4$PbBr$_6$ before and after electron beam exposure. The selected area in (d) is the exposed and destroyed area with electron beam irradiation.

The morphology is consistent with the SEM images in **Figure 5.4(e)**. With sample grinding, crystal fragments of smaller size were obtained and characterised by TEM. The image contrast of **Figure 5.6(b)** indicates that there are nanocrystallites randomly located in the fragments. The inset of **Figure 5.6(b)** illustrates the size distribution of the nanocrystallites. The average

112

size of the nanocrystallites is 3.50 nm. The Cs_4PbBr_6 crystals are sensitive to the electron beam. **Figure 5.6(c)** and (**d**) show a Cs_4PbBr_6 crystal before and after electron beam exposure. The selected area is the destroyed area under the exposure of electron beam for 5 min.

Subsequently, HRTEM images from the sample of 2 : 1 ratio were collected to demonstrate the crystallographic directions of Cs_4PbBr_6 rhombohedral crystals and the embedding feature of $CsPbBr_3$ nanocrystallites. **Figure 5.7(a)** shows an HRTEM image with both the fringes of bulk Cs_4PbBr_6 as well as those of $CsPbBr_3$ nanocrystallites. The d-spacing from the expanded domain is measured at 3.94 Å and assigned to the $(3\bar{3}00)$ plane of hexagonal Cs_4PbBr_6. The d-spacing in the white dashed circle is measured at 4.16 Å and assigned to the (110) plane of cubic $CsPbBr_3$. The crystallographic direction $[1\bar{1}00]$ of hexagonal Cs_4PbBr_6 is derived from the fringes. And to see the (110) plane of $CsPbBr_3$ phase, the viewing axis may be the [111] of $CsPbBr_3$. **Figure 5.7(b)** shows the corresponding low magnification TEM image. With the $[1\bar{1}00]$ direction in **Figure 5.7(a)** and the hexagonal morphology, directions a and b in **Figure 5.7(b)** are derived, associating with the crystallographic directions.
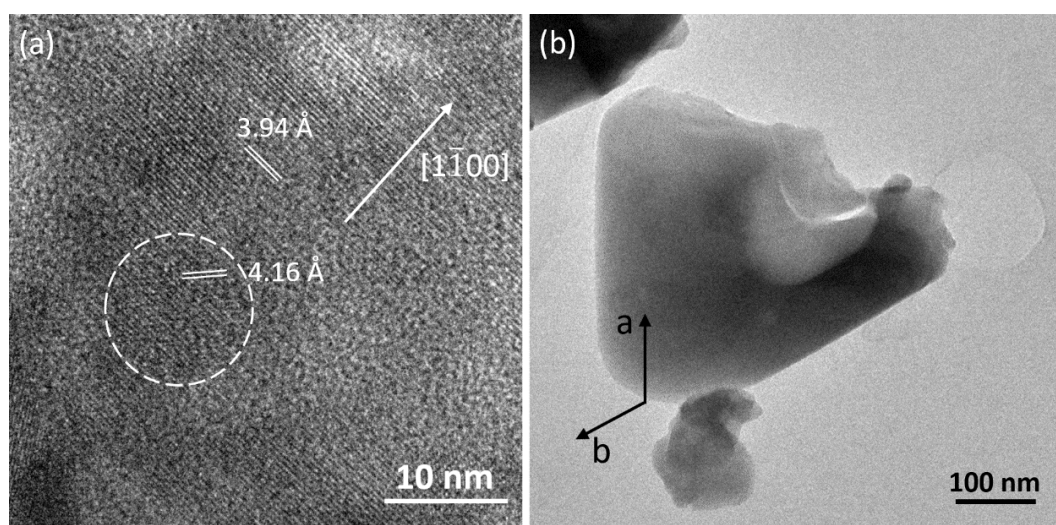
Figure 5.7 (a) HRTEM image showing the fringes of Cs_4PbBr_6 and $CsPbBr_3$. The d-spacings are respectively marked. The white circled area indicates the $CsPbBr_3$ nanocrystallite. (d) Low magnification TEM image with crystallographic directions derived.

Figure 5.8 demonstrates the observation of Cs_4PbBr_6 crystal domain and multiple $CsPbBr_3$ nanocrystallites. The d-spacing measured at 3.13 Å is indexed to the $(\bar{3}214)$ plane of Cs_4PbBr_6.

The d-spacings from CsPbBr$_3$ nanocrystallites measured at 2.92 Å are indexed to the (200) plane of CsPbBr$_3$.
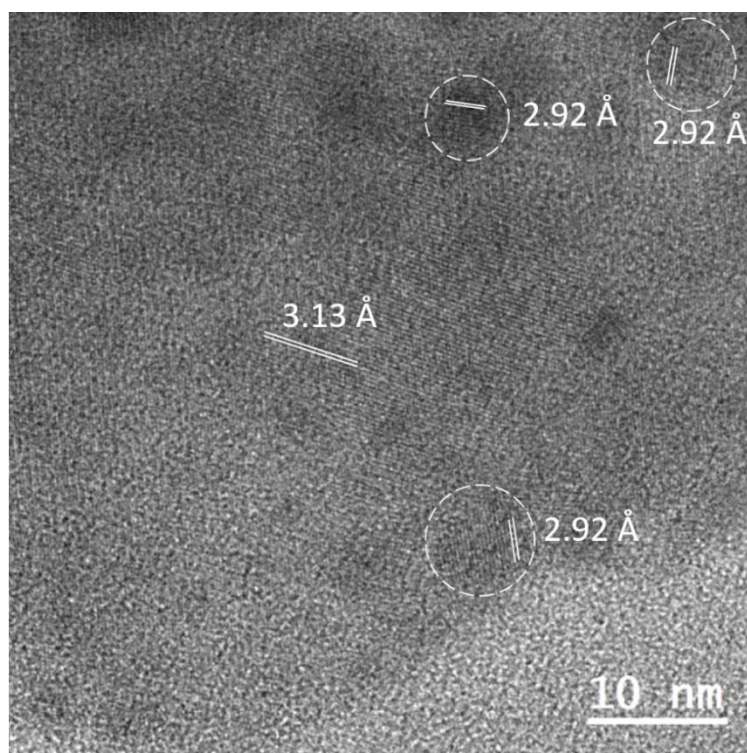
Figure 5.8 HRTEM image demonstrating the simultaneous observation of bulk big Cs$_4$PbBr$_6$ and multiple CsPbBr$_3$ nanocrystallites. White circled areas indicate the CsPbBr$_3$ nanocrystallites. D-spacings from the Cs$_4$PbBr$_6$ domain and CsPbBr$_3$ nanocrystallites are marked, respectively.

Based on the TEM and HRTEM observation of the embedded CsPbBr$_3$ in Cs$_4$PbBr$_6$ in **Figure 5.7**, from the c direction of hexagonal Cs$_4$PbBr$_6$, the $(3\bar{3}00)$ plane of hexagonal Cs$_4$PbBr$_6$ and (110) of CsPbBr$_3$ can both be seen. And based on the crystal structures of Cs$_4$PbBr$_6$ and CsPbBr$_3$ illustrated in **Figure 5.2** and the mathematic relation between the d-spacings of the two phases, the possible embedding behaviour at the structural scale from the top view is proposed, as demonstrated in **Figure 5.9(a)**. From the c direction of Cs$_4$PbBr$_6$, $\{30\bar{3}0\}$ plane family of Cs$_4$PbBr$_6$ as well as {110} plane family of CsPbBr$_3$ are visible. The connection of embedded CsPbBr$_3$ and Cs$_4$PbBr$_6$ host can be achieved by the bonding of Cs$^+$ cations from Cs$_4$PbBr$_6$ and [PbBr$_6$]$^{4-}$ polyhedra from CsPbBr$_3$ (**Figure 5.9a**). Such embedding is permitted from the perspective of the d-spacing mathematic approximation (**Figure 5.9b**). The $(10\bar{1}0)$ d-spacing of Cs$_4$PbBr$_6$ is 11.89 Å while the (110) d-spacing of CsPbBr$_3$ is 4.15 Å. The $(10\bar{1}0)$ d-

spacing of Cs_4PbBr_6 approximates 3 times the (110) d-spacing of $CsPbBr_3$ with 4.71 % expansion. The minor difference does not impact the structure drastically and allows the embedding to occur.
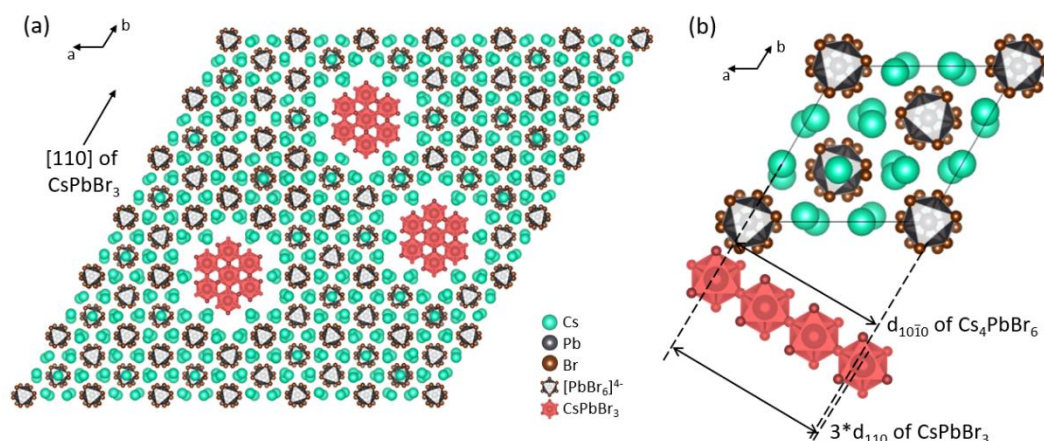
Figure 5.9 (a) The embedding of $CsPbBr_3$ nanocrystallite in Cs_4PbBr_6 matrix from c direction of Cs_4PbBr_6. (b) The mathematic approximation between ($10\bar{1}0$) d-spacing of Cs_4PbBr_6 and 3 times the (110) d-spacing of $CsPbBr_3$, which offers the possibility of hosting $CsPbBr_3$ in the Cs_4PbBr_6 matrix without generating a large lattice tension.

Rotating **Figure 5.9(a)** for 90 °, the embedding behaviour of $CsPbBr_3$ in Cs_4PbBr_6 from the front view (a direction of Cs_4PbBr_6) can be visualised, as illustrated in **Figure 5.10(a)**. From the front view, the connection of the two phases is also achieved by the bonding of Cs^+ cations from Cs_4PbBr_6 and $[PbBr_6]^{4-}$ polyhedra from $CsPbBr_3$. From this direction, the connection of embedded $CsPbBr_3$ and Cs_4PbBr_6 host is also achieved by the bonding of Cs^+ cations from Cs_4PbBr_6 and $[PbBr_6]^{4-}$ polyhedra from $CsPbBr_3$ as seen in **Figure 5.10(a)**. Additionally, mathematic approximation of d-spacings is also achieved from the a direction of Cs_4PbBr_6. The (0001) d-spacing of Cs_4PbBr_6 is 17.32 Å while the (111) d-spacing of $CsPbBr_3$ is 3.39 Å. The (0001) d-spacing of Cs_4PbBr_6 approximates 5 times the (111) d-spacing of $CsPbBr_3$ with 2.14 % expansion. The d-spacing approximations in both the c direction and a direction of Cs_4PbBr_6 shown in **Figure 5.9** and **Figure 5.10** demonstrate the possible 3-dimensional lattice match of embedding $CsPbBr_3$ and Cs_4PbBr_6 matrix.
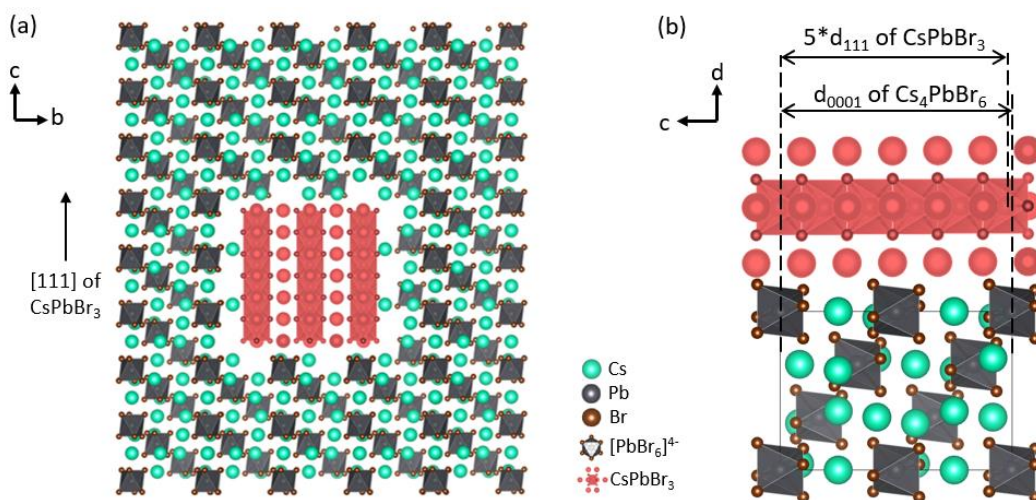
Figure 5.10 (a) The embedding of $CsPbBr_3$ nanocrystallite in Cs_4PbBr_6 matrix from a direction of Cs_4PbBr_6. The viewing direction of $CsPbBr_3$ is $[1\bar{2}1]$. (b) The mathematic approximation between (0001) d-spacing of Cs_4PbBr_6 and 5 times of (111) d-spacing of $CsPbBr_3$ which makes the possibility of hosting $CsPbBr_3$ in the Cs_4PbBr_6 matrix without changing the structure dramatically and generating a drastic lattice tension at the interface.

However, the aligned embedding phenomenon demonstrated in **Figure 5.9** and **Figure 5.10** only provides an ideal situation with least structural change, closest d-spacing approximation, same directional alignment of $[PbBr_6]^{4-}$ groups from $CsPbBr_3$ and Cs_4PbBr_6, and connection of Cs^+ from Cs_4PbBr_6 and $[PbBr_6]^{4-}$ from $CsPbBr_3$. The embedding feature in **Figure 5.7** satisfies such alignment while **Figure 5.8** does not. The reason could be either a rapid growth not leading to perfect alignment or long-time electron beam exposure deteriorating the crystal structure, therefore changing the orientation.

5.3.3 Formation Mechanism of $CsPbBr_3$ Embedded Cs_4PbBr_6

The growth of Cs_4PbBr_6 rhombohedral crystals is instant, making it unrealistic to cut the growth into different stages to obtain crystals chronologically. However, the supersaturation in the first and second mixing with toluene is the focus point. When 10 ml DMF/DMSO mother solution of Cs^+ to Pb^{2+} ratio at 2 : 1 was added into 10 ml toluene, due to the low solubility of ions in the non-polar solvent, Cs^+, Pb^{2+} and Br^- proceeded precipitation in the solution mixture of DMF/DMSO/toluene. The volume ratio of DMF/DMSO portion in which the ions were soluble and toluene portion in which the ions were insoluble is 1 : 1, and a large amount of

Cs$^+$, Pb^{2+} and Br$^-$ ions were still in the DMF/DMSO solution and not affected by toluene treatment, therefore would not precipitate. From the perspective of supersaturation in toluene, during the first addition into toluene, the supersaturation of the ions was not at a high level which indicated that the crystal growth during the first addition was not finished and early-stage crystals from first toluene treatment could be observed.

Figure 5.11(a) and (b) show the Cs$_4$PbBr$_6$ crystals in the early growth stage collected from the first addition into toluene. The squared crystal in Figure 5.11(a) is in its growth process of morphology fulfilment. Figure 5.11(b) shows smaller rhombohedral crystals with sticky coating layers.
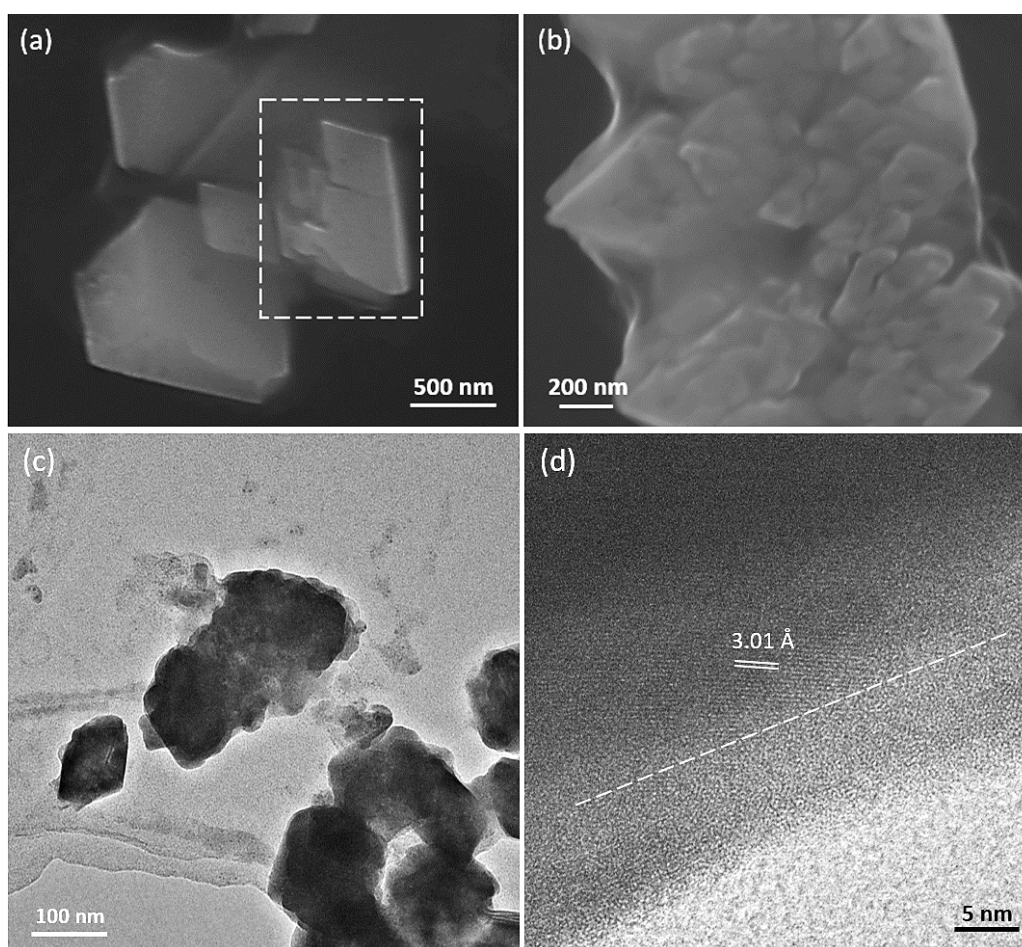
Figure 5.11 (a, b) SEM images of the Cs$_4$PbBr$_6$ crystals from the CsBr to PbBr$_2$ ratio at 2 : 1 with only the first addition into toluene. (c) Low magnification TEM of nanoscale rhombohedral Cs$_4$PbBr$_6$ crystals from the sample of Cs$^+$ to Pb^{2+} ratio at 1 : 1. The image contrast indicates there is an amorphous phase adhered to the crystals. (d) HRTEM image of a rhombohedral nanocrystal with fringes and amorphous phase covering. The marked fringe is measured at 3.01 Å. The dashed line indicates the boundary between the fringes and the amorphous domain.

During the antisolvent precipitation, most of the DMF/DMSO/toluene solution from the first toluene treatment was removed, leaving the bottom layer of solid precipitates for a second toluene treatment. The filtered solid precipitates from the first toluene treatment were quickly transferred into another 10 ml toluene for further growth. At this stage, the liquid phase was mainly toluene with a small amount of excess DMF/DMSO solution. A high percentage of toluene guaranteed the complete precipitation of ions in the excess DMF/DMSO solution, therefore Cs_4PbBr_6 crystals further grew to a larger scale. **Figure 5.4(e)** shows the grown rhombohedral Cs_4PbBr_6 crystals from the Cs^+ to Pb^{2+} ratio at 2 : 1.

Figure 5.11(c) also demonstrates the covering of amorphous layers on small Cs_4PbBr_6 nanocrystals from the sample with full antisolvent procedure. The marked d-spacing in **Figure 5.11(d)** is assigned to the $(4\bar{2}23)$ plane of Cs_4PbBr_6. The white dashed line in **Figure 5.11(d)** indicates the interface between crystalline Cs_4PbBr_6 and amorphous coating layer. TEM and HRTEM indicates that there is an amorphous phase covering grown rhombohedral crystals. And from **Figure 5.11(d)**, the amorphous phase and grown crystalline Cs_4PbBr_6 have similar contrast, which implies that the amorphous phase may also be composed by the 3 elements (Cs, Pb, Br).

Amorphous calcium carbonate (ACC) before the production of more stable crystalline $CaCO_3$ polymorphs has been reported[24,25], which is regarded as an example of non-classical nucleation. ACC phase transforms quickly to crystalline $CaCO_3$.[26] Such amorphous phase mediated growth has also been reported for the case of Ni nanocrystals.[27] We then deduce that in the fast antisolvent precipitation system, metastable amorphous precursor phase form initially, followed by subsequent atom arrangement and crystal structure formation.

Additionally, in the field of inorganic crystal growth, ionic polymers and oligomers have been identified to be pre-nucleation amorphous phases.[28,29] We reckon for this present project, an ionic polymer can be achievable by the connection of Cs^+ cations and $[PbBr_6]^{4-}$ clusters. We hereby hypothesise the polymerised Cs_xPbBr_y phase, as illustrated in **Figure 5.12**. The 3D extension of the polymerised Cs_xPbBr_y is achieved by the bonds between individual -Cs- and Br- from $[PbBr_6]^{4-}$ polyhedra.
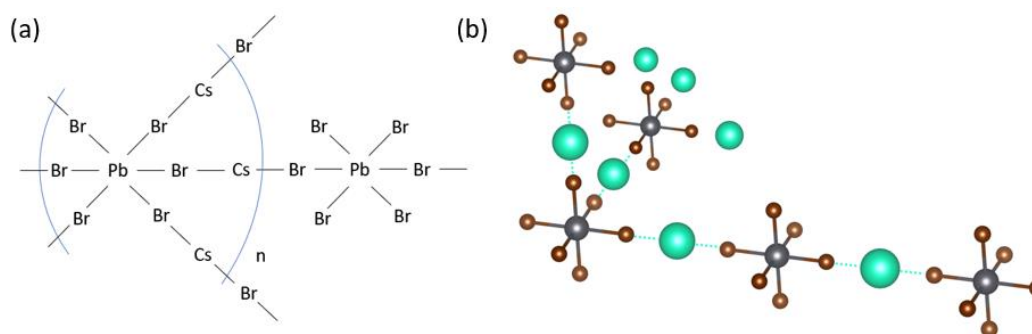
Figure 5.12 (a) 2D representation of the formula of the polymerised Cs_xPbBr_y. (b) 3D extension of the polymerised Cs_xPbBr_y.

In the proposed polymerised Cs_xPbBr_y formula, the ratio of Cs^+ and Pb^{2+} is 3 : 1, which falls in between 4 : 1 and 1 : 1. Such a formula makes it realistic to split the ratio and form both Cs_4PbBr_6 and $CsPbBr_3$ during further crystallisation.

EDX spectra were recorded to obtain the ratio of Cs and Pb, as shown in **Figure 5.13(a)** and **(b)**. We expect the quantitative EDX results to be relatively accurate for heavier elements. The ratio of Cs^+ to Pb^{2+} is about 3.14 : 1, which aligns with our proposed formula for the polymerised Cs_xPbBr_y in **Figure 5.12**.

As discussed earlier, cations in the DMF/DMSO solution are in the form of M-OA and M-OLA (M = Cs or Pb). The binding to OA and OLA restricts the slow release of metal cations. Furthermore, the OA and OLA binding to Pb^{2+} is stronger than that to Cs^+ (**Figure 5.5**), making the antisolvent precipitation process Cs-rich. In the process of producing the polymerised Cs_xPbBr_y, free Br^- ions constantly substitute the ligands, breaking their binding to Pb^{2+} and Cs^+, creating $[PbBr_6]^{4-}$ and further Cs_xPbBr_y. **Figure 5.13 (c)** shows a particle from the sample of the cation ratio at 4.5 : 1. The marked d-spacing is measures at 2.09 Å and indexed to $(5\bar{5}04)$ plane of Cs_4PbBr_6. Amorphous phase encompasses the crystalline. Unlike **Figure 5.11 (d)**, the phase contrast of **Figure 5.13 (c)** is obvious, which may indicate there is a massive elemental difference between crystalline Cs_4PbBr_6 and the surrounding amorphous phase. Considering those light elements from the ligands OA and OLA (H, C, N, O), and that Cs_xPbBr_y and Cs_4PbBr_6 may not have strong contrast difference due to similar composition, we reckon OA and OLA partially constitute the early-stage amorphous phase, generating strong phase contrast in **Figure 5.13 (c)**.
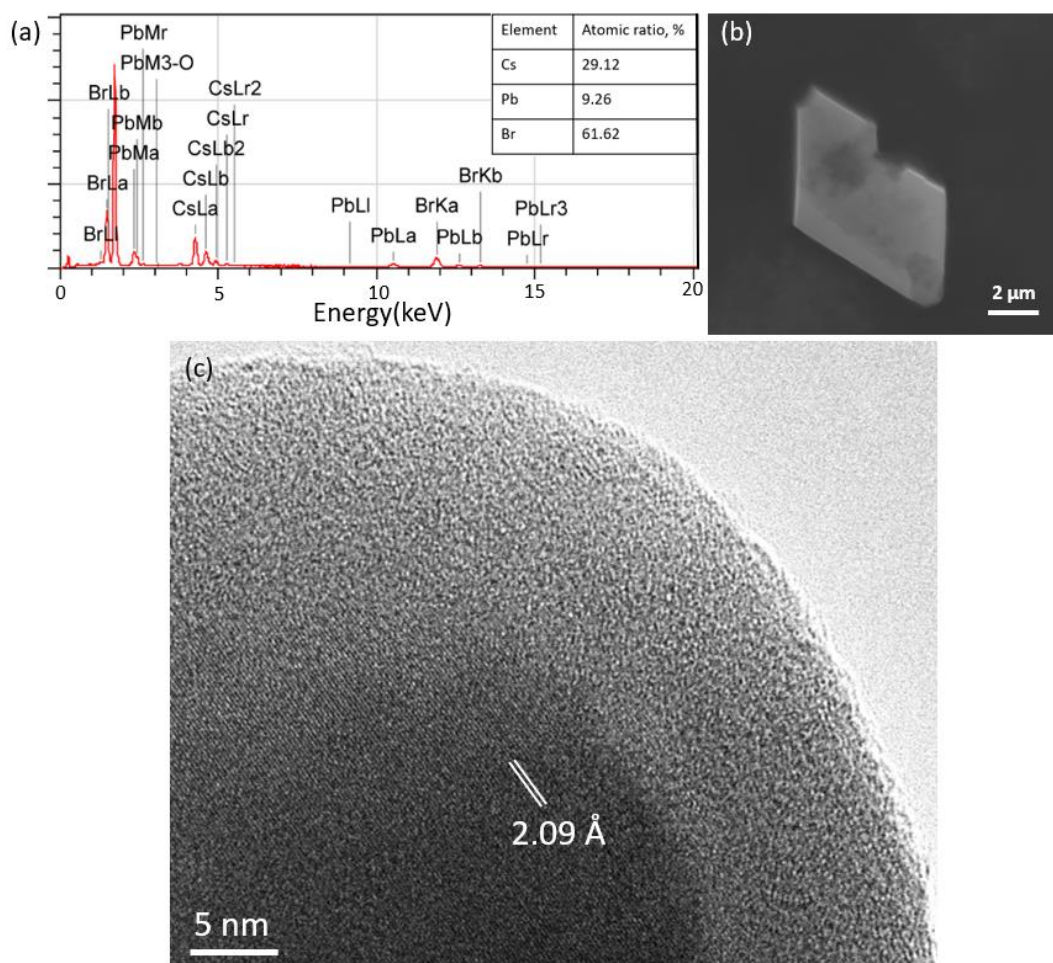
Figure 5.13 (a) EDX spectrum of a grown rhombohedral crystal. The inset is the quantitative atomic ratio results of Cs, Pb and Br. (b) SEM image of the corresponding rhombohedral crystal. (c) HRTEM image of a particle with interior crystalline fringes and encompassing amorphous layer. The amorphous phase is much brighter than the fringes, indicating a obvious elemental composition difference. The marked d-spacing is measured at 2.09 Å.
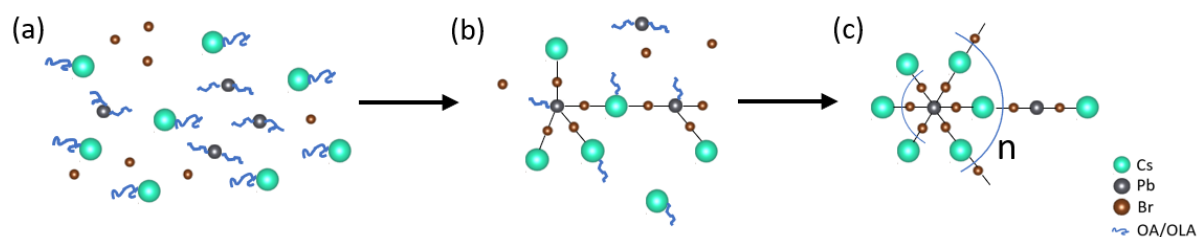
Figure 5.14 Production of the polymerised Cs_xPbBr_y at structural scale. (a) Free Br^- ions, M-OA and M-OLA in DMF/DMSO solution. (b) Substituting behaviour of ligands by Br- ions to produce polymerised Cs_xPbBr_y. (c) Polymerised Cs_xPbBr_y.

Amorphous M-OA and OLA generate initially and are substituted by Br- ions to form polymerised Cs_xPbBr_y. With OA and OLA present in early-stage amorphous phase, the image

120

contrast is light (**Figure 5.13c**). While polymerised Cs_xPbBr_y and Cs_4PbBr_6 have similar image contrast (**Figure 5.11d**). **Figure 5.14** demonstrates the precipitation process of the polymerised Cs_xPbBr_y from M-OA and M-OLA.
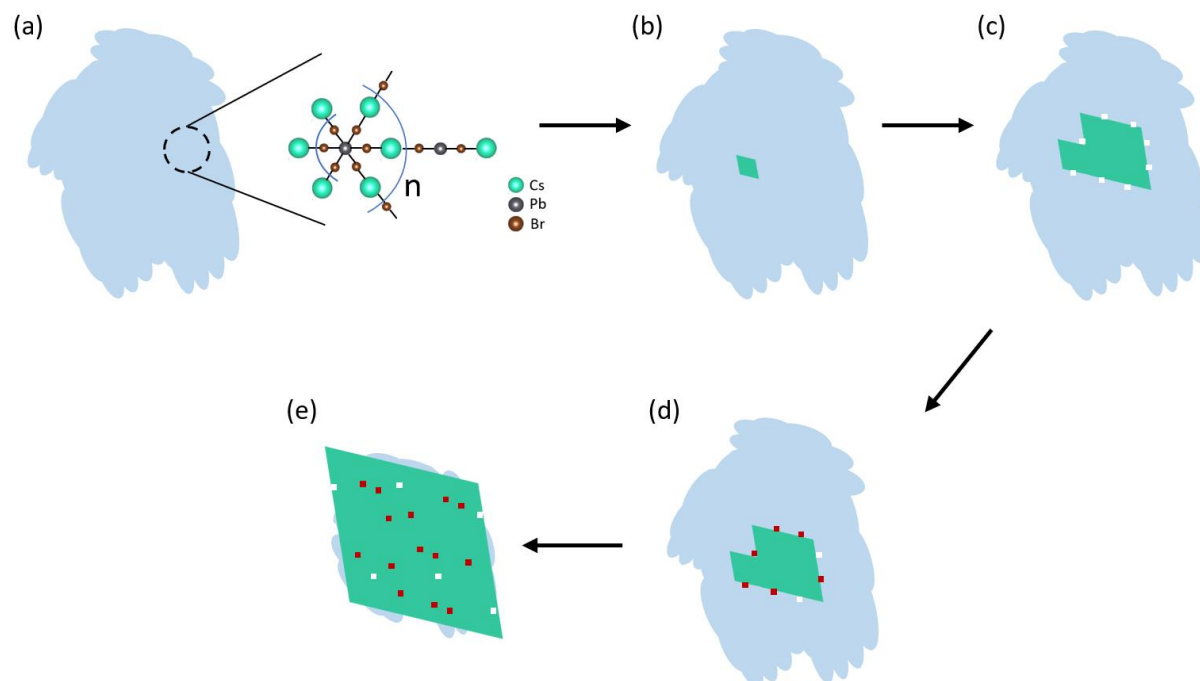
Figure 5.15 Formation process of rhombohedral Cs_4PbBr_6 crystals in the polymerised Cs_xPbBr_y phase. (a) Polymerised Cs_xPbBr_y with structural formula illustrated. (b) Creation of initial Cs_4PbBr_6 nucleus inside polymerised Cs_xPbBr_y phase. (c) Growth of Cs4PbBr6 crystal. As Cs+ consume more quickly in the ratio of $Cs^+ : Pb^{2+}$ at 4 : 1, localised Cs+ absent sites are created. (d) Formation of local $CsPbBr_3$ nanocrystallites due to the localised absence of Cs^+ and abundance of Pb^{2+}. (e) Grown Cs_4PbBr_6 rhombohedral crystals with embedded $CsPbBr_3$ nanocrystallites, cavities due to Cs^+ absence and surface amorphous coating layers.

In the fast antisolvent precipitation process, the amorphous phase forms first, followed by atomic arrangement and crystallisation inside the amorphous phase. **Figure 5.15** demonstrates the formation of $CsPbBr_3$ embedded Cs_4PbBr_6 rhombohedral crystals. Initially, fast antisolvent precipitation leads to the production of polymerised Cs_xPbBr_y (**Figure 5.15a**). Polymerised Cs_xPbBr_y with partial ordering may not be stable and will proceed with crystallisation. A Cs^+ to Pb^{2+} ratio at about 3 : 1 indicates a Cs-rich state and leads to the crystallisation of Cs_4PbBr_6. With nucleus presented, crystallisation further occurs, in the interface between polymerised Cs_xPbBr_y and the nucleus. Crystallisation allows the growth of

Cs_4PbBr_6 crystals inside the polymerised Cs_xPbBr_y and pushes the interface outwards (**Figure 5.15b** and **c**).

As Cs-rich Cs_4PbBr_6 phase grows and Cs ions consumes in the Cs^+ to Pb^{2+} ratio at 4 : 1 inside the polymerised Cs_xPbBr_y which has a Cs^+ to Pb^{2+} ratio at about 3:1, localised Cs-absent sites emerge, creating vacancies. Furthermore, crystallisation proceeds even with localised vacancy defects presented. In the meantime, Cs-absence in these vacancies indicates Pb-rich status in the surroundings. To stabilise the high-energy vacancy defects, with surrounding Pb^{2+} cations, Pb-rich $CsPbBr_3$ phase forms internally. Eventually, rhombohedral Cs_4PbBr_6 with embedded $CsPbBr_3$ nanocrystallites, localised cavities and amorphous coating layers form (**Figure 5.15d** and **e**).

Such internal formation of crystalline phases inside polymerised Cs_xPbBr_y can also be proven by the evidence that no individual $CsPbBr_3$ nanocrystallites are observed outside the rhombohedral Cs_4PbBr_6 crystals. TEM observation conveys the information that $CsPbBr_3$ nanocrystallites aside from bulk Cs_4PbBr_6 crystals do not exist, as can be concluded from the clear background of **Figure 5.6** and **Figure 5.16(a)** and **(b)**. Significantly, even with sample grind treatment before TEM characterisation, the nanocrystallites always disperse in the Cs_4PbBr_6 matrix, as shown in **Figure 5.6(b)**. Additionally, if the $CsPbBr_3$ phase grows itself individually and simultaneously with Cs_4PbBr_6 crystals, the size of $CsPbBr_3$ crystals will not be restricted only in several nanometres. Distinct cubic $CsPbBr_3$ crystals can then be observed. While cubic $CsPbBr_3$ crystals are not observed using TEM. We then eliminate the possibility that the $CsPbBr_3$ phase forms individually outside the Cs_4PbBr_6 matrix.

Localised absence of Cs in certain sites represents Pb-rich in the surroundings, therefore Pb-rich $CsPbBr_3$ phase form. Formation of Pb-rich $CsPbBr_3$ nanocrystallites requires Pb^{2+} cations. As the crystallisation undergoes, the consumption of Pb^{2+} to form $CsPbBr_3$ conversely makes the surrounding area Cs-rich again. Cs-rich sites favour the production of Cs_4PbBr_6. The overall crystallisation of Cs_4PbBr_6 and $CsPbBr_3$ is the repeated process of lacking Pb^{2+} and Cs^+. With the repeated process, like squeeze bubbles, the Cs-absent vacancies are pushed outwards by the crystallisation. Therefore, cavities on the rhombohedral crystals exist.

Interestingly, magnified SEM images of grown Cs_4PbBr_6 rhombohedral crystals show that there are cavities and coating layers on the surface, as displayed in **Figure 5.15(c)** and **(d)**.

Such existence of cavities and coated layers are consistent with the proposed theory involving the formation of polymerised Cs_4PbBr_6 and localised absence of Cs cations.
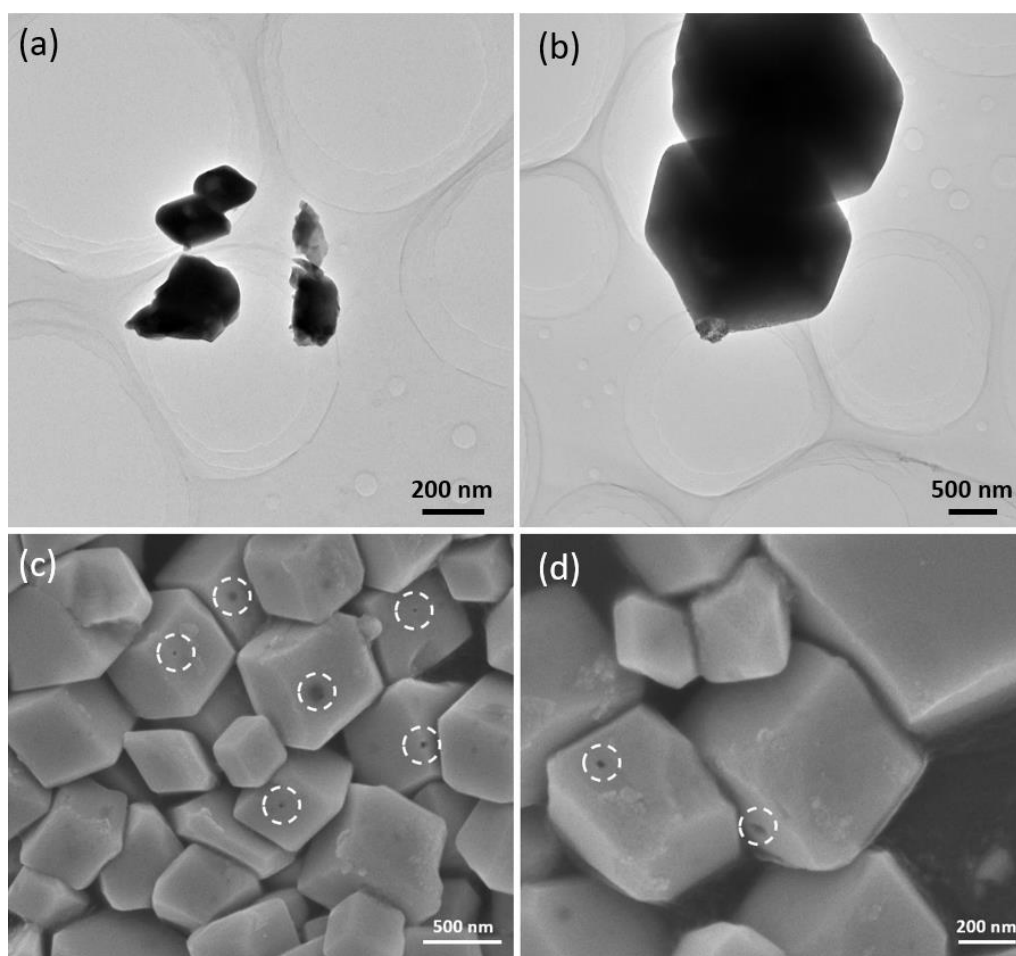
Figure 5.16 (a) Low magnification TEM image of the sample from 2 : 1 cation ratio with sample uncrushed which demonstrates the Cs_4PbBr_6 crystals with the clear background without possible individual nanocrystallites. (b) Low magnification TEM of the sample from 1 : 1 cation ratio displaying Cs_4PbBr_6 crystals with clean background. (c, d) SEM images of rhombohedral Cs_4PbBr_6 crystals which demonstrate cavities and coating layers on the surface. White dashed circles indicate the cavities.

For the time being, we conclude that the formation of $CsPbBr_3$ is actually achieved inside the Cs_4PbBr_6 matrix. Both are formed after the production of and inside the amorphous Cs_xPbBr_y precursor.

The growth of nanocrystallites in certain matrix is an effective way to control the size and prohibit further growth. Artificial and manipulated growth of $CsPbBr_3$ quantum dots in silica spheres and SiO_2 shells have been reported in order to stabilise the $CsPbBr_3$ quantum dots

and keep the excellent photoluminescence property of the quantum dots.[10,12] In contrast, for this present project, the growth of $CsPbBr_3$ in rhombohedral Cs_4PbBr_6 crystals is spontaneous.

Moreover, no matter what the starting Cs^+ to Pb^{2+} ratio is, polymerised Cs_xPbBr_y phase with constant Cs^+ to Pb^{2+} ratio at 3 : 1 always form. The faster the crystallisation, the shorter the time for perfect atomic arrangement, therefore amorphous precursor generally forms. In Cs_xPbBr_y amorphous phase with a Cs^+ and Pb^{2+} ratio at 3 : 1, Cs^+ cations are at a rich degree, inducing the crystallisation of the Cs-rich Cs_4PbBr_6 phase. Localised abundance of Pb and lack of Cs lead to the formation of localised $CsPbBr_3$ nanocrystallites. Therefore, all the samples from different cation ratios are CsPbBr3 embedded Cs4PbBr6, as indicated by **Figure 5.3**.

Such an internal crystallisation mechanism explains the uniform size of embedded $CsPbBr_3$ nanocrystallites and the absence of individual $CsPbBr_3$ crystals outside Cs_4PbBr_6 crystals. Due to the small size of $CsPbBr_3$ nanocrystallites inside Cs_4PbBr_6 crystals, XRD is not able to detect the $CsPbBr_3$ phase.

Based on the above analyses, the formation mechanism of embedded $CsPbBr_3$ in Cs_4PbBr_6 can now be proposed, as schematically demonstrated in **Figure 5.17**.

Initially, CsBr and $PbBr_2$ are dissolved in the DMF/DMSO solution of OA, OLA and MeIm to form a colourless transparent solution (**Figure 5.17a**). The ligands, OA and OLA, bind to the cations, confine the motion of the cations.

The antisolvent toluene is then mixed with DMF/DMSO solution, creating an environment in which the cations are insoluble. The precipitation of polymerised Cs_xPbBr_y with Cs^+ to Pb^{2+} ratio at about 3 : 1 is then triggered by the supersaturation with the presence of toluene (**Figure 5.17b**). Significantly, the polymerised Cs_xPbBr_y originates from the deposition of M-OA and M-OLA and further substitution of the ligands by free Br^- ions. In the polymerised Cs_xPbBr_y, with overall Cs-rich condition, rhombohedral crystalline Cs-rich Cs_4PbBr_6 forms(**Figure 5.17c**). As the crystallisation of Cs_4PbBr_6 executes in the consumption ratio of Cs^+ to Pb^{2+} at 4 : 1 in the polymerised Cs_xPbBr_y with Cs^+ to Pb^{2+} ratio at 3 : 1, local absence of Cs^+ cations is generated (**Figure 5.17d**). The Cs^+ vacancies, in contrast, represents Pb-rich in the surroundings. To avoid the high-energy vacancy defects, localised formation of $CsPbBr_3$ nanocrystallites is triggered (**Figure 5.17e** and **g**). Further crystallisation is the repeated behaviour of 4 : 1 consumption resulting in Cs_4PbBr_6 and local absence of Cs leading to local $CsPbBr_3$ nanocrystallites.

Grown rhombohedral Cs_4PbBr_6 crystals with embedded $CsPbBr_3$ finally form (**Figure 5.17f** and **h**).
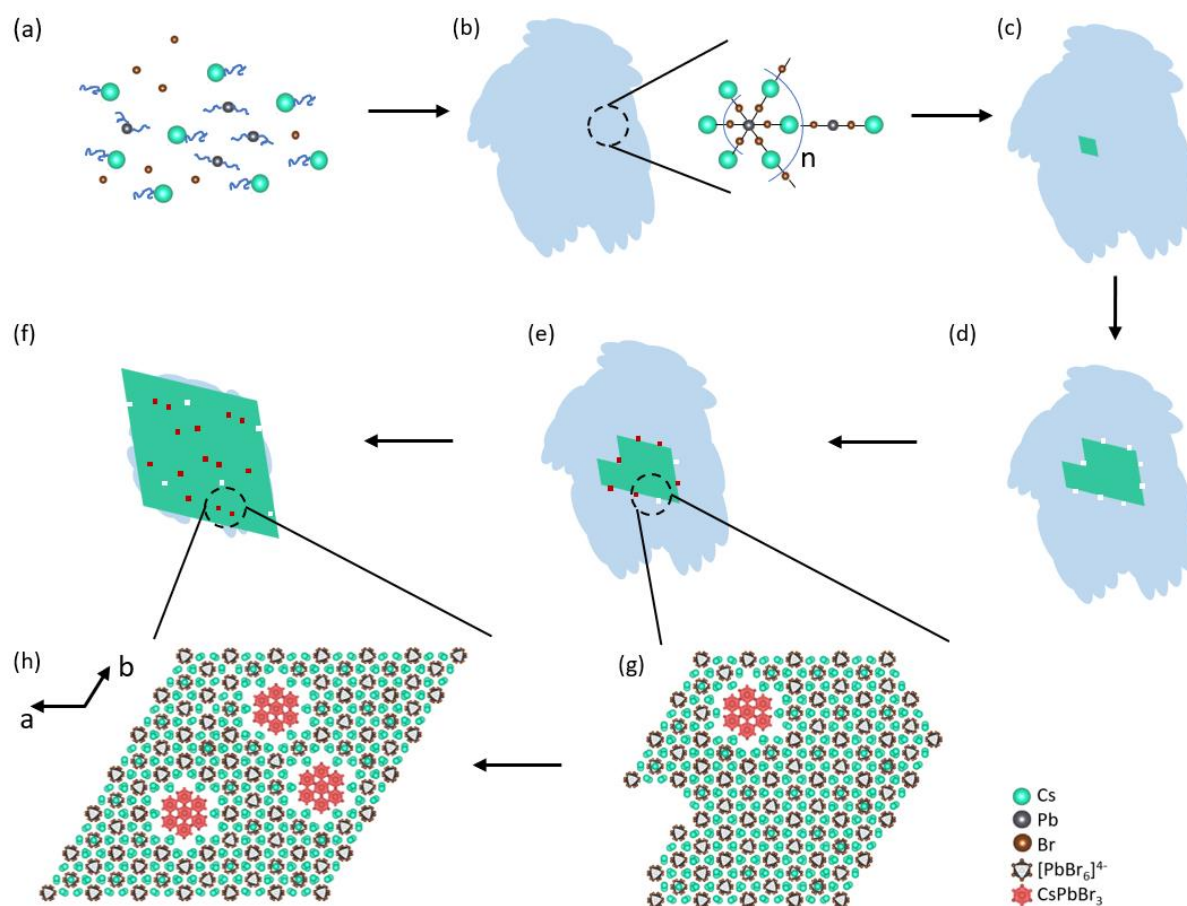
Figure 5.17 Formation mechanism of embedding phenomenon of $CsPbBr_3$ nanocrystallites in Cs_4PbBr_6 rhombohedral crystals. (a) The DMF/DMSO solution of Cs^+, Pb^{2+}, Br^-, OA, OLA and MeIm. Cations bind to OA and OLA in the solution. (b) Precipitation of Cs_xPbBr_y amorphous phase after toluene treatment. The precipitation is achievable by the deposition of M-OA and M-OLA, and further substitution of OA and OLA by free Br^- ions. (c) Immediate formation of crystalline Cs_4PbBr_6 inside the amorphous phase. (d) Growing behaviour of Cs_4PbBr_6 in the amorphous phase. Consumption of the Cs^+ and Pb^{2+} is at the ratio of 4 :1, therefore creating Cs vacancies and local abundance of Pb. (e) Growing Cs_4PbBr_6 rhombohedral crystals with embedded $CsPbBr_3$ nanocrystallites and vacancies. Due to the local abundance of Pb in the Cs-vacant sites, Pb-rich $CsPbBr_3$ crystallises. (f) Grown Cs_4PbBr_6 rhombohedral crystals with embedded $CsPbBr_3$ nanocrystallites and vacancy defects. (g) Growing crystalline Cs_4PbBr_6 with embedded $CsPbBr_3$ nanocrystallite and vacancies in crystal structure scale. (h) Grown crystalline Cs_4PbBr_6 with embedded $CsPbBr_3$ nanocrystallites in crystal structure scale.

Furthermore, the orientation of the two crystalline phases is fixed which can be explained by the ionic bonding of Cs^+ cations from neighbouring Cs_4PbBr_6 and $[PbBr_6]^{4-}$ groups from

CsPbBr$_3$ nanocrystallites. Such orientation is achievable also from the 3-dimensional d-spacing approximation. The (10$\bar{1}$0) d-spacing of Cs$_4$PbBr$_6$ approximates 3 times the (110) d-spacing of CsPbBr$_3$ with 4.71 % expansion while rotating for 90 °, the (0001) d-spacing of Cs$_4$PbBr$_6$ approximates 5 times the (111) d-spacing of CsPbBr$_3$ with 2.14 % expansion (**Figure 5.9** and **Figure 5.10**). The 3-dimensional d-spacing approximation allows the existence of CsPbBr$_3$ nanocrystallites inside Cs$_4$PbBr$_6$ crystals without changing the original structure drastically.

From the perspective of defects, the embedded CsPbBr$_3$ nanocrystallites inside Cs$_4$PbBr$_6$ crystals can be regarded as 3-dimensional inclusion defects. And such inclusion defects with lattice matches are generated to avoid high-energy vacancy defects.

5.3.4 Effect of Antisolvents' Polarity on Crystallisation

Antisolvent is the solvent in which a solute is less soluble. Antisolvent crystallisation is a precipitation method to obtain solid crystals by utilising the solubility difference in different solvents.[30,31]

Table 5.1 Solvents and the corresponding solvent polarity indexes.

Solvent	Formula	Solvent Polarity Index
Hexane	C_6H_{14}	0.1
Toluene	C_7H_8	2.4
Isopropanol	C_3H_8O	3.9
Methanol	CH_3OH	5.1
Acetone	C_3H_6O	5.1
Ethanol	C_2H_5OH	5.2
DMF	C_3H_7NO	6.4
DMSO	$(CH_3)_2SO$	7.2
Water	H_2O	10.2

For the present project to grow Cs$_4$PbBr$_6$ and CsPbBr$_3$, the starting chemicals CsBr and PbBr$_2$ are soluble in polar solvents (water, DMF, DMSO, etc.) but not soluble in non-polar ones (toluene, isopropanol, acetone, etc.), which makes it possible to achieve the synthesis via

antisolvent precipitation. Different antisolvents were applied to examine the effect of antisolvents' polarity on either morphology and crystallography of the synthesised Cs_xPbBr_y. The antisolvent and solvent candidates, and the corresponding polarity indexes are listed in **Table 5.1**.[32] Apart from toluene, the antisolvents hexane, isopropanol, methanol, acetone and ethanol were practised in the same amount of toluene when the molar ratio of CsBr and PbBr₂ was set at 2:1. The obtained samples synthesised from the above antisolvents were characterised by SEM and/or XRD to demonstrate the influence of polarity. Due to the different solubility of reactants (CsBr, PbBr₂) and additives (OA, OLA, MeIm) in the antisolvents, not all the precipitations were successful and obtained solid Cs_xPbBr_y might not be separated or satisfy the quantity to run XRD experiments. **Figure 5.18** shows the images of the solution/solid samples from hexane, isopropanol, methanol, acetone and ethanol.
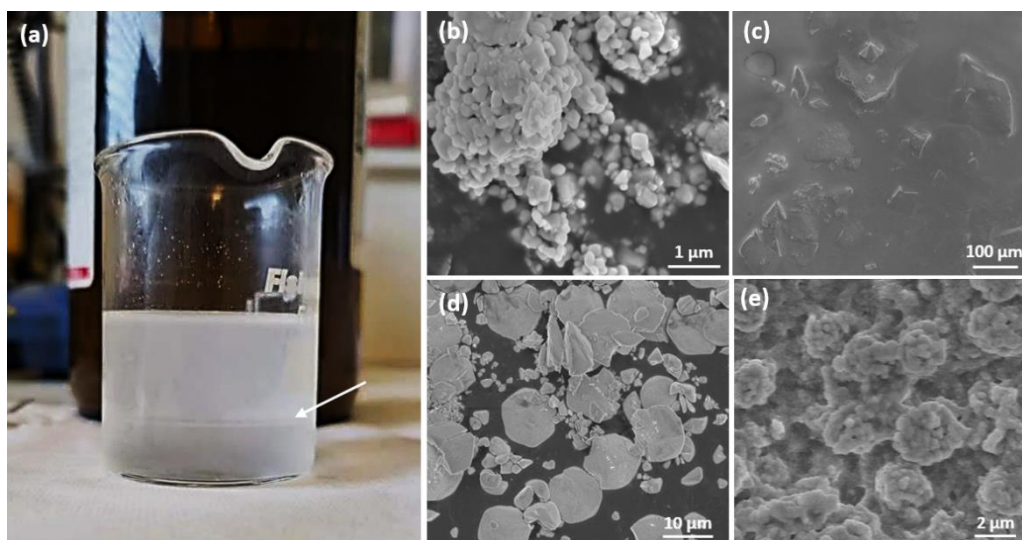
Figure 5.18 (a) The solution mixture of DMF/DMSO and hexane. An interface between DMF/DMSO and hexane is shown and pointed by the arrow. (b) SEM image of the sample from isopropanol treatment. (c) SEM image of the sample from methanol treatment. (d) SEM image of the sample from acetone treatment. (e) SEM image of the sample from ethanol treatment.

Interestingly, the mix of the most non-polar solvent hexane does not produce any solid precipitates. The mixture of DMF/DMSO solution and hexane preserves a distinct interface indicating that the mixture is heterogeneous. The polarity difference between hexane and DMF/DMSO is significant. Therefore the compatibility is low. There will be no possibility for DMF/DMSO and hexane to dissolve each other to form a homogeneous mixture, which

guarantees the safe storage of ions in DMF/DMSO and zero possibility of precipitation. We then conclude that the polarity index of the chosen antisolvent for precipitation should be at an intermediate value in order to be compatible with the DMF/DMSO solution to induce the supersaturation and precipitation. The solvents with intermediate polarity indexes, isopropanol, methanol, acetone and ethanol in **Table 5.2** all manage to produce solid precipitates. Corresponding SEM images are shown in **Figure 5.18(b)** to **(e)**.
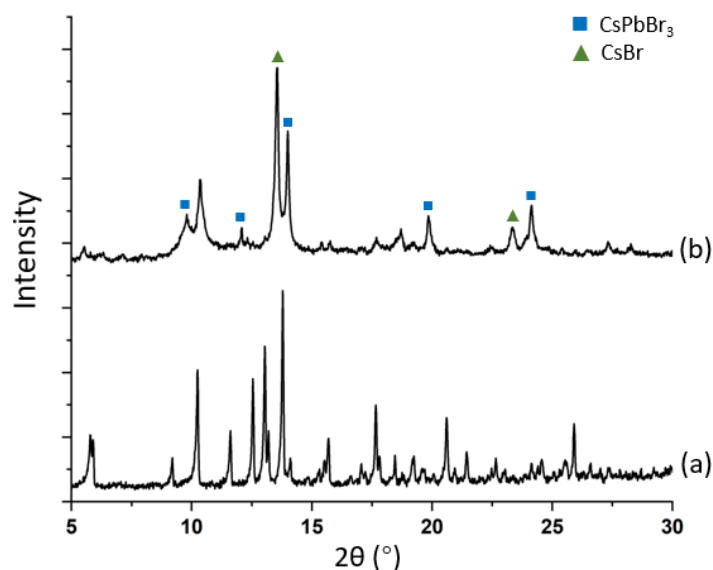
Figure 5.19 XRD patterns of the samples from (a) acetone and (b) ethanol experiments. The green triangles represent the peaks from CsBr and the blue cubes indicate the peaks from monoclinic $CsPbBr_3$ (ICOD Code: 00-054-0751). Unmarked distinct peaks can be assigned to the planes of Cs_4PbBr_6. The XRD patterns are based on the Mo Kα1 X-ray source.

Despite that the precipitates were collected, using the same antisolvent, OA, OLA and MeIm were not successfully removed, which makes the solid samples sticky, therefore not all the samples were managed to be characterised by XRD. **Figure 5.19** shows the XRD patterns of the samples from acetone and ethanol experiments. The acetone precipitation method produces Cs_4PbBr_6 (**Figure 5.19a**) which is consistent with the toluene precipitation (**Figure 5.1e**). Meanwhile, ethanol precipitation produces mainly CsBr and non-luminescent $CsPbBr_3$ crystals. The non-luminescent $CsPbBr_3$ is interpreted to be monoclinic (ICOD Code: 00-054-0751) and has its parameter a = 9.84 Å, b= 4.13 Å, c= 6.87 Å, β = 122.61 °.

Images under visible light and UV light (365 nm) of these samples were collected, as displayed in **Figure 5.20**. The samples from isopropanol, methanol and acetone treatments

are all optically yellow. The photoluminescence property of those indicates that they all contain cubic $CsPbBr_3$. However, the sample from ethanol treatment which contains CsBr and non-luminescent monoclinic $CsPbBr_3$ crystals are optically white and shows no photoluminescence under UV light (365 nm). Taking the SEM images (**Figure 5.18b, c** and **d**) into consideration, as the polarity of the antisolvent gets higher, the size of the $CsPbBr_3$ containing Cs_4PbBr_6 crystals increases. Ethanol helps produce individual CsBr and non-luminescent $CsPbBr_3$, not Cs_4PbBr_6 which is the formula combination of CsBr and $CsPbBr_3$.
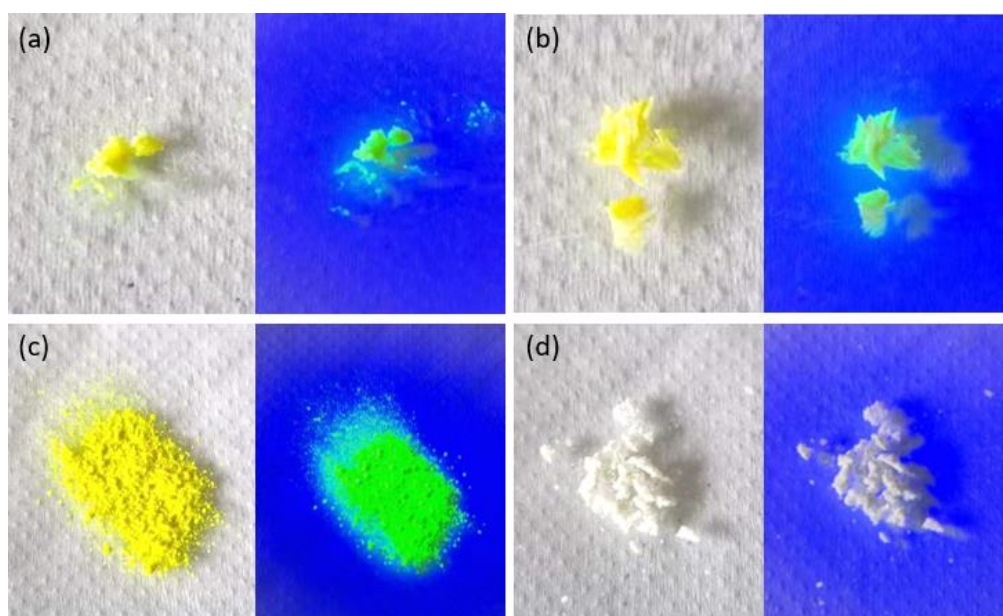
Figure 5.20 Images of the samples from the antisolvent (a) isopropanol, (b) methanol, (c) acetone and (d) ethanol under visible light (left) and UV light (365 nm, right).

To summarise, the polarity of the antisolvents used to induce the precipitation have significant effects on the composition and morphology of the synthesised samples. Immediate precipitation of white solids is induced when the DMF/DMSO solution is mixed with toluene. Precipitation takes place about 5 minutes later when mixing the solution with methanol and acetone. Precipitation takes place about 10 minutes later when mixing the solution with ethanol. For the samples from toluene and isopropanol, the size of the $CsPbBr_3$ containing Cs_4PbBr_6 is at the sub-micron scale and several μm scale. In comparison, the crystals from methanol and acetone are over 10 μm. Therefore, we conclude that the lower the polarity index of the antisolvent, the faster the precipitation happens and the smaller the size of the crystals. Surprisingly, the least polar solvent hexane induces no crystallisation as it fails to

form a homogeneous mixture with DMF/DMSO solution to contact with the solutes in the solution. Furthermore, the most polar candidate ethanol triggers the formation of CsBr and CsPbBr$_3$, not Cs$_4$PbBr$_6$. We may deduce that antisolvents with high polarity favour CsPbBr$_3$.

### 5.3.5 Transformation from Cs$_4$PbBr$_6$ to CsPb$_2$Br$_5$ and CsPbBr$_3$

The insertion and removal of Cs$^+$, Pb^{2+} cations and Br$^-$ ions can be applied to generate the transformation between Cs$_4$PbBr$_6$ and CsPbBr$_3$.[13,33] The transformation experiments of Cs$_4$PbBr$_6$ to CsPbBr$_3$ were performed using the most polar solvent water, in which CsBr is highly soluble. The solubility of CsBr in water is 1232 g/L (25 °C). In contrast, the solubility of NaCl in water is 359.6 g/L (25 °C) and that of PbBr$_2$ is 9.75 g/L (25 °C).[34]

The sample from Cs$^+$ to Pb^{2+} ratio at 4.5 : 1 contains mainly Cs$_4$PbBr$_6$ and CsBr was used for water treatment to trigger the transformation (**Figure 5.1a**). With water treatment, the combination of Cs$_4$PbBr$_6$ and CsBr transformed to CsBr, CsPb$_2$Br$_5$, CsPbBr$_3$ and PbBr$_2$. The XRD pattern is shown in **Figure 5.21(a)**. From the aspect of optical colour change, the white sample (**Figure 5.3a**) changed to yellow quickly, indicating the immediate phase transformation in the polar solvent water.

The sample contains distinct CsPbBr$_3$ and Cs$_4$PbBr$_6$ was synthesised with Cs$^+$ to Pb^{2+} ratio at 2 : 1, 0 mL OA and 0 mL OLA. The absence of OA and OLA produces no restriction to Cs$^+$ and Pb^{2+} cations, and an intermediate cation ratio leads to the synthesis of both CsPbBr$_3$ and Cs$_4$PbBr$_6$. The XRD pattern is shown in **Figure 5.21(b)**. With water treatment, the two phases transformed to CsBr. Furthermore, from the aspect of optical colour change, the yellow sample was quickly dissolved into water, forming the colourless solution. After dring in the oven, white precipitates mixed with a small portion of yellow solids were obtained. The total dissolution in water might indicate the quick transformation to water-soluble CsBr and PbBr$_2$. While as water evaporated, a small amount of CsBr underwent precipitation with PbBr$_2$ to form Cs$_4$PbBr$_6$, CsPbBr$_3$ and CsPb$_2$Br$_5$. The XRD pattern of the sample after water treatment is shown in **Figure 5.21(c)**.

CsPb$_2$Br$_5$ crystallises in the tetragonal crystal system with its unit cell parameter a = 8.48 Å and c = 15.25 Å (ICSD Code: 254290) and appears to be light yellow.[11] PbBr$_2$ crystallises in

the orthorhombic crystal system with its unit cell parameter a = 4.72 Å, b = 8.04 Å and c = 9.50 Å (ICSD Code: 36170), and appears to be white powder.
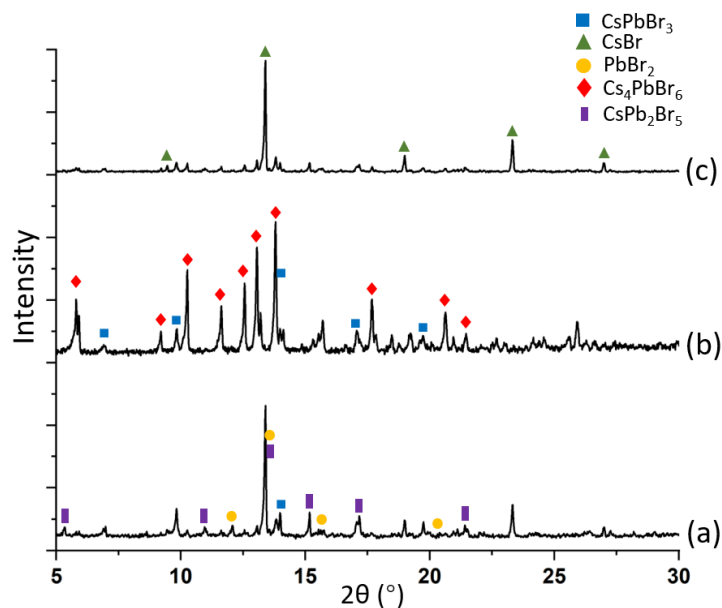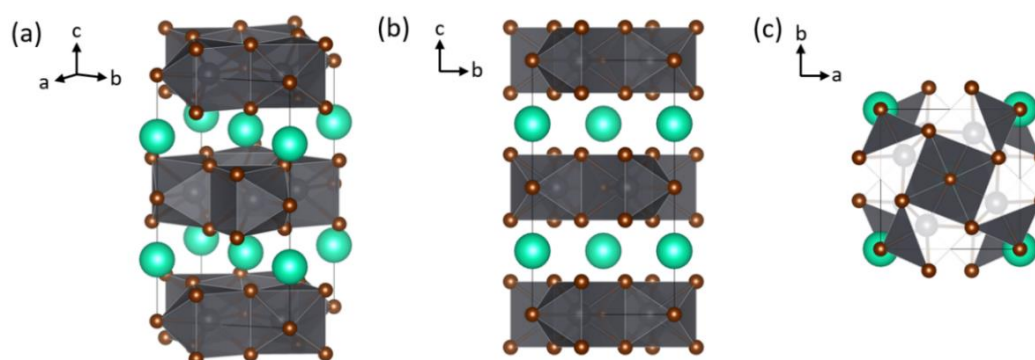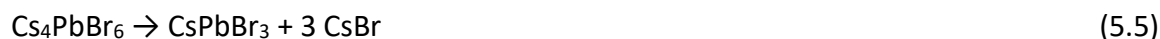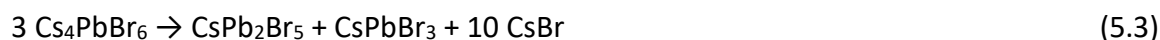

Figure 5.21 XRD patterns of (a) the sample collected after the water treatment of the sample from the synthesis of 4.5 : 1 cation ratio, (b) the sample from the synthesis of 2 : 1 cation ratio, 0 mL OA and 0 mL OLA, (c) the sample after water treatment. The XRD patterns are based on the Mo Kα1 X-ray source.
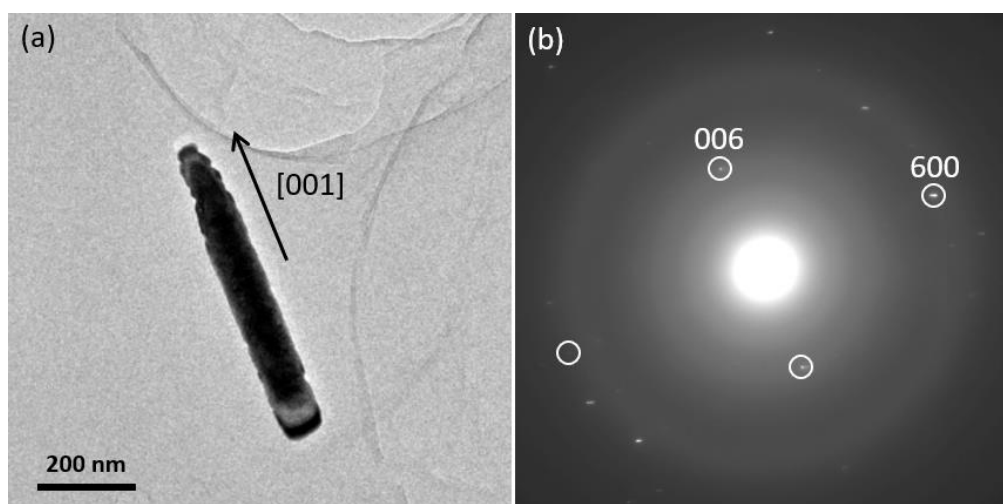
Figure 5.22 (s) Low magnification of a $CsPb_2Br_5$ rod with crystallographic direction marked. (b) Corresponding SAED pattern of the rod with principal diffraction spots interpreted.

The intermediate phase $CsPb_2Br_5$ obtained from the decomposition of Cs_4PbBr_6 in DI water was captured by low magnification TEM and SAED, as demonstrated in **Figure 5.22**. The d-spacing of the assigned plane (006) is 2.53 Å and that of (600) is 1.41 Å.

Based on the phase transformation from Cs_4PbBr_6 to $CsPb_2Br_5$, $CsPbBr_3$ and $CsBr$, the reactions throughout the whole decomposition process are inferred as below,

$$3\ Cs_4PbBr_6 \rightarrow CsPb_2Br_5 + CsPbBr_3 + 10\ CsBr \tag{5.3}$$

$$2\ Cs_4PbBr_6 \rightarrow CsPb_2Br_5 + 7\ CsBr \tag{5.4}$$

$$Cs_4PbBr_6 \rightarrow CsPbBr_3 + 3\ CsBr \tag{5.5}$$

$$Cs_2PbBr_5 \rightarrow CsPbBr_3 + PbBr_2 \tag{5.6}$$

$$Cs_4PbBr_6 \longrightarrow 4\ CsBr + PbBr_2 \tag{5.7}$$

$$CsPbBr_3 \longrightarrow CsBr + PbBr_2 \tag{5.8}$$

Figure 5.23 Schematic representations of $CsPb_2Br_5$ crystal structure (a) in the 3-dimensional view, (b) viewed from the a axis, (c) viewed from the c axis.

The driving force of the transformations of these versatile structures is deduced to be the high water solubility of CsBr and the Cs-stripping behaviour by water.[16,33] From the crystal structure perspective, due to the high solubility of Cs^+ cations and Br^- ions in water, Cs_4PbBr_6 become Cs and Br lacking. To produce $CsPb_2Br_5$, Pb^{2+} cations in $[PbBr_6]^{4-}$ polyhedra change the coordination number to form face-sharing $[PbBr_8]^-$ polyhedral. **Figure 5.23** illustrates the crystal structure of $CsPb_2Br_5$. While to produce $CsPbBr_3$, $[PbBr_6]^{4-}$ polyhedra simply rotate and align with Cs^+ cations, creating a cubic structure. Continuous Cs and Br stripping by water then further decomposes the $[PbBr_8]^-$ polyhedra in $CsPb_2Br_5$ crystals and $[PbBr_6]^{4-}$ polyhedra in $CsPbBr_3$ crystals to individual soluble Cs^+, Pb^{2+} and Br^- ions.

5.4 Conclusion

To summarise, the monodisperse rhombohedral Cs_4PbBr_6 crystals with embedded $CsPbBr_3$ nanocrystallites are synthesised by applying DMF/DMSO as the initial solvent, OA and OLA as ligands to control the releasing of cations, toluene as the antisolvent to induce the precipitation. With the observed evidence of embedded $CsPbBr_3$ nanocrystallites and the d-spacing approximation of the two phases, the structural scale embedding phenomenon is proposed. The c axis of Cs_4PbBr_6 aligns with the [111] direction of $CsPbBr_3$ and the connection of the two phases is achieved by the bonding of Cs+ cations and $[PbBr_6]^{4-}$ polyhedra.

The absence of individual $CsPbBr_3$ crystals outside the Cs_4PbBr_6 host and the fixed size of the crystallite exclude the possibility of growing $CsPbBr_3$ individually during the precipitation. Quantitative EDX results, proposed polymerised Cs_xPbBr_y formula and amorphous covering on rhombohedral Cs_4PbBr_6 crystals indicate that both Cs_4PbBr_6 and $CsPbBr_3$ are formed after the immediate precipitation of the amorphous Cs_xPbBr_y phase. Localised $CsPbBr_3$ nanocrystallites are produced due to the consumption of Cs during the crystallisation of Cs-rich Cs_4PbBr_6.

The effect of various antisolvents with different polarity has been examined on crystallography and morphology aspects. The higher the polarity of the antisolvent, the slower the precipitation is and the larger the crystal size is. While hexane fails to form a homogeneous mixture and precipitation does not proceed. Ethanol which has a high polarity, on the other hand, favours the production of $CsPbBr_3$.

With water treatment, the transformation all the way from Cs_4PbBr_6 to $CsPb_2Br_5$, $CsPbBr_3$ and eventually to CsBr and $PbBr_2$ is achieved. With CsBr stripping by water, the crystal structure becomes Cs insufficient, triggering the transformation.

However, the actual formula of the polymerised Cs_xPbBr_y may require further identification. And the behaviour of the cations during the structural transformation from Cs_4PbBr_6 to $CsPb_2Br_5$ and $CsPbBr_3$ merits discussion.

References

1   L. Protesescu, S. Yakunin, M. I. Bodnarchuk, F. Krieg, R. Caputo, C. H. Hendon, R. X. Yang, A. Walsh and M. V. Kovalenko, *Nano Lett.*, 2015, **15**, 3692–3696.

2   X. Yu, L. Wu, H. Hu, M. Chen, Y. Tan, D. Yang, Q. Pan, Q. Zhong, T. Supasai and Q. Zhang, *Langmuir*, 2018, **34**, 10363–10370.

3   Q. A. Akkerman, A. L. Abdelhady and L. Manna, *J. Phys. Chem. Lett.*, 2018, **9**, 2326–2337.

4   S. Seth and A. Samanta, *J. Phys. Chem. Lett.*, 2017, **8**, 4461–4467.

5   M. De Bastiani, I. Dursun, Y. Zhang, B. A. Alshankiti, X. H. Miao, J. Yin, E. Yengel, E. Alarousu, B. Turedi, J. M. Almutlaq, M. I. Saidaminov, S. Mitra, I. Gereige, A. AlSaggaf, Y. Zhu, Y. Han, I. S. Roqan, J.-L. Bredas, O. F. Mohammed and O. M. Bakr, *Chem. Mater.*, 2017, **29**, 7108–7113.

6   Q. A. Akkerman, S. Park, E. Radicchi, F. Nunzi, E. Mosconi, F. De Angelis, R. Brescia, P. Rastogi, M. Prato and L. Manna, *Nano Lett.*, 2017, **17**, 1924–1930.

7   J. Xu, W. Huang, P. Li, D. R. Onken, C. Dun, Y. Guo, K. B. Ucer, C. Lu, H. Wang, S. M. Geyer, R. T. Williams and D. L. Carroll, *Adv. Mater.*, 2017, **29**, 1703703.

8   L. N. Quan, R. Quintero-Bermudez, O. Voznyy, G. Walters, A. Jain, J. Z. Fan, X. Zheng, Z. Yang and E. H. Sargent, *Adv. Mater.*, 2017, **29**, 1605945.

9   X. Chen, F. Zhang, Y. Ge, L. Shi, S. Huang, J. Tang, Z. Lv, L. Zhang, B. Zou and H. Zhong, *Adv. Funct. Mater.*, 2018, **28**, 1706567.

10   Q. Xiang, B. Zhou, K. Cao, Y. Wen, Y. Li, Z. Wang, C. Jiang, B. Shan and R. Chen, *Chem. Mater.*, 2018, **30**, 8486–8494.

11   K. H. Wang, L. Wu, L. Li, H. B. Yao, H. S. Qian and S. H. Yu, *Angew. Chemie. Int. Ed.*, 2016, **55**, 8328–8332.

12   C. Rossi, R. Scarfiello, R. Brescia, L. Goldoni, G. Caputo, L. Carbone, D. Colombara, L. De Trizio, L. Manna and D. Baranov, *Chem. Mater.*, 2022, **34**, 405–413.

13   Y. Li, H. Huang, Y. Xiong, S. V. Kershaw and A. L. Rogach, *CrystEngComm*, 2018, **20**, 4900–4904.

14   C. Y. Huang, S. H. Huang, C. L. Wu, Z. H. Wang and C. C. Yang, *ACS Appl. Nano Mater.*, 2020, **3**, 11760–11768.

15   G. Hu, W. Qin, M. Liu, X. Ren, X. Wu, L. Yang and S. Yin, *J. Mater. Chem. C*, 2019, **7**, 4733–4739.

16   L. Wu, H. Hu, Y. Xu, S. Jiang, M. Chen, Q. Zhong, D. Yang, Q. Liu, Y. Zhao, B. Sun, Q. Zhang and Y. Yin, *Nano Lett.*, 2017, **17**, 5799–5804.

17   T. Xuan, S. Lou, J. Huang, L. Cao, X. Yang, H. Li and J. Wang, *Nanoscale*, 2018, **10**, 9840–9844.

18   X. Li, Y. Wu, S. Zhang, B. Cai, Y. Gu, J. Song and H. Zeng, *Adv. Funct. Mater.*, 2016, **26**, 2435–2445.

19   L. Xu, J. Li, T. Fang, Y. Zhao, S. Yuan, Y. Dong and J. Song, *Nanoscale Adv.*, 2019, **1**, 980–988.

20   M. Aebli, B. M. Benin, K. M. McCall, V. Morad, D. Thöny, H. Grützmacher and M. V Kovalenko, *Helv. Chim. Acta*, 2020, **103**, e2000080.

21   Z. Bao, Y. J. Tseng, W. You, W. Zheng, X. Chen, S. Mahlik, A. Lazarowska, T. Lesniewski, M. Grinberg, C. Ma, W. Sun, W. Zhou, R.-S. Liu and J. P. Attfield, *J. Phys. Chem. Lett.*, 2020, **11**, 7637–7642.

22   Y. M. Chen, Y. Zhou, Q. Zhao, J. Y. Zhang, J. P. Ma, T. T. Xuan, S. Q. Guo, Z. J. Yong, J. Wang, Y. Kuroiwa, C. Moriyoshi and H. T. Sun, *ACS Appl. Mater. Interfaces*, 2018, **10**, 15905–15912.

23   Q. Jing, Y. Xu, Y. Su, X. Xing and Z. Lu, *Nanoscale*, 2019, **11**, 1784–1789.

24   P. Raiteri and J. D. Gale, *J. Am. Chem. Soc.*, 2010, **132**, 17623–17634.

25   J. Cavanaugh, M. L. Whittaker and D. Joester, *Chem. Sci.*, 2019, **10**, 5039–5043.

26   J. D. Rodriguez-Blanco, S. Shaw and L. G. Benning, *Nanoscale*, 2011, **3**, 265–271.

27   J. Yang, J. Koo, S. Kim, S. Jeon, B. K. Choi, S. Kwon, J. Kim, B. H. Kim, W. C. Lee, W. B. Lee, H. Lee, T. Hyeon, P. Ercius and J. Park, *J. Am. Chem. Soc.*, 2019, **141**, 763–768.

28   R. Demichelis, P. Raiteri, J. D. Gale, D. Quigley and D. Gebauer, *Nat. Commun.*, 2011, **2**, 590.

29   Z. Liu, C. Shao, B. Jin, Z. Zhang, Y. Zhao, X. Xu and R. Tang, *Nature*, 2019, **574**, 394–398.

30   S. Mostafa Nowee, A. Abbas and J. A. Romagnoli, *Chem. Eng. Sci.*, 2008, **63**, 5457–5467.

31   M. Shahid, G. Sanxaridou, S. Ottoboni, L. Lue and C. Price, *Org. Process Res. Dev.*, 2021, **25**, 969–981.

32   L. R. Snyder, J. J. Kirkland and J. L. Glajch, *Practical HPLC Method Development*, John Wiley & Sons, Ltd, 2nd edn., 1997.

33   L. Rao, X. Ding, X. Du, G. Liang, Y. Tang, K. Tang and J. Z. Zhang, *Beilstein J. Nanotechnol.*, 2019, **10**, 666–676.

34   B. Z. Krumgalz, *Mineral Solubility in Water at Various Temperatures*, Israel Oceanographic and Limnological Research Ltd., Haifa, 1994.

Chapter 6 Degradation of Layered $Ti_3C_2T_x$ Structures to $Ti_3C_2T_x$ Nanowire Clusters

6.1 Introduction

The novel 2D layered material, MXene, is the family of early metal carbides or carbonitrides rising in the area of energy storage, supercapacitor and batteries since 2011. The formula can be expressed as $M_{n+1}AX_n$, where M is an early transition metal, A is an element from triels or tetrels (Al for this project), X is C and/or N and n = 1,2 or 3.[1,2]

In the layered Ti_3AlC_2 structure, Ti-Al bonds are relatively weaker than Ti-C bonds, making Al element easy to be exfoliated.[3] $Ti_3C_2T_x$ and Ti_3C_2 materials with distinct layers can be produced via the exfoliation of Al layers. In $Ti_3C_2T_x$, T stands for termination groups (-F, -O, -OH) and x is typically 2 or 1. Such exfoliation process can be achieved in a H^+ and F^- environment, so the termination groups of $Ti_3C_2T_x$ are mostly -F and -OH. Ti_3C_2 is also in MXene family but with no termination groups, therefore x = 0.

Because of the layered structure, the hydrophilic surface terminations and outstanding conductivity, $Ti_3C_2T_x$ MXene shows superior potential in energy storage.[4–6] Using alkalisation and/or oxidant treatment, $Ti_3C_2T_x$ layered structure can be transformed into clustered nanoribbons, which shows high performance in sodium and potassium ion batteries.[7,8] Lian *et al.* reported the fabrication of Ti_3C_2 nanowire composed frameworks by applying alkaline treatment on $Ti_3C_2T_x$ MXene and tested the application of Ti_3C_2 as negative electrode material. They claimed that such morphology with nanowires and porous network enabled swift electron transfer and ion diffusion.[8]

The nanowire cluster morphology also exhibits excellent catalysis activity for hydrogen storage and hydrogen production reaction. Such high catalysis performance derives from the high specific surface area and the abundant exposed active sites.[9,10]

Despite that the nanowire clustered structure of $Ti_3C_2T_x$ behaves superbly in battery and catalyst fields, the intrinsic mechanism of its formation is rarely discussed. Revealing the formation mechanism in crystallographic scale and experimentally may help to gain a better understanding towards the structure and offer the possibility of morphology design for further application.

In this present project, the nanowire clusters of Ti_3C_2O and Ti_3C_2 are prepared by applying KOH solution treatment to $Ti_3C_2(OH)_2$ layered structure. SEM observation of the morphological evolution over time reveals the dimensional degradation from layers to nanowires. The degradation is triggered by the continuous oxidation during solution stirring. Subsequently, the oxidation reactions of $Ti_3C_2(OH)_2$ to produce Ti_3C_2O, Ti_3C_2 and other by-products are proposed. The schematic illustration of the oxidation at crystal structure scale is drawn. The present work may provide new perspective towards the crystal structural engineering of $Ti_3C_2T_x$ MXene and the top-down degradation crystal growth route.

6.2 Experimental Methods

The synthesis experiments were performed by Jin Zhang at Beijing Normal University. The XRD patterns and some SEM images were collected by Jin Zhang at Beijing Normal University.

Chemicals:

Ti_3AlC_2 (Jilin Yiyi Tech.), HCl (37%, Beijing Chemical), LiF (Beijing Chemical), KOH (Tianjin Dalu Chemical), H_2O_2 (30%, Beijing Chemical), deionised water (DI water).

All chemicals unless specified, are analytical reagents. All chemicals were used without further purification.

Preparation of Layered $Ti_3C_2T_x$ by HCl/LiF method:

60 mL 9 mol/L HCl solution was kept stirring while 3 g LiF was slowly added. The mother solution was kept stirring for 30 min until the total dissolution of LiF. 3g Ti_3AlC_2 solid was then added into the solution. The final solution was kept in an oil bath at 35 °C for 24 h. After 24 h reaction, the precipitates were centrifuged and washed with DI water until the pH value of the filtered liquid was between 6.0 and 7.0. Finally, the precipitates were transferred into 100 mL DI water and sonicated in Ar atmosphere for 2 h and centrifuged for 30 min. The top layer is the $Ti_3C_2T_x$ colloidal solution.

Preparation of $Ti_3C_2T_x$ Nanowire Clusters:

Into the 40 mL stirring $Ti_3C_2T_x$ colloidal solution, KOH was continuously added to set the KOH concentration at 2 mol/L. The solution was then kept stirring for 72 h at room

temperature. Reaction time was set at 36, 48 and 60 h to obtain samples from earlier stages. DI water was then used to wash the obtained precipitates until the pH value of the filtered liquid was about 7.0. The precipitates were then dehydrated at a freeze drying condition.

6.3 Results and Discussion

6.3.1 Morphology Evolution, Crystallography and Elemental Composition

To begin with, the raw material Ti_3AlC_2 before the LiF/HCl treatment and produced $Ti_3C_2T_x$ after the LiF/HCl treatment were studied by XRD, as shown in **Figure 6.1**. The major phase of the two materials is hexagonal Ti_3AlC_2 (ICOD Code: 00-052-0875) with a = 3.069 Å and c = 18.50 Å. Subcomponents, rutile TiO_2 and Al_2O_3, are present in Ti_3AlC_2 starting material but absent in $Ti_3C_2T_x$ sample, which may be attributed to the washing process after the preparation. Rutile TiO_2 (ICOD Code: 01-076-0318) crystallises in tetragonal system with a = 4.60 Å and c = 2.97 Å. Al_2O_3 (ICOD Code: 00-011-0661) crystallises in rhombohedral system with a = 4.76 Å and c = 12.99 Å. Ti_3AlC_2 appears to be dense and preserves an almost polyhedral morphology.[11]
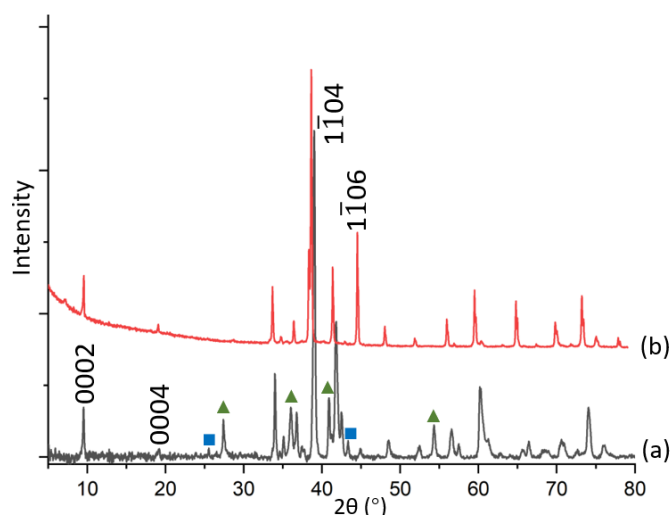
Figure 6.1 XRD patten of (a) Ti_3AlC_2 before LiF/HCl treatment and (b) as-prepared $Ti_3C_2T_x$ after LiF/HCl treatment. The indices in black refer to the characteristic planes of MXene structure. The peaks marked with green triangles refer to the planes of rutile TiO_2 and those marked with blue cubes refer to the planes of Al_2O_3. The XRD patterns were collected using Cu Kα1 X-ray source.

The comparison of the two patterns before and after LiF/HCl treatment demonstrates the slight shift to the left, indicating the expansion of crystal structure from Ti_3AlC_2 to $Ti_3C_2T_x$.
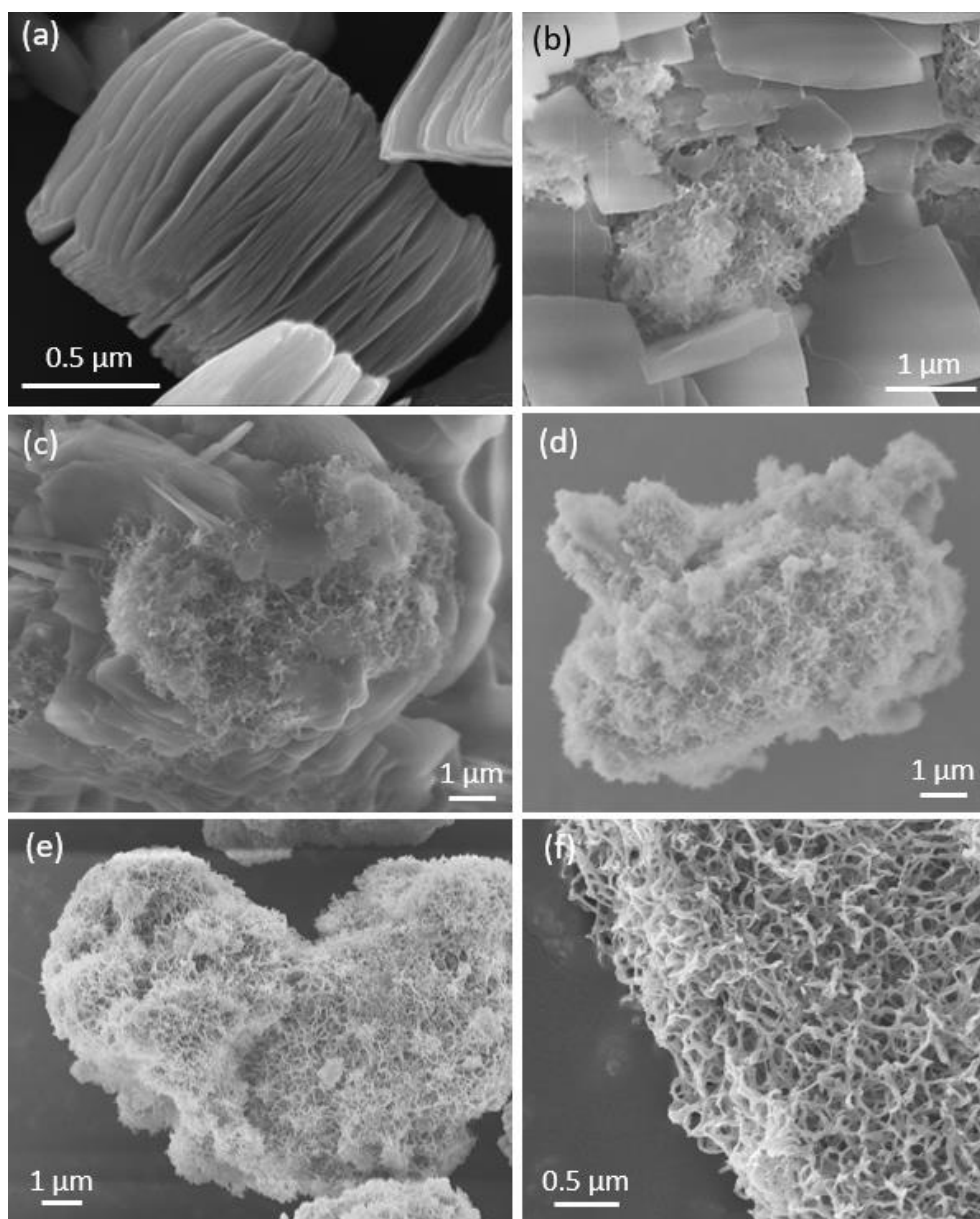

Figure 6.2 SEM images of $Ti_3C_2T_x$ at different alkalisation time. Alkalised-$Ti_3C_2T_x$ at the reaction time of (a) 36 h, (c) 48 h and (d) 60 h. (e) Final morphology of clustered nanowires at 72 h. (f) A close-up towards nanowires of the final morphology.

With LiF/HCl treatment, the Al layers at atomic scale were exfoliated and replaced by termination groups F^- and OH^-, forming $Ti_3C_2T_x$.[1] The produced $Ti_3C_2T_x$ show a layered structure, as shown in **Figure 6.2(a)**. Subsequently, the layered $Ti_3C_2T_x$ was applied to produce nanowire clusters. The sample series obtained from different reaction times were firstly

studied on their morphologies, as shown in **Figure 6.2(b)** to **(f)**. Primary $Ti_3C_2T_x$ MXene before alkalisation appears to be layers with clear gaps in between (**Figure 6.2a**). After the reaction in KOH solution with continuous stirring, layers, thick strips and wires co-existing in early stage (**Figure 6.2b**, **c** and **d**). As the alkalisation time in KOH solution extends, wires begin to dominate the morphology. Eventually, nanowire interconnected clusters are produced (**Figure 6.2e** and **f**).

From the aspect of dimension, the initial structure of $Ti_3C_2T_x$ is a layered structure, which is the typical morphology of $Ti_3C_2T_x$ MXene.[1] As the reaction proceeds, degradation from the initial 3D structure occurs. The layers individually change to 2D flakes and to strips in the middle stage. While the flakes and strips are still holding together based on the initial framework. Then the flakes and strips convert to 1D wires. The 1D wires are interconnected which is also based on the initial framework. Morphologically, the dimensional degradation of $Ti_3C_2T_x$ proceeds in the alkali environment.
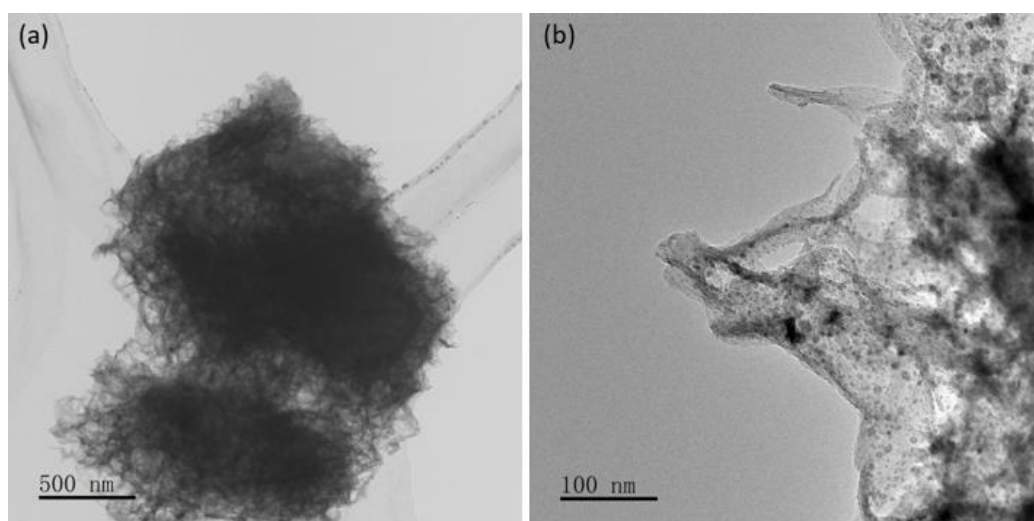
Figure 6.3 (a) Low magnification TEM image of an alkalised-$Ti_3C_2T_x$ nanowire composed cluster. (b) A close-up towards the nanowires of the alkalised-$Ti_3C_2T_x$ cluster.

Low-magnification TEM images (**Figure 6.3**) show a loose nanowire cluster of alkalised-$Ti_3C_2T_x$. Alkalised-$Ti_3C_2T_x$ indicates the nanowire phase produced from the reaction in KOH solution at this stage. From **Figure 6.3(a)**, the dark contrast of the centre of the cluster indicates that the core might be solid. To prepare $Ti_3C_2T_x$ from dense structured Ti_3AlC_2[11], the LiF/HCl method gives a lower yield of $Ti_3C_2T_x$ layered structure in comparison with the HF

method, which means the exfoliation of Al is slow and not complete and Ti_3AlC_2 still exists in the structure.[12,13] Furthermore, the thick layers of the layered $Ti_3C_2T_x$ structure actually interconnect with each other by the unexfoliated Ti_3AlC_2 otherwise the layers would be individually separated. Therefore, we deduce that alkalised-$Ti_3C_2T_x$ structure also preserves a dense Ti_3AlC_2 core.

From the preparation process, Ti_3AlC_2 serves as the core to hold the layered structure of $Ti_3C_2T_x$ MXene and after the KOH treatment, serves as the core where the roots of the nanowires sticks on, so that the nanowires will not fall into the solution and become individual nanowires, but are all interconnected, forming loose clusters.
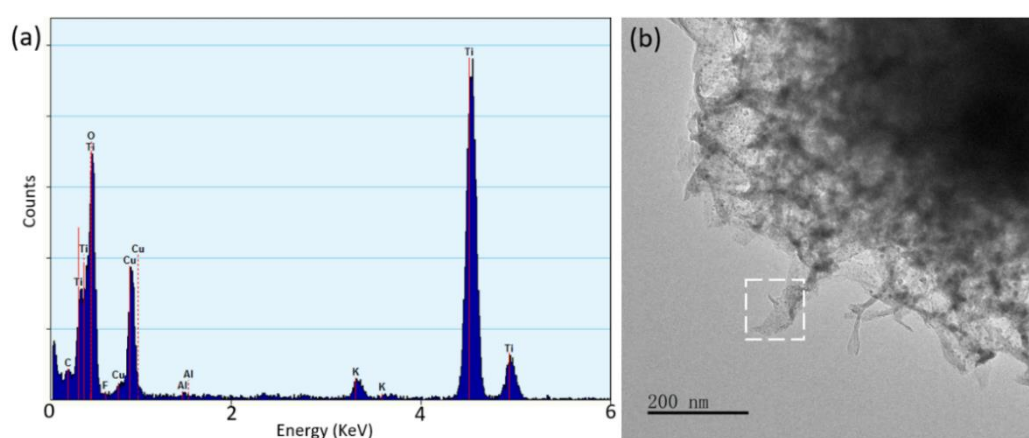
Figure 6.4 (a) EDX spectrum of a nanowire. (b) TEM image of an alkalised-$Ti_3C_2T_x$ crystal, squared nanowire is selected for EDX data collection.

With the mild LiF/HCl exfoliation of Al layer, the two $Ti_3C_2T_x$ MXenes produced are $Ti_3C_2F_2$ and $Ti_3C_2(OH)_2$. **Figure 6.4** shows the EDX spectrum of the selected nanowire area. The existence of Ti, C, O and F elements are deduced to be from the two typical MXenes, $Ti_3C_2F_2$ and $Ti_3C_2(OH)_2$. K exists in the nanowire area, indicating the intercalation of K^+ ions during the reaction in alkali solution.[8,14]

For the termination groups in $Ti_3C_2T_x$, the LiF-HCl method produces $Ti_3C_2T_x$ with less F terminations but more OH terminations than the strong HF method.[15–17] Therefore, before KOH treatment, the percentage of $Ti_3C_2(OH)_2$ exceeds that of $Ti_3C_2F_2$. And after KOH treatment, -F terminations are further substituted by -OH terminations, making the signals from the element F even less. Cu is from the TEM grid on which the samples are deposited.

6.3.2 Phase Transformation of $Ti_3C_2T_x$

The phases involved in this project, their crystallographic parameters and the characteristic (0002) d-spacings are listed in **Table 6.1**.[1,18] The phase Ti_3C_2O is simulated using the software *Diamond*. Those crystallographic data is used to visualise the crystal structure and interpret the phases from HRTEM results. Crystal structures of Ti_3AlC_2, $Ti_3C_2(OH)_2$, Ti_3C_2O and Ti_3C_2 are all demonstrated in **Figure 6.5**.

Table 6.1 Crystallographic parameters of the some $Ti_3C_2T_x$ phases.

| Phase		Crystal System	a (Å)	c (Å)	(0002) d-spacing (Å)
Ti_3C_2			3.05	15.01	7.51
Ti_3AlC_2			3.07	18.50	9.25
$Ti_3C_2T_x$	$Ti_3C_2(OH)_2$	Hexagonal	3.02	19.49	9.75
	$Ti_3C_2F_2$		3.06	21.54	10.77
$Ti_3C_2T_2$-KOH			3.05	~25	~12.5
Ti_3C_2O			3.02	18.52	9.26
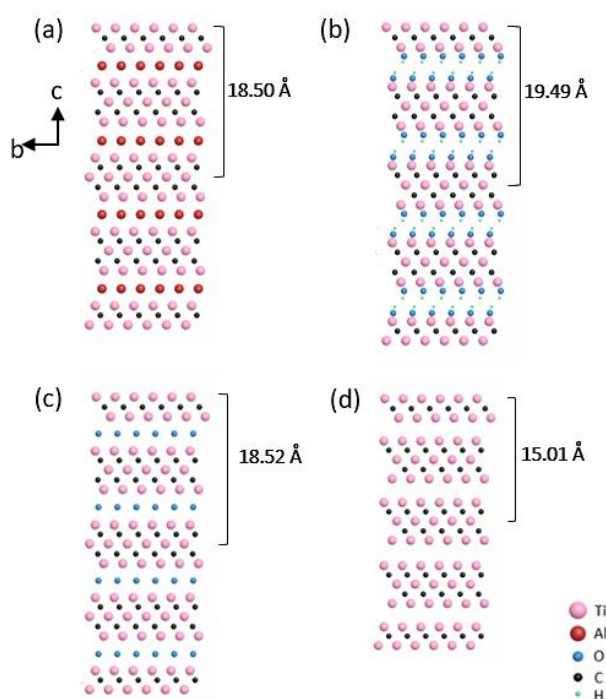
Figure 6.5 Crystal structures of (a) Ti_3AlC_2, (b) $Ti_3C_2(OH)_2$, (c) Ti_3C_2O and (d) Ti_3C_2 from a direction with the c parameters marked.

HRTEM images of the $Ti_3C_2T_x$ before and after the reaction in KOH solution were recorded to check the d-spacings and thus identify the phases. **Figure 6.5** displays the HRTEM image of $Ti_3C_2T_x$ layered structure before KOH treatment. The two d-spacings were measured at 10.11 Å and 10.21 Å, respectively. The values could be assigned to the (0002) plane of $Ti_3C_2(OH)_2$ with a d-spacing at 9.75 Å (**Table 6.1**). And as aforementioned, LiF-HCl method produces $Ti_3C_2T_x$ with less F terminations but more OH terminations.[19] Therefore, we conclude that the main $Ti_3C_2T_x$ before KOH treatment is $Ti_3C_2(OH)_2$.
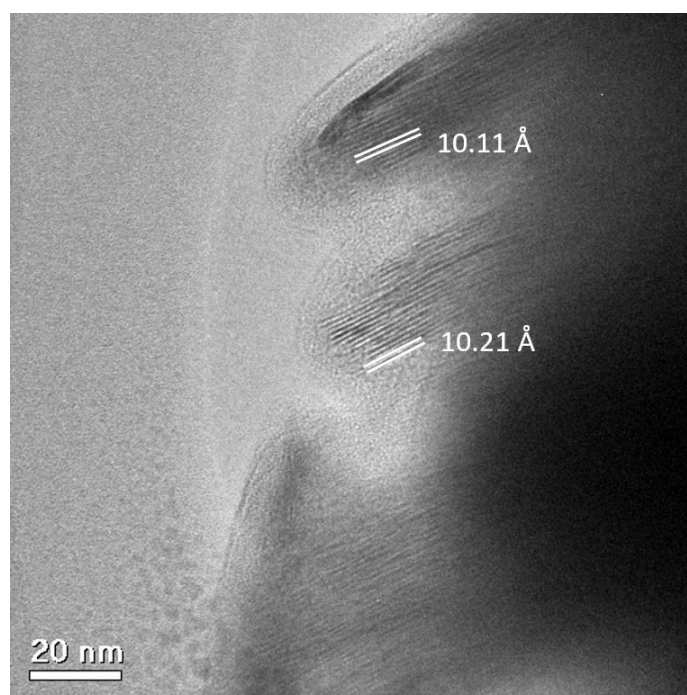
Figure 6.6 HRTEM image of $Ti_3C_2T_x$ layered structure before KOH treatment with two d-spacings measured and marked.

HRTEM was also applied to study the nanowire obtained after KOH treatment. For the most easily observed (0002) plane, there are two sets of d-spacing values, as shown in **Figure 6.7**. For the characteristic (0002) planes of the whole $Ti_3C_2T_x$ MXene family, the d-spacings are listed in **Table 6.1**. With the given (0002) d-spacing values, we conclude that the d-spacing measured at about 7.60 Å in **Figure 6.7(a)** can be indexed to (0002) plane of the phase Ti_3C_2. The d-spacing measured at about 9.09 Å in **Figure 6.7(b)** is close to (0002) planes of both Ti_3AlC_2 and Ti_3C_2O. While from the EDX spectrum (**Figure 6.4a**), Al is not one of main element composing alkalised-$Ti_3C_2T_x$ nanowires, but derives from the unreacted Ti_3AlC_2 core. Therefore, we deduce the d-spacing at about 9.09 Å belongs to the (0002) plane of Ti_3C_2O.
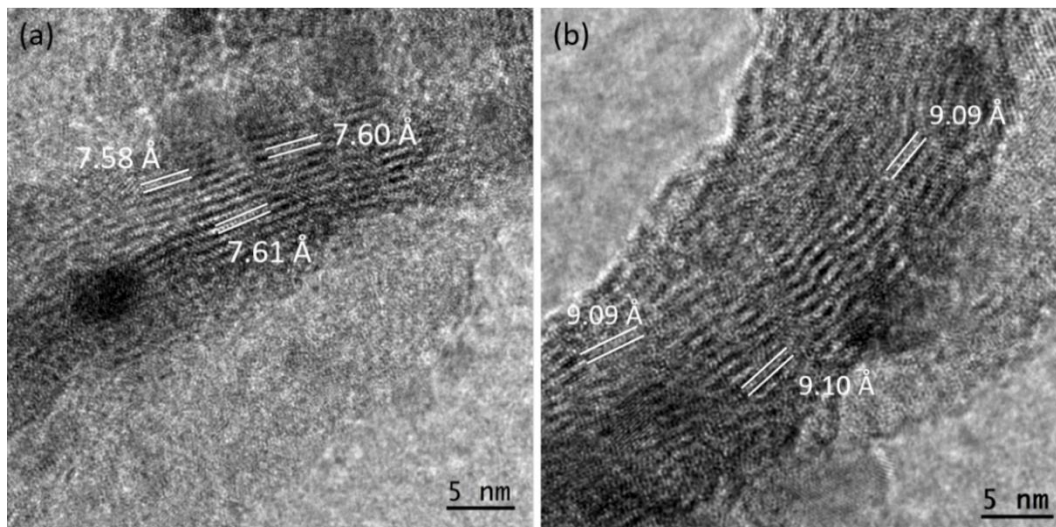
Figure 6.7 (a) HRTEM of a nanowire with the d-spacing at about 7.60 Å. (b) HRTEM of a nanowire with the d-spacing at about 9.09 Å.

Ti_3C_2O is rarely discussed in comparison to other $Ti_3C_2T_x$ MXene family members. This $Ti_3C_2T_x$ phase can be obtained from the dehydration of $Ti_3C_2(OH)_2$,[20,21]

$$Ti_3C_2(OH)_2 \rightarrow Ti_3C_2O + H_2O \tag{6.1}$$

Based on the Ti-O bond length (1.95 Å) and the similar layered crystal structure of $Ti_3C_2(OH)_2$, we simulate and visualise the crystal structure of Ti_3C_2O and measure its c parameter at 18.52 Å, as shown in **Figure 6.5(c)**.
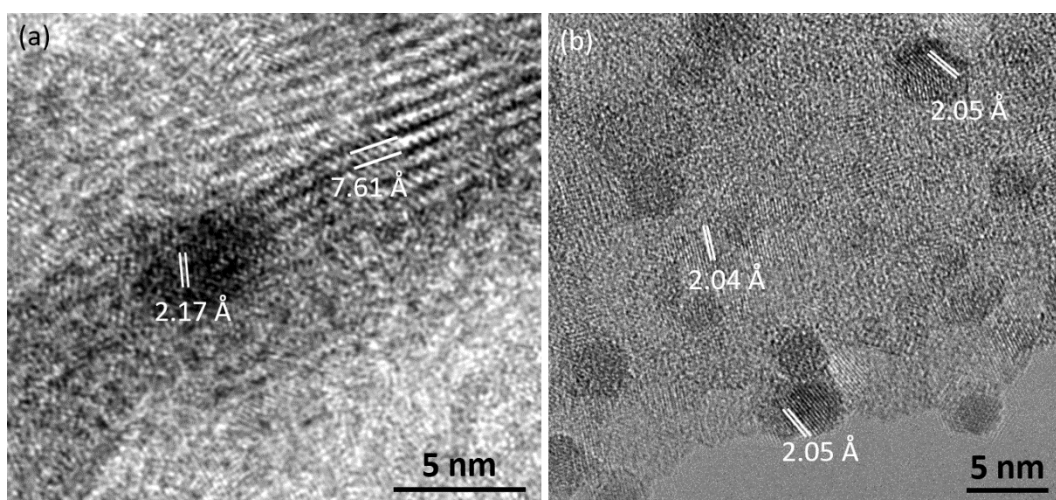

Figure 6.8 (a, b) HRTEM images of TiO_2 alongside nanowires with d-spacings indexed. The d-spacing measured at 7.61 Å in (a) belongs to Ti_3C_2 nanowire.

From the low-magnification TEM (**Figure 6.3b**), there are nanodots co-existing with alkalised-$Ti_3C_2T_x$ nanowires. TiO_2 can be one of the by-products in $Ti_3C_2T_x$ alkalisation.[22] Hydrothermal method and annealing can also produce TiO_2 using $Ti_3C_2T_x$ MXene, which is believed to be from the oxidation of $Ti_3C_2T_x$.[23,24] Rutile TiO_2 (ICOD Code: 01-076-0318) crystallises in tetragonal system with a = 4.59 Å and c = 2.96 Å. HRTEM of TiO_2 nanoparticles alongside the nanowires are captured, as shown in **Figure 6.8**. **Figure 6.8(a)**, which is the magnified image of **Figure 6.7(a)**, demonstrates a nanoparticle on the nanowire of Ti_3C_2. The large d-spacing at 7.61 Å is assigned to the (0002) plane of Ti_3C_2. The d-spacing measured at 2.17 Å can be indexed to the (111) plane of rutile TiO_2. Further in **Figure 6.8(b)**, the d-spacings measured at 2.04 and 2.05 Å can be assigned to the (210) plane of rutile TiO_2. Based on the HRTEM investigation of alkalised-$Ti_3C_2T_x$, we concluded that throughout the alkalisation treatment, the $Ti_3C_2(OH)_2$ layers proceed with oxidation and phase transformation, generating Ti_3C_2O and Ti_3C_2 nanowires, and simultaneously producing the by-product TiO_2.

K^+ cations could intercalate the crystal layers to form so-called $Ti_3C_2T_x$-KOH, which has its (0002) d-spacing at about 12.5 Å and c parameter at about 25 Å. HRTEM shows that the d-spacings of (0002) face is below 10 Å, not comparable to that of $Ti_3C_2T_x$-KOH from previous studies which is about 12.5 Å. Therefore, we deduce that the grown nanowires are not $Ti_3C_2T_x$-KOH phase, although it may intercalate $Ti_3C_2T_x$ to trigger the phase transformation. Meanwhile, the reaction time (5 h, 12 h, 24 h) of $Ti_3C_2T_x$ in KOH in previous works is less than that of our project (72 h).[3,14,18,25] Thus, we believe that in the early time of reaction, K^+ cations firstly intercalate into the layers of $Ti_3C_2T_x$, expanding the spacing between the layers allowing O_2 readily going into the structure to trigger oxidation and morphology degradation. As the reaction goes, layers are peeled off and cut into strips and even wires, K^+ cations fall off the structure and go back into the solution again, which explains that there are no d-spacings of $Ti_3C_2T_x$-KOH captured.

6.3.3 Oxidation of $Ti_3C_2T_x$

To reveal how the phase transformation from $Ti_3C_2(OH)_2$ to Ti_3C_2O and Ti_3C_2 occurs, the oxidation state change of Ti in nanowire area are analysed based on EELS spectrum. The EELS spectrum was recorded in selected area using Titan Themis in STEM mode (**Figure 6.9**).
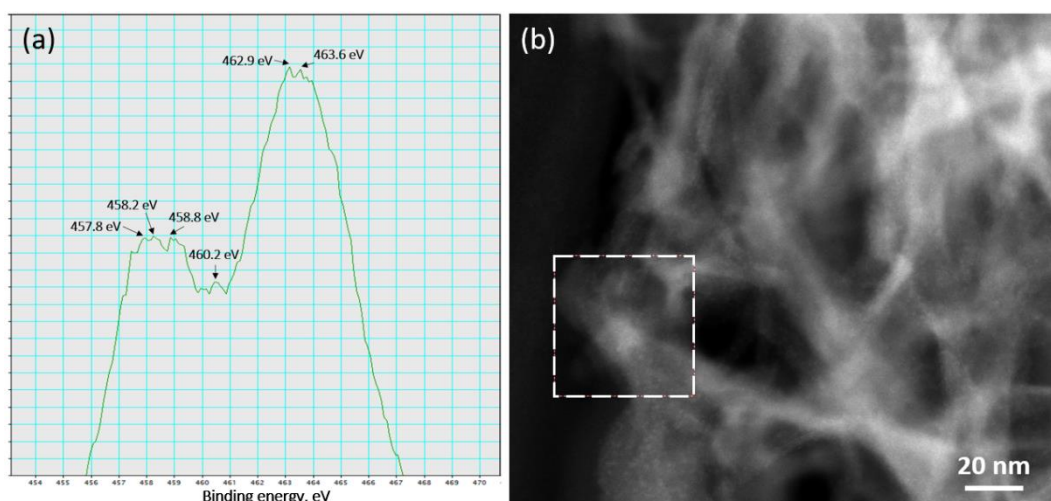
Figure 6.9 (a) EELS spectrum at Ti binding energy range. (b) Low magnification HAADF image of alkalised-$Ti_3C_2T_x$ nanowire. The selected area is the area for EELS spectrum collection.

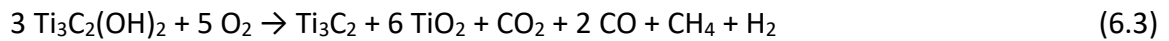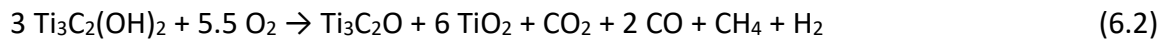**Table 6.2** Orbitals and assignments of the binding energies of Ti in EELS spectrum.

Binding energy, eV	Orbital energy level	Assignment
457.8	Ti $2P_{3/2}$	Ti (III)
458.2		
458.8	Ti $2P_{3/2}$	Ti-O in TiO_2
460.2	Ti $2P_{1/2}$	Ti-C
462.9, 463.6	Ti $2P_{1/2}$	Ti (III)

The split peaks of Ti binding energy area are interpreted and assigned, as shown in **Table 6.2**.[24,26,27] From the EELS assignments, we can conclude that in the nanowire domain, there are Ti^{3+}, TiO_2 (Ti^{4+}). However, no split peaks of Ti^{2+} are shown.[27,28] If there are any Ti^{2+} binding energy signals, they would appear between 454.0 to 456.0 eV.[29,30] While those peaks from Ti^{2+} are very easily to be covered by the peaks from Ti^{3+} and Ti^{4+} which are above 457.0 eV, making the peaks of Ti^{2+} unperceivable and the existence of Ti^{2+} debatable.

For Ti_3AlC_2, $Ti_3C_2(OH)_2$, Ti_3C_2O, the oxidation states of Ti and C are the same because there are only changes of functional groups from -Al to 2 -OH and -O, as shown in **Figure 6.5**. The oxidation state of Ti should be positive. The total number of the oxidation states of Ti cations in $Ti_3C_2T_x$ and Ti_3C_2 would be a sum of +2, +3 and +4. And the oxidation state of C can be from -4 to +4.

Taking $Ti_3C_2(OH)_2$ for example, presumably, if C are all in the lowest oxidation state, -4, considering the total oxidation number of 2 OH^- groups, -2, to achieve neutral, the highest total oxidation number of Ti ions can only reach +10. Therefore, there will be no circumstance for the 3 Ti ions to be all +4. Furthermore, $Ti_3C_2(OH)_2$ is the main phase undergoing reaction in KOH environment, because the oxidation states of the Ti ions are not all +4, to produce TiO_2 with Ti^{4+}, oxidation must happen.

On the other hand, H_2, CH_4, CO and CO_2 have been reported to be produced during the oxidation of MXenes.[31,32] During the stirring in KOH solution, O_2 molecules are continuously introduced into the solution, making the oxidation realistic and achievable. For the time being, the reactions to produce Ti_3C_2O and Ti_3C_2 can now be deduced as follows,

$$3\ Ti_3C_2(OH)_2 + 5.5\ O_2 \rightarrow Ti_3C_2O + 6\ TiO_2 + CO_2 + 2\ CO + CH_4 + H_2 \qquad (6.2)$$

$$3\ Ti_3C_2(OH)_2 + 5\ O_2 \rightarrow Ti_3C_2 + 6\ TiO_2 + CO_2 + 2\ CO + CH_4 + H_2 \qquad (6.3)$$

Furthermore, due to the law of charge conservation, from the reactions, the oxidation states of Ti ions can be deduced in $Ti_3C_2(OH)_2$, Ti_3C_2O and Ti_3C_2. In $Ti_3C_2(OH)_2$ and Ti_3C_2O, 1 Ti ion is +2 while the other two are +3 and the oxidation state of C atoms are all -3. The crystal structure of Ti_3AlC_2 is similar to that of $Ti_3C_2(OH)_2$ except for the substitution of the Al layers by the 2*-OH layers. We then conclude that the oxidation of Al would be -2 which equals to 2 OH^-. The electron configuration of Al is $[Ne]3s^23p^1$. Two additional electron makes the configuration of Al^{2-} be $[Ne]3s^23p^3$. The 3p orbital is half-full and relatively stable, therefore the oxidation state of Al^{2-} is rational.

As for Ti_3C_2, from **Figure 6.5(d)**, the T_x layers are extracted, leaving only the chain of Ti-C-Ti-C-Ti in c axis. With the removal of -OH layers, we reckon the electrons from -OH layers are transferred to the negative C atoms. Then the 2 C would be -4 and Ti is the same as $Ti_3C_2(OH)_2$.

**Table 6.3** Oxidation states of the respective elements of all the $Ti_3C_2T_x$.

MXene	Ti	C	Termination
Ti_3AlC_2		-3	Al^{2-}
$Ti_3C_2(OH)_2$		-3	OH^-
Ti_3C_2O	+2, +3	-3	O^{2-}
Ti_3C_2		-4	

Table 6.3 demonstrates the proposed oxidation states of the respective elements in the $Ti_3C_2T_x$ formulae. Nevertheless, oxidation state is a formalism calculated based on the assumption that the ionic bonds preserve 100% charges without considering the electronegativity and electron density just to make the understanding of chemical reactions simpler.[33] In this work, oxidation states of the elements are analysed to reasonably align with the proposed oxidation reactions.

6.3.4 Amorphous Layers to Prevent Further Degradation

For the time being, we deduce the morphological degradation is derived from the continuous oxidation of the structure by O_2. And the corresponding reactions are demonstrated in equations (6.2) and (6.3).

Theoretically, because the oxidation states of Ti cations are not all +4 in Ti_3C_2O and Ti_3C_2, with constant stirring in open air, further oxidation by O_2 will keep proceeding until all the Ti cations are oxidised to TiO_2 nanoparticles. However, 1 D nanowires composed by Ti_3C_2O and Ti_3C_2 seem to be the terminated morphology. As shown in **Figure 6.10**, there are amorphous coating layers attached on the surface of the nanowires. Abundant TiO_2 nanoparticles are also attached on the nanowires. The amorphous phase and stable TiO_2 nanoparticles produced from the oxidation cover the Ti_3C_2O and Ti_3C_2 nanowires, prohibiting further oxidation of Ti_3C_2O and Ti_3C_2 by O_2 to the ultimate TiO_2 phase.
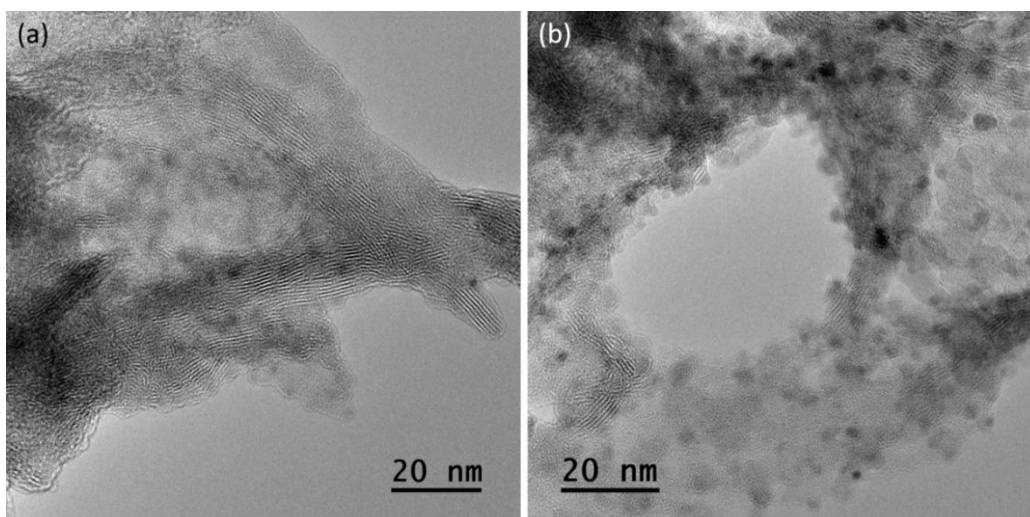
Figure 6.10 (a, b) HRTEM images of nanowires with attached amorphous coating layers and accompanying TiO_2 nanoparticles.

As we can see from equations (6.2) and (6.3), to generate 1 portion of Ti_3C_2O or Ti_3C_2, there are 6 portions of the by-product TiO_2 produced stoichiometrically. Additionally, the EDX spectrum in **Figure 6.4** indicates the abundance of O in the nanowire area, which majorly originates from TiO_2. And considering the reported wide existence of amorphous TiO_2[34,35], it is hypothesised that the main phase of amorphous coating layers is amorphous TiO_2.

Furthermore, as shown in **Figure 6.7** and **Figure 6.11**, the nanowires do not appear to preserve long chain of Ti_3C_2O and Ti_3C_2, but are discontinuous. Due to the oxidation, the crystal structure of $Ti_3C_2(OH)_2$ is decomposed, creating amorphous $Ti_3C_2(OH)_2$. After the oxidation, some produced Ti_3C_2O and Ti_3C_2 may not undergo the build of their crystal structures, leaving in the amorphous status. Therefore, we hypothesis that with the majority being TiO_2, amorphous $Ti_3C_2(OH)_2$, Ti_3C_2O and Ti_3C_2 also comprise the amorphous coating layers. Those amorphous coating layers prevent the contact of O_2 with crystalline nanowires and further oxidation, resulting in the 1D final nanowire morphology.
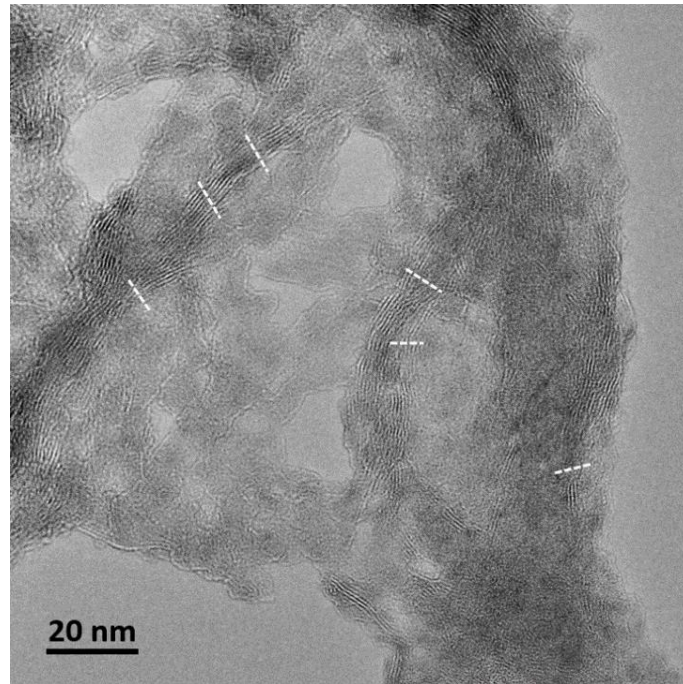
Figure 6.11 HRTEM image of nanowires which demonstrates the discontinuity. The white dashed line indicates the boundaries between the crystalline fringes. Additionally, the amorphous domains can be clearly seen in accompany with the crystal fringes.

6.3.5 Formation Mechanism of Nanowire Clusters

Based on the above analyses, we now propose the formation mechanism of the morphological degradation from MXene layered structure to nanowire clusters and the oxidation process of $Ti_3C_2(OH)_2$ leading to the formation of Ti_3C_2O and Ti_3C_2 nanowires.
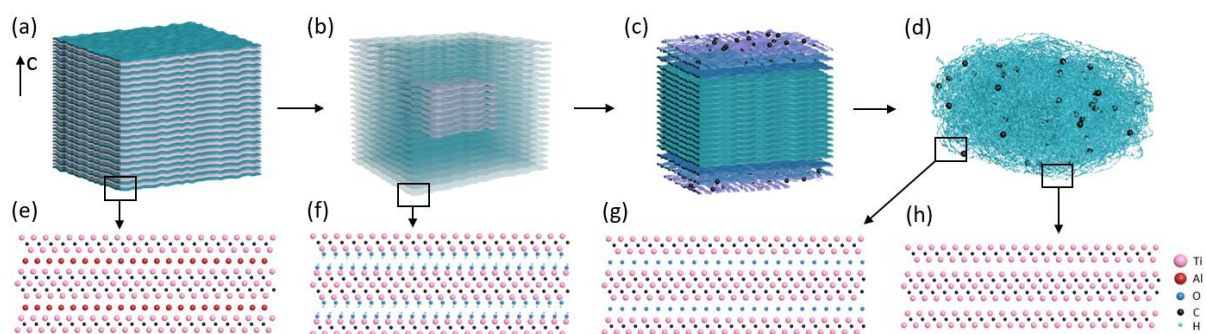

Figure 6.12 Morphological degradation route to generate nanowire cluster. (a) Ti_3AlC_2 solid. (b) $Ti_3C_2(OH)_2$ layered structure. (c) $Ti_3C_2(OH)_2$ layered structure in the process of oxidation and degradation. The surface layers are decomposing to strips and wires. (d) Nanowire cluster. The dark dots in (c) and (d) indicate the produced TiO_2 nanoparticles. (e) Crystal structure of Ti_3AlC_2 in the solid. (f) Crystal structure of $Ti_3C_2(OH)_2$ in the layered structure. (g, h) Crystal structure of Ti_3C_2O and Ti_3C_2 in the nanowire cluster.

From the SEM image series over time (**Figure 6.2**), dimensional degradation from Ti_3AlC_2 solids, to $Ti_3C_2(OH)_2$ MXene layers (3 D) to thick strips (2 D) and to nanowires (1 D) is the basic route for generating nanowire clusters morphologically. HRTEM images (**Figure 6.7**) indicate that the nanowires are Ti_3C_2O and Ti_3C_2 phases produced from the oxidation of $Ti_3C_2(OH)_2$. **Figure 6.12** demonstrates the degradation process morphologically with the detailed corresponding crystal structure illustrations.

Initially, with the treatment of LiF/HCl, Ti_3AlC_2 solid transform to layered $Ti_3C_2T_x$ structure. $Ti_3C_2(OH)_2$ is the main $Ti_3C_2T_x$ phase to be produced by LiF/HCl method. At crystal structure scale, the transformation is triggered by the exfoliation of -Al layers by -OH layers (**Figure 6.12a** and **b**).

K^+ cations could intercalate into the gaps between MXene layers, expanding the d-spacing during the alkalisation process, allowing O_2 molecules go into the layers to oxidise $Ti_3C_2(OH)_2$.[8,14] With the continuous introduction of O_2 into the alkali solution during stirring, the layers keep being oxidised and dimensionally decompose to strips and nanowires (**Figure 6.12c** and **d**).

Crystallographically, the continuous oxidation of the $Ti_3C_2(OH)_2$ to Ti_3C_2O and Ti_3C_2 is the intrinsic reason for the morphological degradation. **Figure 6.13** demonstrates the crystal structure transformation along with the morphological degradation during the oxidation.
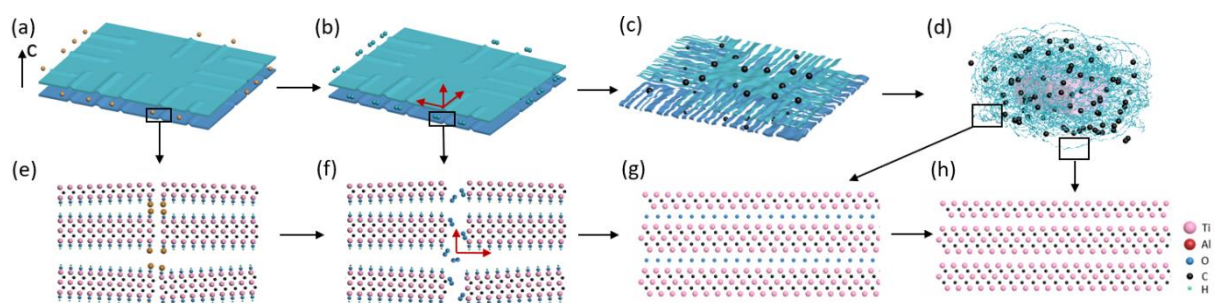
Figure 6.13 (a) Two layers of $Ti_3C_2(OH)_2$ MXene with the intercalation of K cations. (b) The attack of O_2 towards the K^+ intercalated sites. The red arrows indicate the oxidation directions. (c) The decomposed $Ti_3C_2T_x$ strips and wires. (d) Nanowire cluster with Ti_3AlC_2 core and TiO_2 nanoparticles. (e) Crystal structure of $Ti_3C_2(OH)_2$ with K^+ intercalation. (f) Intercalated $Ti_3C_2(OH)_2$ with the attack of O_2 molecules. The red arrows indicates the oxidation directions. (g, h) Crystal structure of Ti_3C_2O and Ti_3C_2 in the nanowire cluster.

To trigger the phase transformation, from the structural scale, K^+ ions intercalate the $Ti_3C_2(OH)_2$ crystal structures, expanding the d-spacings (**Figure 6.13e**). With the expanded

sites in the crystal structure, O_2 molecules continuously attack the expanded structure (**Figure 6.13f**). To achieve the morphological degradation of $Ti_3C_2(OH)_2$, O_2 can corrode the structure in all directions. The inward attacking behaviour is like a scissor, cutting the layer to strips and to nanowires through the intercalated sites. The oxidation can also happen in horizontal and vertical directions, cracking the structure.

Figure 6.13 emphasises the oxidation process of the $Ti_3C_2(OH)_2$ crystal structure. As the oxidation by O_2 executes, the structure is cracked. O_2 molecules contact with -OH, Ti and C. Subsequently, electron transfer occurs, triggering the oxidation reaction at crystal structure scale as demonstrated in equations (6.2) and (6.3).

As aforementioned, there are Ti^{2+} and Ti^{3+} and C^{3-} in $Ti_3C_2(OH)_2$ (**Table 6.3**). The electrons in Ti and C are oxidised by O_2 molecules, producing TiO_2, CO_2 and CO. While a portion of C and H atoms acquire the electrons, producing CH_4 and H_2. Abundant TiO_2 is produced, forming amorphous TiO_2 and crystalline TiO_2 (rutile phase). Oxidation creates Ti_3C_2O and Ti_3C_2, also either in amorphous phase or crystalline phase. The two phases undergo crystallisation to form crystalline discontinuous Ti_3C_2O and Ti_3C_2 nanowires which are covered by amorphous layers composed of TiO_2, Ti_3C_2O and Ti_3C_2, preventing further oxidation of the structure, leading to the finalised nanowire interconnected cluster morphology.

6.4 Conclusion

To summarise, this work demonstrates a top-down degradation way to prepare crystalline nanomaterials. The nanowire interconnected cluster morphology is prepared via the KOH aqueous solution treatment with continuous stirring. Based on the SEM images at different growth stages, morphologically, the formation route from layers to strips and to wires is illustrated. Phase identification implementing electron microscopic and spectroscopic information indicates the phase transformation is from $Ti_3C_2(OH)_2$ to Ti_3C_2O, Ti_3C_2 and TiO_2.

The oxidation reactions of $Ti_3C_2(OH)_2$ to create Ti_3C_2O and Ti_3C_2 are deduced to be the intrinsic reason of morphological degradation. From the perspective of crystal structure, with K^+ intercalation and d-spacing expansion, O_2 molecules are offered the opportunity to contact with the Ti^{2+}, Ti^{3+} and C^{3-} in the $Ti_3C_2(OH)_2$ crystal structure, inducing the continuous breakage

of the structure. Final morphology of nanowires composed of Ti_3C_2O and Ti_3C_2 with amorphous coating layers is then produced.

Even though the mechanism of producing Ti_3C_2O and Ti_3C_2 interconnected nanowires have been proposed. There are many aspects worth exploration. The quantitative elemental composition of the amorphous phase covering the crystalline nanowires has not been addressed. The concentration of O_2 in the stirring solution during the reaction and the produced gases (CH_4, H_2, CO, CO_2) may be detected and quantified to elucidate the oxidation reaction thoroughly. Electron density of Ti, C and O can also be further investigated to examine the electron transfer at structural scale.

References

1   M. Naguib, M. Kurtoglu, V. Presser, J. Lu, J. Niu, M. Heon, L. Hultman, Y. Gogotsi and M. W. Barsoum, *Adv. Mater.*, 2011, **23**, 4248–4253.

2   M. Naguib, V. N. Mochalin, M. W. Barsoum and Y. Gogotsi, *Adv. Mater.*, 2014, **26**, 992–1005.

3   J. Li, X. Yuan, C. Lin, Y. Yang, L. Xu, X. Du, J. Xie, J. Lin and J. Sun, *Adv. Energy Mater.*, 2017, **7**, 1602725.

4   M. R. Lukatskaya, O. Mashtalir, C. E. Ren, Y. Dall'Agnese, P. Rozier, P. L. Taberna, M. Naguib, P. Simon, M. W. Barsoum and Y. Gogotsi, *Science*, 2013, **341**, 1502–1505.

5   S. J. Kim, M. Naguib, M. Zhao, C. Zhang, H. T. Jung, M. W. Barsoum and Y. Gogotsi, *Electrochim. Acta*, 2015, **163**, 246–251.

6   M. Cao, F. Wang, L. Wang, W. Wu, W. Lv and J. Zhu, *J. Electrochem. Soc.*, 2017, **164**, A3933–A3942.

7   Y. Dong, Z. S. Wu, S. Zheng, X. Wang, J. Qin, S. Wang, X. Shi and X. Bao, *ACS Nano*, 2017, **11**, 4792–4800.

8   P. Lian, Y. Dong, Z. S. Wu, S. Zheng, S. Wang, C. Sun, J. Qin, X. Shi and X. Bao, *Nano Energy*, 2017, **40**, 1–8.

9   Q. Kong, H. Zhang, Z. Yuan, J. Liu, L. Li, Y. Fan, G. Fan and B. Liu, *ACS Sustain. Chem. Eng.*, 2020, **8**, 4755–4763.

10   W. Yuan, L. Cheng, Y. An, H. Wu, N. Yao, X. Fan and X. Guo, *ACS Sustain. Chem. Eng.*, 2018, **6**, 8976–8982.

11   C. E. Shuck, M. Han, K. Maleski, K. Hantanasirisakul, S. J. Kim, J. Choi, W. E. B. Reil and Y. Gogotsi, *ACS Appl. Nano Mater.*, 2019, **2**, 3368–3376.

12   T. Zhang, L. Pan, H. Tang, F. Du, Y. Guo, T. Qiu and J. Yang, *J. Alloys Compd.*, 2017, **695**, 818–826.

13   J. C. Lei, X. Zhang and Z. Zhou, *Front. Phys.*, 2015, **10**, 276–286.

14   M. R. Lukatskaya, O. Mashtalir, C. E. Ren, Y. Dall'Agnese, P. Rozier, P. L. Taberna, M. Naguib, P. Simon, M. W. Barsoum and Y. Gogotsi, *Science*, 2013, **341**, 1502–1505.

15   E. Lee, A. Vahidmohammadi, B. C. Prorok, Y. S. Yoon, M. Beidaghi and D. J. Kim, *ACS Appl. Mater. Interfaces*, 2017, **9**, 37184–37190.

16   A. D. Dillon, M. J. Ghidiu, A. L. Krick, J. Griggs, S. J. May, Y. Gogotsi, M. W. Barsoum and A. T. Fafarman, *Adv. Funct. Mater.*, 2016, **26**, 4162–4168.

17   D. Xiong, X. Li, Z. Bai and S. Lu, *Small*, 2018, **14**, 1–29.

18   Z. Wei, Z. Peigen, T. Wubian, Q. Xia, Z. Yamei and S. ZhengMing, *Mater. Chem. Phys.*, 2018, **206**, 270–276.

19   Z. Fan, Y. Wang, Z. Xie, D. Wang, Y. Yuan, H. Kang, B. Su, Z. Cheng and Y. Liu, *Adv. Sci.*, 2018, **5**, 1800750.

20   B. Anasori, M. R. Lukatskaya and Y. Gogotsi, *2D metal carbides and nitrides (MXenes) for energy storage*, 2017.

21   J. Halim, PhD Thesis, Drexel University, 2018.

22   N. Li, Y. Jiang, C. Zhou, Y. Xiao, B. Meng, Z. Wang, D. Huang, C. Xing and Z. Peng, *ACS Appl. Mater. Interfaces*, 2019, **11**, 38116–38125.

23   C. Yang, Y. Liu, X. Sun, Y. Zhang, L. Hou, Q. Zhang and C. Yuan, *Electrochim. Acta*, 2018, **271**, 165–172.

24   H. Pazniak, I. A. Plugin, M. J. Loes, T. M. Inerbaev, I. N. Burmistrov, M. Gorshenkov, J. Polcak, A. S. Varezhnikov, M. Sommer, D. V. Kuznetsov, M. Bruns, F. S. Fedorov, N. S. Vorobeva, A. Sinitskii and V. V. Sysoev, *ACS Appl. Nano Mater.*, 2020, **3**, 3195–3204.

25   X. Zhu, B. Liu, H. Hou, Z. Huang, K. M. Zeinu, L. Huang, X. Yuan, D. Guo, J. Hu and J. Yang, *Electrochim. Acta*, 2017, **248**, 46–57.

26   Q. Yue, J. Sun, S. Chen, Y. Zhou, H. Li, Y. Chen, R. Zhang, G. Wei and Y. Kang, *ACS Appl. Mater. Interfaces*, 2020, **12**, 18570–18577.

27   J. Liu, X. Ma, L. Yang, X. Liu, A. Han, H. Lv, C. Zhang and S. Xu, *RSC Adv.*, 2018, **8**, 7142–7151.

28   H. Zhang, X. Shi, A. Tian, L. Wang and C. Liu, *Appl. Surf. Sci.*, 2018, **436**, 579–584.

29   Q. Wu, C. Zhang, B. Zhang, X. Li, Z. Ying, T. Liu, W. Lin, Y. Yu, H. Cheng and F. Zhao, *J. Colloid Interface Sci.*, 2016, **463**, 75–82.

30   V. V. Atuchin, V. G. Kesler, N. V. Pervukhina and Z. Zhang, *J. Electron Spectros. Relat. Phenomena*, 2006, **152**, 18–24.

31   S. Huang and V. N. Mochalin, *Inorg. Chem.*, 2019, **58**, 1958–1966.

32   S. Huang and V. N. Mochalin, *ACS Nano*, 2020, **14**, 10251–10257.

33   A. Walsh, A. A. Sokol, J. Buckeridge, D. O. Scanlon and C. R. A. Catlow, *Nat. Mater.*, 2018, **17**, 958–964.

34   S. Sun, P. Song, J. Cui and S. Liang, *Catal. Sci. Technol.*, 2019, **9**, 4198–4215.

35   M. A. Vargas and J. E. Rodríguez-Páez, *J. Non. Cryst. Solids*, 2017, **459**, 192–205.

Chapter 7 Conclusions and Future Work

7.1 Conclusions

To conclude, synthesised crystals are studied on their novel morphologies and related crystal growth mechanisms primarily by applying electron microscopy, diffractometry and spectroscopy techniques. The corresponding non-classical crystal growth mechanisms are proposed in the expression of schematic modelling and visualisation.

Pseudo-icosahedral Cu crystals are discovered to possess independent 20 {111} facets and distinct gaps instead of twin defects, which challenges current multi-twinning mechanism. During the solvothermal synthesis, $Cu_4SO_4(OH)_6 \cdot H_2O$ microflakes and Cu_2O spherulites appear chronologically as intermediate phases. Multi-functional PVP acts as nanoparticle dispersant, weak reducing agent and structural holding surfactant in the process. Based on the crystallographic and morphological features at different growth stages, a growth route is revealed involving the two intermediate phases, the production of separate {111} facets on spherical Cu/PVP particles and the extension of {111} facets inwards. We reckon this work sheds light on the growth mechanism of polyhedral morphology and multi-twinned structure.

In the crystal growth system to form pseudo-icosahedral Cu crystals, Cu_2O/PVP spherulites transform to spherical particles consisting of polyhedral surface crystals fleetly and are reduced to Cu subsequently. Substituting the starting reactant $CuSO_4 \cdot 5H_2O$ by $Cu(NO_3)_2 \cdot 2H_2O$, Cu_2O/PVP spherulites are managed to be preserved. The intrinsic dipole field of Cu_2O nanocrystallites and the polarity of PVP are deduced to be the driving forces to hierarchically form spherulites with needle-like bundles containing Cu_2O nanocrystallites. This study provides a novel example of dipole field driven crystal growth.

Photoluminescent Cs_4PbBr_6 rhombohedral microscale crystals with embedded $CsPbBr_3$ nanocrystallites are synthesised using antisolvent precipitation method. Utilising HRTEM, the embedding feature is captured. With d-spacing approximation, the model of embedding phenomenon is schematically drawn. Considering the quick crystallisation and amorphous layer on the crystals, amorphous precursor Cs_xPbBr_y with Cs : Pb ratio at 3 : 1 is proposed. Cs is in a rich status, leading to the crystallisation of Cs_4PbBr_6. As Cs ions are consumed more quickly, local Pb-rich domains appear, resulting in the formation of $CsPbBr_3$ nanocrystallites,

producing embedded feature. Different antisolvents are examined on their impacts in crystallographic and morphologic aspects. Homogeneous mixture is required to induce the low solubility and crystal precipitation. Transformation from Cs_4PbBr_6 to $CsPb_2Br_5$ and $CsPbBr_3$ is discussed, which is triggered by the high solubility of CsBr in water. This work is a vanguard in revealing the formation mechanism of crystal embedding phenomenon in spite of the beam sensitivity of Cs_4PbBr_6.

Ti$_3$C$_2$O and Ti$_3$C$_2$ nanowire clusters are produced by the dimensionally degradation from $Ti_3C_2T_x$ layered structure to interconnected layers, strips and nanowires. Phase transformation from $Ti_3C_2(OH)_2$ to Ti_3C_2O and Ti_3C_2 is proved by HRTEM. The oxidation of $Ti_3C_2T_x$ induces the morphology degradation.

Overall, crystals with novel morphologies, Cu pseudo-icosahedra, Cu_2O/PVP spherulites, Cs_4PbBr_6 rhombohedral crystals with embedded $CsPbBr_3$ nanocrystallites, Ti_3C_2O and Ti_3C_2 nanowire clusters, are investigated. The corresponding growth mechanisms are successfully proposed. The projects provide new insights of non-classical crystal growth.

7.2 Future Work

Although the growth mechanisms of the studied crystals are proposed, there are several aspects and details to be investigated and addressed.

In the solvothermal system to individually prepare Cu pseudo-icosahedra and Cu_2O/PVP spherulites, the starting materials applied are $CuSO_4 \cdot 5H_2O$ and $Cu(NO_3)_2 \cdot 2H_2O$. Using $CuSO_4 \cdot 5H_2O$, the intermediate phase, posnjakite, is generated initially, and Cu^+ does not stay for a long time but is quickly reduced to Cu. While using $Cu(NO_3)_2 \cdot 2H_2O$, Cu_2O spherulites are quickly synthesised and also preserved. In-depth discussion of the functions of ion groups (sulphate and nitrate) during the synthesis may be necessary. PVP demonstrates its reducing ability, while due to the complexity of its formula, the change of PVP at molecular scale is not revealed. Further spectroscopic characterisation can be attempted to identify the produced polymer product of PVP after reducing Cu^{2+}.

Amorphous layers and amorphous precursors are regarded to be important for the preparation of Cs_4PbBr_6 rhombohedral crystals with embedded $CsPbBr_3$ nanocrystallites and Ti_3C_2O and Ti_3C_2 nanowire clusters. However, the localised precise composition of amorphous

phase is not yet determined. EDX may not provide accurate quantitative results locally. TEM characterisation with low dose electron beam is necessary to get impeccable images of the crystal fringes. And further modelling of the embedded phenomenon is acquired to verify the orientation of $CsPbBr_3$ nanocrystallites in Cs_4PbBr_6 matrix.

For $Ti_3C_2T_x$ project, electron density transfer from Ti to O merits examine to prove the phase transformation at structural scale. Collaboration in computational chemistry may be a good alternative. Meanwhile, how the amorphous $Ti_3C_2T_x$ production from oxidation recombines to Ti_3C_2O and Ti_3C_2 needs to be further addressed. We believe the detailed transformation may contribute to the understanding of profound crystal growth mechanism.

A parallel project to synthesis Cs_4PbI_6 rhombohedral crystals with embedded $CsPbI_3$ nanocrystallites has also been proceeded. The embedding phenomenon is also identified. Meanwhile, further experiments can be done to examine the growth mechanism. If the mechanism is consistent with Cs_4PbBr_6/$CsPbBr_3$, a universal growth route of Cs_4PbX_6 (X represents halogen elements) crystals with embedded $CsPbX_3$ may be proposed to demonstrate such embedding phenomenon.

From the perspective of electron microscope operations, Cs_4PbBr_6/$CsPbBr_3$ and Ti_3C_2O /Ti_3C_2 specimens are both beam sensitive, which makes it demanding and difficult to capture HRTEM images with good quality. The control of electron microscope conditions is pivotal for the study of electron beam sensitive materials. We have demonstrated the success of capturing the two beam sensitive materials. Endeavour is worth to be done in visualising more beam sensitive crystalline materials using electron microscopes.

Furthermore, non-classical crystal growth is still a significant research area in material science and crystal engineering. Novel morphologies and their growth routes beyond the cases in this project require to be addressed.